Wang, P., Prell, W.L., Blum, P., et al., 2000
Proceedings of the Ocean Drilling Program, Initial Reports Volume 184

9. Site 1148[1]

Shipboard Scientific Party[2]

BACKGROUND AND OBJECTIVES

The objectives of Site 1148 (SCS-5C) were to (1) recover a continuous sequence of hemipelagic sediments to reconstruct the early paleoclimate history (Oligocene to Miocene) of the South China Sea (SCS); (2) identify the onset of monsoonal variability in the South China Sea and to establish its evolution in the Oligocene–Miocene interval; and (3) establish whether the Oligocene–Miocene pattern of accumulation rates is consistent with models of the SCS continental margin evolution and with changes in Himalayan-Tibetan uplift, monsoon intensification, and sea-level change.

Site SCS-5C was initially located near the base of the continental slope on seismic Line SO95-5 at common depth point 7500 (Figs. **F5,** p. 17, **F15,** p. 30, both in the "Seismic Stratigraphy" chapter). Pollution Prevention and Safety Panel evaluation of the *JOIDES Resolution* seismic Line JR184-1 moved the final Site 1148 location ~1.05 nmi east to 18°50.169′N, 116°33.939′E, at shotpoint 1980 at a water depth of ~3294 m (Fig. **F9,** p. 53, in the "Leg 184 Summary" chapter; Figs. **F5,** p. 17, **F16B,** p. 32, both in the "Seismic Stratigraphy" chapter). This placed Site 1148 within the scar of a slump feature. Site 1147, ~0.45 nmi upslope from Site 1148, was cored to recover surface sediments missing at Site 1148 (see **"Background and Objectives,"** p. 1, in the "Site 1147" chapter). The approved penetration depth of Site 1148 was 700 meters below seafloor (mbsf), and the sediment thickness above acoustical basement was ~0.85 s two-way traveltime (TWT), or ~790 mbsf.

Site 1148 (SCS-5C) is located on the lower continental slope of China near the continent/ocean crust boundary. Drilling at the site was planned to reach Oligocene-age sediments and possibly recover sediments coincident with the major postrifting subsidence of the basin. Therefore, we expected to recover mostly hemipelagic muds and silts and possibly some shallow-water facies near the base of the hole. On

[1]Examples of how to reference the whole or part of this volume.
[2]Shipboard Scientific Party addresses.

Ms 184IR-109

the basis of the *Sonne* seismic records (Fig. F15, p. 30, in the "Seismic Stratigraphy" chapter) and their correlation with Chinese reflector stratigraphy (H.-K. Wong, pers. comm., 1998), Site 1148 was targeted for 700 m penetration. Initial interpretation of the seismic stratigraphy identified Reflector T_1 (top of Miocene, 5.2 Ma) at ~0.2 s subsurface and Reflector T_7 (mid-Oligocene, ~30 Ma) at ~0.52 s subsurface. These same reflectors are clear in the *JOIDES Resolution* seismic lines (Fig. F16A, p. 31, F16B, p. 32, in the "Seismic Stratigraphy" chapter), but their age assignments are somewhat in doubt. On the basis of in situ downhole velocity logs from Site 1146, the 700 mbsf penetration at Site 1148 is equivalent to ~0.78 s subsurface. This revised TWT indicates that Site 1148 should penetrate both T_1 and T_7 reflectors and come within ~100 m of the basement reflector (T_g).

We hoped that Site 1148 would shed some light on the opening of the SCS and its relation to the Cenozoic deformation of Asia. The Central Basin of the SCS is underlain by oceanic crust that was actively spreading from ~32 to 16 Ma (Briais et al., 1993). During and after the seafloor spreading phase, the continental margin of China experienced crustal extension, subsidence, and rapid deposition of terrigenous and marine sediments. On the continental shelf near the Pearl River Mouth Basin (close to the Leg 184 sites), the sedimentary basins have a two-layer structure. The lower section is characterized by half-grabens formed during Paleogene rifting and filled with syn-rift sediments, whereas the upper section is characterized by a wider distribution of deposits formed during the broad subsidence during the Neogene (Ru et al., 1994). The Cenozoic stratigraphy of the Pearl River Mouth Basin shows nonmarine intercalations in the northern part of the basin that thin and decrease in proportion southward toward the deeper part of the slope (Jiang et al., 1994; Wu, 1994; Huang, 1997). Major depositional hiatuses have been observed on the shelf in the lower part of the lower Miocene, near the end of the middle Miocene, and around the Pliocene/Pleistocene boundary (L. Huang, pers. comm., 1998). The lower accumulation rates and greater penetration at Site 1148 should recover a record that will establish stratigraphic ties between the SCS marine record and the terrestrial record of China. In particular, the recovery of sediments associated with the T_1 and T_7 reflectors should help to correlate the terrestrial and marine records and thereby constrain the timing of basin subsidence, changes in denudation/accumulation, and monsoon intensification.

The original drilling plan for Site 1148 included three advanced hydraulic piston corer (APC) holes to refusal, one extended core barrel (XCB) hole to refusal, and a rotary core barrel (RCB) hole to the target depth. Hole 1148A was to be APC/XCB cored to refusal or to the target depth of 700 mbsf. Depending on the depth of XCB refusal, Hole 1148B was designed to be APC/XCB cored to a target depth that would ensure time to use the RCB for the deeper section. For Hole 1148C, we planned to change to the RCB, wash down to the depth of XCB refusal, and RCB core to the 700 mbsf target depth. We planned to log the deepest and best-conditioned hole with a standard program, including the triple combination tool, Formation MicroScanner (FMS)–sonic tool suite, and geological high-resolution magnetic tool (GHMT). Hole 1148A was scheduled to be logged if it reached the target depth of 700 mbsf and hole conditions were adequate. Alternatively, we planned to log Hole 1148C, which would be the deepest RCB-cored section. Hole 1148A reached the depth of 704 mbsf and was successfully logged. Permission

to deepen Hole 1148B to basement, or 850 mbsf, was received. To achieve the target depth, intervals between 145 and 440 mbsf and between 646 and 700 mbsf were drilled ahead. Given the leg objectives and the available time, we ultimately modified the drilling plan to include two deep holes in which to recover the Oligocene–Miocene section.

OPERATIONS

Site 1148 (Proposed Site SCS-5C)

The beacon was deployed on the Global Positioning System coordinates of Site 1148 (proposed site SCS-5C) at 2015 hr on 30 March.

Hole 1148A

Hole 1148A was spudded with the APC at 2215 hr on 30 March. The seafloor depth calculated from the recovery of the first core was 3308.7 m. Piston coring advanced with 16 APC cores to 143.3 mbsf with an average recovery of 101.1%. The cores were oriented starting with Core 4H. During piston coring, downhole temperature measurements with the advanced hydraulic piston corer temperature tool (APCT) were obtained at 29, 58, and 105 mbsf. Based upon these measurements, a temperature gradient of 83°C/km was calculated (see **"Physical Properties,"** p. 23).

Coring was resumed with the XCB and advanced to 450 mbsf with 100% recovery. At 152.9 mbsf, the Davis-Villinger temperature probe was deployed. The data obtained at 153 mbsf confirmed the temperature gradient calculated from the three APCT measurements. At ~460 mbsf, a sharp transition from clayey chalk to an underconsolidated clayey formation was encountered, and recovery dropped off sharply. From 460 to ~600 mbsf, the average recovery was 47%, with several cores around 500 mbsf having almost no recovery. In an effort to increase recovery, some core barrels were recovered after advancing only 5 m instead of the nominal 9.6 m. Between 600 mbsf and the bottom of the hole at 704 mbsf, average recovery returned to almost 100%. The XCB average recovery for Hole 1148A was 86.9%; the average recovery for this hole was 89.8% (Tables **T1, T2,** both also in **ASCII format**).

T1. Site 1148 coring summary, **p. 87.**

T2. Site 1148 coring summary by section, **p. 90.**

Headspace analysis indicated that the concentration of methane was below 10 ppmv down to 430 mbsf. It then increased gradually to a maximum concentration of 569 ppmv at 580 mbsf. More complex hydrocarbon molecules were not detected above 468 mbsf. Below this depth, the abundance of both ethane and propane followed a trend similar to that of methane, peaking at 570–580 mbsf (25 and 10 ppmv, respectively). Butane and pentane were detected from samples taken below 570 mbsf, with maximum readings of 28 and 32 ppmv, respectively, from the last core (77X) (see **"Organic Geochemistry,"** p. 16).

A wiper trip was made up to 107 mbsf and then back to bottom. Approximately 19 m of soft fill was found at the bottom of the hole. The hole was washed and reamed from 685 to 704 mbsf. After the hole was flushed with a 30-bbl mud treatment, the bore was displaced with an additional 215 bbl of sepiolite. The bit was pulled back and positioned at 107 mbsf for logging. Wireline logging in Hole 1148A was completed with three successful runs: triple combo (111.5–711 mbsf), FMS-sonic (200.7–711 mbsf), and GHMT (200–711 mbsf). With the exception of a

washed-out interval above 200 mbsf, the hole was in the best condition of any of those logged on this leg. The drill string was lowered after the first logging run because of several zones of reduced hole diameter that were attributed to swelling clays. After logging, the hole was abandoned with 30 bbl of 10.5-lb/gal heavy mud. The bit cleared the seafloor at 1600 hr on 5 April.

Hole 1148B

The vessel was offset 20 m east of Hole 1148A. Before spudding the new hole, a near-bottom-water temperature was obtained with the APCT. Hole 1148B began at 2045 hr from a seafloor depth of 3303.4 m, and piston coring advanced to 145.1 mbsf with 96.2% recovery. Several liners split during the piston coring, which resulted in less than expected recovery. Cores were oriented starting with Core 3H. A 4-m interval was washed ahead from 36.6 to 40.6 mbsf to ensure a stratigraphic overlap with Hole 1148A.

While piston coring in Hole 1148B, we received permission from the Ocean Drilling Program to deepen Hole 1148B to basement or to a maximum of 850 mbsf, as long as rigorous safety monitoring did not preclude further drilling. After piston coring in Hole 1148B, it was decided to drill ahead with a center bit in place through the interval from 145 to 440 mbsf that was well recovered in Hole 1148A in order to save time for deepening the site. The XCB recovery from 460 to 600 mbsf was 44%, slightly less than in the same interval in Hole 1148A. Recovery in the interval from 600 to 646 mbsf improved again to 92%.

To save further time for coring the deep objectives of this site, the interval from 646 to 700 mbsf was drilled ahead with the center bit in place. At midnight on 8 April, XCB coring resumed and advanced from 700 to 809 mbsf with 83.5% average recovery at an average rate of penetration of 15 m/hr. Results of the headspace analysis were closely monitored to observe any trends suggesting that we were approaching an accumulation of hydrocarbons. The drillers had instructions that if any sudden change in drilling rate or torque was observed, the core barrel would be recovered and a headspace analysis performed before coring resumed. While coring from 774 to 775 mbsf, the drillers experienced higher than normal torque, with an apparent increase in bit weight of ~5,000 lb. These symptoms suggested that there was some hydraulic levering of the bit off bottom due to a packed-off annulus. The core barrel was recovered early, and the core-catcher sample was subjected to hydrocarbon analysis. While we waited for the results, a 30-bbl sepiolite mud sweep was circulated through the annulus. After the headspace analysis results confirmed that there was no change in hydrocarbon concentration, coring resumed.

The interval from 809 to 853 mbsf was cored at a low rate of penetration of 6 m/hr with very low recovery (22%) because of frequent jamming of the brittle claystone in the core catcher. At 1300 hr on 10 April, the last core was recovered from the target depth of 853 mbsf. The total core recovered in this hole was 364.4 m, representing 72.8% of the cored interval of 500.6 m (Tables **T1, T2**). The drilled-down interval was 352.6 m, with a total penetration of 853.2 m. The hole was displaced with 30 bbl of 10.5-lb/gal heavy mud, and the bit cleared the seafloor at 1535 hr on 10 April. The drill string was recovered, and the beacon was retrieved before the drilling equipment, hydrophones, and thrusters were secured. At 2215 hr on 10 April, the vessel began the 267-nmi voyage to the Hong Kong pilot station.

COMPOSITE SECTION

We built a meters composite depth (mcd) scale (as defined in "Composite Section," p. 3, in the "Explanatory Notes" chapter) that ranges from 0 to 852 mcd and spans the entire cored sequence. Because Site 1148 was only double cored (Holes 1148A and 1148B), aligned core recovery gaps are common throughout the sequence. Thus, the mcd scale is discontinuous ("floating") and is not linked to the sediment/water interface. However, we were able to construct a short floating splice that extends from Sample 184-1148B-5H-5, 32 cm, to the bottom of Core 184-1148A-16H (from 46.57 to 155.34 mcd). Core recovery gaps both above and below this interval precluded the construction of a longer splice. Nevertheless, a continuous mcd and splice can be constructed—not for the site but for the local region—if data from Site 1148 are combined with data from nearby Site 1147. A continuous mcd and splice, extending from 0 to 155.34 mcd, can be assembled by combining the interval from 0 to 49.22 mcd from Site 1147 to the interval from 46.57 to 155.34 mcd at Site 1148. The splicing is accomplished by tying Sample 184-1147C-6H-4, 112 cm, at 49.22 mcd to Sample 184-1148B-5H-5, 32 cm, at 46.57 mcd.

The mcd scale and splice at Site 1148 are based on the stratigraphic correlation of whole-core multisensor track (MST) and split-core color spectral reflectance (CSR) data (lightness, L*) collected at 4- to 5-cm intervals (see "Physical Properties," p. 23, for details). From the MST, we used magnetic susceptibility (MS), gamma-ray attenuation (GRA) bulk density, and natural gamma radiation (NGR) data. These data and the splice constructed from them are presented on the mcd scale in Figures F1, F2, F3, and F4 (also as Synergy Software KaleidaGraph plots and Microsoft Excel data files [see the "Supplementary Materials" contents list]; the spliced records are also available in ASCII format). The depth offsets that comprise the mcd scale are given in Table T3 (also in ASCII format). The splice tie points (Table T4, also in ASCII format) should be used as a guide for detailed postcruise sampling.

Magnetic susceptibility data were the most useful stratigraphic tool for correlation at this site. Natural gamma radiation and CSR data were helpful in intervals where structure in the MS profile was ambiguous.

LITHOSTRATIGRAPHY

Lithologic Units

Seven lithologic units were identified at Site 1148 on the basis of composition, depositional facies, and especially color variations (Fig. F5). The sediment at Site 1148 is more variable than the other sites drilled on Leg 184. The dominant lithology is clay with variable concentrations of nannofossils. Unit I is composed of grayish green clay with quartz and nannofossils, Unit II contains olive-gray and reddish brown clay with nannofossils, Unit III contains light grayish green clayey nannofossil ooze, Unit IV contains brown nannofossil clay with intervals and patches of reduced, green nannofossil ooze, and Unit V is composed of greenish gray nannofossil clay mixed sediment and nannofossil clay. None of these units shows any evidence of large-scale, episodic sediment redeposition and represents continuous hemipelagic sedimentation. Units VI and VII, although still composed of nannofossil clay and nannofossil clay mixed sediment, are unique because they

F1. Smoothed/correlated MS data and splice, p. 31.

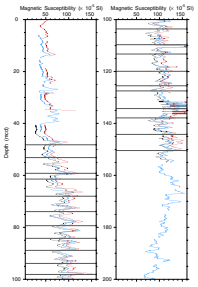

F2. Smoothed/correlated NGR data and splice, p. 36.

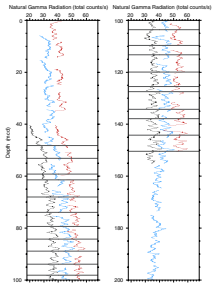

F3. Smoothed/correlated GRA data and splice, p. 41.

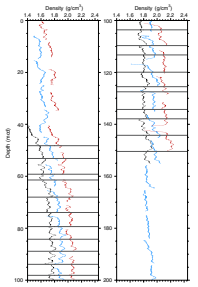

F4. Smoothed/correlated L* values from the CSR data and splice, p. 46.

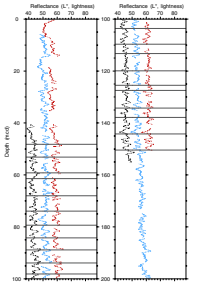

T3. Composite depths, p. 91.

contain slumped and faulted intervals. A 2.5-m.y. hiatus marks the base of Unit VI. Thus, sediments of Units VI and VII were affected by the tectonic activity associated with the opening of the South China Sea.

Unit I (0.0–194.02 mcd)

Interval: Cores 184-1148A-1H through 20X; Cores 184-1148B-1H through 15X
Depth: 0–181.8 mbsf (Hole 1148A); 0–145.1 mbsf (Hole 1148B)
Age: late Miocene–Pleistocene

Subunit IA

Interval: Core 184-1148A-1H through Section 16H-1; Cores 184-1148B-1H through 15X
Depth: 0–133.8 mbsf (Hole 1148A); 0–145.1 mbsf (Hole 1148B)
Age: late Pliocene–Pleistocene

Subunit IB

Interval: Section 184-1148A-16H-1 through Core 20X
Depth: 133.8–181.8 (Hole 1148A); washed interval (Hole 1148B)
Age: late Miocene–late Pliocene

Unit I is composed of clay with quartz and nannofossils and is divided into two subunits on the basis of nannofossil content. The upper Subunit IA, above Section 1148A-16H-1 (133.8 mbsf; 146.02 mcd), is more clay-rich than the lower part of the unit. Green clay layers and irregular green clay mottles, characterized by a clay that is stiffer than the normal background sediment, occur frequently and are well developed above ~110 mcd in Unit I (Fig. **F6**). These features decrease in frequency until they become absent in the lower part of the unit (Subunit IB). Lighter intervals with increased nannofossil content are observed below 85 mcd; color fluctuations above this depth are only detectable with the spectrophotometer. The light intervals in the lower subunit correspond to increases in nannofossil abundance as observed in the smear slides. The downward increase of lighter intervals commences in the lower part of Subunit IA and continues throughout Subunit IB (Table **T5**). The light layers are generally thinner and less pronounced than those recovered at Sites 1144, 1145, and 1146. Many of the light layers exhibit a characteristic "lightening-upward" signature, consisting of a very gradational lower contact with a continuous lightening over several tens of centimeters and a comparatively sharp but bioturbated upper contact with the overlying dark interval. The abundance of light layers increases further downsection into Unit II. The boundary between Unit I and Unit II is drawn where the light carbonate-rich nannofossil clay layers dominate, as shown clearly by an increase in the a* parameter of the spectrophotometer data (Fig. **F5**). Units I and II are also distinguished by the frequency of pyrite concretions that are abundant within Unit I and are almost absent from Unit II. The common occurrence of "iron sulfide" in the middle part of Unit I decreases to a minimum at the unit base (Fig. **F6**). Features observed within the light layers include abundant visible foraminifers on the cut core surface, common green clay layers (typically 1–3 cm thick), well-defined bioturbation, and slightly yellowish gray patches or mottles, which probably represent traces of bioturbation. Smear-slide estimates indicate calcareous nannofossil contents of more than 10%, compared to ~0%–5% in the background clay.

T4. Site 1148 splice tie points, **p. 92.**

F5. Site 1148 section summary, **p. 51.**

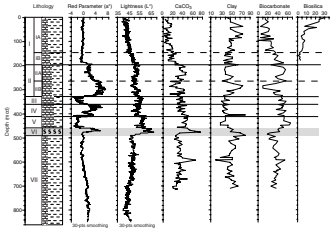

F6. "Iron sulfide," pyrite concretions, and green layers, **p. 52.**

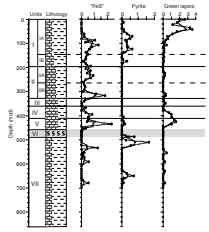

T5. Light-colored, carbonate-rich layers, **p. 93.**

Bioturbation is intense throughout Unit I. The sediment is generally completely homogenized, and individual burrows are only rarely observed. Pyrite-filled burrows are the exception to this pattern. They occur at a frequency of about one to two burrows per core section (1.5 m) within the lower part of Unit I. Large pyrite-filled burrows reach several centimeters in length and up to 2 cm in diameter. Downsection, pyrite-filled burrows first appear at Sample 184-1148A-8H-4, 136 cm (63.66 mbsf; 71.03 mcd), although disseminated pyrite occurs above this interval. Significant numbers of siliceous microfossils are only observed in the upper part of Unit I; their abundance, as measured by smear-slide analysis, gradually decreases downsection and remains <5% below Subunit IA (Fig. F5).

We observed vitric ash infilling burrows, finely dispersed within the sediment, and as isolated pumice clasts in Subunit IA (Table T6). Most ashes are a light color, reflecting the high silica content of the constituent grains. Continuous dark gray (presumably more mafic) ash layers occur at intervals 184-1148A-11H-2, 133–136 cm (97.85–97.88 mcd) and 12H-4, 39–45 cm (110.36–110.42 mcd).

T6. Volcanic ash layers, p. 97.

Unit II (194.02–328.82 mcd)

Interval: Cores 184-1148A-21X through 34X
Depth: 181.8–316.6 mbsf (Hole 1148A); washed interval (Hole 1148B)
Age: middle–late Miocene

Subunit IIA

Interval: Cores 184-1148A-21X through 27X
Depth: 181.8–249.2 mbsf (Hole 1148A); washed interval (Hole 1148B)
Age: late Miocene

Subunit IIB

Interval: Cores 184-1148A-28X through 34X
Depth: 249.2–316.6 mbsf (Hole 1148A); washed interval (Hole 1148B)
Age: middle–late Miocene

F7. Density of light-colored, carbonate-rich layers, p. 53.

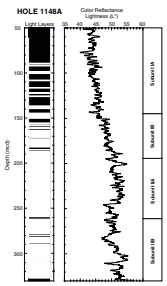

Unit II is defined and subdivided on the basis of color. Olive-gray sediment is found in the upper part of the unit (Subunit IIA), and reddish brown sediment comprises the lower part of the unit (Subunit IIB), which is clearly reflected in the a* values (Fig. F5). The dominant lithology in both subunits is clay with nannofossils. The total carbonate content is higher than in Unit I, mainly as a result of a significantly higher frequency of light-colored, carbonate-rich layers (Fig. F7). Quartz grains and siliceous microfossils are practically absent from smear slides taken in Unit II, whereas the content of calcareous nannofossils may reach 50%. This contrasts with maximum nannofossil contents of 20% in Unit I. "Iron sulfide" occurrence is moderate; pyrite concretions and green clay layers are almost absent throughout the Unit II (Fig. F6).

F8. Dark, graded tephra layer, p. 54.

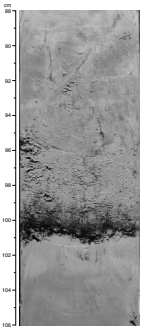

Volcanic ash layers are absent in Unit II with the exception of a strongly bioturbated dark ash layer at interval 184-1148A-33X-3, 114–121 cm (313.67 mcd), and a graded black ash layer with a sharp base at 184-1148A-33X-5, 95–101 cm (316.47 mcd) (Fig. F8). Both ash layers are characterized by unusually low magnetic susceptibility.

Unit III (328.82–360.22 mcd)

Interval: Core 184-1148A-35X through Sample 38X-2, 120 cm
Depth: 316.6–348.0 mbsf (Hole 1148A); washed interval (Hole 1148B)
Age: early middle–middle Miocene

Unit III consists of a grayish green clayey nannofossil ooze with intercalations of dark reddish brown clayey nannofossil ooze or clay with nannofossils, typically 10–50 cm thick. These intercalations compose <10% of the total sediment. Color changes are gradational over lengths of a few centimeters. Unit III is defined on the basis of its dominantly greenish color and the disappearance of a distinguishable contrast between lighter carbonate-rich and darker clay-rich layers below Section 184-1148A-34X-CC, 30 cm (327.8 mcd). This change is seen as a significant decrease in the a* value collected by the spectrophotometer (Fig. F5). The top of the unit can be defined in Section 184-1148A-34X-CC, where a distinct color change from brown (Unit II) to greenish gray (Unit III) sediment color is observed. Green layers rarely occur, "iron sulfide" stains decrease, and no pyrite concretions are observed within this unit (Fig. F6).

Unit IV (360.22–412.22 mcd)

Interval: Cores 184-1148A-38X through 43X
Depth: 348–400 mbsf (Hole 1148A); washed interval (Hole 1148B)
Age: early–middle Miocene

Unit IV comprises brownish nannofossil clay mixed sediment with a minor amount of greenish gray nannofossil clay intercalations. Again, the transition across the lithologic Unit III/IV boundary is illustrated best by a significant increase in the a* value (Fig. F5). The sediment generally appears reddish and oxidized, although thin reduced greenish intervals and irregular greenish reduction zones, several centimeters in diameter, occur throughout the unit. Well-defined green clay layers and "iron sulfide" stains occur infrequently in the upper part of the unit, and their abundance increases downward. Few pyrite concretions are found in Unit IV (Fig. F6).

Bioturbation is intense throughout Unit IV. The sediment is generally completely homogenized, and individual burrows are observed only in exceptional cases in the upper part of the unit. Below Core 184-1148A-40X (386.42 mcd), single burrows become more evident, with the bathyal assemblage of *Zoophycos, Chondrites,* and *Planolites* trace fossils dominating.

A distinct single turbidite layer composed of foraminiferal tests and a small number of quartz grains is observed in the upper part of Unit IV (Section 184-1148A-38X-5, 82–90 cm; 364.3 mcd) (Fig. F9). This deposit shows a graded, parallel-laminated lower portion corresponding to the B division of a classic Bouma sequence (Bouma, 1962). A convolute upper part with mud clasts represents the C division.

F9. Carbonate sand turbidite, p. 55.

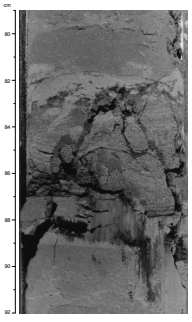

Unit V (412.22–457.22 mcd)

Interval: Cores 184-1148A-43X through 48X; Core 184-1148B-17X
Depth: 400–445 mbsf (Hole 1148A); 439.9–449.5 mbsf (Hole 1148B)

Age: early Miocene

Unit V consists of greenish gray nannofossil clay mixed sediment interbedded with nannofossil clay and very minor amounts of clay with nannofossils. The unit is distinguished from the overlying Unit IV on the basis of its greenish rather than reddish brown appearance, illustrated by a decrease in the a* value (Fig. F5). The total carbonate content of the sediment measured by coulometer is 40%–50% (see "Organic Geochemistry," p. 16). The variation in lithology is a result of fluctuations in the relative proportions of clay and carbonate, variations that show up in color changes traced by the spectrophotometer, usually over intervals of 50–300 cm. Color variations are usually gradational, because of the strong homogenization of the sediment by bioturbation (Fig. F10), but, occasionally, they are sharp.

The upper part of this unit is characterized by the abundant occurrence of green clay layers. Unit V also shows relatively high concentrations of diagenetically precipitated "iron sulfide," seen as black, fine-grained material (Fig. F6). Diagenesis has caused a common light green staining around pieces of "iron sulfide," associated with local reduction and probably linked to the presence of organic material in the original sediment. In addition, concentrations of "iron sulfide" surrounded by green mottling is frequently noted in the background sediment. Trace fossils are often recognized throughout the length of the unit, most notably *Zoophycos* and *Chondrites,* both characteristic deep-water (bathyal) forms, although numerous deformed, typically unlined horizontal circular burrows, up to 2 cm across, are also noted. *Chondrites* fossils are often found within the fill of larger burrows.

Evidence for redeposition is sparse in Unit V, although at the top of the sequence, two thin carbonate sand turbidites were noted at intervals 184-1148A-43X-3, 73–76 cm (397.23–397.26 mbsf; 409.45–409.48 mcd), and 43X-5, 103–105 cm (400.53–400.55 mbsf; 412.75–412.77 mcd). Sedimentation through the rest of Unit V is typically deep-water hemipelagic.

F10. Strongly bioturbated lithologic boundary, p. 56.

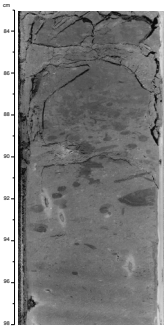

Unit VI (457.22–494.92 mcd)

Interval: Cores 184-1148A-48X through 53X; Cores 184-1148B-17X through 21X
Depth: 445.0–482.7 mbsf (Hole 1148A); 449.5–487.9 mbsf (Hole 1148B)
Age: late Oligocene–early Miocene

This unit differs from the overlying Unit V on the basis of facies and color. Unit V is light greenish gray at the top but rapidly changes to tan at the Unit V/VI boundary, making it easy to spot using the a* value from the spectrophotometer data (Fig. F5). The distinction is more pronounced in the sediment facies and structure, which, despite being similar in composition (i.e., dominantly clay nannofossil mixed sediment and nannofossil clay), do not represent continuous hemipelagic sedimentation. Instead, they signify episodic gravitational redeposition, including mass flows and slumping. As evidence of this origin, the interval contains convolute bedding, soft sediment plastic deformation, and light-colored carbonate mud clasts within a massive bed of light gray to grayish brown nannofossil clay such as those at intervals 184-1148A-48X-4, 57–70 cm (441.87–441.90 mbsf; 454.09–454.12 mcd) (Fig. F11), 50X-1, 144–150 cm (462.44–462.50 mbsf; 474.66–474.72 mcd), and

F11. Plastic, soft-sediment deformation, p. 57.

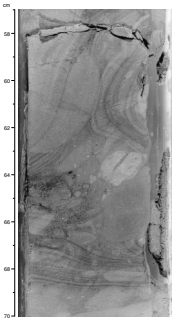

50X-2, 140–150 cm (463.90–464.00 mbsf; 476.12–476.22 mcd). The matrix sediments often contain a deep-water trace fossil assemblage of *Zoophycos* and *Chondrites*. The sediment composition and texture suggest that the water depths did not differ significantly from those of Units I–V. Both "iron sulfide" stains and pyrite concretions are rarely observed (Fig. F6). The green clay layers that were so common in Unit V are almost absent throughout this unit. Unit VI is the first part of the cored stratigraphy, going downsection, to show clear evidence of brittle faulting in the form of small normal microfaults that cannot be attributed to drilling disturbance (Fig. F12). Despite its modest thickness, the unit is quite different in character from all sediment deposited since that time, which suggests that this period was one of tectonic activity in the formation of the South China Margin.

F12. Small-scale normal faulting, p. 58.

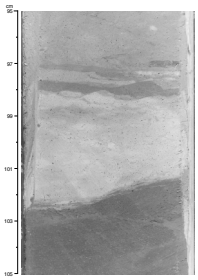

Unit VII (494.92–859.45 mcd)

Interval: Cores 184-1148A-54X through 77X; Cores 184-1148B-22X through 56X
Depth: 482.7–704.2 mbsf (Hole 1148A); 487.9–853.2 mbsf (Hole 1148B)
Age: early–late Oligocene

Unit VII is composed of an intensely bioturbated sequence of grayish olive-green nannofossil clay. The whole sequence is extremely monotonous and comprises only very minor lithologic variation from Cores 184-1148A-53X and 184-1148B-21X to the bottom of the hole (492.22–859.76 mcd). The abundant bioturbation traces are strongly compacted and give the sediment a laminated appearance. Visual description reveals two intervals (one at ~492.2–552.2 mcd and another at 652.2–682.2 mcd) in which relatively abundant occurrences of pyrite concretions are observed. Between these two intervals, stains of "iron sulfides" are relatively common (Fig. F6). Ichnofossils include *Chondrites, Zoophycos,* and *Planolites*. Most of the burrows are filled with dark brownish sediment, and *Chondrites* often is observed within fillings of larger burrows. The occasional occurrence of pyrite concretions indicates reducing conditions in the subsurface, although the abundance of trace fossils indicates that the bottom water itself could not have been anoxic. Authigenic dolomite rhombohedral crystals are observed in smear slides, usually from the dark brown sediment found in burrow fills or rare layers (Fig. F5). Dolomite occurrence is higher in the lower part of the unit.

Toward the base of the cored section, the general picture of hemipelagic sedimentation is disrupted by the identification of occasional flaser sandstone laminae, the first occurrence being in Core 184-1148B-48X (784.4 mbsf; 790.65 mcd) (Fig. F13). These compose a tiny fraction (<1%) of the total sediment over these intervals. Compositionally, the sandstones are dominated by quartz and lithic fragments, with mica, glauconite, and foraminifer fragments in smaller quantities. The nannofossil claystone closest to the sandstone often contains parallel laminations suggesting current-related deposition. In spite of this, little sedimentological evidence suggests that Unit VII was deposited in substantially shallower water than the younger units. In addition, slumping and other forms of soft sediment deformation affect normal hemipelagic sediment below interval 184-1148B-51X-2, 81 cm (811.0 mcd).

F13. Flaser-bedded sandstone laminae, p. 59.

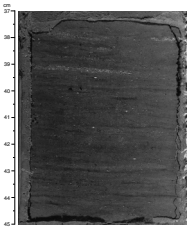

As in Unit VI, we found frequent evidence of fracturing and faulting. Quartz and calcite-filled fractures are noted but are not abundant.

Faulted zones can be discrete but often range up to 30 cm in length, forming an anastomosing network of small faults. Faulting is often found in association with slumped sediment sequences.

X-Ray Diffraction

The major mineral phases determined by bulk X-ray diffraction (XRD) are illustrated in Figure F14. Most notable is the variation in quartz concentration, which is relatively high in the deepest part of the recovered section and decreases to the lowest concentrations ~100 m below the slumped sediments of Unit VI. Above Unit VI, the quartz concentration monotonically increases to the base of Unit I, where it remains high until the top of the sediment column. Plagioclase is present in relatively high concentrations in Unit I. Calcite concentration determined by XRD analysis shows the same pattern as the lightness and coulometer-determined carbonate contents (i.e., low values in Unit I and higher concentrations in the older sediments).

The clay minerals demonstrate fairly unusual behavior, in that ~20 m below the base of Unit VI they are no longer detected by bulk XRD analysis. The clays are replaced by a single unidentified mixed layer phase that exists in the upper 120 m of Unit VII. It is unlikely that all of these clay phases are absent from the sediments, but the concentration has dropped below the detection limit for bulk XRD analysis. Dolomite was only detected in trace amounts in a few samples.

F14. Variation of bulk mineralogy, p. 60.

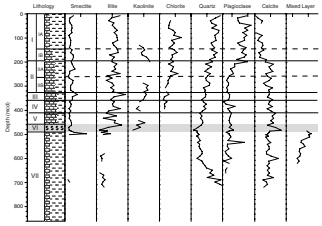

Discussion

The stratigraphy at Site 1148 spans most of the postrift history of the South China Sea, including the entire duration of active seafloor spreading (Briais et al., 1993). Despite this, beyond a series of sharp color changes, very little lithologic variation occurs since the early Oligocene, beyond a general trend toward decreasing carbonate content since Unit VI times. Although the lithology does not change, the mineral variation in the post-Unit VI sediments demonstrates a tendency toward a more strongly physically weathered mineral assemblage, based on the increasing quartz, plagioclase, and chlorite concentrations. This could represent changing sea level, accelerated uplift in the source regions, and/or aridification of the source areas. The upsection trend of decreasing quartz in Unit VII may reflect the progressive degradation of a rift-generated topography. Importantly, we found no apparent deepening or shallowing of the water depth of sedimentation, remaining hemipelagic and probably bathyal throughout. This is surprising given the anticipated thermal subsidence following mid-Eocene rifting (e.g., Taylor and Hayes, 1980) and may lend support to models that propose a deep-water basin in the area during the early Paleogene and even the Late Cretaceous (e.g, Wissmann et al., 1996).

The most noteworthy sedimentary unit is the mass-flow sequences of Unit VI, which also marks the point in the core above which no significant normal faulting is noted. Given the seismic constraints and the observations laid out here, the top of Unit VI may be interpreted as marking the end of active extension deformation, assuming a simple mid-Eocene rifting of the type proposed by most workers. Certainly, the association of slumping and faulting at the base of Unit VII suggests sedimentation in a tectonically active environment. In effect, this implies that the Unit VI/Unit V boundary is equivalent to the breakup unconformity of Falvey (1974). This layer also marks an important change

in the mineralogy. The mixed-layer clay phase found beneath the slumps of Unit VI may be produced by diagenesis induced by slumping.

BIOSTRATIGRAPHY

Calcareous Nannofossils

Calcareous nannofossil biostratigraphy for Site 1148 was done mainly on core-catcher samples from Holes 1148A and 1148B and from selected samples within the cores (Table T7; Fig. F15). Sediments at Site 1148 yielded abundant nannofossils whose preservation varied downhole. Above 367.4 mcd (middle Miocene through Pleistocene), the nannofossils exhibit moderate to good preservation with moderate to strong etching on placoliths in different intervals (e.g., good preservation at 0.7 mcd and from 213.5 to 261.7 mcd; strong etching at 54.2 mcd, from 104.6 to 115.3 mcd and from 329.0 to 338.5 mcd). These variations in nannofossil preservation are possibly caused by fluctuations in the lysocline since the middle Miocene. Nannofossils are moderately preserved below 367.4 mcd with *Discoaster* spp. showing various degrees of postburial overgrowth within different intervals.

Reworked nannofossils are commonly seen at this site. Early Miocene Sample 184-1148A-44X-CC (425.3 mcd) contains common late Oligocene nannofossil species (e.g., *Reticulofenestra bisectus, Sphenolithus delphix,* and *Zygrhablithus biijugatus*) that indicate pronounced reworking.

Thirty-nine nannofossil biostratigraphic datums were recognized in the early Oligocene to Pleistocene sediments at Site 1148 (Table T8). The first occurrence (FO) of *Discoaster druggii,* a marker for the bottom of Zone NN2, is difficult to identify between 405.7 and 472.7 mcd because of heavy overgrowth. A few moderately preserved *D. druggii* were observed at 425.3 and 454.4 mcd, which place these two samples within Zone NN2 (19.2–23.2 Ma). Several discoaster specimens that resembled *D. druggii* were observed at 454.4 mcd, suggesting that this sample is probably still in Zone NN2. No nannofossil index species can be identified confidently in Sample 184-1148A-49X-CC (472.7 mcd). At 477.3 mcd, common *Sphenolithus ciperoensis,* the marker for Zone CP19 (Zone NP24 and the lower part of Zone NP25), was observed. Its common occurrence places the sample in the lowermost part of Zone CP19b (lower part of Zone NP25). Abundant *Sphenolithus distentus* was also seen at 477.3 mcd, which places this sample in the uppermost part of Zone NP24 (>27.5 Ma). These data suggest that sediments between the lowermost part of Zones NP25 and NN2 are missing at Site 1148. This interpretation agrees with the lithologic and physical property changes observed in the same interval (see "Lithostratigraphy," p. 5, and "Physical Properties," p. 23).

S. distentus does not occur continuously at Hole 1148A; therefore, its first occurrence was not used as a biozone marker. Nannofossil assemblages and biomarkers above 716.4 mcd in Hole 1148B are similar to those in Hole 1148A. *Reticulofenestra umbilicus* does not occur between 716.4 and 851.4 mcd, which suggests that the bottom of Hole 1148B is still within Zone NP23 (<32.3 Ma).

T7. Summary of biohorizons, p. 98.

F15. Age-depth plot, p. 61.

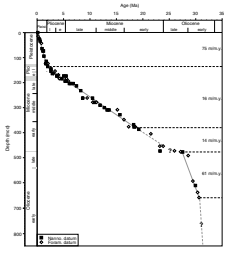

T8. Calcareous nannofossil checklist, p. 100.

Planktonic Foraminifers

Planktonic foraminifers were examined in all core-catcher samples from Hole 1148A and in core-catcher samples from Hole 1148B below 710 mcd. Removing the clay in these samples often required soaking in a heated solution of equal parts Calgon, hydrogen peroxide, and tap water for several hours before washing through a 150-µm sieve. A 63-µm sieve was used for washing samples below ~490 mcd because of the smaller size of the planktonic foraminiferal biomarkers. Site 1148 yields poor to moderately preserved planktonic foraminifers as documented by frequent test breakage (fragmentation >10%), clear evidence of genera-specific dissolution (e.g., *Globigerinoides),* and recrystallization in the lower section (below ~510 mcd). In general, the upper part of Hole 1148A has moderate preservation that rapidly degrades below ~110 mcd.

At several intervals in Hole 1148A, the abundance of the planktonic foraminifers varied greatly from one core catcher to the next. Qualitatively, although the amount of core washed may have varied by as much as a factor of two between samples, the yield obtained after washing may have changed by an order of magnitude or more. This difference was particularly noticeable in the intervals 300.0–309.4 mcd, 329.0–338.5 mcd, and 357.7–367.4 mcd.

The planktonic foraminiferal biostratigraphy for Site 1148 is based on the combined study of Hole 1148A and the lower part of Hole 1148B (see Tables **T7, T9**). The biostratigraphy of Site 1148 had several notable conventions and exceptions.

T9. Planktonic foraminifer checklist, **p. 105.**

Within Zone N22, we used the last occurrence (LO) (0.12 Ma; Thompson et al., 1979) and FO (0.40 Ma; Li, 1997) of pink *Globigerinoides ruber* as two biostratigraphic control points. We noted that both the FO of *Globigerinoides fistulosus* and the FO of *Globorotalia truncatulinoides* (bottom of Zone N22; Blow, 1969) appeared at 125.8 mcd.

For Zone N21, the LO of *Globorotalia multicamerata* was found at 135.5 mcd, which corresponds to an age of 2.4 instead of 3.09 Ma (see Table **T3,** p. 43, in the "Explanatory Notes" chapter). This observation is supported by studies of the South China Sea northern shelf (Wang et al., 1991). The coiling change of *Pulleniatina* from sinistral to dextral was quite distinct and served as a useful marker for the bottom of Zone N20 (169.5 mcd). At Site 1148, we observed that the FO of *Sphaeroidinella dehiscens* s.l. appeared at 184.5 mcd and used it as a marker for the bottom of Zone N19.

Although *Pulleniatina primalis* is observed higher in the section, we did not find its FO to be a useful marker for the bottom of Zone N17b. Instead, we relied on the FO of *Globigerinoides conglobatus* as an indicator of Zone N17b (203.8 mcd). Because we observed both dextral and sinistral forms of *Neogloboquadrina acostaensis* throughout Zone N17a, its coiling change was not used as a datum to mark 6.6 Ma. The FO of *Globorotalia pleisotumida* was seen at 261.66 mcd and marked the bottom of Zone N17a. Gradational specimens of *N. acostaensis* and *Paragloborotalia mayeri* were found down to a depth of 279.5 mcd; we thus assigned cores above this level an age of N16–N15.

The FO of *Orbulina* spp. was quite distinct and clearly marked the bottom of Zone N9 (309.5 mcd), whereas the FO of *Praeorbulina sicana* was used to mark the lower boundary of Zone N8 (348.3 mcd). At this site, we used the multiple occurrence of *Paragloborotalia kugleri, Globoquadrina dehiscens,* and *Globigerinoides trilobus* to indicate the lowermost Miocene (Zone N4) at 454.4 mcd. Below this level, we found *Para-*

globorotalia opima opima of Zone P21b at 477.3 mcd. This suggests a hiatus between the lowermost Miocene and the upper Oligocene and that sediments between the lowermost Zone N4 and the lowermost Zone P22 are missing at Site 1148.

Although gradational specimens *Globoturborotalia anguilisuturalis* and *Globigerina ciperoensis* were observed, we used the FO of typical *G. anguilisuturalis* and the LO of *Turborotalia ampliapertura* to define the top (593.6 mcd) and bottom (639.3 mcd), respectively, of Zone P20. In the last core-catcher sample, we observed *Paragloborotalia opima nana* but not *P. opima opima* and *Pseudohastigerina*. This confines the bottom of Hole 1148A (716.4 mcd) to within Zone P19 (30.6 to 32.0 Ma).

Selected core-catcher samples from Hole 1148B were examined from 733.9 to 869.5 mcd (bottom of hole). We observed *T. ampliapertura* and *Cassigerinella chipolensis*—but not *Pseudohastigerina*—in all samples in this interval. These observations led us to assign an age of P19 to the interval and the bottom of Hole 1148B.

Benthic Foraminifers

Site 1148 yields few to abundant deep-sea benthic foraminifers. The ratio of benthic to planktonic foraminifers is high in Hole 1148A because of strong carbonate dissolution. The benthic foraminifers (e.g., *Heterolepa, Gavelinopsis, Globocassidulina, Martinottiela, Sigmoilopsis, Textularia,* and *Uvigerina*) in the lower part of Hole 1148A (>~ 510 mcd) are comparable with those observed at 1000–2000 m in the modern South China Sea. An increase in the abundance of *Globobulimina* and *Chilostomella* (indicative of high productivity) was observed in the upper (above ~50 mcd) and lower (below ~500 mcd) sections of Hole 1148A. This corresponds to the higher organic carbon content and abundant siliceous fossil content (radiolarians and diatoms) found in the two intervals. The LO of *Stilostomella* was observed at a depth of 43.7 mcd, which (for the latitude of this site) assigns it an age of 0.75 Ma (Schönfeld, 1996).

Summary

At Site 1148, calcareous nannofossils are common to abundant, but preservation varies in different intervals. Planktonic foraminifers are abundant but with poor to moderate preservation. Benthic foraminifers are generally few to common but become more abundant in lower sections.

An age-depth plot shows that the biohorizons from the three fossil groups generally agree except for the interval of ~454 to ~477 mcd (Fig. **F15**). The Pleistocene/Pliocene boundary is constrained by the LO of *Calcidiscus macintyrei* and *Discoaster brouweri* and is located between 125.8 and 135.5 mcd. The Pliocene/Miocene boundary is constrained by the LO of *Triquetrorhadulus rugosus* and the LO of *Discoaster quinqueramus* between 184.5 and 193.8 mcd. Both the calcareous nannofossil and planktonic foraminifer data suggest a hiatus between the lowermost Miocene and upper Oligocene (~454 and ~477 mcd, respectively). The sedimentation rate at Site 1148 has been calculated based on biostratigraphic data (Table **T7**) and is depicted in Figure **F15.**

PALEOMAGNETISM

Shipboard paleomagnetic measurements in Holes 1148A and 1148B consisted of long-core measurements of the natural remanent magnetization (NRM) at 8-cm intervals before and after alternating field (AF) demagnetization at 15 mT or 10 and 20 mT, carried out on the archive halves of all APC cores. In addition, discrete samples were collected from the working halves of Hole 1148A, at an average spacing of two samples per section (1.5 m) from Cores 184-1148-2H through 8H and one sample per section farther downcore. The ordinary cutting shoe was used with a standard core barrel for Holes 1148A and 1148B. Cores 184-1148A-4H through 16H and 184-1148B-3H through 15H were oriented using the Tensor tool.

Hole 1148A

Long-core measurements of NRM were carried out at 8-cm intervals before and after one demagnetization step at 15 mT from Cores 184-1148-2H through 5H. A two-step demagnetization routine (10 and 20 mT) was then used for Cores 184-1148A-6H through 7H, where we were expecting the Brunhes/Matuyama boundary based on the results from Site 1147. The one-step procedure (with one demagnetization at 20 mT) was then resumed for all other cores.

The direction of the NRM (after demagnetization at 15 or 20 mT and correction using the Tensor tool data where available) is shown in Figure **F16.** The Brunhes/Matuyama boundary can be tentatively placed at 55.2 mcd. The upper Jaramillo transition appears at 69.1 mcd; the lower, at 73 mcd. The upper Olduvai transition is encountered at 111.4 mcd, and the lower is tentatively placed at 118.5 mcd (Table **T10**). Below 67 mcd, however, the record appears somewhat unstable. Inclinations are largely negative down to 110 mcd, where a clear transition to positive inclination is observed in connection with a 180° declination swing to north-seeking directions.

Fourteen discrete samples were demagnetized with a 10-step routine up to a 50-mT AF field. Unfortunately, after the very first steps the magnetization in most cases fell to values comparable to or even lower than the signal of the tray used for discrete samples. Measurements were therefore stopped and will be resumed on shore, where a small-access cryogenic magnetometer will provide the necessary sensitivity.

Hole 1148B

Long-core measurements were done at a spacing of 8 cm using a two-step demagnetization routine at 10 and 20 mT for all cores from 184-1148B-1H through 15H. The direction of the NRM (after demagnetization at 20 mT and correction using the Tensor tool data where available) is shown in Figure **F17.** The Brunhes/Matuyama boundary was identified at 55.1 mcd by a 180° swing in declination and a jump to negative inclination. Unfortunately, just below the boundary some of the liners were crushed and the core highly disturbed, which strongly affected the direction of the magnetization. It was impossible to identify the Jaramillo Subchron and the sequences of magnetic reversals below, although changes in inclination and declination were suggested by the general trends of the record. We did not attempt to measure the XCB cores.

F16. Declination and inclination for Hole 1148A, 0–180 mcd, **p. 62.**

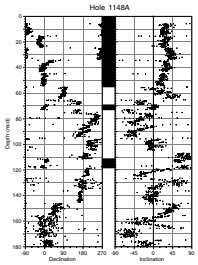

T10. Age-depth relationship from the magnetic polarity time scale, **p. 108.**

F17. Declination and inclination for Hole 1148B, 0–150 mcd, **p. 63.**

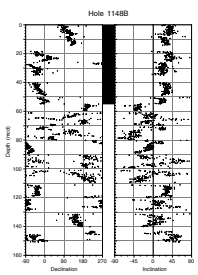

SEDIMENTATION AND ACCUMULATION RATES

Site 1148 recovered the longest sediment record for the leg (~33 Ma), and its chronostratigraphy is based on 74 datum levels: five paleomagnetic (Table T10), 39 nannofossil, 29 planktonic, and one benthic foraminiferal (Table T7) events. Sediment slumping and mass flows occur in some intervals (such as Unit VI, near the Oligocene/Miocene boundary; see "Lithostratigraphy," p. 5), but no quantitative estimates have been attempted.

Figure F18 (also given as Synergy Software KaleidaGraph plots and Microsoft Excel data files [see the "Supplementary Materials" contents list]) shows the linear sedimentation rate and mass accumulation rate curves based on calculations described in "Sedimentation and Accumulation Rates," p. 13, in the "Explanatory Notes" chapter. The resultant average sedimentation rates decreased from a maximum of 68 m/m.y. for the early Oligocene to ~11–17 m/m.y. in the Miocene and have risen again since the late Pliocene, reaching 63 m/m.y. in the Pleistocene (Table T11). When converted to mass accumulation rates (g/cm²/k.y.) and partitioned into the carbonate and noncarbonate components, extremely high accumulation rates occurred in the early Oligocene, with 3.6 g/cm²/k.y. for carbonate and 15.2 g/cm²/k.y. for noncarbonate, mainly terrigenous material. After a hiatus of 1–3 m.y. near the Oligocene/Miocene boundary, accumulation was low and relatively constant during the Miocene, followed by an increase in the Pliocene and Pleistocene. However, the Pleistocene accumulation rates (0.5 g/cm²/k.y. for carbonate and ~5 g/cm²/k.y. for noncarbonate) are much lower than those of the Oligocene (Fig. F18; Table T11). The high accumulation rates of the early Oligocene must be related to the active tectonic regime and paleoenvironmental conditions at the early stage of seafloor spreading of the South China Sea.

F18. Age-depth model, LSR, and MAR, p. 64.

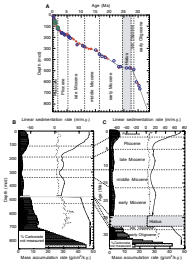

T11. Sedimentation and accumulation rates for selected intervals, p. 109.

ORGANIC GEOCHEMISTRY

Overview

The concentration of methane (headspace analysis) in sediments from Hole 1148A remained at background levels (<10 ppmv) to 440 mcd. Below this depth, concentrations increased to 53 ppmv at 475 mcd but decreased again between 475 and 505 mcd. A second increase in methane to the bottom of the hole (711 mcd) was accompanied by the presence of ethane and propane as well as heavier hydrocarbons (HC) downhole. Maximum methane and ethane concentrations were detected at 593 mcd (569 and 25 ppmv, respectively). From the first detection of ethane at 480 mcd, the C_1/C_2 ratio declined rapidly from 99 to a minimum of 15 at the bottom of Hole 1148A. Gases were measured in Hole 1148B below 614 mcd to compare with Hole 1148A and below 715 mcd for safety and pollution prevention monitoring. Between 715 and 851 mcd, methane concentrations remained low (<200 ppmv) and generally decreased with depth downhole. The C_1/C_2 ratio decreased to as low as 4; however, this is expected for the small amounts of organic matter in these poor source rocks as they enter the zone of petroleum maturation. As much as 50 ppmv of C_5 and lesser amounts of other light hydrocarbons were detected. The concentration of carbonate ranged from 1 to 76 wt%. Total organic carbon (TOC) obtained by dif-

ference (total carbon [TC] – inorganic carbon [IC]) decreases systematically from a maximum of 0.8 wt% at the top of the hole to <0.2 wt% by 130 mcd. It remains at this level to 485 mcd (Fig. F19B). A sudden increase in TOC is noted below 485 mcd (>0.4 wt%). The concentration of TOC remains near this value downhole (0.2–0.5 wt%), with just one exception coincident with a calcite-rich layer. Based on C/N values, a purely marine organic source for organic matter (OM) is suggested for the upper 130 m of Hole 1148A; higher C/N values at the bottom of the hole may indicate increasing terrestrial input. However, the interval of low abundance of organic carbon (130–485 mcd) results in a similarly low C/N ratio, and the values cannot be used to characterize OM. The variation in sulfur abundance follows that of TOC in the top 130 m of the hole, decreasing slowly with depth but exhibiting a normal marine S/C ratio (0.4). Below this, S values are zero, coincident with very low to zero OM. From 485 mcd to the bottom of the hole, total sulfur (TS) concentration increases, following TOC. However, the S/C ratio is anomalously high for normal marine sediments (>1), suggesting the addition of S from another source.

F19. Carbonate, TOC, and organic C/N ratio at Site 1148 vs. depth, p. 65.

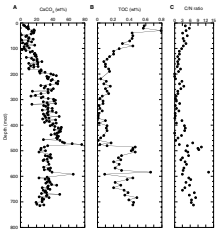

Hydrocarbon Gases

Headspace gas analysis was performed on every core taken from Hole 1148A. Sampling and analysis were conducted as described in "Organic Geochemistry," p. 14, in the "Explanatory Notes" chapter. The concentration of methane (headspace) is low (<10 ppmv) to a depth of 440 mcd, increasing gradually downhole (Table T12; Fig. F20A). A significant increase is then observed to the top of a carbonate-rich layer at 475 mcd (53 ppmv). The concentration of methane is once again low (<30 ppmv) within this lithologic unit, coincident with low core recovery. Below 510 mcd, methane increases rapidly to a maximum concentration of 569 ppmv at 593 mcd. A brief decrease occurs at 574 mcd (64 ppmv). Upon further heating (20 min) of the headspace sample, we concluded that such a reduction may be produced by heating time insufficient to completely release all trapped hydrocarbon gases. No significant changes in sediment composition were reported within this nannofossil clay interval.

T12. Methane, ethane, ethene, propane, butane, and pentane concentrations, Hole 1148A, p. 110.

F20. Methane, ethane, and propane concentrations and C_1/C_2 ratio vs. depth, p. 66.

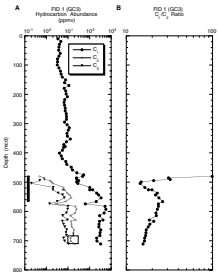

No higher hydrocarbons were noted above 480 mcd. Below this depth, the abundance of both ethane and propane follow a similar trend to that of methane, peaking at 583–593 mcd (25 and 10 ppmv, respectively). Methane concentrations increase in the final Core 184-1148A-77X to 327 ppmv, and ethane and propane increase as well, achieving a second maximum of 21 and 11 ppmv, respectively. Ethylene (C_2H_4) was observed between 480 and 567 mcd, coincident with the onset of low core recovery (Fig. F20A). Ethylene was observed previously during ODP Leg 112 (Shipboard Scientific Party, 1988a, 1988b) and is the product of high drill-bit temperatures (caused by loss of drill-water circulation). Pyrolysis of OM in the surrounding sediment under dry conditions (suggested by the dry condition of the core in the core catcher) also produces additional methane and ethane that cannot be distinguished from biogenic or catagenic methane by gas chromatographic analysis. This may account for the increased methane, ethane, and propane in this interval. From the initial appearance of ethane at 480 mcd, the methane/ethane ratio declines rapidly from 99 to a minimum of 14 at 505 mcd (Table T12; Fig. F20B). The ratio then increases to 26 at 567 mcd but steadily declines to the base of the hole (ratio of 15.7).

Several samples analyzed on the GC3 (flame ionization detector [FID] 1) indicated a significant presence of higher HC. Six samples were therefore re-analyzed on the natural gas analyzer (FID 2) to determine concentrations of C_4–C_5 (Table T12; Fig. F20A; see "Organic Geochemistry," p. 14, in the "Explanatory Notes" chapter). C_5 was first detected at 583 mcd, but the lack of a C_4 peak may suggest contamination of this sample (see "Organic Geochemistry," p. 18, in the "Site 1143" chapter). The first conclusive occurrence of C_1–C_5 is in Core 184-1148A-75X. Total concentrations of C_4 and C_5 appear to increase downhole, with a maximum abundance at 711 mcd (28 and 32 ppmv, respectively). The methane/ethane ratio calculated from these few samples resembles that calculated from the GC3.

Hydrocarbon gas abundance was measured in Hole 1148B below 614 mcd (Table T13). Concentrations similar to those in Hole 1148A were detected above 715 mcd. Below 715 mcd, methane concentrations remained low (38–190 ppmv) and decreased with depth. The C_1/C_2 ratio reached a minimum of 4. Although these conditions might normally be cause for concern and even hole abandonment (see "Volatile Hydrocarbons," p. 14, in the "Explanatory Notes" chapter), the small amounts of organic matter in these poor source rocks and low absolute concentrations of gas did not suggest a potential petroleum reservoir. As much as 50 ppmv of C_5 and lesser amounts of other light hydrocarbons were measured, suggesting limited maturation. Ethylene was again detected in zones of poor recovery as a result of drill-bit heating.

T13. Methane, ethane, ethene, propane, butane, and pentane concentrations, Hole 1148B, p. 112.

In summary, the most significant change in HC gas abundance occurs immediately beneath the lithologic change evident between 475 and 480 mcd, just below the slumped sediments of Unit VI in an interval of poor core recovery (see "Lithostratigraphy," p. 5). The maintenance of higher HC abundance below this depth suggests in situ generation of HC (see "Organic Matter Characterization," p. 20), without the addition of HC by migration. It is possible that the increase in methane between 445 and 485 mcd results from gas-phase migration through an underlying low permeability layer. No evidence exists for aqueous-phase migration of heavier HC, nor was any significant pore-water diffusion observed (see "Inorganic Geochemistry," p. 21). The lack of significant variation in the C_1/C_2 ratio below 490 mcd suggests minimal lateral migration to the site and is consistent with very high sedimentation rates (see "Biostratigraphy," p. 12). Bottom-hole thermal gradient estimates suggest a sediment temperature of ~60°C (see "Physical Properties," p. 23), which is generally considered high enough for the onset of petroleum generation. This confirms the observation of increasing sediment maturation and heavier HC generation with depth (see "Organic Matter Characterization," p. 20) instead of the alternative explanation of migrated HC. Gas values for the onset of petroleum generation are 10^{-2} to 10^{-3} g, C_1 to C_5 per gram of carbon (Barker, 1979). We have detected ~0.5 to ~10^{-3}g, C_1 to C_5 per gram of carbon.

Inorganic Carbon

Sampling for carbonate was conducted in three sections per core for Hole 1148A (Table T14; Fig. F19A). The distribution of carbonate downhole can be subdivided into five intervals, approximately corresponding to lithologic Units I, II, III–V, VI, and VII (see "Lithostratigraphy," p. 5). The interval 0–180 mcd includes samples with the lowest carbon-

T14. IC, $CaCO_3$, TC, TOC, TN, and TS contents, p. 113.

ate abundance, ranging from 1.2 to 26.7 wt% (average [AV] = 12.4 wt%; standard deviation [SD] = 6.1). A significant increase occurs at 183 mcd. The second interval (183–320 mcd) contains samples of higher, but significantly more variable, carbonate content (AV = 33.0 wt%; SD = 8.7), coinciding with a shift from clay with nannofossils to nannofossil clay that contains alternations of yellowish and reddish brown clayey ooze (see **"Lithostratigraphy,"** p. 5). A strong change in appearance of sediments below 320 mcd marks a transition to an interval of higher and less variable carbonate content. This interval (323–453 mcd) exhibits gradually increasing carbonate abundance (AV = 39.6 wt%; SD = 7.2) but cannot be conclusively subdivided according to lithologic Units III, IV, and V. A brief and dramatic increase in carbonate abundance (29–76 wt%) occurs between 457 and 476 mcd (lithologic Unit VI). The final sample of this interval (184-1148A-50X-2, 107–108 cm) is nannofossil chalk. Very poor recovery was noted in Cores 184-1148A-51X through 56X, the upper cores of lithologic Unit VII and the lowermost carbonate interval (480–715 mcd). This lithologic unit is better defined by the higher abundance of TOC (see **"Organic Carbon and Nitrogen,"** p. 19) but is also characterized by lower carbonate abundance (AV = 32.5 wt%; SD = 7.1). It contains one sample of unusually high carbonate content (66 wt%; Sample 184-1148A-65X-1, 103–105 cm), taken from a discrete interval of coarse-grained calcite-rich sediment underlying a calcite/quartz sand layer.

Coulometer reaction times of complete dissolution of carbonate were observed to increase toward the bottom of the hole, which coincides with the appearance of authigenic rhombohedral dolomite crystals in smear slides (see **"Lithostratigraphy,"** p. 5). The longer reaction times may also indicate carbonate bound with increased amounts of OM.

Organic Carbon and Nitrogen

The TOC concentration by difference (TC – IC) was determined for one sample per core (Table **T14;** Fig. **F19B**). As observed at Site 1147 (**"Organic Geochemistry,"** p. 7, in the "Site 1147" chapter), TOC declines gradually from a maximum close to the top of Hole 1148A (0.79 wt%; 30 mcd) (high values >1 wt% seen at Site 1147 are missing from the very top; see **"Organic Geochemistry,"** p. 7, in the "Site 1147" chapter) to ≤0.2 wt% below 110 mcd. This low TOC abundance is maintained to 485 mcd with concentrations of <0.1 wt% between 280 and 380 mcd. The abundance of TOC increases sharply at 485 mcd to >0.4 wt%, coincident with the top of lithologic Unit VII (see **"Inorganic Carbon,"** p. 18). This amount of organic matter is above average for carbonates (0.2 wt%) and below average for shales (0.95 wt%) (Tissot and Welte, 1984) but appears to approximate the minimum of 0.4 wt% (or somewhat less in carbonates) required to be a petroleum source rock (Barker, 1979). With the exception of the calcite-rich sediment found at 592 mcd (Sample 184-1148A-65X-1, 103–105 cm; see **"Inorganic Carbon,"** p. 18), TOC remains relatively high downhole (AV = 0.35 wt%; SD = 0.12).

Variations in total nitrogen follow those of TOC, but the calculated C/N ratio appears to be dominated by the concentration of TOC (>0.4 wt%) (Table **T14;** Fig. **F19C**). Thus, a degraded marine origin may be suggested for sediments of the upper 130 m in Hole 1148A. Very low to zero OM abundance in the sediment between 130 and 480 mcd cannot be characterized. Below this depth, some elevated TOC concentrations produce C/N ratio values >6 and as high as 13 (Sample 184-1148A-64X-

2, 107–108 cm; 584 mcd). This may indicate a possible terrestrial source, but the absence of a marked reduction in nitrogen content makes this unlikely. No conclusive evidence exists for a terrestrial source of OM at this site.

Sulfur

Total sulfur and TOC values covary as expected for a normal marine depositional environment (Berner, 1984) in the upper part of the hole, where the TS values range from 0.1 to 0.4 wt% (Table T14). Below 480 mcd, TS values are much higher (0.3–1.2 wt%). Below 475 mcd, the TS/TOC ratios are two to 10 times greater than those expected for normal marine sediments (Berner, 1984). This indicates either (1) that unusually high amounts of metabolizable organic matter were available from a much shallower (<1000 m) or nearshore environment or (2) that an external diagenetic or epigenetic source for TS (like sulfate or sulfide) existed some time in the past. Such external (nonindigenous) sulfide or sulfate could come from basin brines or migrated H_2S gas, but no clear evidence for these was observed.

Pyrite is described in two ways (see "Lithostratigraphy," p. 5): as millimeter and larger crystalline deposits (pyrite) and as pyrite in grains by microscopic smear-slide observation. Black "iron sulfides" are also described in the sediments. The observed pyrite by all these methods agrees with our TS measurements of 0.1–1.0 wt% between 0 and 90 mcd and between 485 and 715 mcd.

Organic Matter Characterization

Rock-Eval pyrolysis was conducted on samples from three intervals: (1) the top of Hole 1148A (Cores 184-1148A-2H through 10H, 10–90 mcd), (2) the zone of poor core recovery (Cores 184-1148A-51X through 56X, 480–505 mcd), and (3) the bottom of the hole (Cores 184-1148A-64X through 77X, 584–712 mcd). The results are shown in Table T15. Sediments from the upper interval (and Core 184-1148A-51X) exhibit low maturation, having low T_{max} and hydrogen index (HI) values. Samples from the other two intervals appear to be within a zone of potential petroleum generation. T_{max} increases steadily from ~400° to 424°C; the latter temperature indicates thermal maturity sufficient for the onset of petroleum generation. In contrast to a noted decline in TOC abundance to <0.1% above the lithology change at 478 mcd, TOC by Rock-Eval pyrolysis in samples from the interval of low core recovery below 493 mcd is ~0.5%; it is 0.4% at the bottom of the hole. These represent a minimum for petroleum source rocks (see "Organic Carbon and Nitrogen," p. 19). A low production index for these samples indicates a low evolution level of the organic matter relative to its hydrocarbon generation potential. This is confirmed by low S_1 values (0.01–0.06), indicating a concentration of volatile C_{3+}HC of 10–60 ppmv. This correspondence with headspace HC concentration suggests predominantly in situ generation of higher HC. A van Krevelen–type plot of HI vs. oxygen index (OI) for samples from interval 3 shows the organic matter from Hole 1148A to be of marine origin (kerogen type II) and of "intermediate" maturity (Fig. F21).

In summary, sediments from the bottom of Hole 1148A are in an early stage of petroleum generation. The TOC is still relatively abundant (≥0.4%) but is too low to have the potential of a source rock. Low

T15. Rock-Eval pyrolysis results for selected samples, Hole 1148A, p. 116.

F21. Rock-Eval pyrolysis results for samples from Cores 184-1148A-64X through 75X, p. 67.

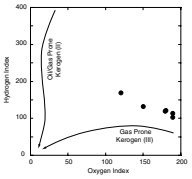

concentrations of detectable HC suggest an early stage of OM evolution relative to HC generation potential.

INORGANIC GEOCHEMISTRY

Inorganic chemical analyses were conducted on 23 interstitial water samples from Hole 1148A squeezed from whole-round samples at a frequency of one per core in the first five cores and one every second core thereafter. Analytical methods are detailed in "Inorganic Geochemistry," p. 17, in the "Explanatory Notes" chapter. The concentrations of dissolved interstitial constituents are presented in Table T16, and the profiles with depth are shown in Fig. F22. Interstitial water profiles in these sediments are dominated by sediment/water exchanges driven by sulfate reduction in the upper 110 mcd, and volcanic ash alteration, clay mineral diagenesis, and calcite recrystallization at depth. The most striking changes in some of the profiles occur between 458 and 492 mcd below a slumped interval (Unit VI; see "Lithostratigraphy," p. 5). Within this interval, salinity and chlorinity values are variable, and ammonium and silica values increase. In conjunction with evidence from hydrocarbon gas and sedimentological data (see "Organic Geochemistry," p. 16, and "Lithostratigraphy," p. 5), the slump may act as a barrier to diffusion of gas and possibly to some elements. The microenvironments within fractures may also lead to variable interstitial water concentrations in this lower interval.

T16. Interstitial water composition, p. 117.

F22. Interstitial water measurements, p. 68.

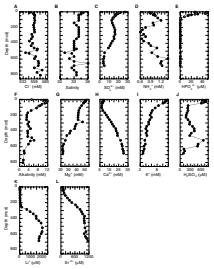

Chloride and Salinity

Chloride (Cl^-) concentrations in interstitial waters at Site 1148 increase from 548 mM near the surface to 559 mM at 39 mcd, are relatively constant between 39 and 458 mcd, and only decrease slightly toward the base of this interval (Fig. F22A; Table T16). Below 458 mcd, Cl^- decreases to 548 mM and then increases to a maximum of 577 mM near the base of the hole. The interstitial water salinity profile is similar (Fig. F22B; Table T16). Salinity decreases from 35 to 34 between 10 and 100 mcd, is relatively constant between 100 and 300 mcd, decreases to 33 at 372 mcd, and stays constant to 458 mcd. Below 458 mcd, salinity decreases to 31 and then increases to a maximum of 36 at 653 mcd. The large decrease in Cl^- and salinity at 458 mcd occurs after a sampling gap of nine cores in Hole 1148A. Above this interval is an ~20-m section of slumped sediments (lithologic Unit VI), the base of which is a nannofossil chalk (see "Lithostratigraphy," p. 5). Below this chalk layer the density increases, and *P*-wave velocity decreases substantially (see "Physical Properties," p. 23), suggesting that these slump deposits have sealed the underlying sediments. Descriptions of the sediments in the low-recovery interval primarily reflect drilling disturbance but also include features such as elongated burrows, extensive shearing, and microfaulting (see "Lithostratigraphy," p. 5). The chalk layer appears to act as a barrier to vertical migration of hydrocarbons (see "Organic Geochemistry," p. 16). This evidence for impedance of the diffusion of gases and the presence of an interval of higher density in the slump and chalk layer overlying a less consolidated, heavily stressed sedimentary sequence suggest that the highly variable Cl^- and salinity values below 470 mcd are trapped and cannot diffuse upward. Furthermore, the extensive fracturing and alteration of fractures, as well as mineralogic alteration observed in fractures (see "Lithostratigraphy," p. 5), suggests

that the more variable Cl^- and salinity values at depth are the expression of microenvironments within a heavily altered sedimentary sequence.

Sulfate, Ammonium, Phosphate, Alkalinity, and pH

Sulfate (SO_4^{2-}) concentrations decrease from 21.6 mM at 10 mcd to 12.6 mM at 110 mcd (Fig. F22C; Table T16). Below 120 mcd, SO_4^{2-} increases slowly to a maximum of 16.2 mM at ~285 mcd and then decreases to 4.9 mM at 518 mcd. Sulfate values never reach zero, indicating that sulfate reduction is incomplete and methanogenesis is not an important process in these sediments. As a result, the upper sediments at Site 1148 have low methane concentrations. High methane values at depth are related to thermogenic production of hydrocarbons (see "Organic Geochemistry," p. 16). Decreasing SO_4^{2-} values with depth below the zone of sulfate reduction at Site 1148 suggest a continuous sink for sulfate, either its incorporation into "iron sulfides," which were observed throughout the sediments at this site (see "Lithostratigraphy," p. 5), or into another mineral phase.

Ammonium (NH_4^+) increases from 0.87 mM at 10 mcd to a local maximum of 1.19 mM at 110 mcd, decreases to a minimum of 0.61 mM at 256 mcd, and then increases downhole (Fig. F22D; Table T16). Dissolved phosphate (HPO_4^{2-}) concentrations are highest at the top of the hole, 63 mM, and then decrease below the detection limit of the technique by 110 mcd (Fig. F22E; Table T16). Alkalinity increases slightly between the first and second cores at Site 1148 to a maximum of 11.8 mM by the third core, then decreases downhole (Fig. F22F; Table T16). All three of these elements increase in the upper 110 mcd at Site 1148 in response to sulfate reduction and, to a lesser extent, methanogenesis. Changes in ammonium, as well as chloride and salinity, below 470 mcd can also be related to the dehydration reaction of clay minerals. In this interval, X-ray diffraction data show that below 470 mcd, smectite, illite, and kaolinite are absent and mixed layer clays increase (see "Lithostratigraphy," p. 5).

Calcium, Magnesium, and Potassium

Magnesium (Mg^{2+}) concentrations progressively decrease downhole from near-seawater values at the top (51.3 mM) to a minimum of ~22.4 mM at the bottom of the hole (Fig. F22G; Table T16). Dissolved calcium concentrations (Ca^{2+}) decrease significantly from 8.8 mM in the second core to a minimum of 6.8 mM around 79 mcd, then increase gradually to reach 30.2 mM at the bottom of the hole. The Ca^{2+} minimum coincides with the base of the upper alkalinity peak and the first pore-water sulfate minimum, which is consistent with carbonate precipitation at the top of the sulfate reduction zone (Fig. F22H; Table T16). As a result of sulfate reduction, the slope of $\Delta Ca/\Delta Mg$ is positive above ~110 mcd and negative below (Fig. F23), with two distinct slopes. The $\Delta Ca/\Delta Mg$ slope in the interval 110–256 mcd is –7 and decreases to –0.6 at the bottom of the hole. The slope of –0.6 may indicate the uptake of Mg^{2+} and release of Ca^{2+} during in situ alteration of volcanic material. This change in slope at 256 mcd corresponds to a change in the lithology (transition between lithologic Subunits IIA and IIB; see "Lithostratigraphy," p. 5).

F23. Plot of Mg^{2+} vs. Ca^{2+}, p. 69.

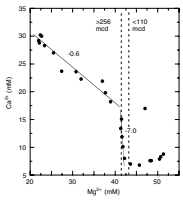

Dissolved potassium (K^+) concentrations decline sharply downhole from 11.7 mM near the surface to 5.5 mM at 198 mcd and then decrease more slowly to 3 mM at the base of the hole (Fig. F22; Table T16). This decrease most likely reflects uptake of K^+ during the alteration of volcanic material and/or diagenesis of the detrital minerals.

Silica, Lithium, and Strontium

Dissolved silica (H_4SiO_4) concentrations are high (>600 mM) in the upper part of the hole, then decrease abruptly to 227 mM at 79 mcd and more slowly thereafter to reach a minimum of 167 mM at 227 mcd (Fig. F22J; Table T16). Below this level, H_4SiO_4 concentrations increase slowly to a maximum of 406 mM at 401 mcd, increase abruptly to a second maximum of 658 mM at 518 mcd, and then decrease abruptly to 104 mM at 629 mcd. The two high-concentration intervals (0–79 mcd and 518–592 mcd) are associated with intervals of higher biogenic silica content (see "Biostratigraphy," p. 12). This suggests, as at all sites of this leg, that higher dissolved silica reflects a greater presence of soluble amorphous silica in the form of microfossils.

The lithium (Li^+) profile is relatively flat in the upper 256 mcd and subsequently increases continuously to a maximum of 2020 mM at 518 mcd (Fig. F22K; Table T16). Below this depth, Li^+ concentrations decrease slightly to the bottom of the hole. The depth of the abrupt increase of Li^+ (256 mcd) corresponds also to changes of the lithology (transition between lithologic Subunit IIA and IIB; see "Lithostratigraphy," p. 5), most likely a result of the alteration of volcanic material in the sediment.

Strontium concentrations (Sr^{2+}) increase slowly from seawater values at the top of the hole (87 mM) to 136 mM at 79 mcd, and then increase continuously with depth to a maximum of 1008 mM at 372 mcd (Fig. F22L; Table T16). Below this level, the profile of Sr^{2+} is flat to the bottom of the hole. This profile is consistent with relatively constant $\%CaCO_3$ at this site and, therefore, with relatively constant calcite recrystallization with depth. The plateau, which is seen in many interstitial water Sr^{2+} profiles, suggests that interstitial water strontium/calcium ratios have reached steady state with respect to the ratios in biogenic and authigenic calcite, so that calcite recrystallization no longer enriches the interstitial waters in Sr^{2+}.

PHYSICAL PROPERTIES

Sampling

At Site 1148, physical properties were measured on whole-round sections, split-core sections, and discrete samples from the latter. Whole-round core logging with the MST included GRA bulk density, MS, and NGR on all cores as well as *P*-wave velocity logging from the top of the holes down to Sections 184-1148A-16H-7 and 184-1148B-15H-7. Sampling intervals were 5 cm for all cores in the two holes. The *P*-wave logger (PWL) data were bad because of instrument problems and/or cracks or voids in the sediment cores. The PWL data are not shown in this text but are available from the ODP JANUS database (see the "Related Leg Data" contents list). One thermal conductivity measurement per core was also performed on Cores 184-1148A-1H through 33X and 184-1148B-1H through 15H as long as sediment conditions allowed. Color

spectral reflectance was measured on the archive halves of all split cores at 4-cm intervals. Moisture, density and *P*-wave velocity were measured on discrete samples from split-core sections at intervals of one measurement per section (1.5 m) (see "Physical Properties," p. 18, in the "Explanatory Notes chapter").

Results

Similar to the previous sites, one feature in the core-logging data is related to the change from APC to XCB coring (155 mcd in Hole 1148A). The XCB cores are moderately disturbed by partial remolding and incorporation of drilling slurry and have slightly smaller diameters than APC cores. This results in an offset of GRA data and has a very minor effect on the MS and NGR data at this site. The other primary features in the physical properties data can be ascribed to changes in sediment composition. We can distinguish two major sediment units from a sharp and drastic offset of all properties at 477 mcd. In addition, the cored interval at this site can be subdivided into eight intervals characterized by clear but less pronounced changes in some physical properties.

Interval 1, 0–46 mcd

Within the first interval, core-logging data as well as moisture and density (MAD) bulk density increase gently, porosity decreases correspondingly, and grain density shows a large scatter around 2.65 g/cm^3 (Figs. F24, F25, F26, F27). Superimposed cyclic fluctuations (which may correspond to glacial–interglacial cycles) in core-logging data have large amplitude and relatively large period (8–10 m). This interval closely resembles the upper interval at Site 1147.

Interval 2, 46–88 mcd

In the second interval, the gradients of the general trends in core-logging and MAD bulk density data are steeper than in the interval above. Cyclic fluctuations are still of high amplitude but with smaller period (~3 m) (Fig. F26).

Interval 3, 88–457 mcd

At the downhole transition to the third interval, the general trend flattens significantly in all data except for the CSR parameters, which increase (L*) and decrease (a*/b*) (Fig. F28). These changes in the long-term trend, as well as the changes over a shorter interval, appear to be controlled by variations in carbonate content. Low carbonate values induce apparent highs in NGR and MS (Figs. F25, F24) and lows in L* reflectance values; high carbonate contents seem to suppress the NGR and MS values (see also "Organic Geochemistry," p. 16). The a*/b* ratio clearly distinguishes several smaller intervals that are also visible in the MS, porosity, and grain density records (Figs. F24, F27) and are very often described by a visual color change from brown to green (see "Lithostratigraphy," p. 5). The a*/b* ratio displays five major offsets that bound intervals of characteristic color spectral reflectance at 175, 318, 345, 400, and 450 mcd (Fig. F28). The MAD bulk density in this interval steadily increases, reflecting compaction. The GRA values are lower than the discrete MAD values because of XCB coring below 155

F24. Magnetic susceptibility measurements, p. 70.

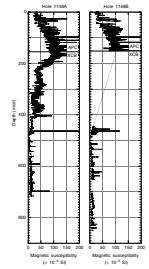

F25. Natural gamma radiation measurements, p. 71.

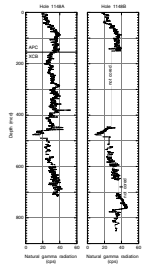

F26. Bulk density measurements from GRA and MAD methods, p. 72.

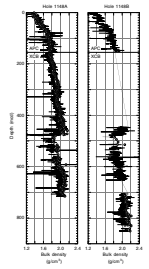

F27. Porosity, grain density, and dry density values, p. 73.

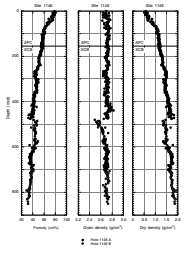

mcd. Also, GRA displays some coring-related variations, especially in the upper part of this interval (Fig. F26).

Interval 4, 457–476 mcd

The short fourth interval is marked at the top by a sharp increase in *P*-wave velocity and L* and a*/b* CSR parameters as well as a drop in porosity (Figs. F27, F28, F29). The MAD bulk density values are distinctively higher within this interval. The bottom is marked even more sharply by a reversal in these physical parameters, which are most likely controlled by the increased carbonate content in this interval (50%–75%; see "Organic Geochemistry," p. 16). This interval is probably responsible for the highly reflective sequence at ~4.9 s in the seismic profiles for the site (see "Sites 1147 and 1148 [SCS-5C]," p. 8, in the "Seismic Stratigraphy" chapter).

Interval 5, 476–517 mcd

Core recovery was poor in the fifth interval, and only a few data points are available. However, a drastically lowered grain density as well as reduction in bulk density and *P*-wave velocity values are significant. All samples from this interval consist of a greenish clay-rich material, which was strongly disturbed by the coring process. Coring disturbance may affect the data for this interval to a certain degree, although the grain density signal is hard to explain.

Interval 6, 517–593 mcd

The sixth interval is characterized by constant values in all data sets. The MS values are very low (Fig. F24). The bottom of this interval is marked by a thin intercalation with increased carbonate content, high *P*-wave velocities, and high bulk densities.

Interval 7, 593–682 mcd

Within the seventh interval, MS and NGR increase; the NGR record, in particular, displays some higher amplitude fluctuations. *P*-wave velocity, bulk density, and porosity records show an archlike feature with increasing values from 593 to 642 mcd and a decrease from 642 mcd to 682 mcd (Figs. F26, F27, F29).

Interval 8, 682–850 mcd

This lowermost (eighth) interval is distinguished by high-amplitude variations in NGR, constant MS and GRA, decreasing L*, and an almost constant a*/b* ratio, indicating very low color variability (Figs. F24, F25, F26, F28). Porosity (Fig. F27) and MAD bulk density show some minor variations in Hole 1148A. In the lower part of Hole 1148B, the discrete samples for MAD follow the downward increasing trend already indicated in Hole 1148A (Fig. F27). The *P*-wave velocities in Hole 1148B (Fig. F29) in the interval from 682 to 850 mcd display constant values until 760 mcd, then rapidly increasing values peak in maximum velocities of 2600 m/s at 792 mcd. Below that narrow horizon, *P*-wave velocities are lower again at ~2300 m/s and show some more scatter.

F28. Color spectral reflectance measurements, p. 74.

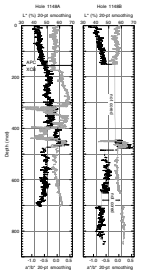

F29. *P*-wave velocity measurements for Hole 1148A, p. 75.

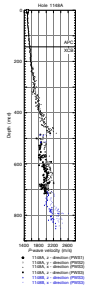

Thermal Conductivity

Thermal conductivity data from the APC and XCB cores range from 0.85 to 1.30 W/(m·K) (Table T17, also in ASCII format; Fig. F30). The values from XCB cores are compromised by poor core quality, particularly in the upper XCB interval. The general trend follows that of bulk density.

Downhole Temperature Gradient

Four downhole temperature measurements with the APC temperature tool were taken in Hole 1148A at depths of 37.3, 68.2, 108.6, and 162.0 mcd, respectively (Fig. F31). The objective was to establish the local heat flow. Original temperature records were analyzed using "Tfit" software to establish the equilibrium temperature at depth. The estimated errors in equilibrium temperature vary from 0.3° to 0.5°C, reflecting the amount of frictional heat introduced by the ship's heave near the sensor during the 10-min measurement. Depth errors are on the order of ±0.5 m. The measurements between 0 and 162 mcd yielded a thermal gradient of 83°C/km (Fig. F32).

WIRELINE LOGGING

Logging Operations

After reaching the target coring depth of 711 mbsf, Hole 1148A was filled with viscous mud, reamed, and flushed of debris. We first ran one full pass and a shorter repeat pass with the triple combo tool string, including the hostile environment natural gamma-ray sonde (HNGS), accelerator porosity sonde (APS), hostile environment lithodensity sonde (HLDS), and dual-induction tool (DIT; resistivity) (Fig. F33). (See the "Related Leg Data" contents list.) The Lamont-Doherty temperature/acceleration/pressure tool was not run because the attempts to start up the tool failed before its deployment.

Next, we ran two full passes with the FMS, long-spaced sonic (LSS), and natural gamma-ray spectrometry tool (NGT) string (Fig. F33). Before this descent, the pipe was lowered to 200.7 mbsf. Finally, we ran three full passes with the GHMT string, including the nuclear magnetic remanence sonde, susceptibility measurement sonde, and NGT (Fig. F33). Before the GHMT descent, another short wiper trip was made to knock out some of the swelling clays and to reset the end of pipe to 200 mbsf. The GHMT tool string encountered slight difficulty in passing through the interval of 395.5–444.5 mbsf.

The wireline heave compensator performed well. Sea heave was between 1.5 and 3.0 m for the duration of the logging. Logging operations started at 0950 hr on 4 April and finished at 1500 hr on 5 April (Table T18).

Log Quality

All three tool strings reached within several meters of the bottom of the hole, indicating that little debris fell from the borehole wall. The two passes for the three tool string runs showed generally excellent repeatability for all the log parameters. During the triple combo run, the hole was in excellent condition from total depth to ~344.5 mbsf. From

T17. Thermal conductivity measurements, p. 118.

F30. Thermal conductivity measurements, p. 76.

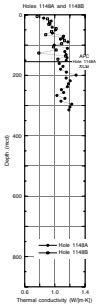

F31. Downhole temperature measurements, p. 77.

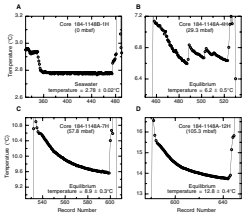

F32. Downhole temperature gradient, p. 78.

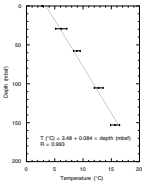

F33. Graphic summary of downhole logging operations for Hole 1148A, p. 79.

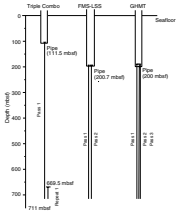

T18. Summary of logging operations, p. 121.

344.5 to 184.5 mbsf, the hole was generally 14 in or less, causing only occasional bogus spikes on the APS and HLDS. Above 184.5 mbsf, most of the hole was washed out beyond 18 in, making APS and HLDS data problematic. Even the HNGS was affected drastically in this upper interval because the caliper did not reflect the true hole size. The APS and HNGS hole-size corrections were performed as always (Fig. F34). The DIT ran a good log. Both the shallow (spherically focused log [SFL]) and medium (medium induction phasor-processed resistivity [IMPH]) resistivity were adversely affected by the washouts in the top part of the hole.

The FMS pad contact in this hole was the best of the leg, almost perfect in the lower interval of the hole. Tool heaves of ~0.3 m were present as usual. Pad orientation did change between the two passes at some intervals. The sonic run was excellent, except that it skipped in the interval from 394.5 to 399.5 mbsf because of a rapid change in the hole diameter caused by swelling clays. The second pass did better in this interval, with only one spike in the sonic velocity at 395.5 mbsf. Otherwise, the two *P*-wave velocity measurements are almost completely superimposed (Fig. F34).

Although the general-purpose inclinometer tool was not run at this site, the magnetic field data showed the same spiky quality as Sites 1144 and 1146 with even more large-amplitude spikes. After noting that the spiking was significantly less on the second pass, we decided to make a third pass. The third pass was of the same quality as the second. Interestingly, the spikes often repeat themselves on subsequent passes at the same depth but with different amplitudes. Thus, we infer that the spikes may be caused by an anisotropic environmental influence with their amplitude determined by tool orientation. These spikes were edited out in the data presented in this report. The MS data were mostly of good quality (Fig. F34).

In general, standard gamma ray (HSGR) and computed gamma ray (HCGR) from the HNGS tool in the triple combo run read 10% to 25% higher than spectroscopy gamma ray or computed gamma ray from the NGT in the FMS-LSS run, a difference easily accounted for by eccentricity and hole-size correction. Contrary to the NGT, the HNGS corrects for borehole diameter and potassium in the borehole fluid, although the corrections near individual large washouts were apparently inadequate. The HNGS is more sensitive than the NGT; hence, its results are presented in Figure F35.

F34. Downhole logs of hole diameter from Hole 1148A, p. 80.

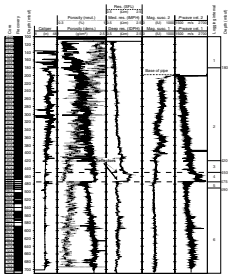

F35. Downhole logs of HSGR, HCGR, potassium, thorium, and uranium, p. 81.

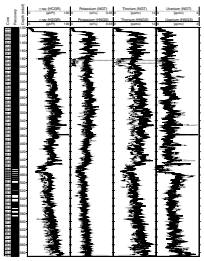

Results

The downhole logging and core sample data together suggest that Hole 1148A can be divided into six main intervals of distinct physical properties below the logging depth of 111.5 mbsf. The general dividing lines seem to be at ~180, ~420, ~450, ~475, and ~490 mbsf (Fig. F34).

Interval 1 (above 180 mbsf)

Above 180 mbsf (interval 1), the caliper frequently saturated, indicating severe hole washouts. Correspondingly, neutron porosity and bulk density from downhole logging are spiky, and the shallow resistivity (SFL) is less than the medium (IMPH) and deep (deep induction phasor-processed resistivity [IDPH]) resistivities (Fig. F34). Gamma ray (reflecting the combined effects of potassium, thorium, and uranium), porosity, and density from downhole logging are noisy from 111.5 to 180.0

mbsf because of poor hole condition. Resistivity values increase with depth in this interval (Figs. F34, F35, F36).

Interval 2 (180–420 mbsf)

Caliper measurements show that the hole condition in this interval is variable with some swelling clays between 285 and 310 mbsf (Fig. F34). Correspondingly, neutron porosity and bulk density logs are still somewhat spiky. In this interval, several physical properties indicators increase with depth, including bulk density, electric resistivity, *P*-wave velocity, and photoelectric effect (PEF) (Figs. F34, F37). Neutron porosity decreases with depth. Magnetic susceptibility reaches maxima at 260, 370, and 400 mbsf and minima at 330 mbsf (Figs. F34, F37). Gamma ray first increases with depth from 180 to 320 mbsf and then decreases from 320 to 420 mbsf (Fig. F35). The decrease in magnetic field with depth in this interval is caused by the proximity of the drill pipes (Fig. F36).

Interval 3 (420–450 mbsf)

Caliper data show excellent hole condition in this interval (Fig. F34). Bulk density, resistivity, *P*-wave velocity, and PEF increase with depth, while magnetic susceptibility remains constant. Neutron porosity and magnetic field decrease slightly with depth (Figs. F34, F37, F36).

Interval 4 (450–475 mbsf)

Hole condition is also excellent in this interval (Fig. F34). The top and bottom of this interval are associated with major discontinuities in *P*-wave velocity and thus likely correspond to the prominent double reflectors seen in seismic reflection profiles. The average *P*-wave velocity of this interval is 2.3 km/s, which is substantially greater than the values of 2.1 and 1.9 km/s at the top and bottom of this interval, respectively. Bulk density is also the greatest in this interval with a major discontinuity at the bottom. Resistivity and PEF also reach maxima at this interval with a major discontinuity again at the base of the interval (Figs. F34, F37). Neutron porosity reaches minima in this layer and again with a discontinuity at the interval base. Magnetic susceptibility decreases slightly with depth with a small maximum at 465 mbsf.

Interval 5 (475–490 mbsf)

The hole condition is still excellent in this interval except for some small rugosity at 480 mbsf as shown by the caliper data (Fig. F34). This interval is characterized by relatively low bulk density, resistivity, magnetic susceptibility, *P*-wave velocity, and PEF, together with relatively high neutron porosity (Figs. F34, F37, F36). The top of this interval at 475 mbsf is the strongest discontinuity in the entire hole for many log parameters.

Interval 6 (490–711 mbsf)

Caliper data show that this interval also has excellent hole condition except for some small rugosity at 680 mbsf (Fig. F34). The trends of bulk density, *P*-wave velocity, and PEF first increase with depth until ~620 mbsf and then decrease slightly toward the bottom of the hole (Figs. F34, F37). Correspondingly, the neutron porosity trend first de-

F36. Comparison of core MAD porosity, downhole log bulk density porosity, GR, and *P*-wave velocity, p. 82.

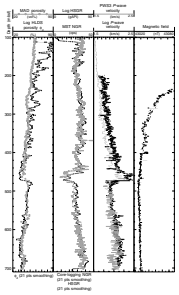

F37. MS from MST measurements of core logs vs. downhole measurements of thorium, p. 84.

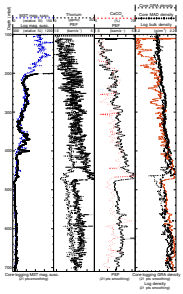

creases and then increases with a transition depth at 620 mbsf. The gamma-ray trend increases with depth, whereas those of resistivity and magnetic susceptibility remain more or less constant (Figs. F34, F35).

The trend in magnetic susceptibility from downhole logging is in good agreement with that from whole-core MST measurements (Fig. F37). The trends of thorium and PEF agree well between 490 and 640 mbsf. $CaCO_3$ measurements of core samples and PEF from downhole logging show similar trends. Downhole logging gamma-ray and MST measurements of core samples agree in their general trends as well (Fig. F36).

The trend of bulk density from downhole logging agrees with that from both MAD measurements of core samples and core logging below 300 mbsf (Fig. F37). Above 300 mbsf, however, the bulk density from downhole logging is very spiky (possibly because of poor hole condition) and is systematically less than that of the core measurements. Similarly, porosity calculated from downhole bulk density agrees better with that calculated from the moisture content of core samples below 300 mbsf. Above 300 mbsf, the logging porosity is very spiky, presumably also because of poor hole condition (Fig. F36). Finally, *P*-wave velocity from core sample measurements is ~0.2 km/s smaller than that from downhole logging above 450 mbsf, 0.3 km/s smaller at 450–475 mbsf, and 0.1–0.2 km/s smaller below 475 mbsf. The FMS data revealed alternating layers of relatively high and low conductive layers (Fig. F38).

F38. FMS image from downhole logging data, p. 86.

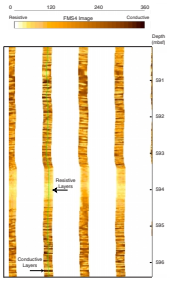

REFERENCES

Barker, C., 1979. *Organic Geochemistry in Petroleum Exploration*. AAPG Continuing Education Course Note Series, 10.

Berner, R.A., 1984. Sedimentary pyrite formation: an update. *Geochim. Cosmochim. Acta,* 48:605–615.

Blow, W.H., 1969. Late middle Eocene to Recent planktonic foraminiferal biostratigraphy. *In* Brönnimann, P., and Renz, H.H. (Eds.), *Proc. First Int. Conf. Planktonic Microfossils, Geneva, 1967:* Leiden (E.J. Brill), 1:199–422.

Bouma, A.H., 1962. *Sedimentology of Some Flysch Deposits: A Graphic Approach to Facies Interpretation:* Amsterdam (Elsevier).

Briais, A., Patriat, P., and Tapponnier, P., 1993. Updated interpretation of magnetic anomalies and seafloor spreading stages in the South China Sea: implications for the Tertiary tectonics of Southeast Asia. *J. Geophys. Res.,* 98:6299–6328.

Falvey, D.A., 1974. The development of continental margins in plate tectonic theory. *APEA J.,* 14:95–106.

Huang, L., 1997. Calcareous nannofossil biostratigraphy in the Pearl River Mouth Basin, South China Sea, and Neogene reticulofenestrid coccoliths size distribution pattern. *Mar. Micropaleontol.,* 32:31–57.

Jiang, Z., Lin, Z., Li, M., Liu, Q., Li, T., et al., 1994. *Tertiary in Petroliferous Regions of China, VIII. The North Continental Shelf Region of South China Sea:* Beijing (Beijing Petroleum Industry Press). (in Chinese)

Li, B., 1997. Paleoceanography of the Nansha Area, southern South China Sea since the last 700,000 years [Ph.D. dissert.]. Nanjing Inst. Geol. Paleontol., Academica Sinica, Nanjing, China. (in Chinese, with English abstract)

Ru, K., Zhou, D., and Chen, H., 1994. Basin evolution and hydrocarbon potential of the northern South China Sea. *In* Zhou, D., Liang, Y., and Zeng, C. (Eds.), *Oceanology of China Seas:* New York (Kluwer Press), 2:361–372.

Schönfeld, J., 1996. The "*Stilostomella* Extinction": structure and dynamics of the last turnover in deep-sea benthic foraminiferal assemblages. *In* Mogurlevsky, A., and Whatly, R. (Eds.), *Microfossils and Oceanic Environments:* Aberystwyth (Univ. Wales, Aberystwyth Press), 27–37.

Shipboard Scientific Party, 1988a. Site 679. *In* Suess, E., von Huene, R., et al., *Proc. ODP, Init. Repts.,* 112: College Station, TX (Ocean Drilling Program), 159–248.

Shipboard Scientific Party, 1988b. Site 682. *In* Suess, E., von Huene, R., et al., *Proc. ODP, Init. Repts.,* 112: College Station, TX (Ocean Drilling Program), 363–436.

Taylor, B., and Hayes, D.E., 1980. The tectonic evolution of the South China Basin. *In* Hayes, D.E. (Ed.), *Tectonic and Geologic Evolution of Southeast Asian Seas and Islands*. Geophys. Monogr., Am. Geophys. Union, 23:89–104.

Thompson, P.R., Bé, A.W.H., Duplessy, J.-C., and Shackleton, N.J., 1979. Disappearance of pink-pigmented *Globigerinoides ruber* at 120,000 yr BP in the Indian and Pacific oceans. *Nature,* 280:554–558.

Tissot, B.P., and Welte, D.H., 1984. *Petroleum Formation and Occurrence* (2nd ed.): Heidelberg (Springer-Verlag).

Wang, P., Xia, L., Wang, L., and Cheng, X., 1991. Lower boundary of the marine Pleistocene in northern shelf of the South China Sea. *Acta Geol. Sinica,* 2:176–187.

Wissmann, G., Kudrass, H., and Hinz, K., 1996. Continuing rifting on the South China Margin: results of cooperation by state geoscience institutes BGR/Hannover and SOA/Hangzhou in SONNE cruises 49 and 58. *Geowissenschaften,* 14:310–312.

Wu, J., 1994. Evaluation and models of Cenozoic sedimentation in the South China Sea. *Tectonophysics,* 235:77–98.

Figure F1. Smoothed (11-point running average)/correlated MS data and the splice for the two holes at Site 1148 (spliced MS data in this figure are also available in **ASCII format**). The order of the three arrays (the splice and Holes 1148A and 1148B) increases outward from the origin. The hole arrays are offset from each other—and from the splice—by a constant (20.0×10^{-5} SI units) so that only the splice is plotted relative to the absolute MS value. Lines identify the splice tie points. (Continued on next four pages.)

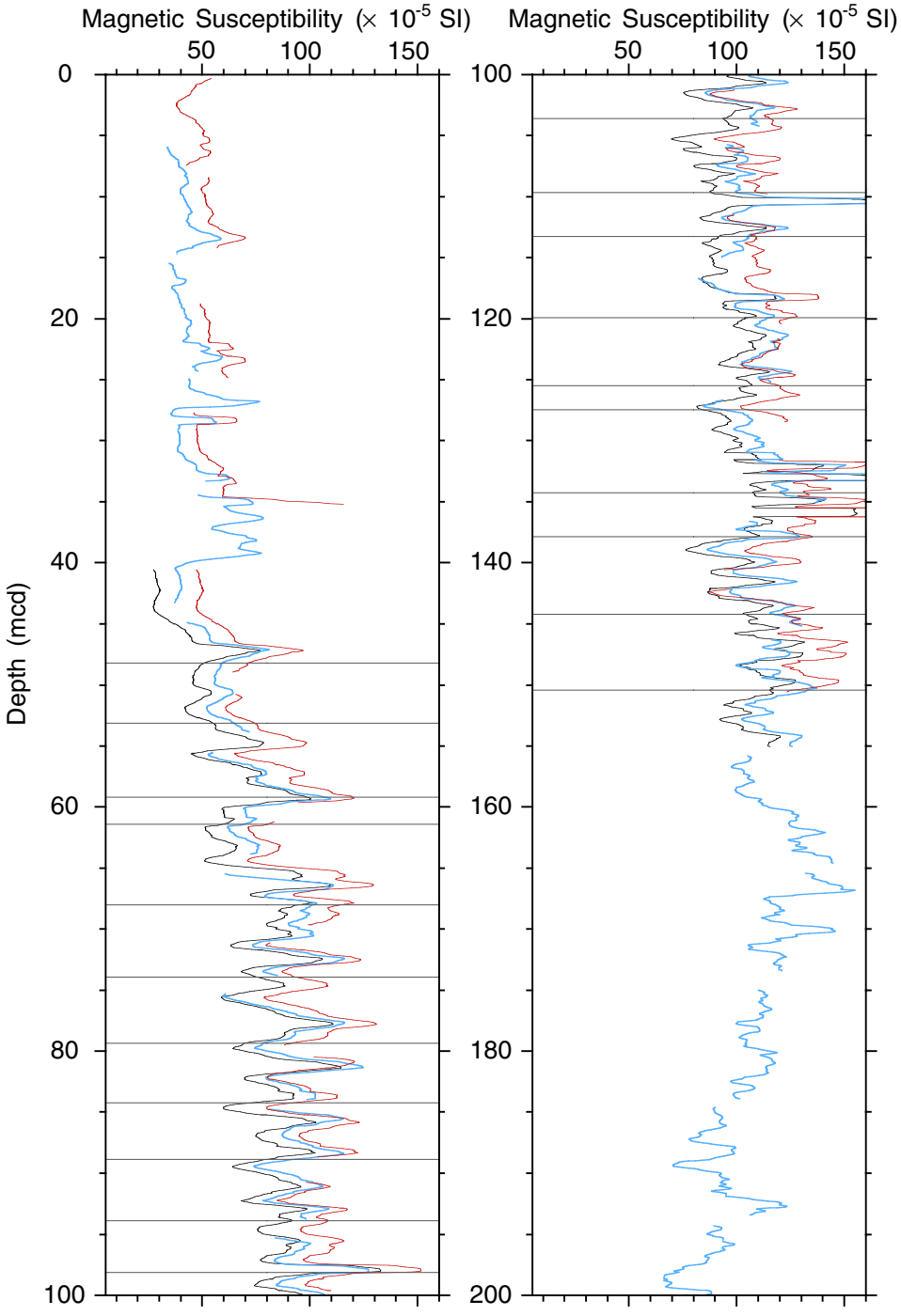

Figure F1 (continued).

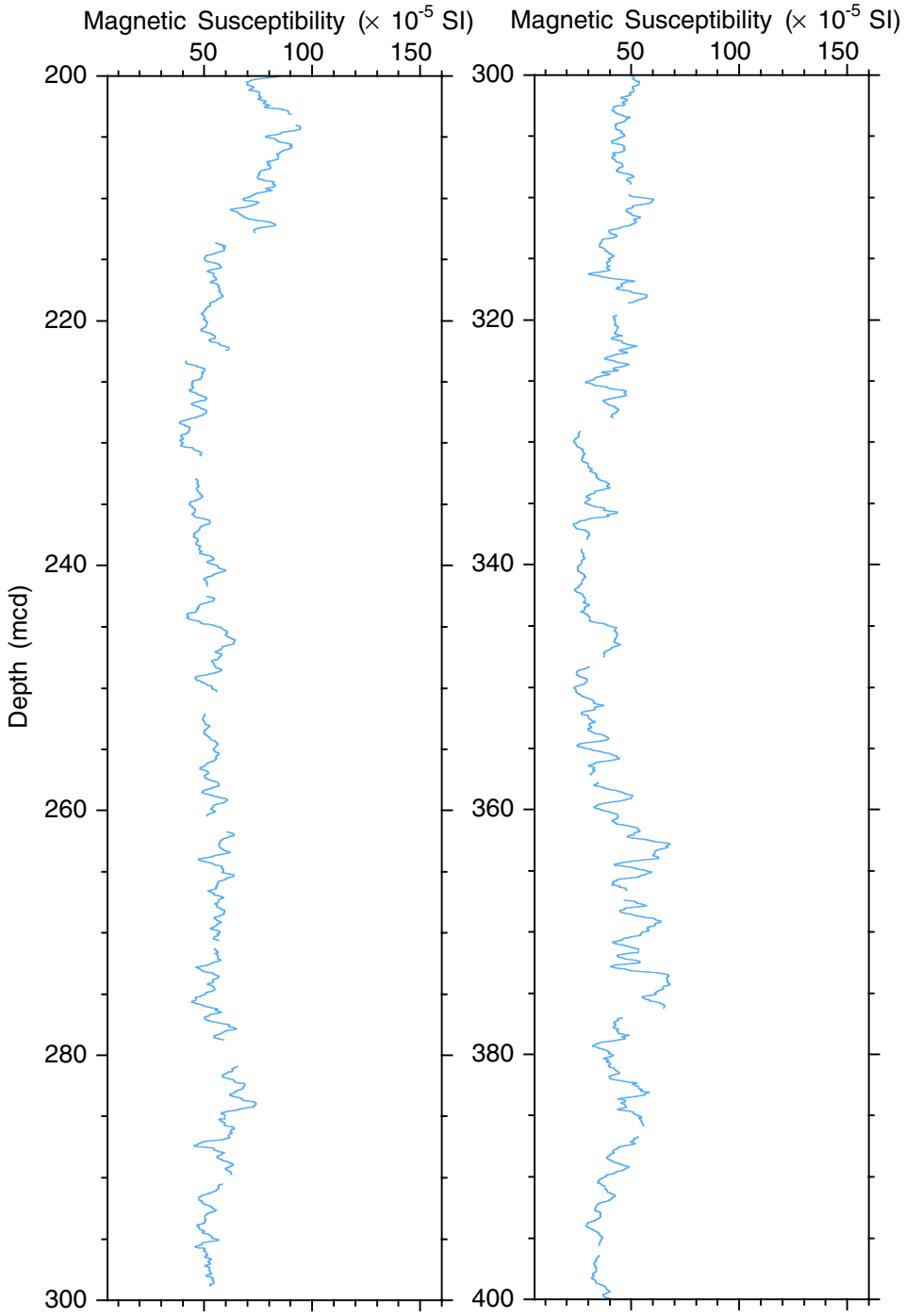

Figure F1 (continued).

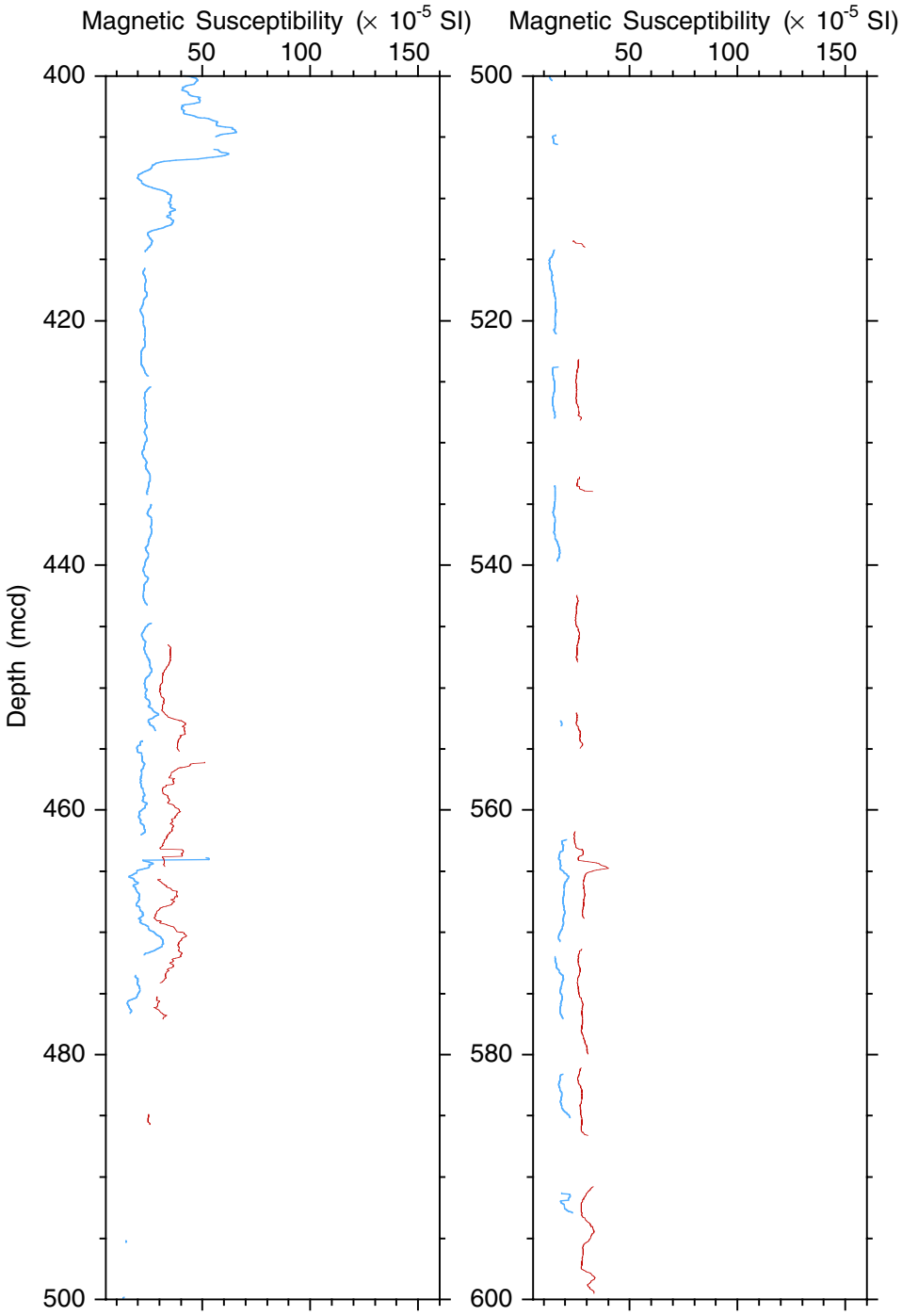

Figure F1 (continued).

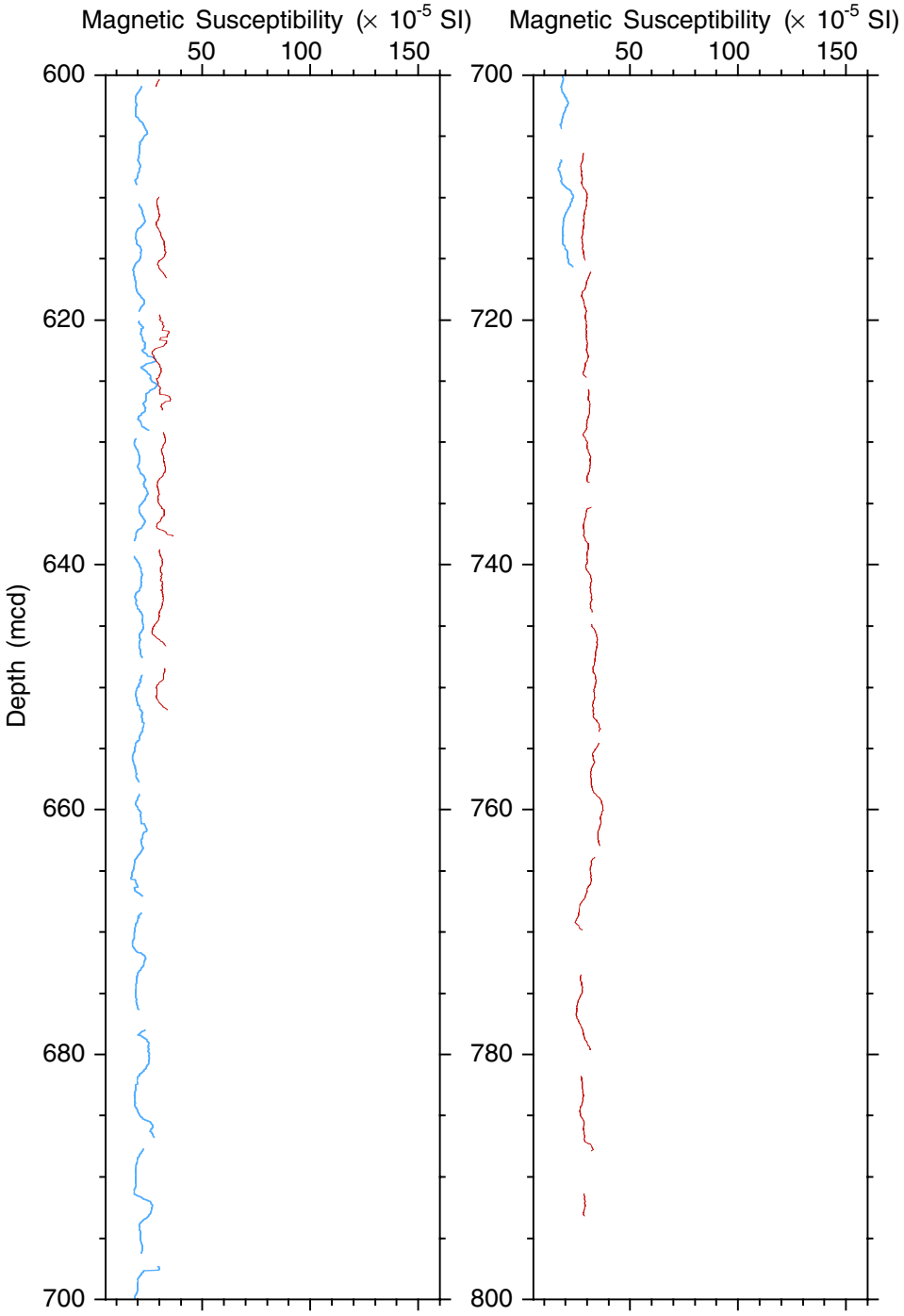

Figure F1 (continued).

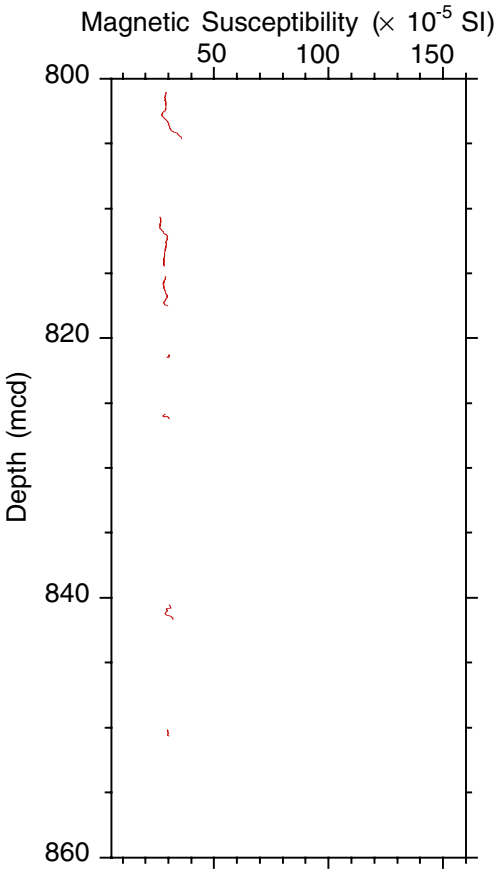

Figure F2. Smoothed (11-point running average)/correlated NGR data and the splice for the two holes at Site 1148 (spliced NGR data in this figure are also available in **ASCII format**). The order of the three arrays (the splice and Holes 1148A and 1148B) increases outward from the origin. The hole arrays are offset from each other—and from the splice—by a constant (9 cps) so that only the splice is plotted relative to the absolute NGR value. Lines identify the splice tie points. (Continued on next four pages.)

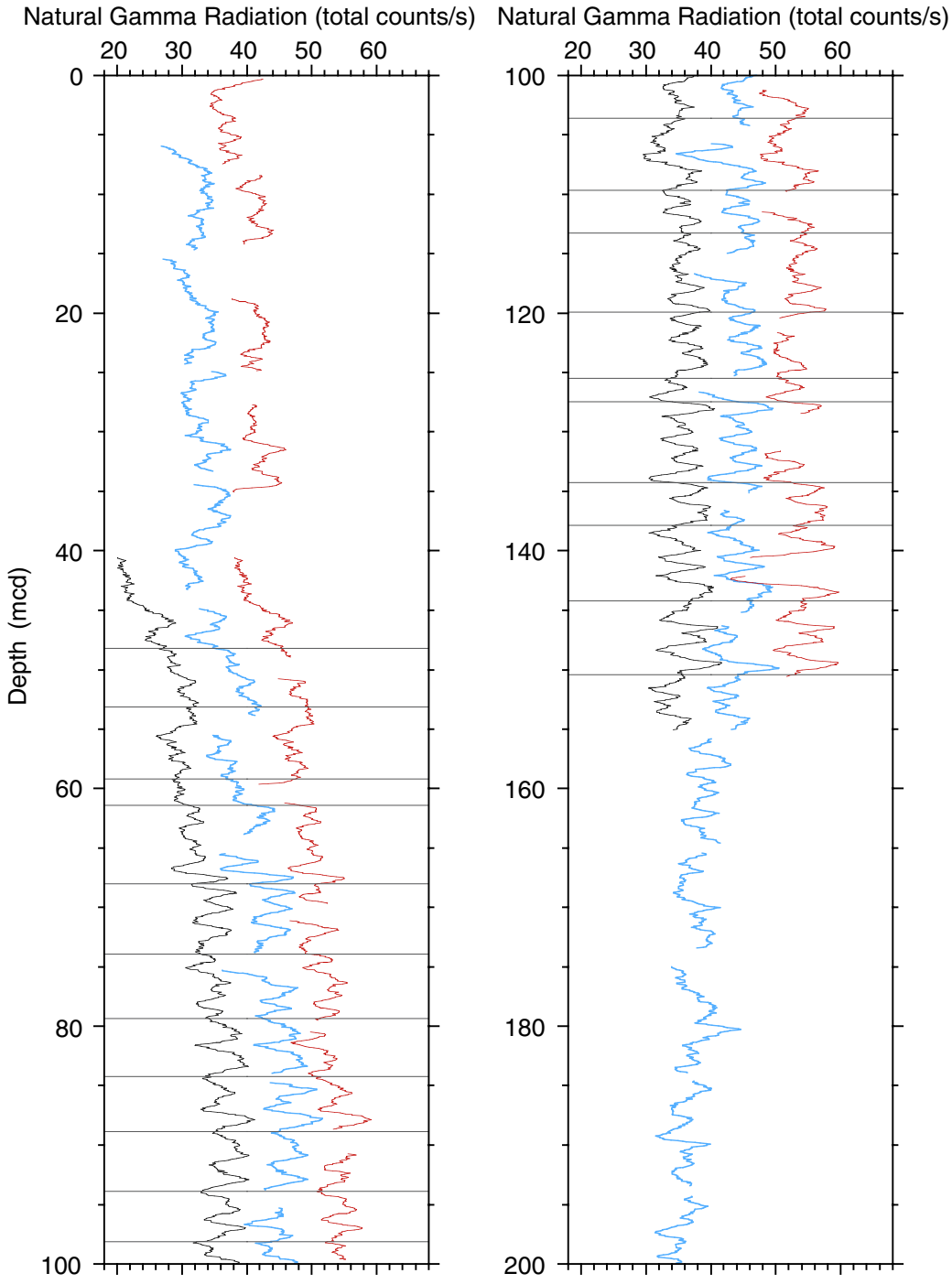

Figure F2 (continued).

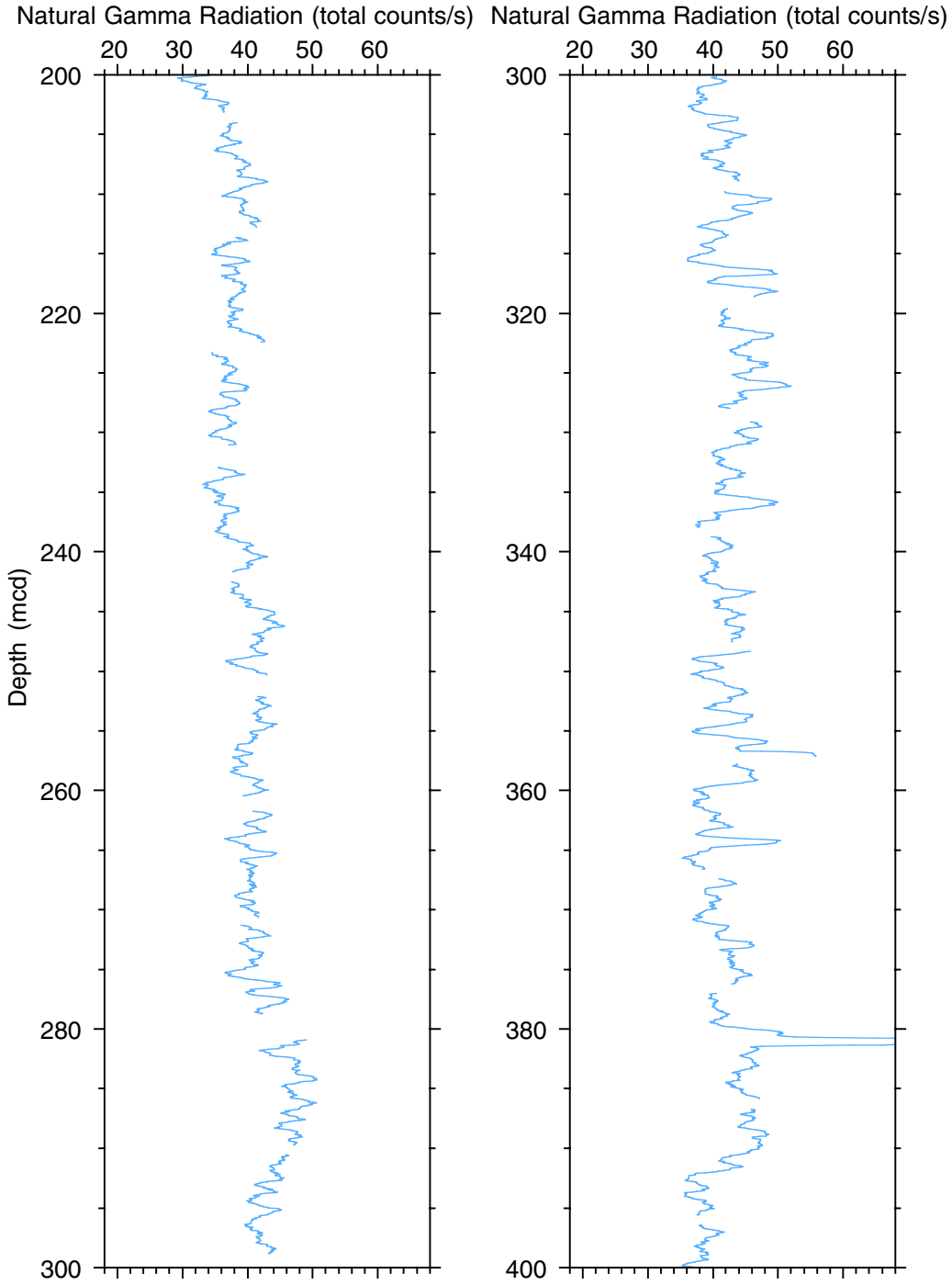

Figure F2 (continued).

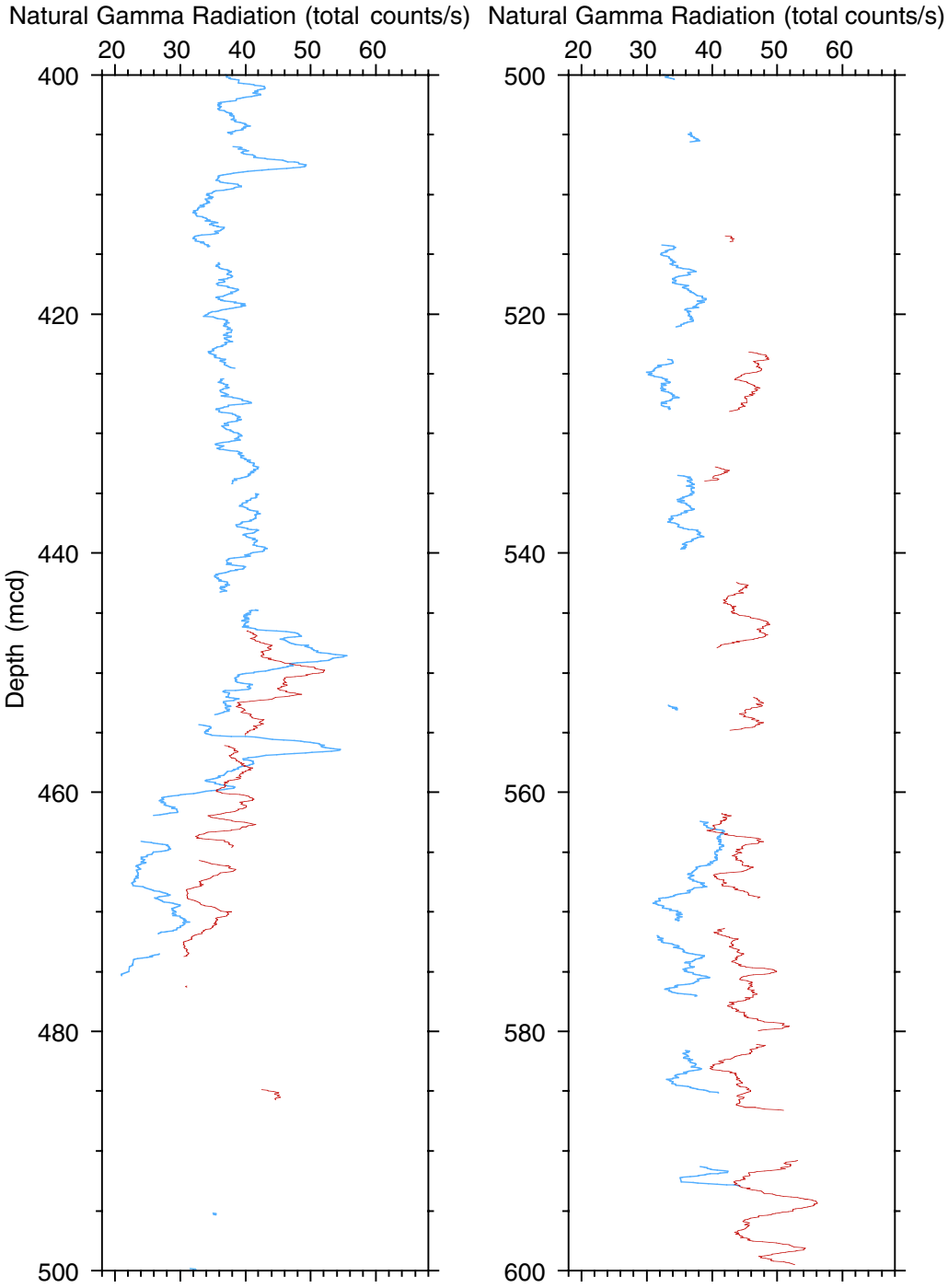

Figure F2 (continued).

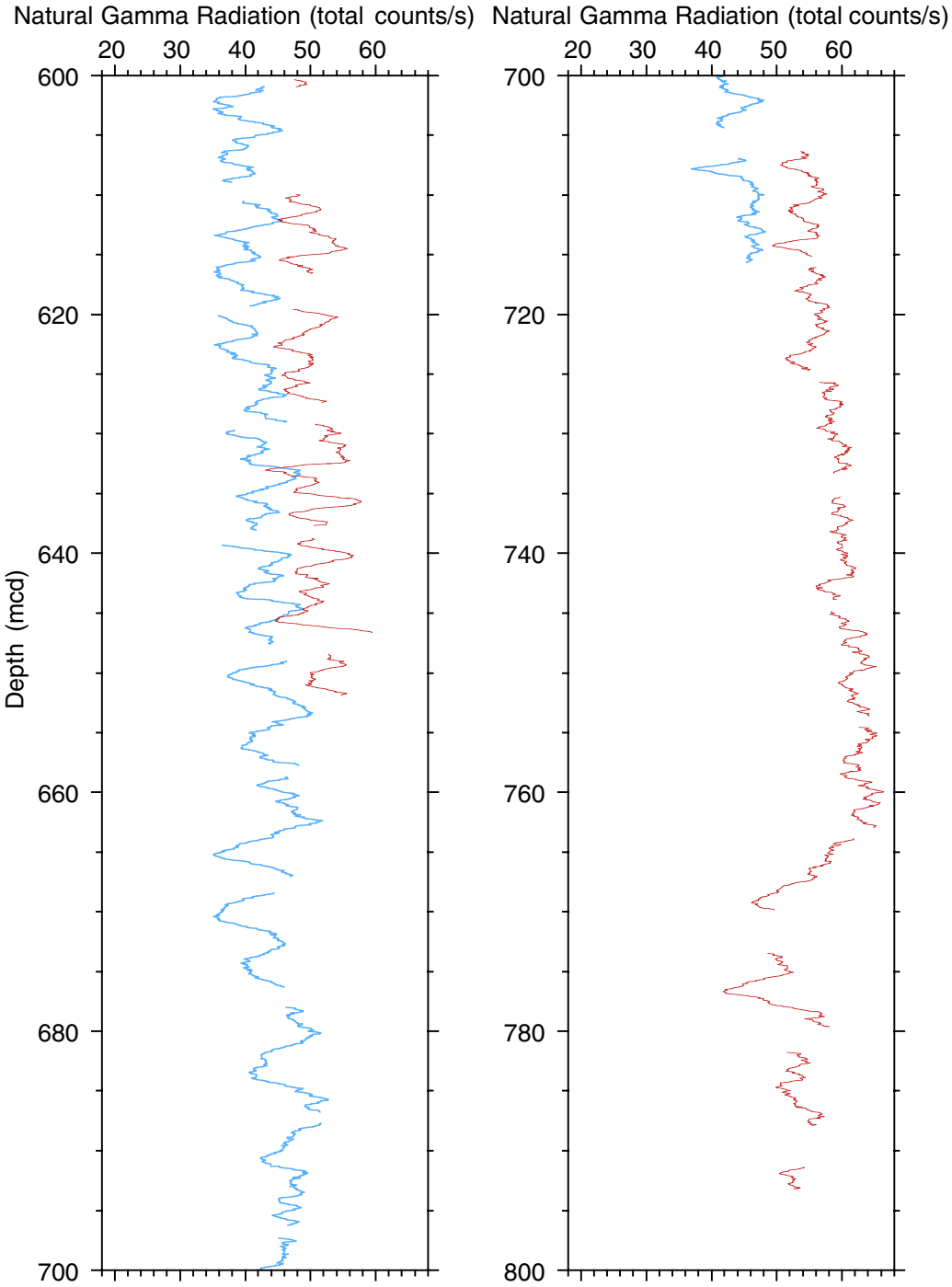

Figure F2 (continued).

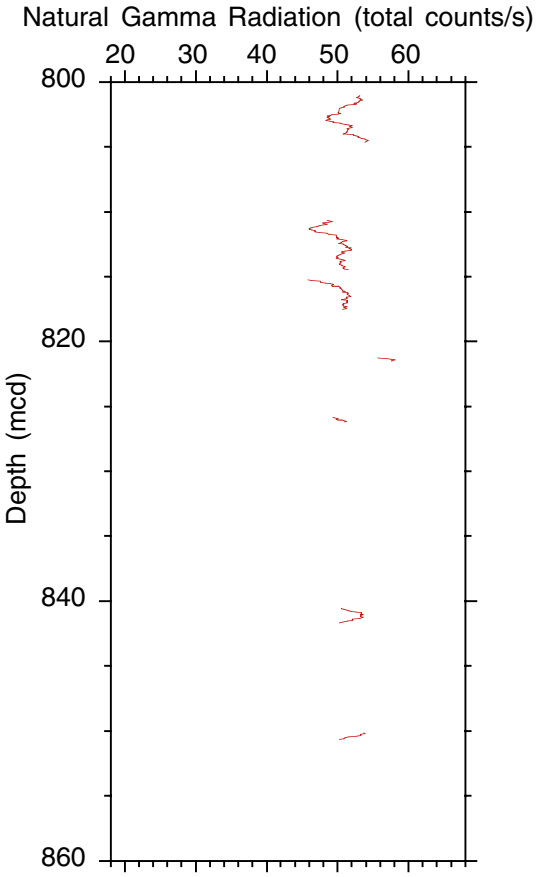

Figure F3. Smoothed (11-point running average)/correlated GRA data and the splice for the two holes at Site 1148 (spliced GRA data in this figure are also available in **ASCII format**). The order of the three arrays (the splice and Holes 1148A and 1148B) increases outward from the origin. The hole arrays are offset from each other—and from the splice—by a constant (0.15 g/cm³) so that only the splice is plotted relative to the absolute GRA value. Values ≤1.03 and ≥2.4 (g/cm³) have been culled. Lines identify the splice tie points. (Continued on next four pages.)

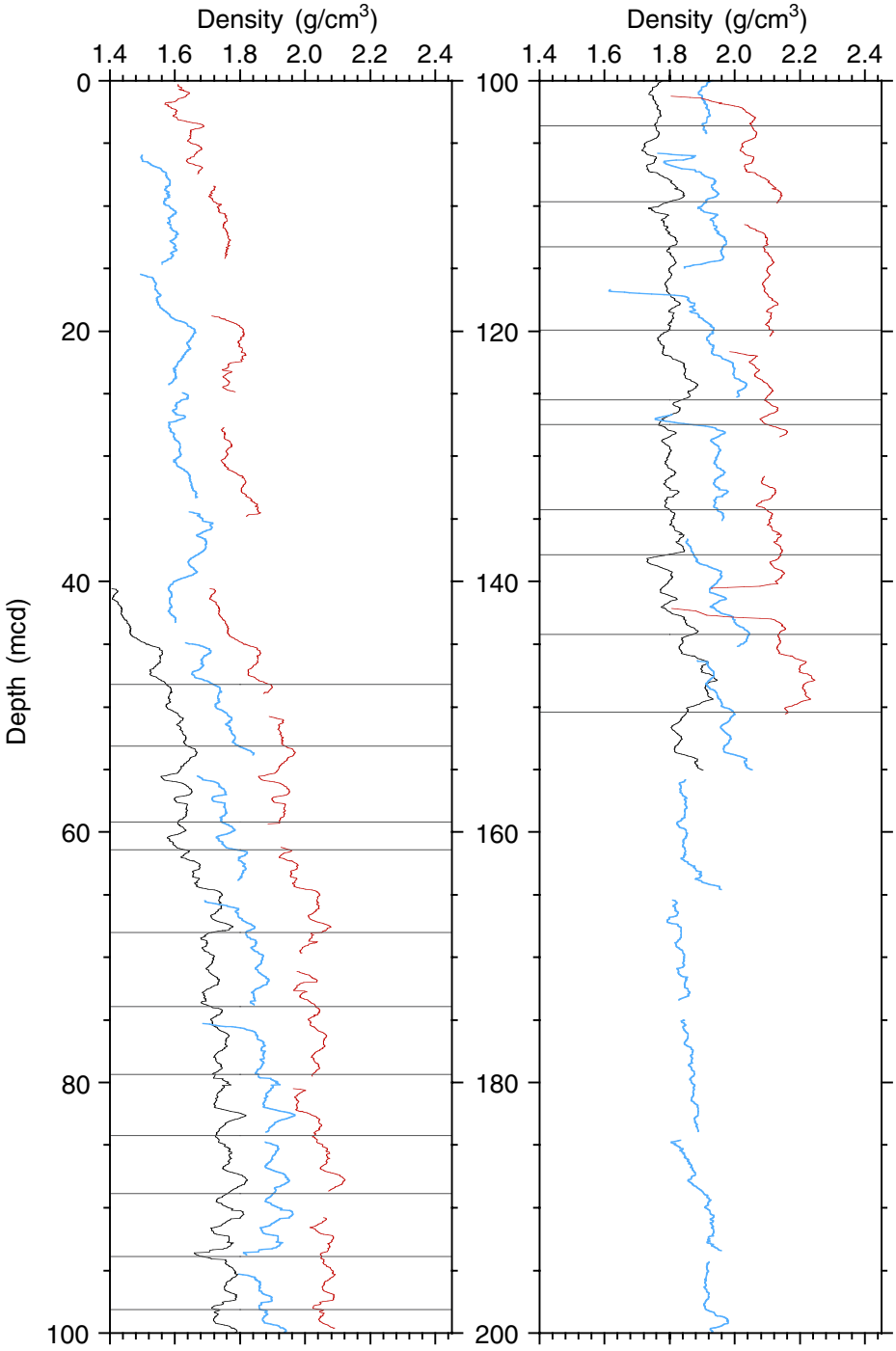

Figure F3 (continued).

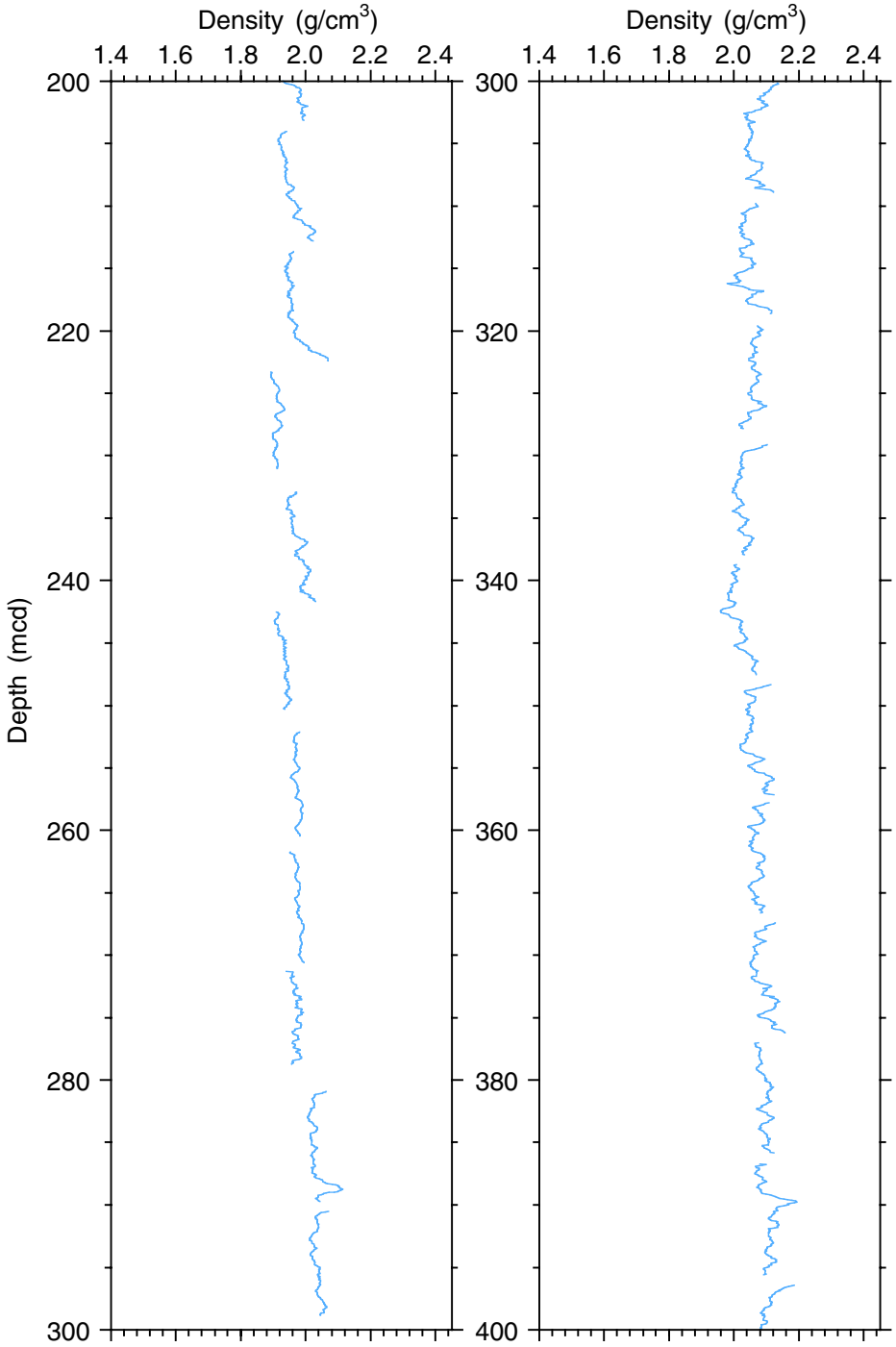

Figure F3 (continued).

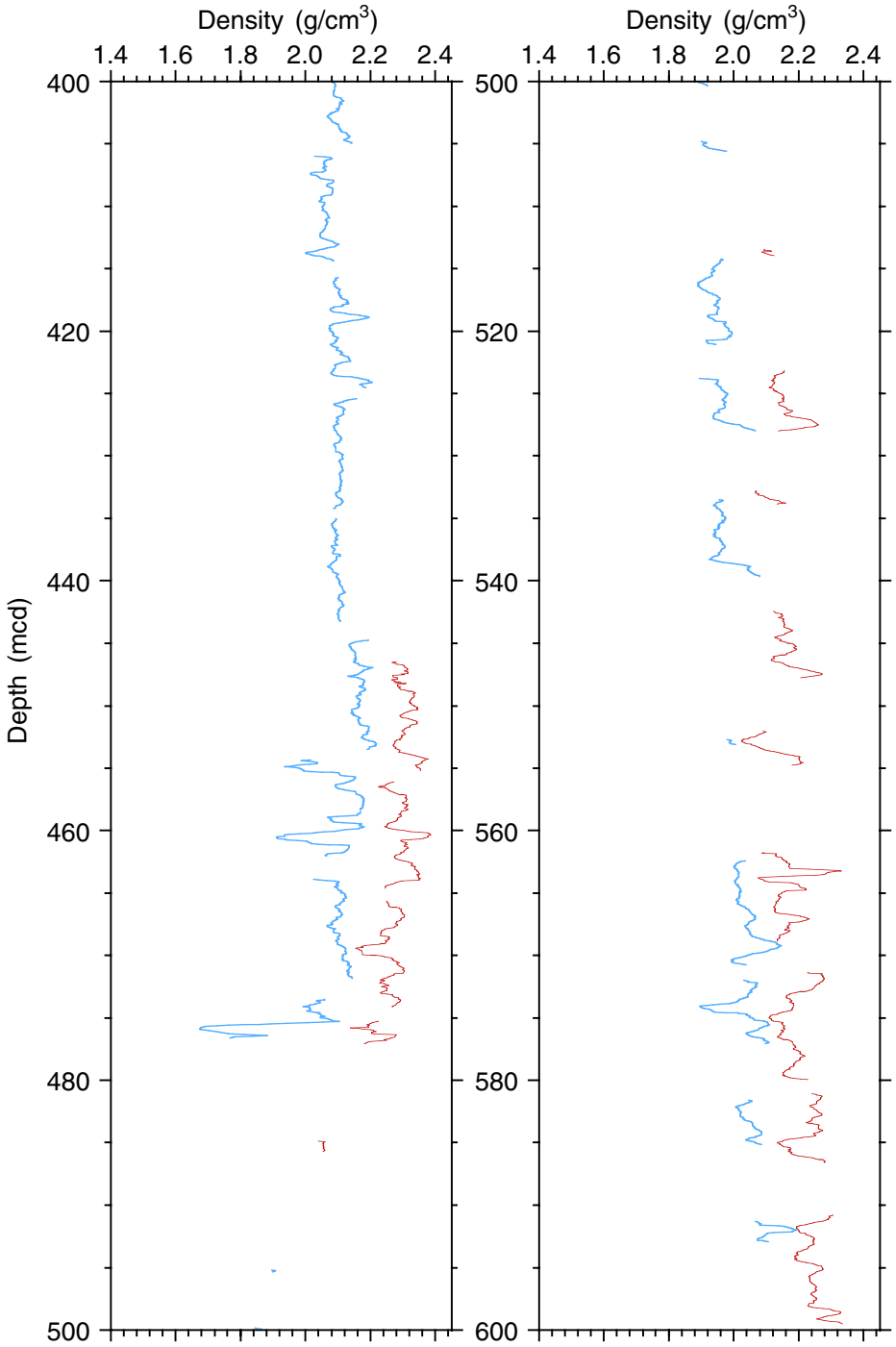

Figure F3 (continued).

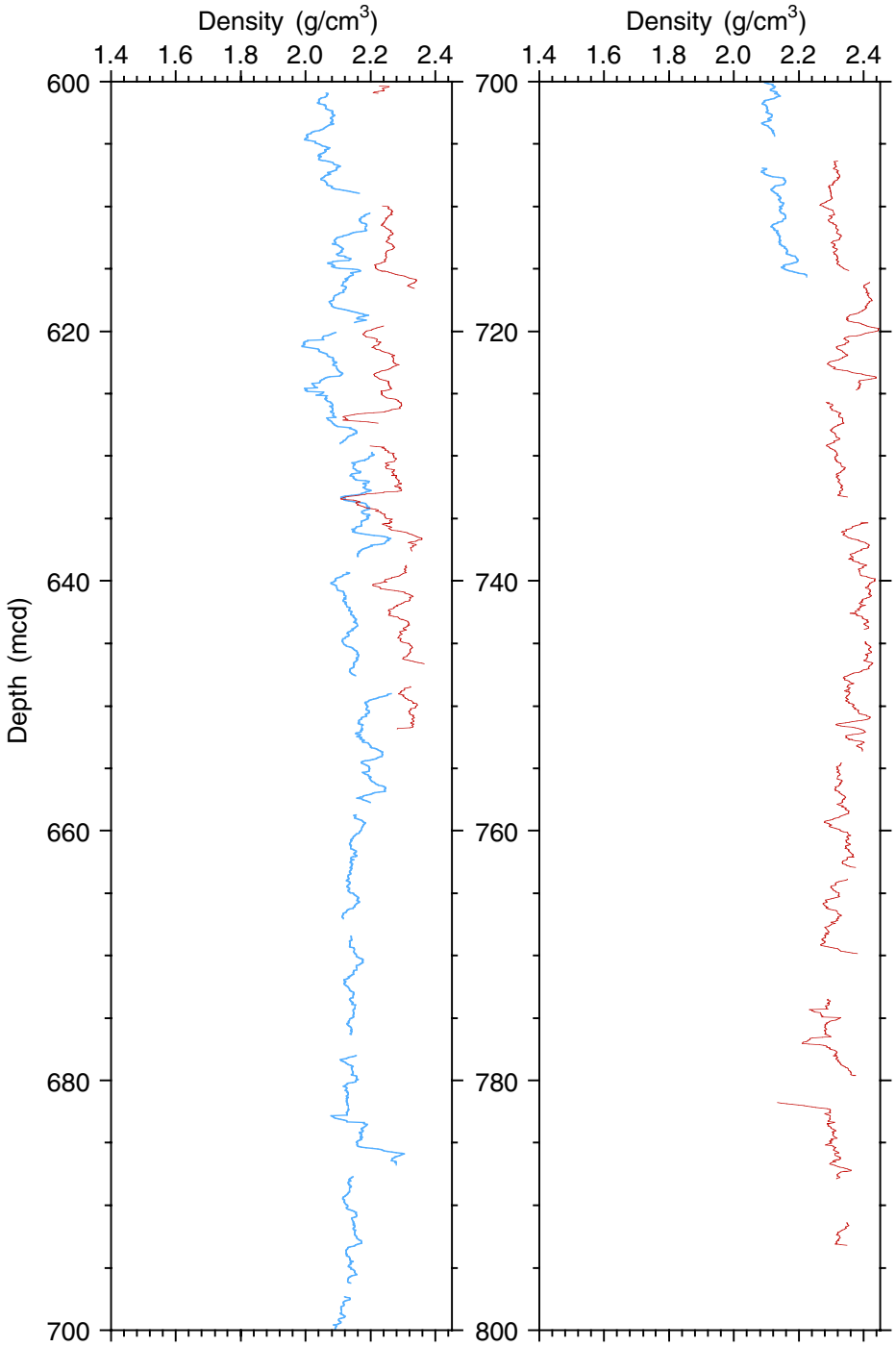

Figure F3 (continued).

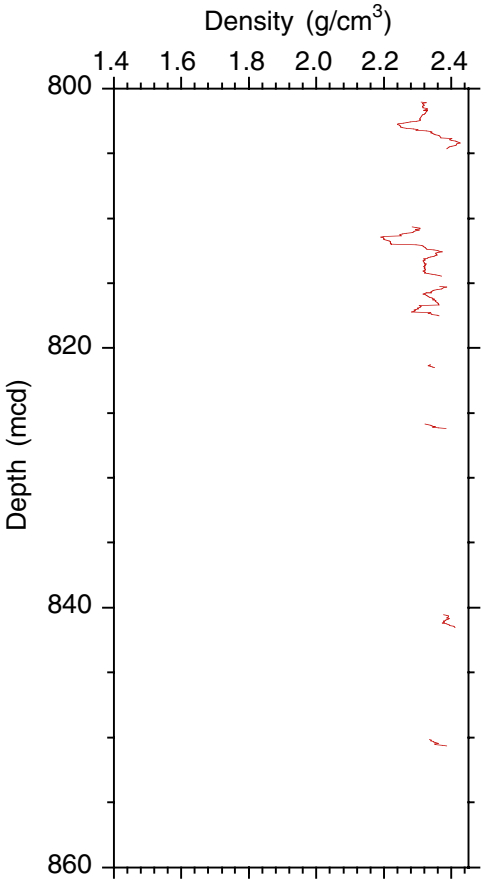

Figure F4. Smoothed (11-point running average)/correlated L* ("lightness") values from the CSR data and the splice for the two holes at Site 1148 (spliced CSR data in this figure are also available in **ASCII format**). The order of the three arrays (the splice and Holes 1148A and 1148B) increases outward from the origin. The hole arrays are offset from each other—and from the splice—by a constant (8%) so that only the splice is plotted relative to the absolute L* value. Values ≤1% have been culled. Lines identify the splice tie points. (Continued on next four pages.)

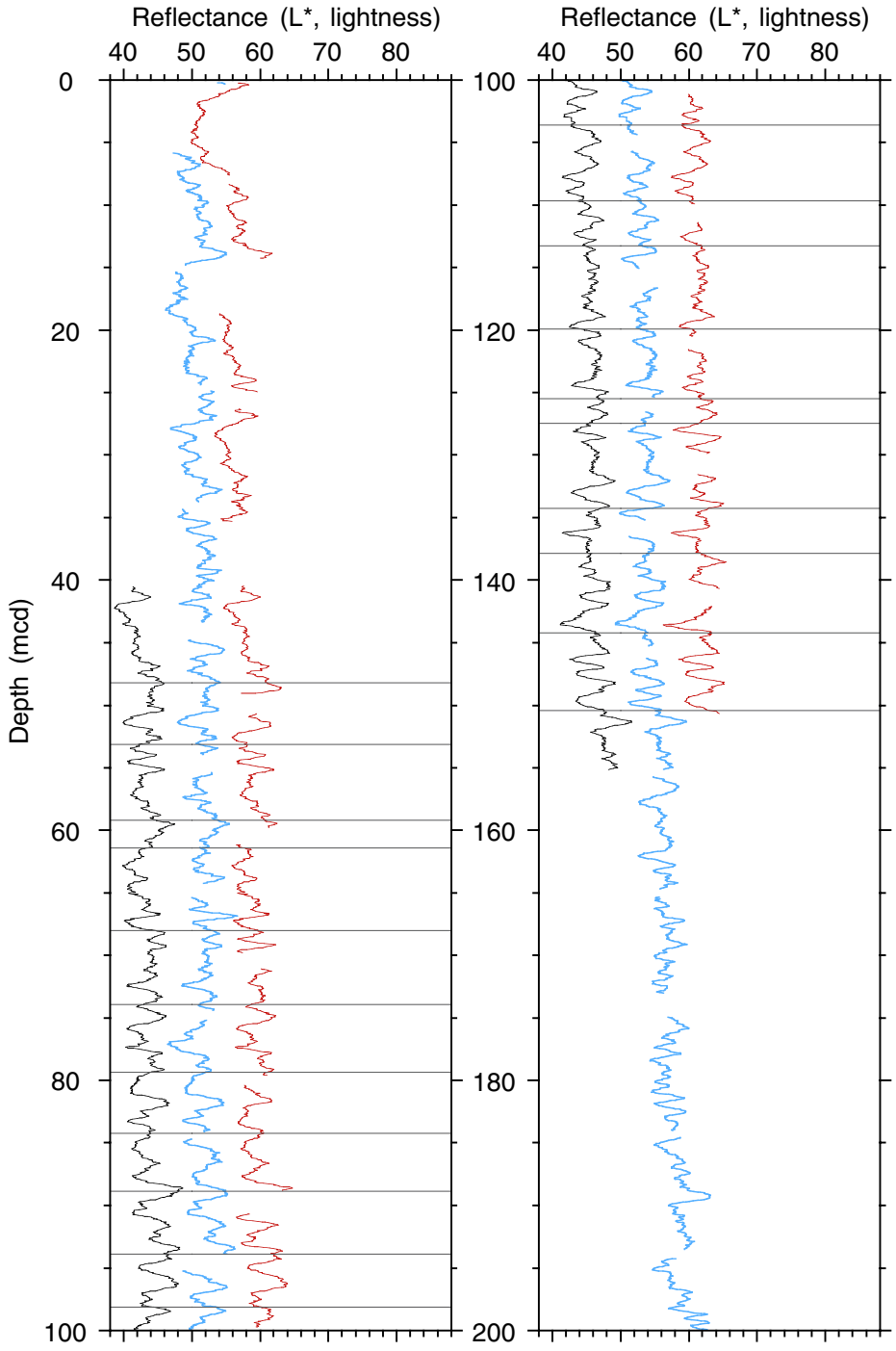

Figure F4 (continued).

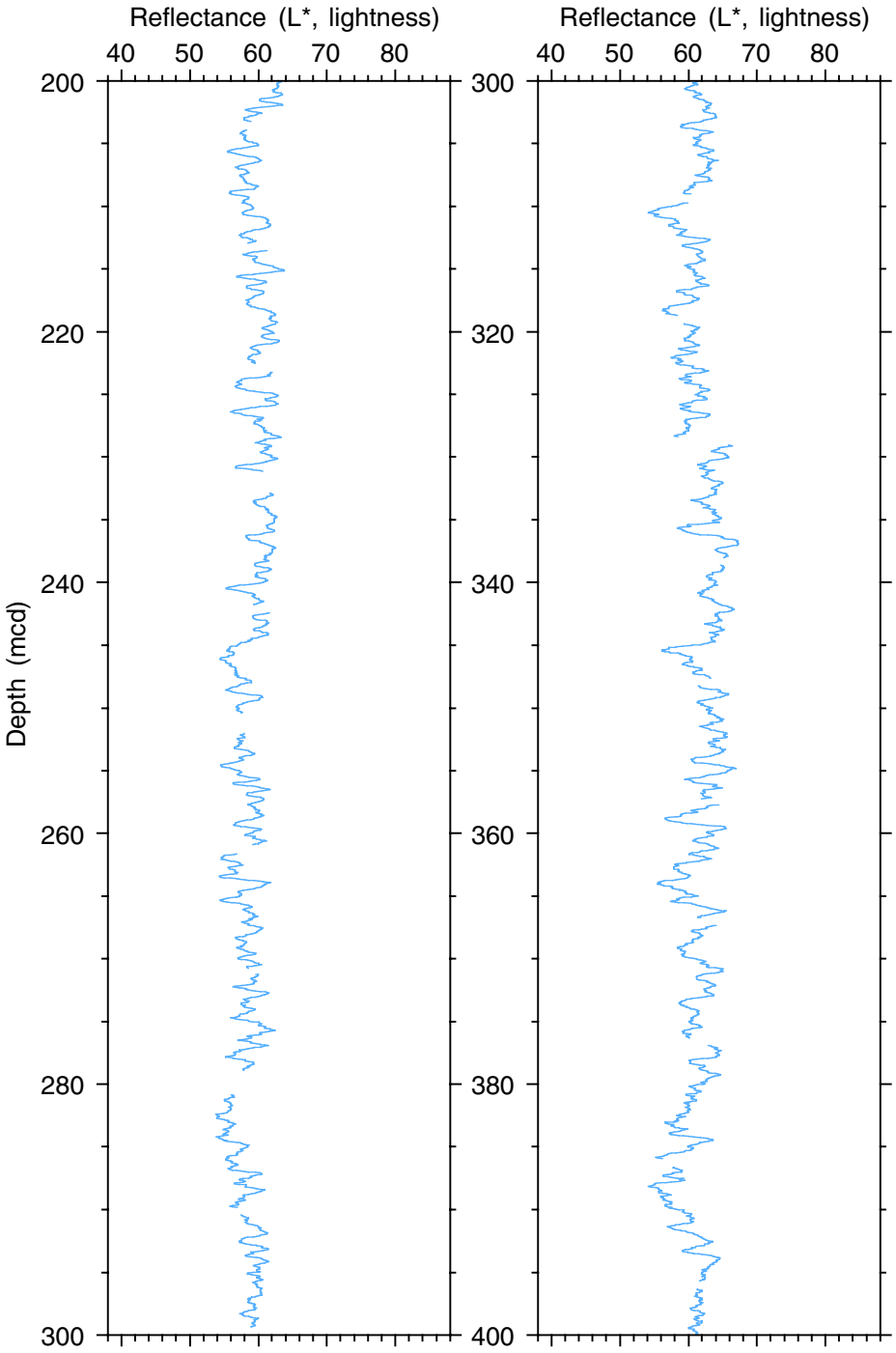

Figure F4 (continued).

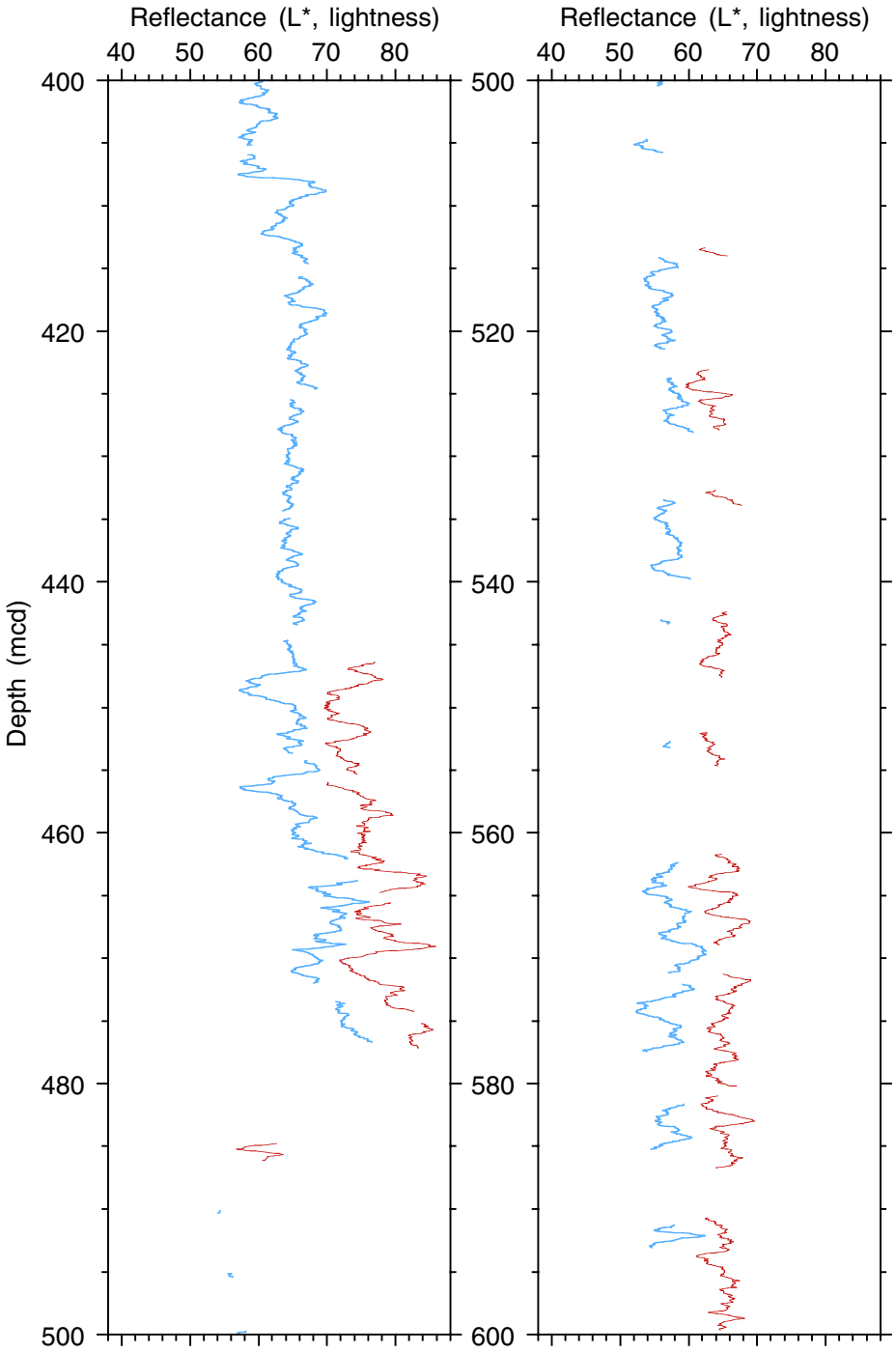

Figure F4 (continued).

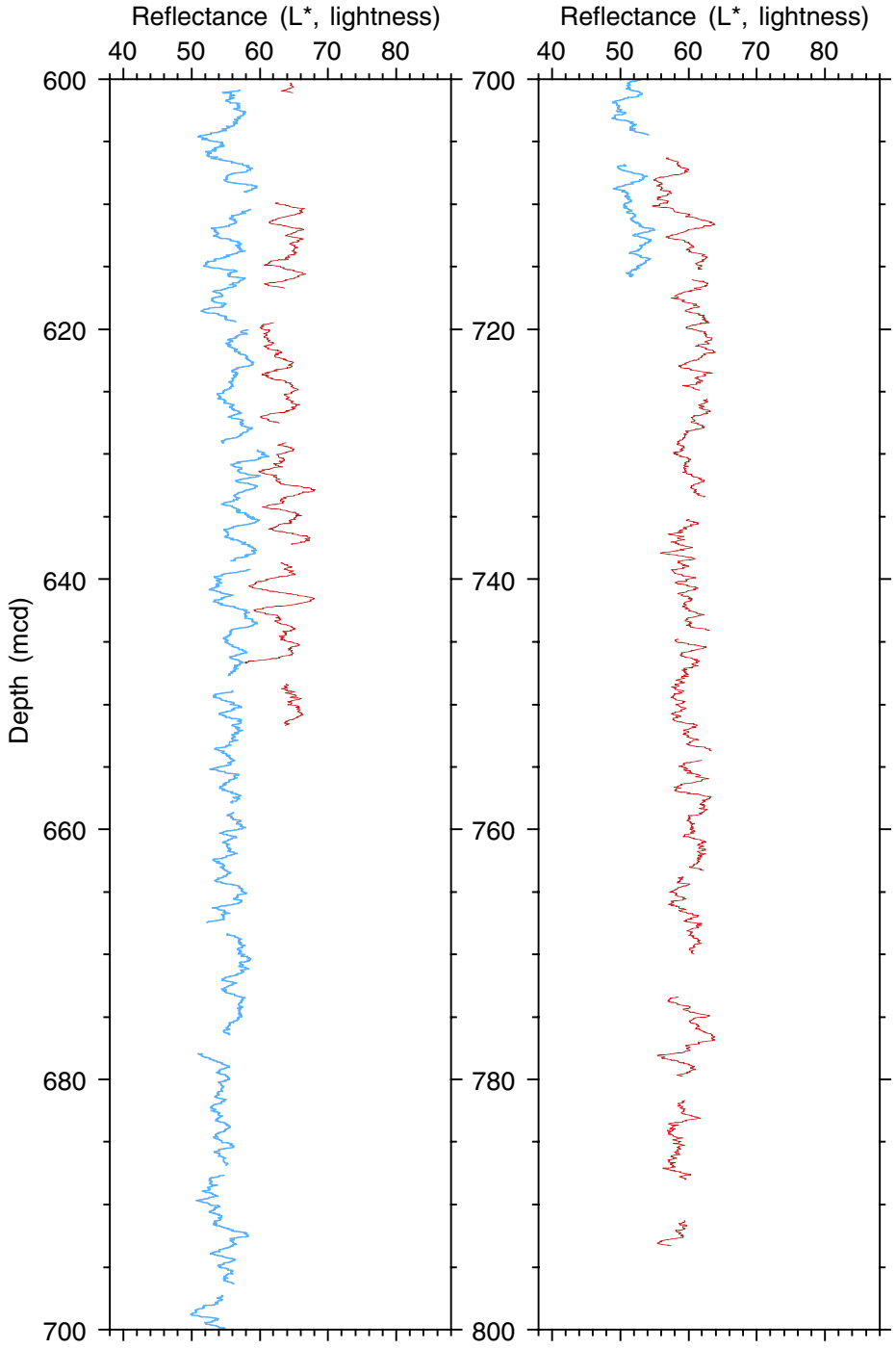

Figure F4 (continued).

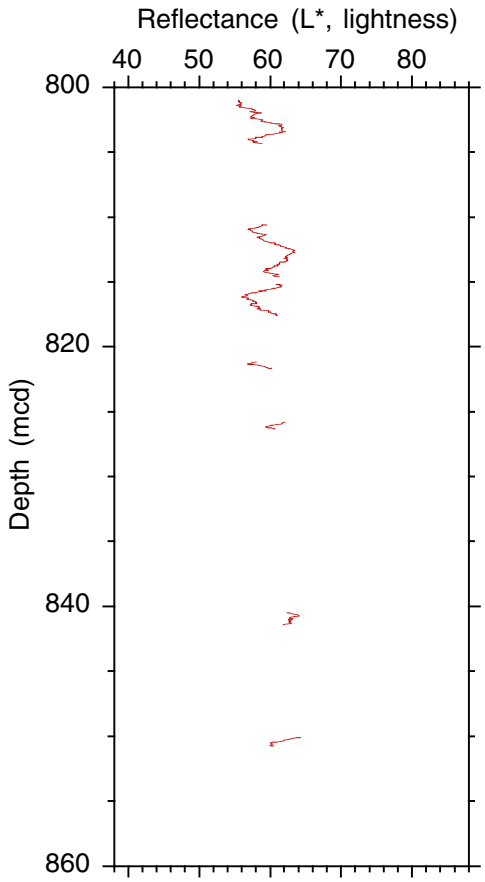

Figure F5. Summary of the recovered section at Site 1148, showing lithologic units, sediment types, lightness intensity (L* parameter) and the a* parameter, coulometer carbonate and clay, biogenic carbonate, and biogenic silica estimates from smear slides. High positive values of a* correspond to high red intensity, whereas high negative values correspond to high green intensity. L* and a* values correspond to measurements from Hole 1148A.

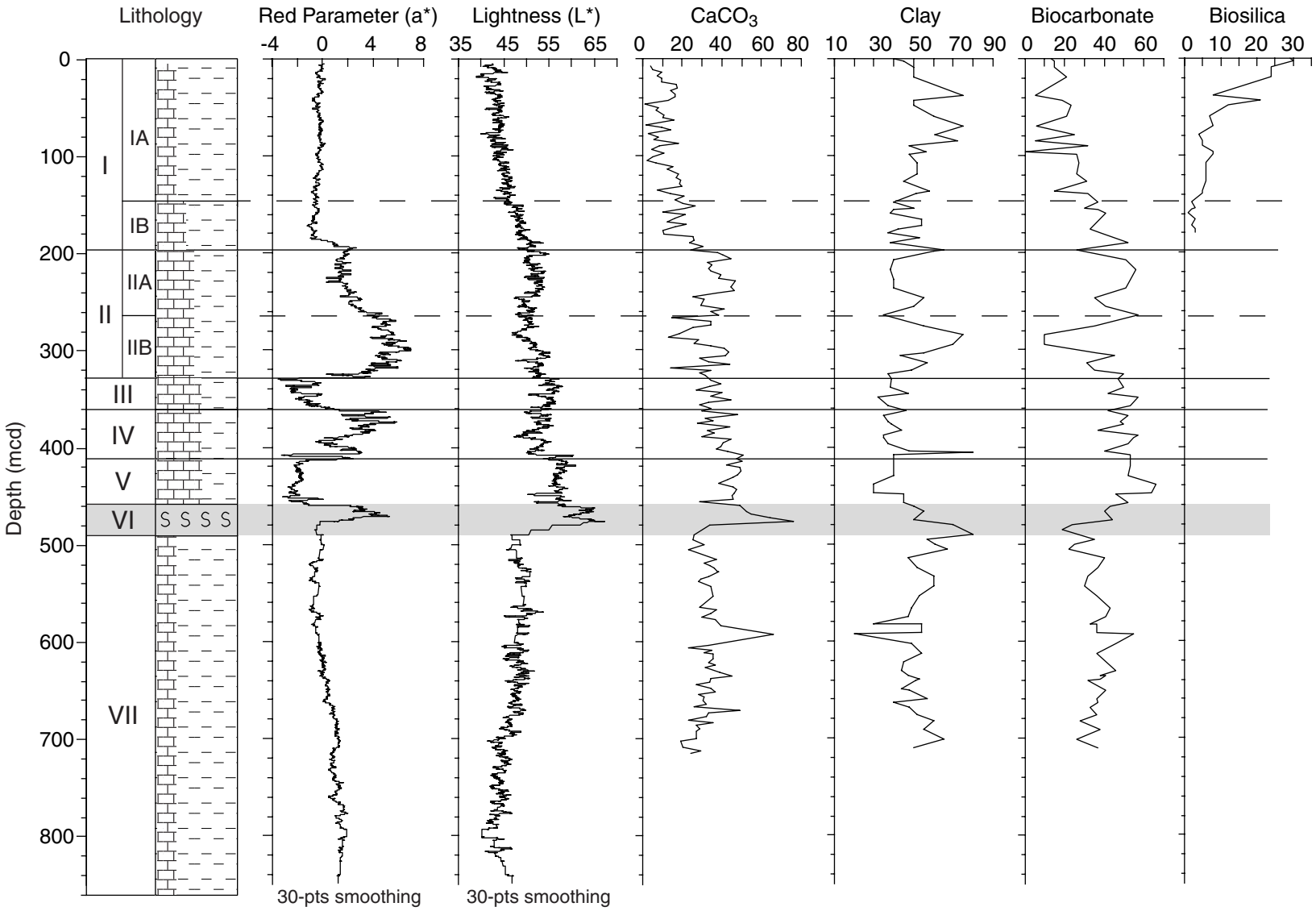

Figure F6. Occurrence of "iron sulfide," pyrite concretions, and green layers in Hole 1148A. The units are the number of occurrences per meter of sediment. Solid lines are the 3-point moving average of the original data.

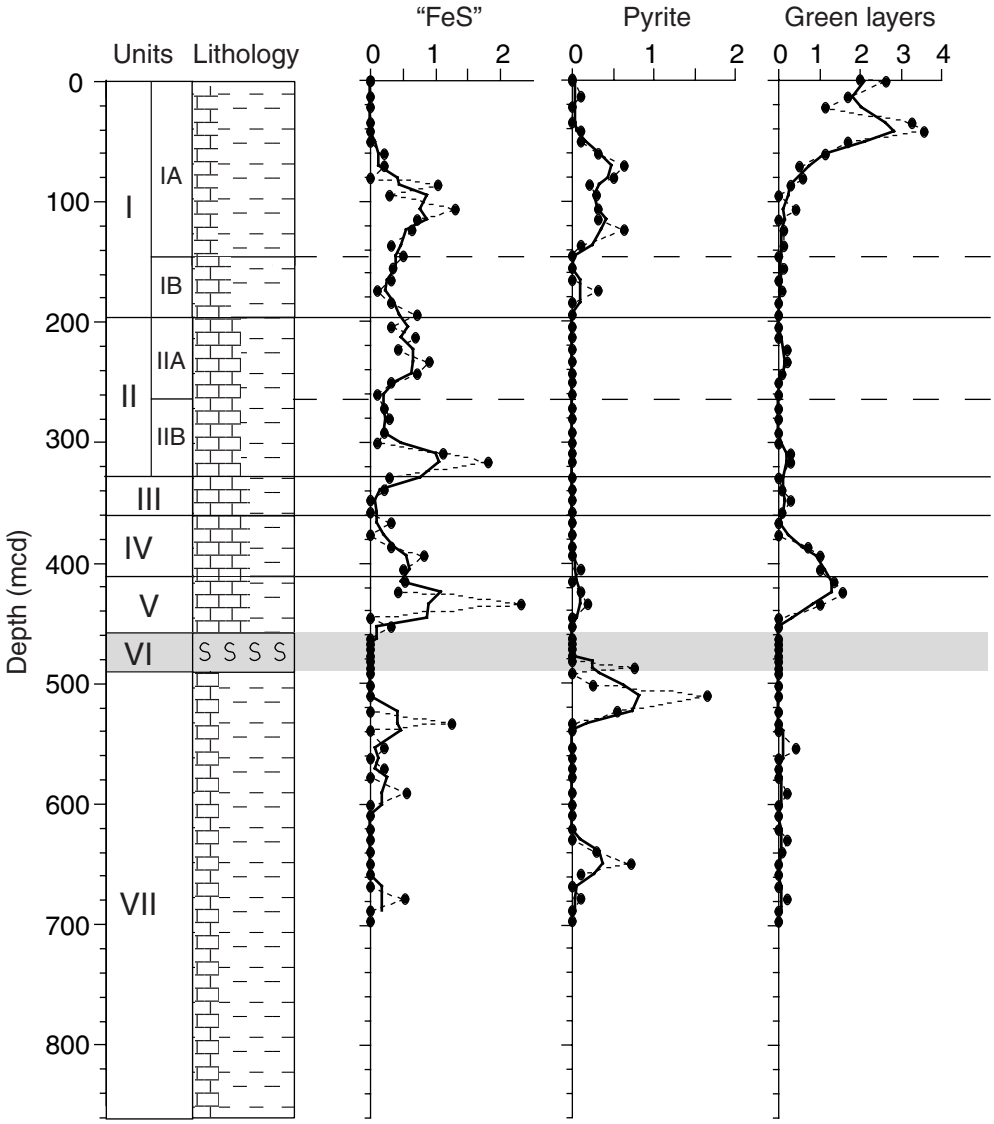

Figure F7. Diagram showing the increasing density downsection of light-colored, carbonate-rich layers within the upper two units at Site 1148.

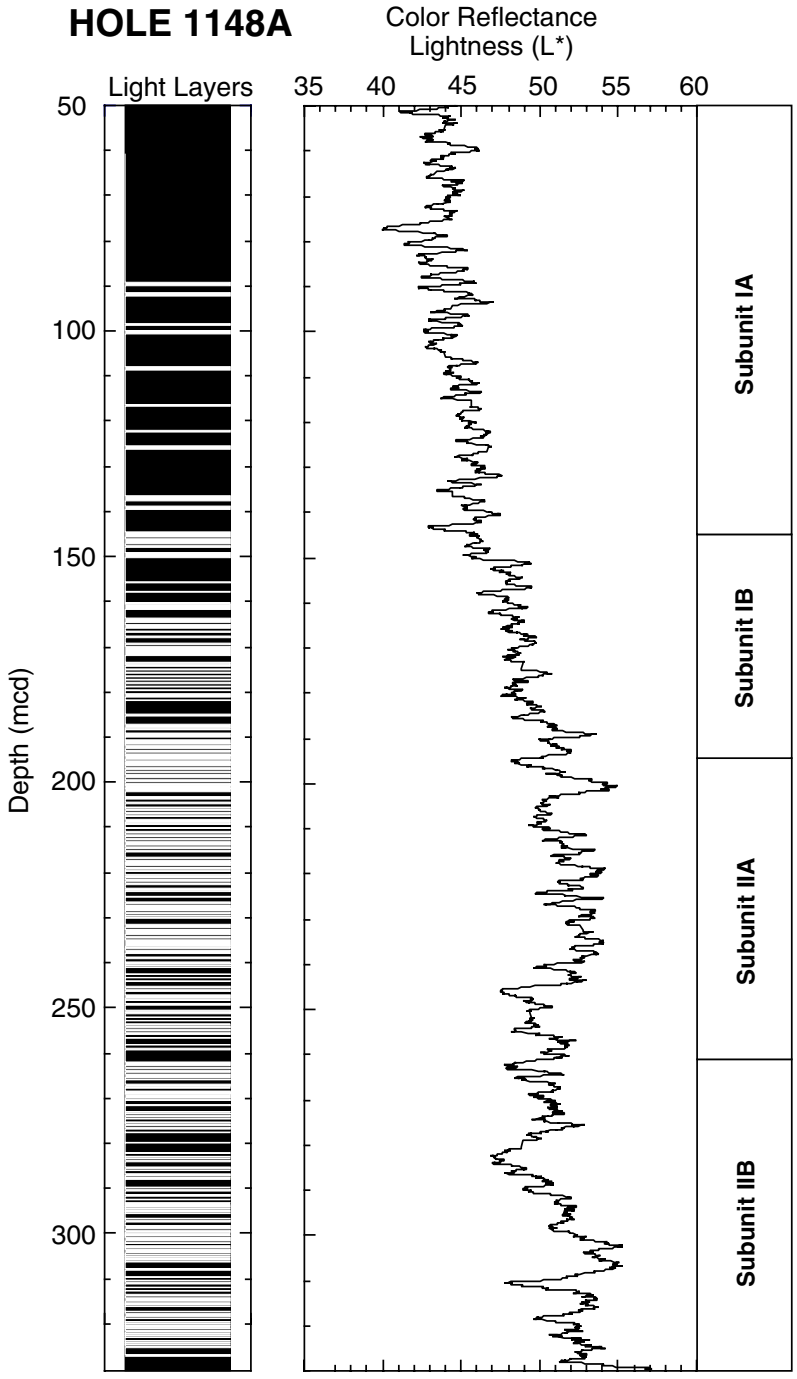

Figure F8. Dark, graded tephra layer within nannofossil clay of Unit II (interval 184-1148A-33X-5, 88–106 cm).

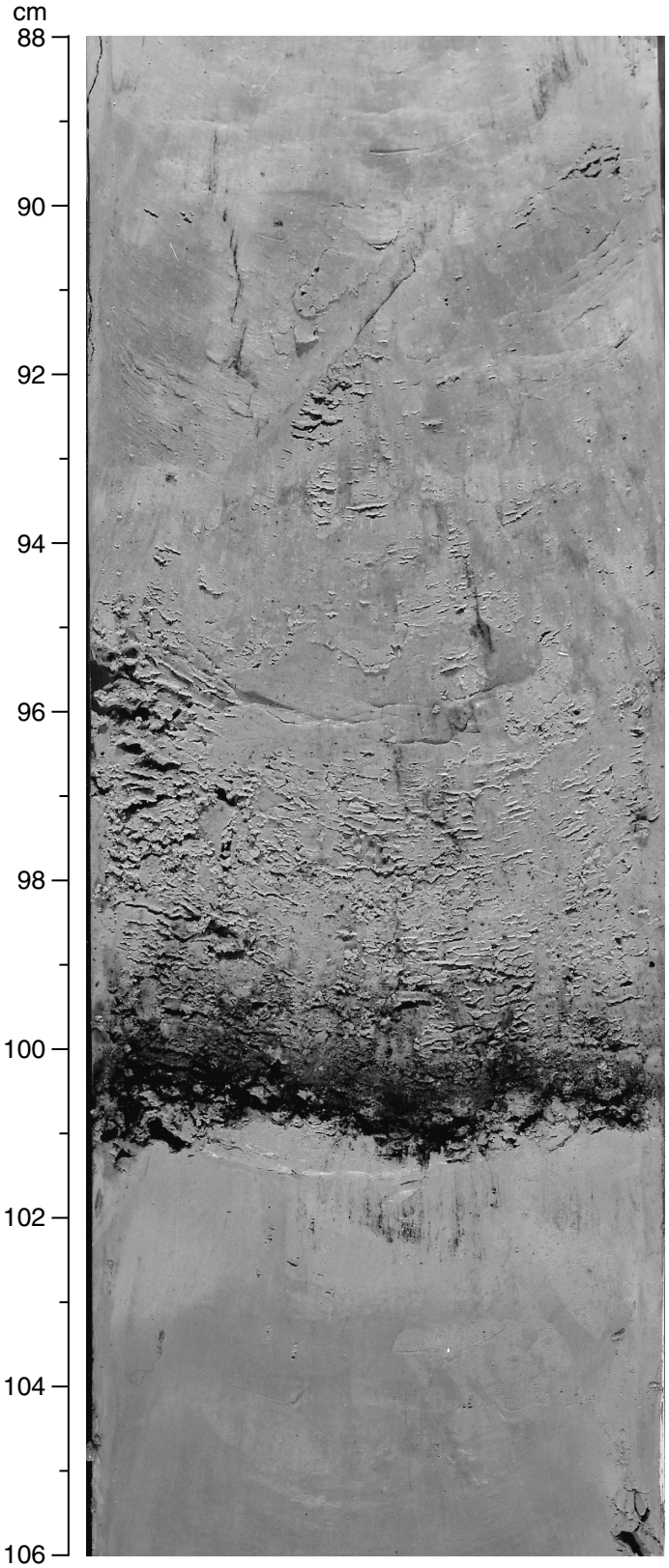

Figure F9. Carbonate sand turbidite within Unit III (interval 184-1148A-38X-5, 79–92 cm).

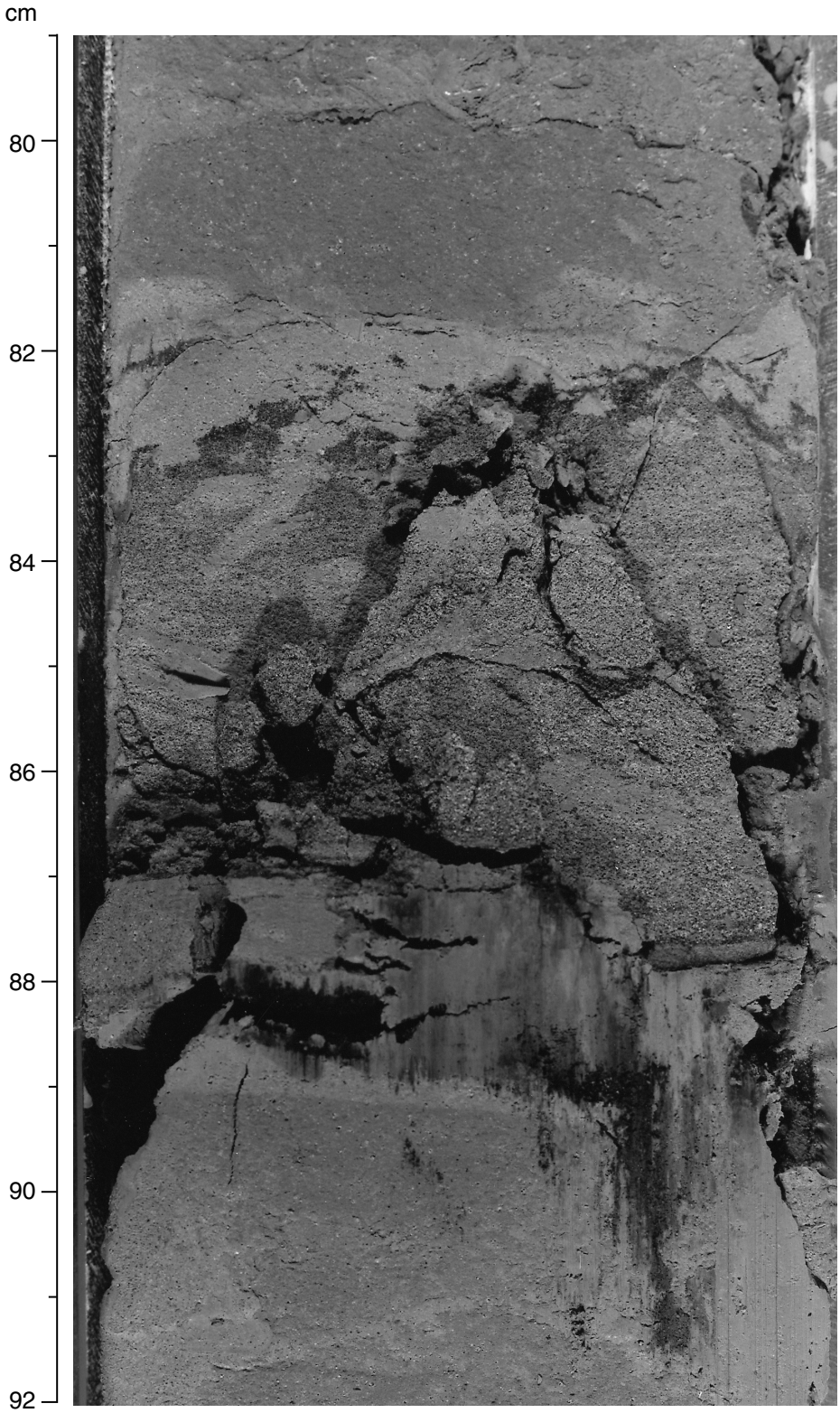

Figure F10. Strongly bioturbated lithologic boundary within Unit V showing the color change associated with varying amounts of clay (interval 184-1148A-43X-1, 83–98 cm).

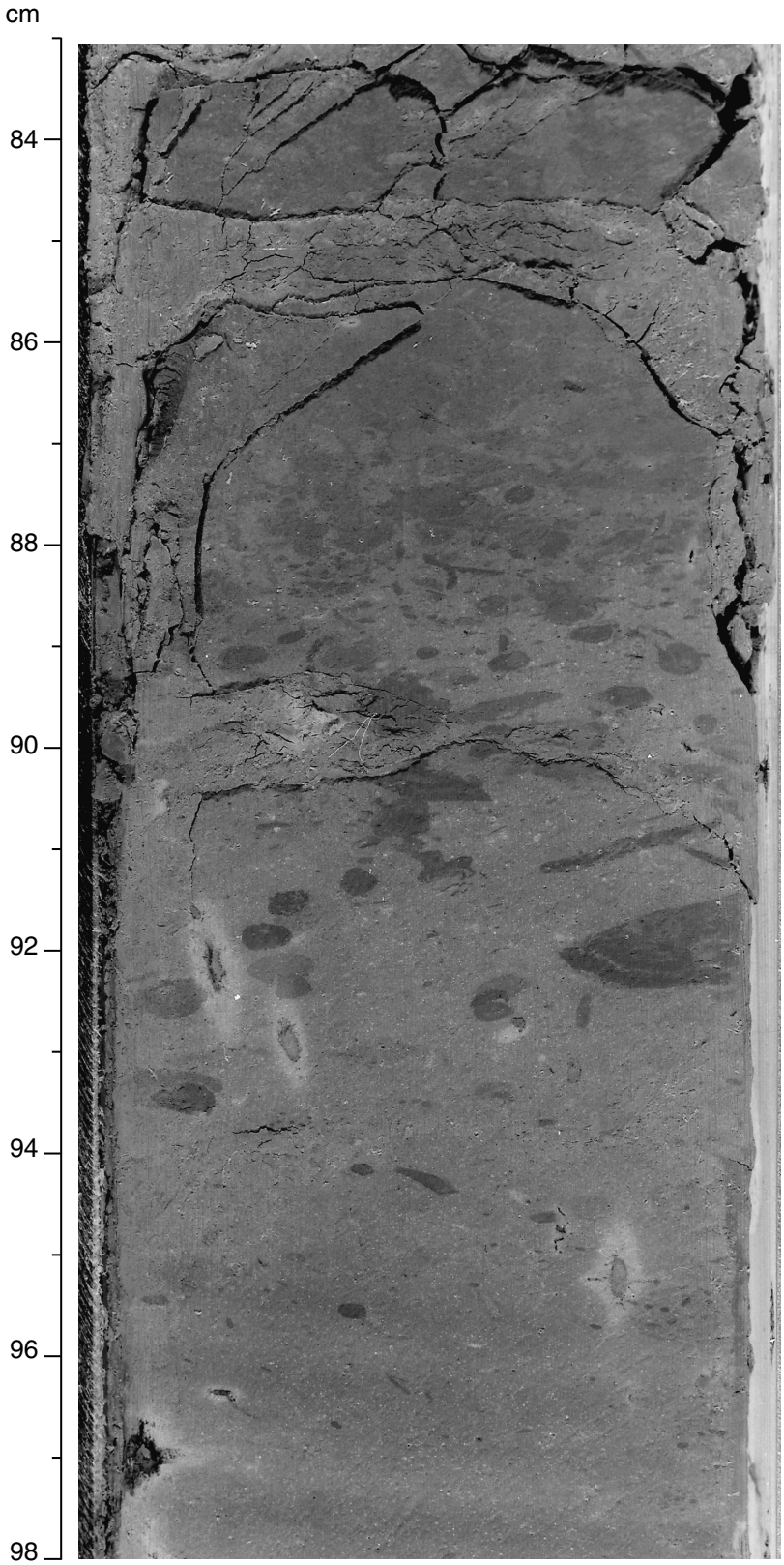

Figure F11. Plastic, soft-sediment deformation in Unit VI shown together with intraformational rip-up clasts (interval 184-1148A-48X-4, 57–70 cm).

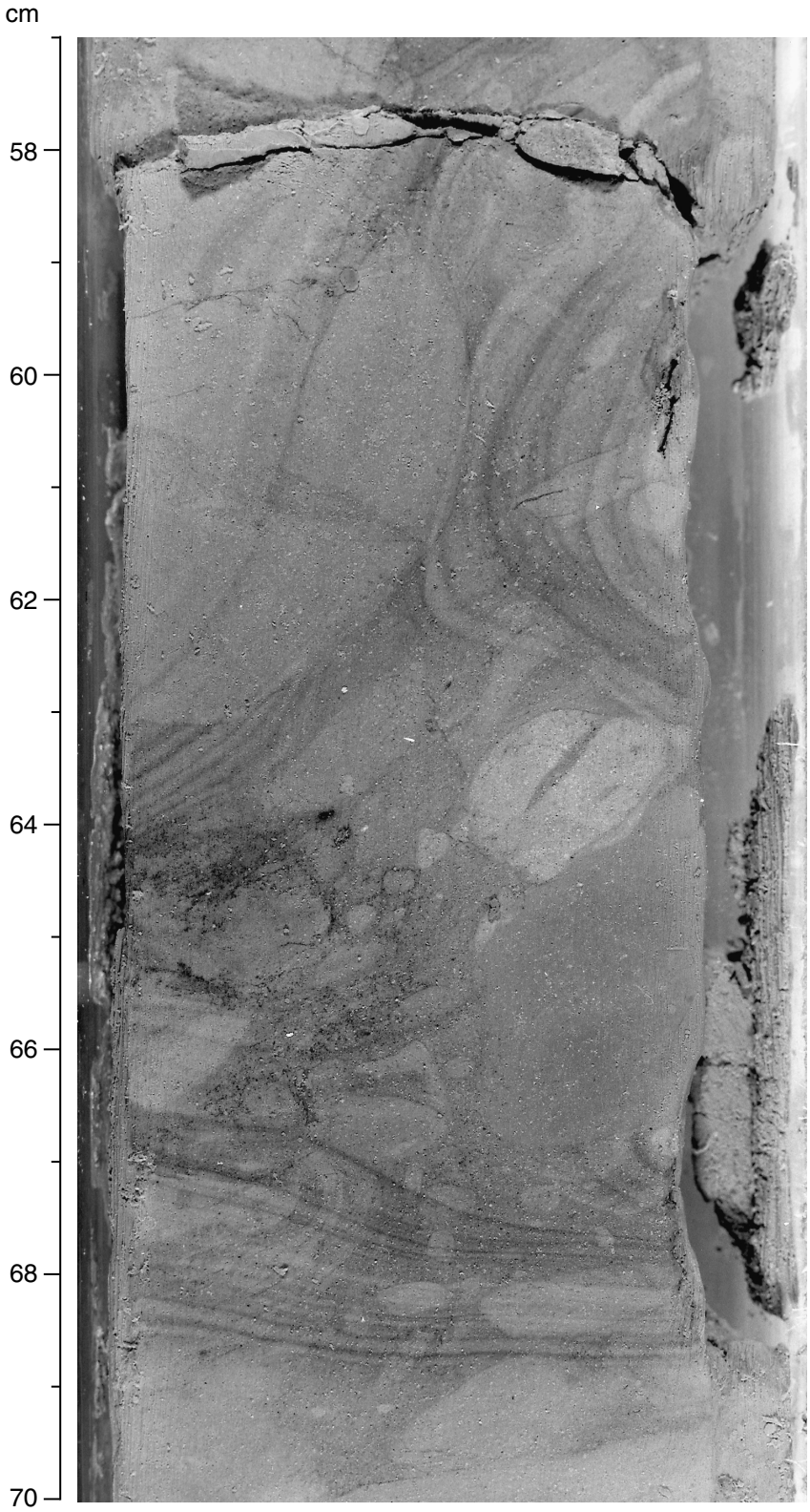

Figure F12. Small-scale normal faulting seen in Unit VI and lower in the drilled section (interval 184-1148A-49X-4, 95–105 cm).

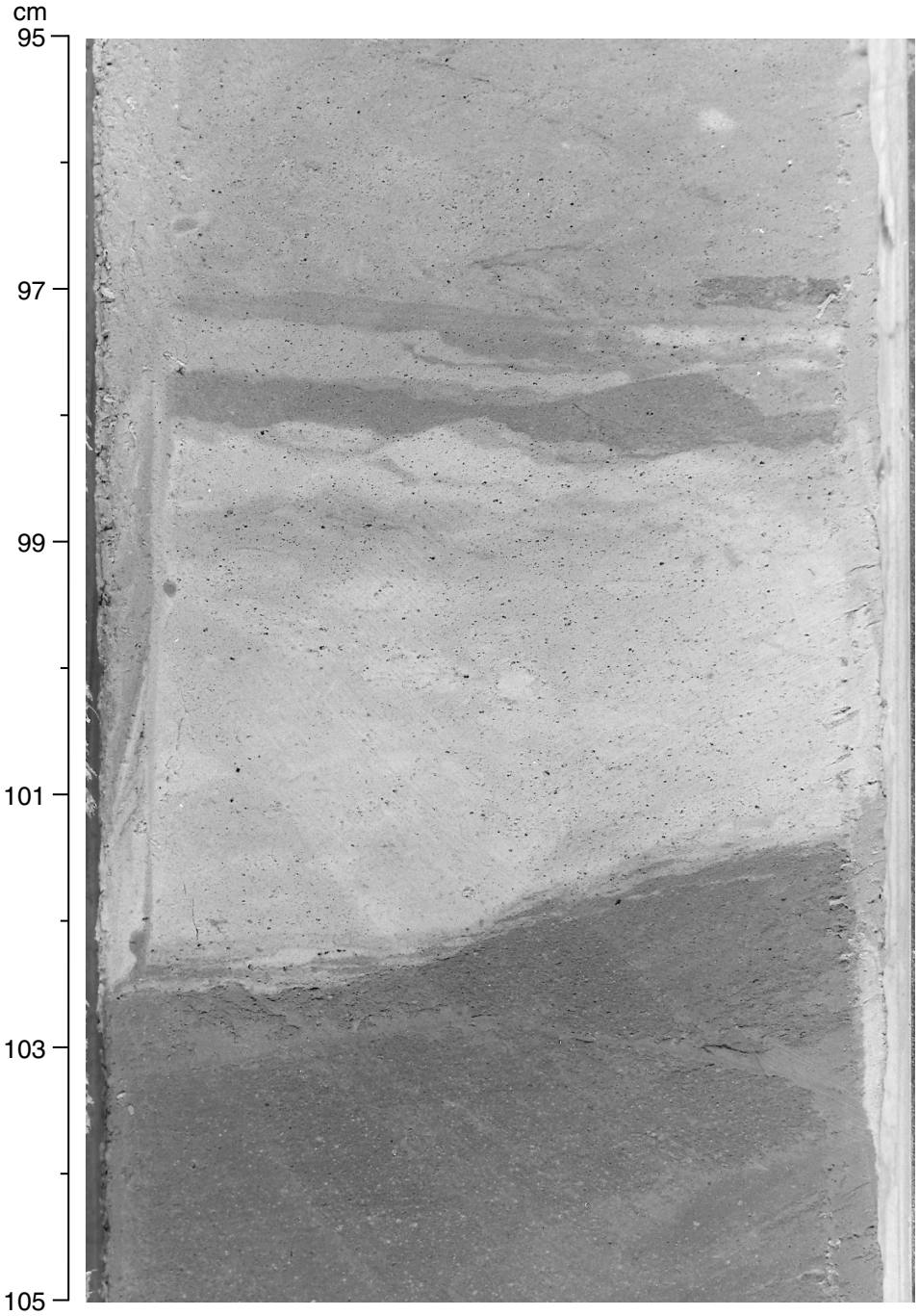

Figure F13. Close-up of flaser-bedded sandstone laminae within parallel laminated claystone with nannofossils in Unit VII (interval 184-1148B-48X-2, 37–45 cm).

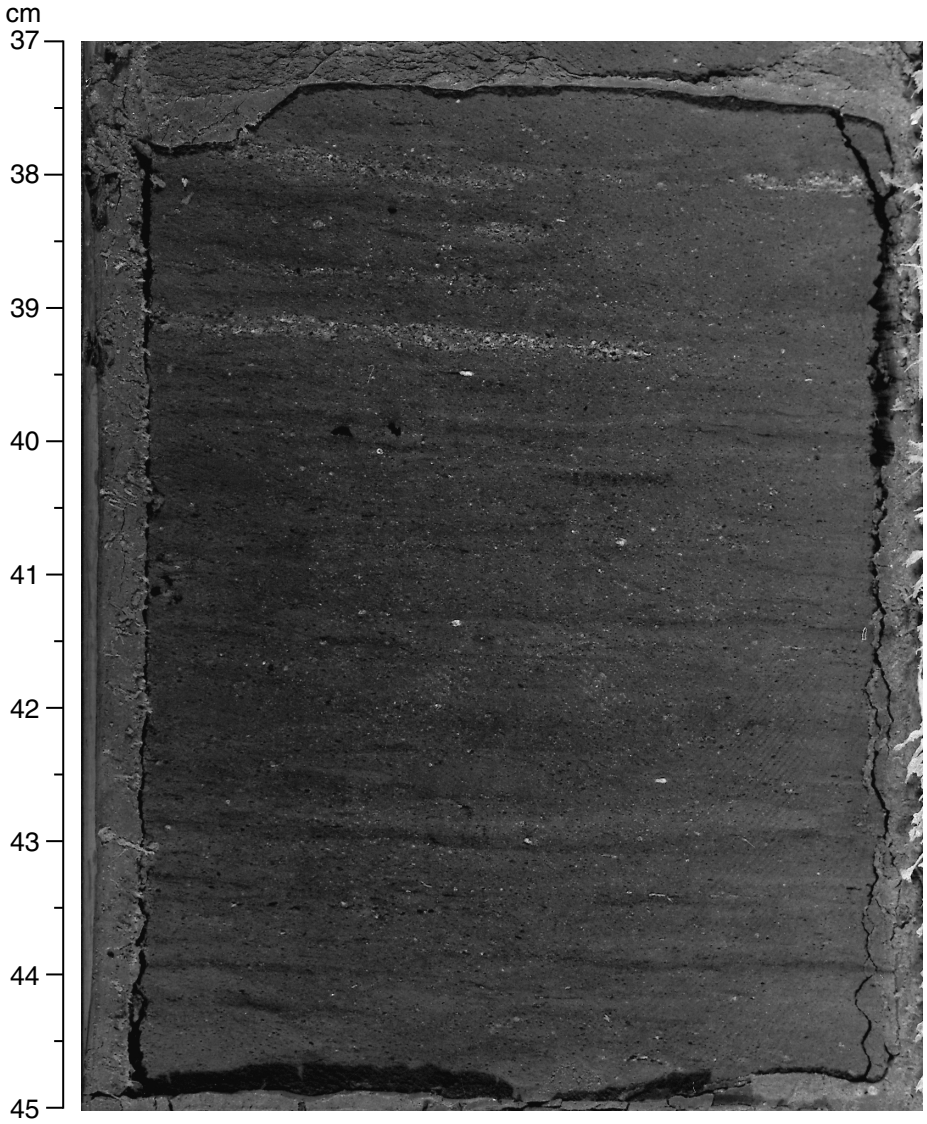

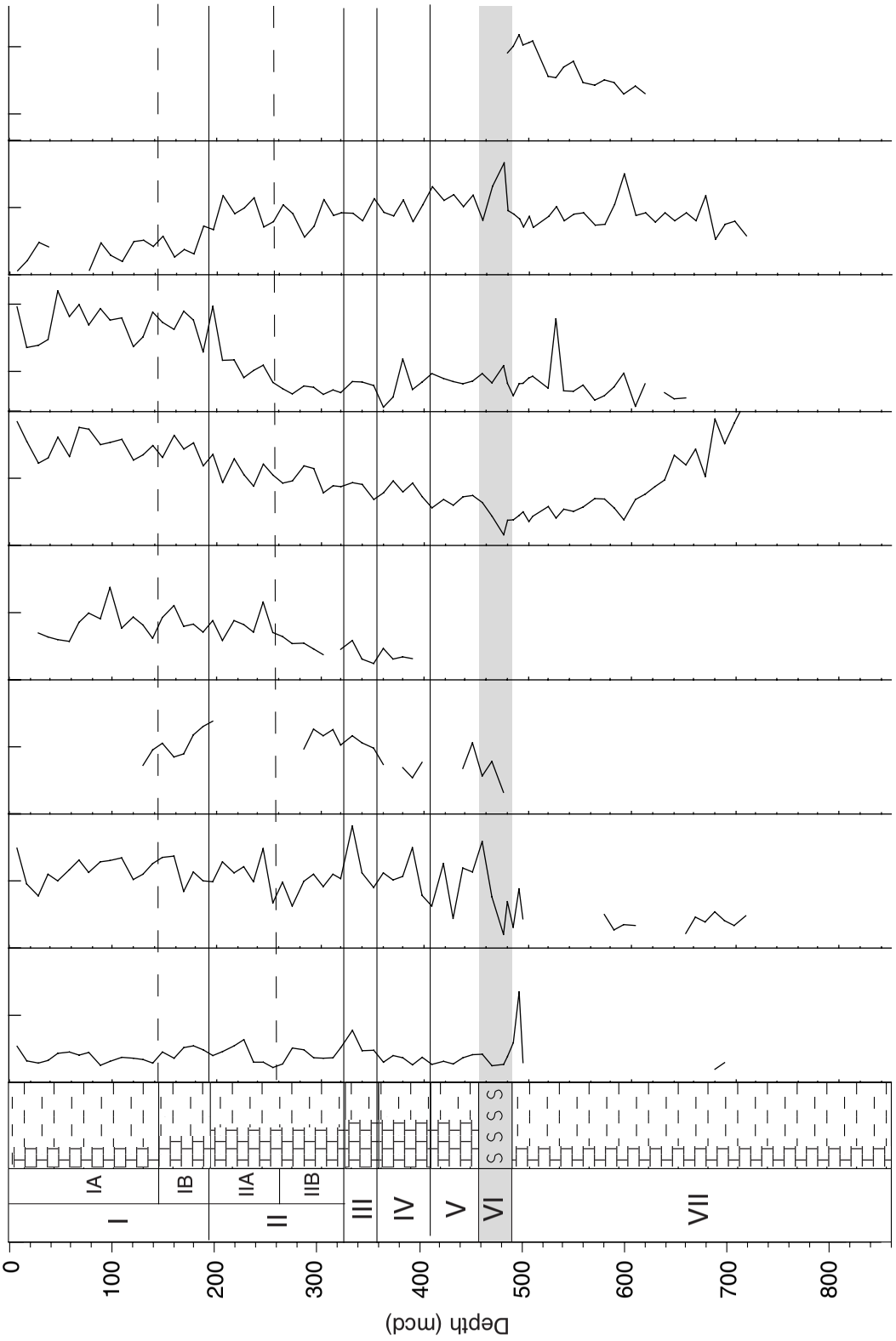

Figure F14. Variation of bulk mineralogy determined by X-ray diffraction in Hole 1148A.

Figure F15. Age-depth plot for Site 1148. All biostratigraphic events are listed in Table T7, p. 98. The average sedimentation rate is calculated based on four control points (marked by * in Table T7, p. 98). Question marks represent a hiatus in the sedimentary record.

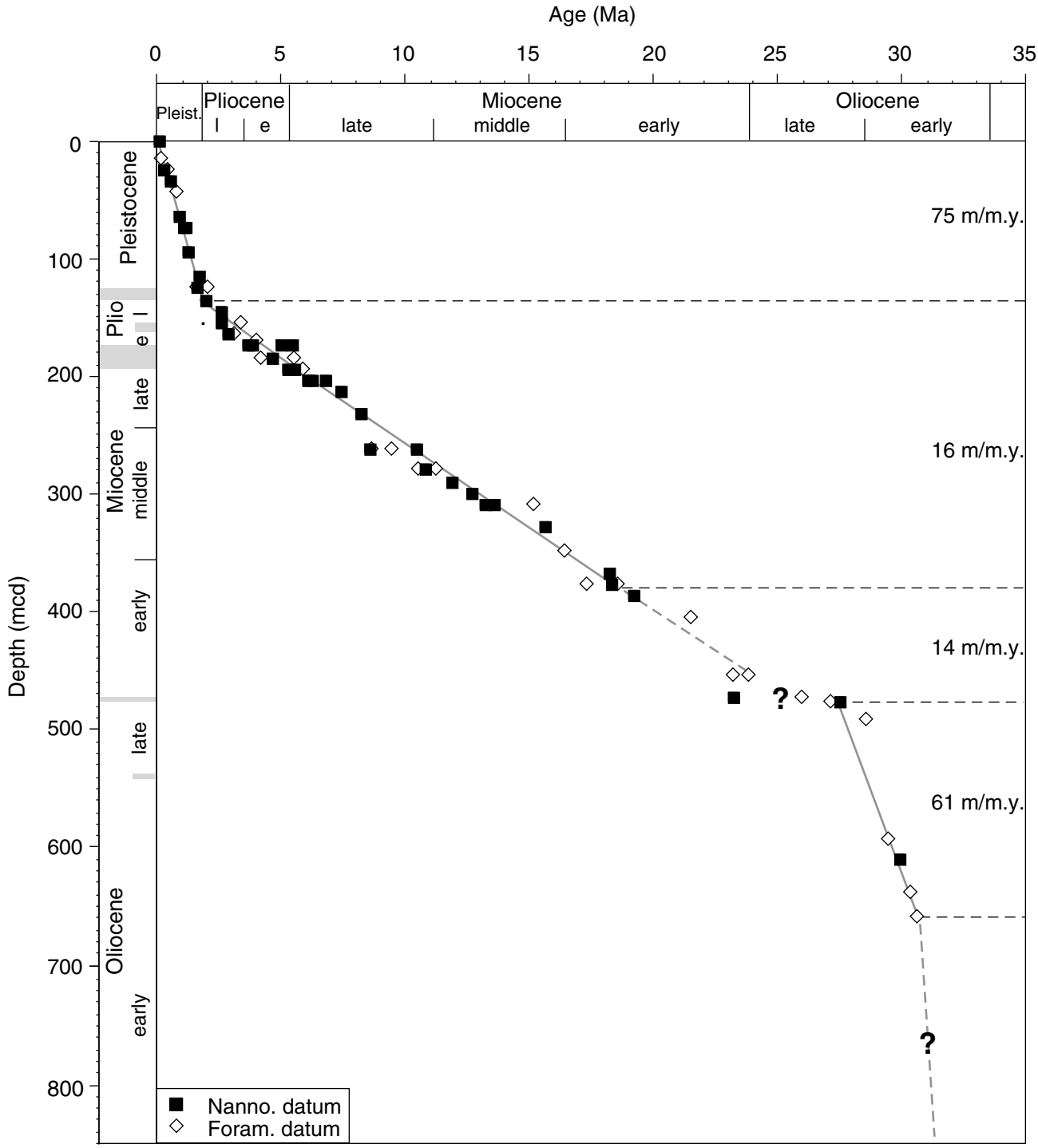

Figure F16. Declination and inclination for Hole 1148A, 0–180 mcd, obtained from long-core measurements (Cores 184-1148A-1H through 3H are not oriented).

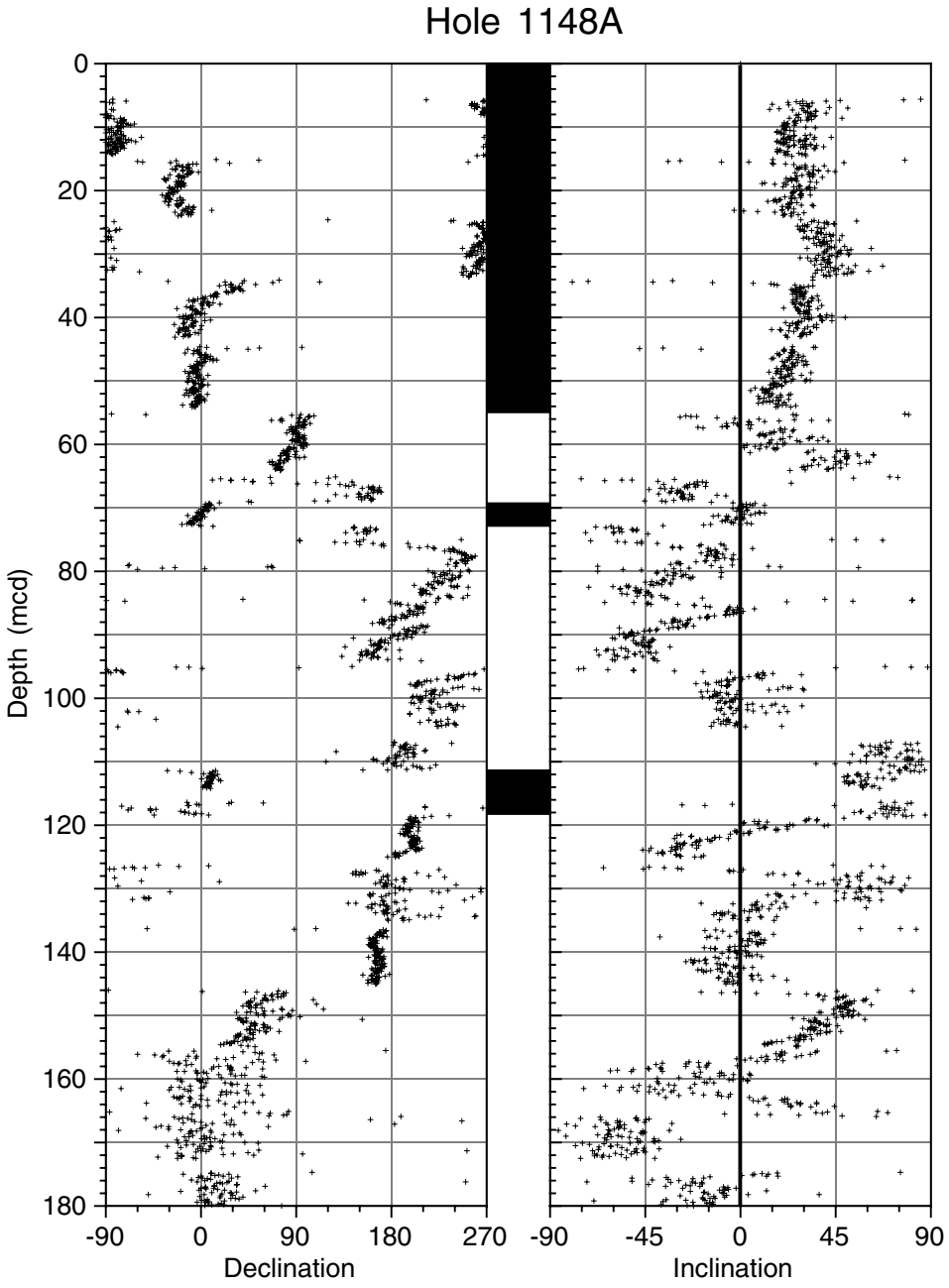

Figure F17. Declination and inclination for Hole 1148B, 0–150 mcd, obtained from long-core measurements (Cores 184-1148B-1H and 2H are not oriented).

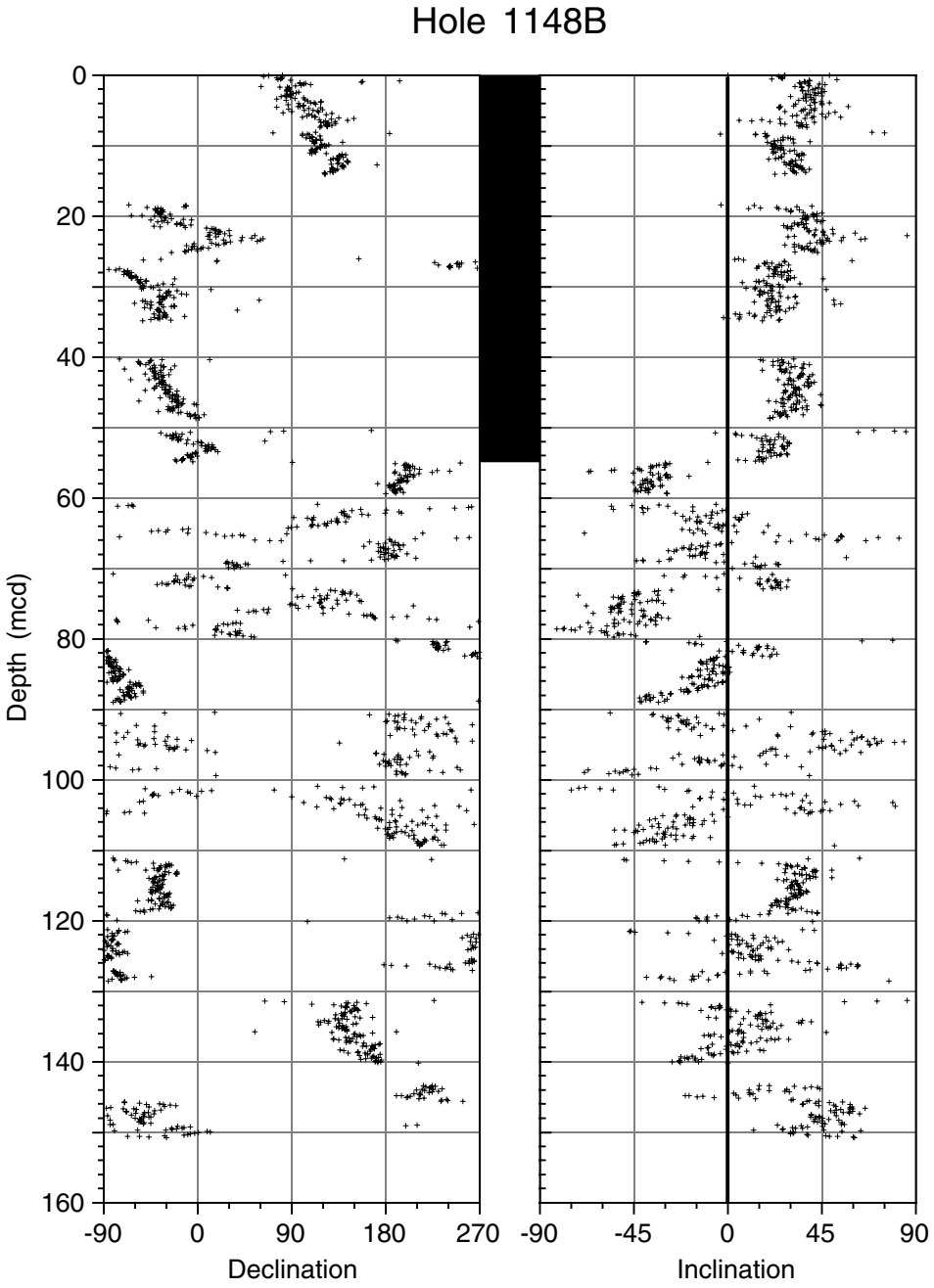

Figure F18. (**A**) Age-depth model, (**B**) linear sedimentation rates (LSR) and mass accumulation rates (MAR) vs. depth, and (**C**) LSR and MAR vs. age for Site 1148. Construction of model rates, LSR, and MAR is explained in "Sedimentation and Accumulation Rates," p. 13, in the "Explanatory Notes" chapter. In (A), diamonds = calcareous nannofossils, circles = foraminifers, squares = paleomagnetic reversals; in (B) and (C), solid lines = total sediment LSR, dashed lines = carbonate LSR, stippled columns = total sediment MAR, solid columns = carbonate MAR.

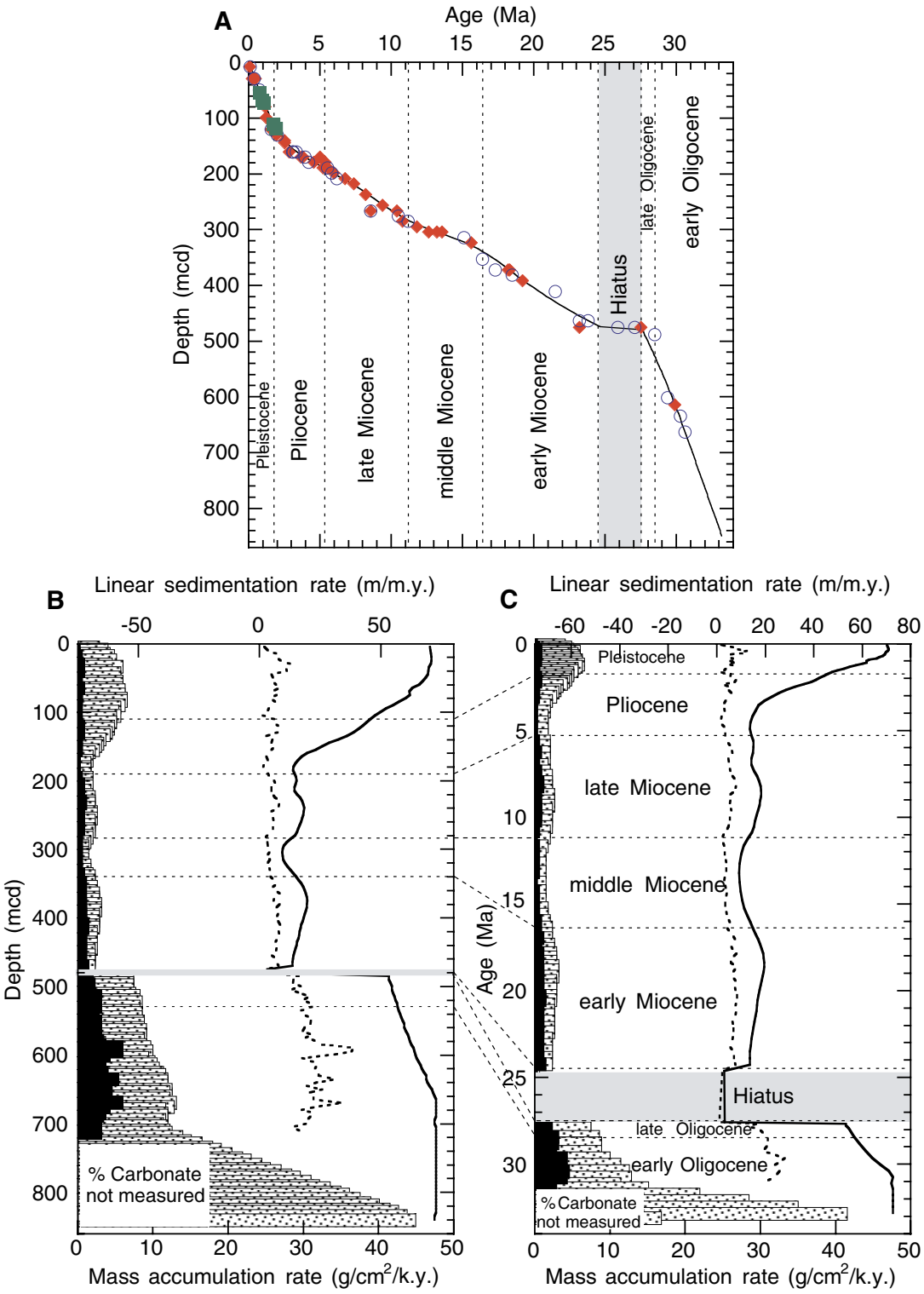

Figure F19. (**A**) Carbonate, (**B**) total organic carbon, and (**C**) organic C/N ratio at Site 1148 vs. depth (Hole 1148A).

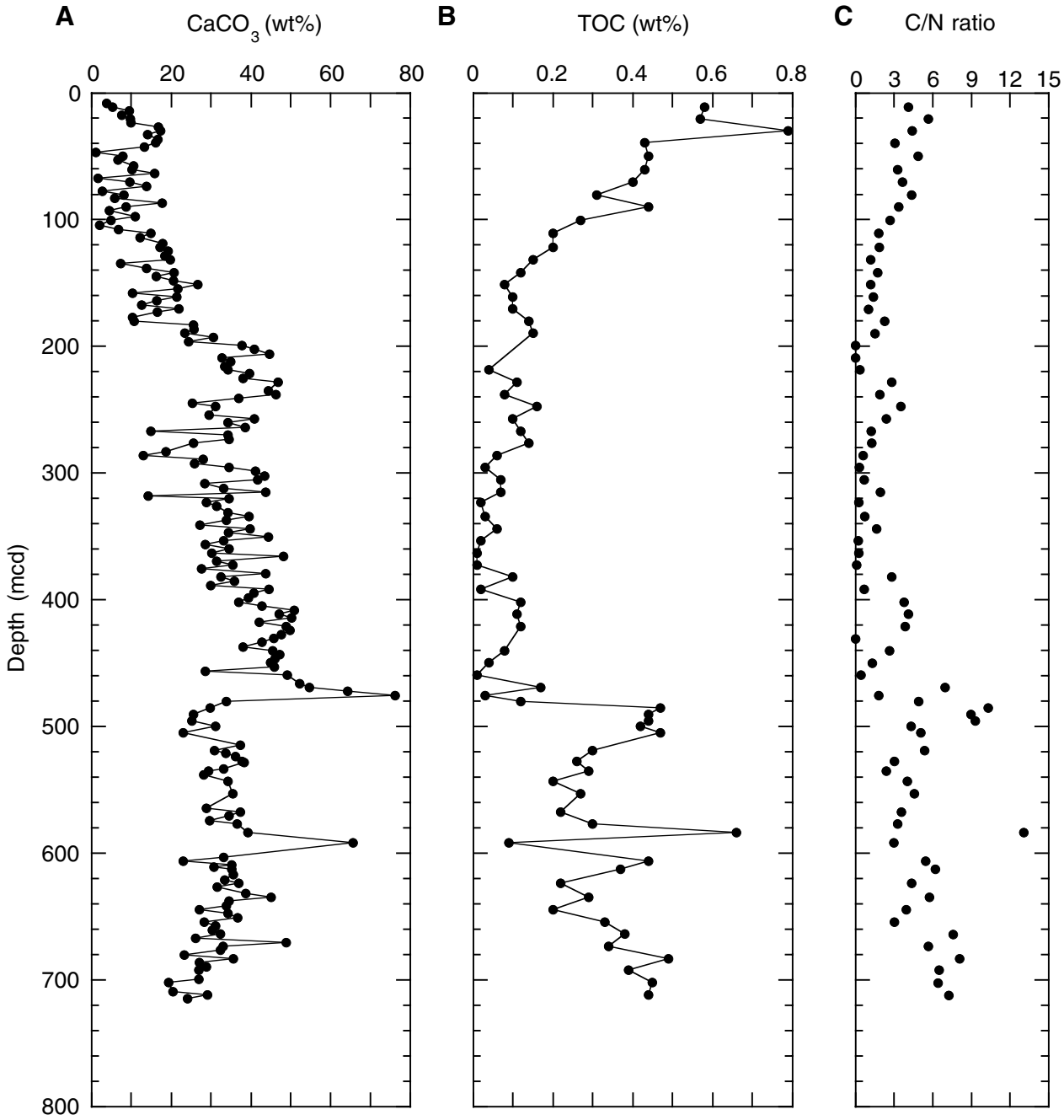

Figure F20. (**A**) Methane, ethane, and propane concentrations (ppmv) and (**B**) C_1/C_2 ratio vs. depth as obtained by the headspace technique, analyzed by the GC3 (FID 1) for Hole 1148A. Solid vertical bar = interval of ethylene presence, open square = depth interval and approximate concentration of C_4 and C_5, FID = flame ionization detector.

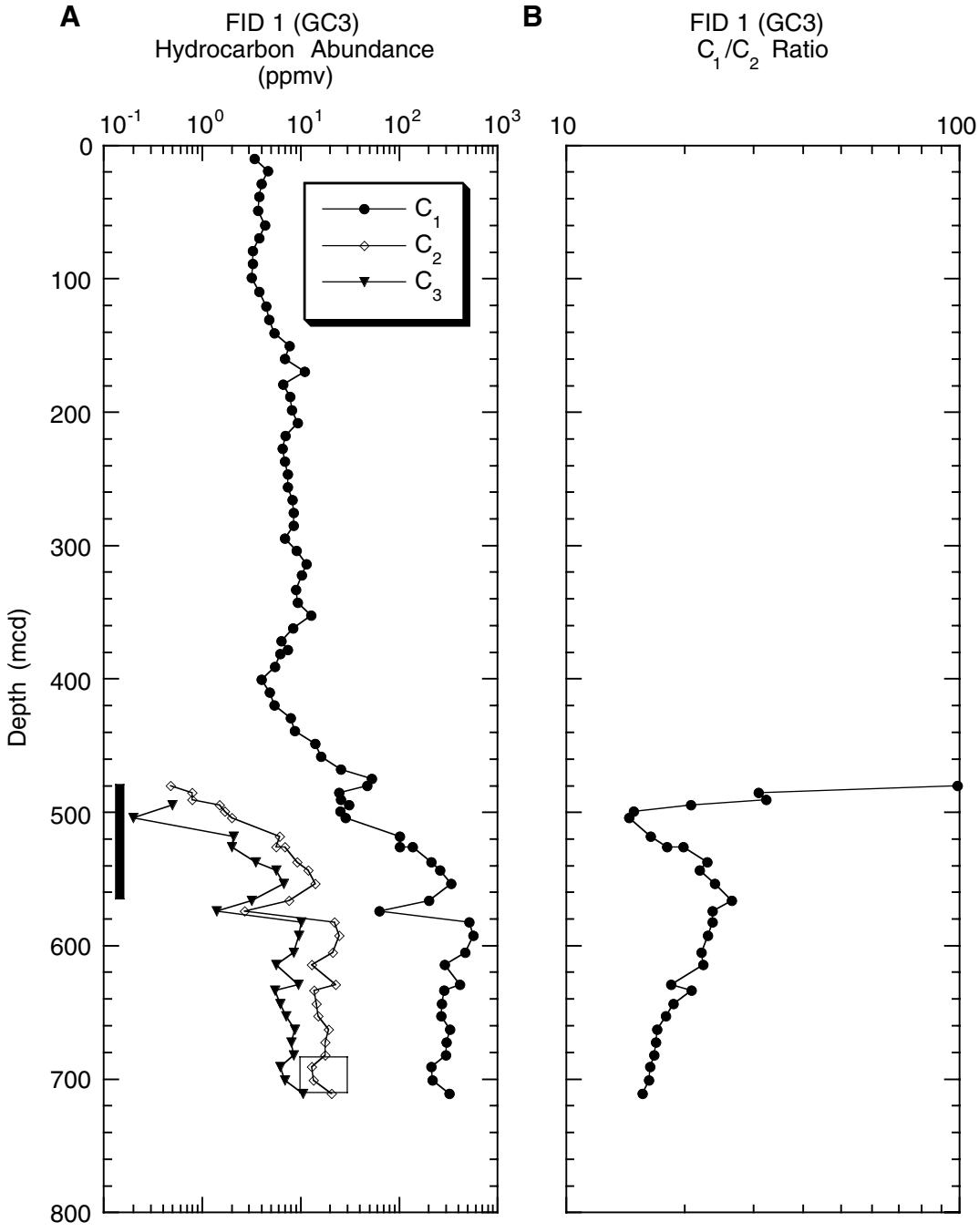

Figure F21. Rock-Eval pyrolysis results for samples from Cores 184-1148A-64X through 75X on a Van Krevelen–type plot of hydrogen index vs. oxygen index. Fields of types II and III organic matter are shown.

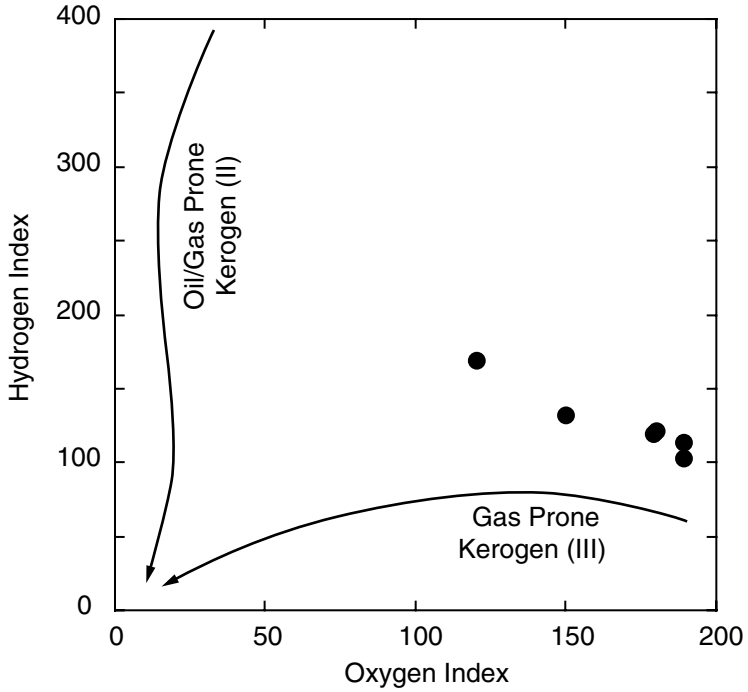

Figure F22. Vertical profiles of interstitial water measurements at Site 1148 (concentrations). **A.** Chloride. **B.** Salinity. **C.** Sulfate at Holes 1148A (solid circles) and 1147A (open circles). **D.** Ammonium. **E.** Phosphate at Holes 1148A (solid circles) and 1147A (open circles). **F.** Alkalinity at Holes 1148A (solid circles) and 1147A (open circles). **G.** Magnesium. **H.** Calcium. **I.** Potassium. **J.** Silica. **K.** Lithium. **L.** Strontium.

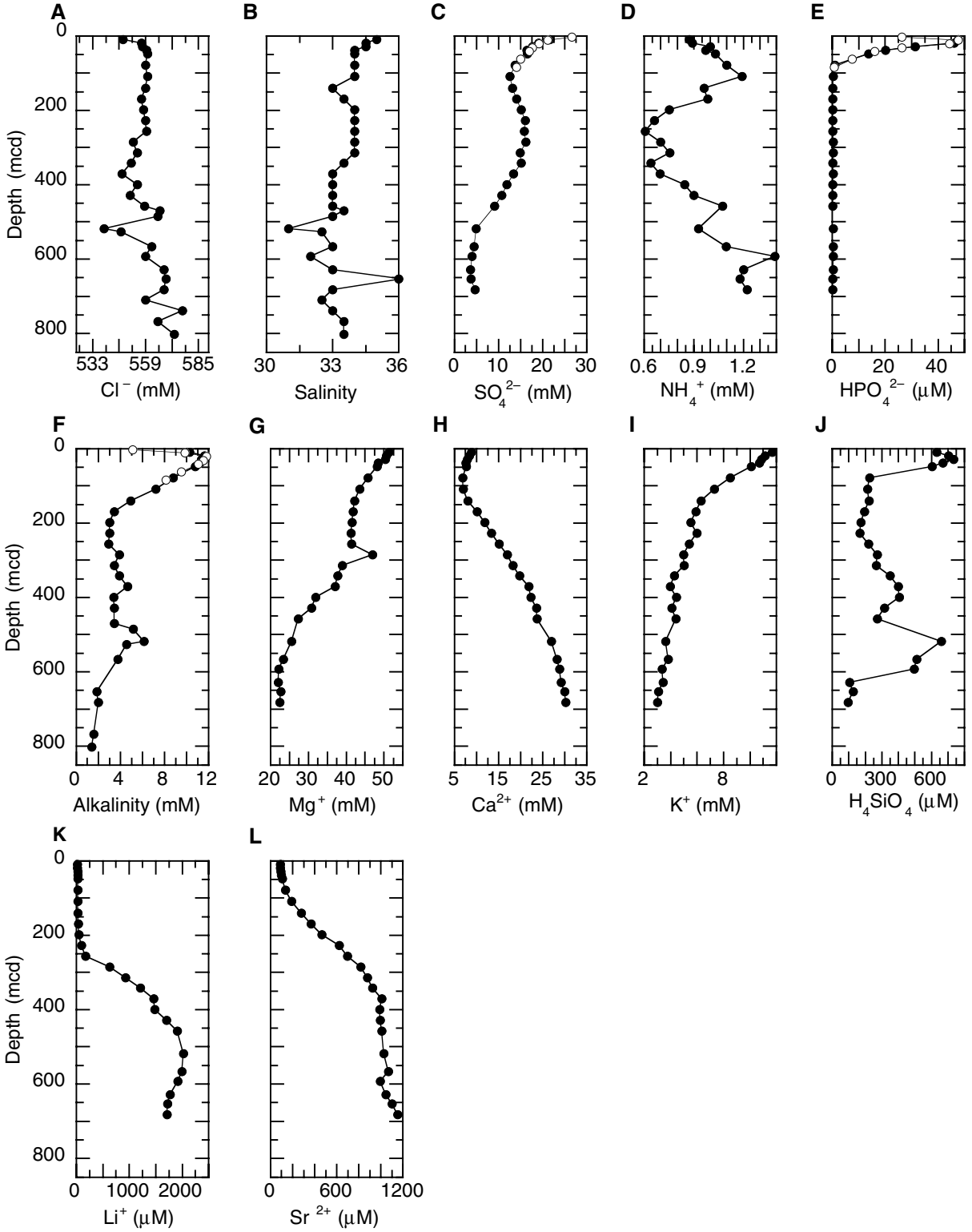

Figure F23. Plot of Mg^{2+} vs. Ca^{2+}.

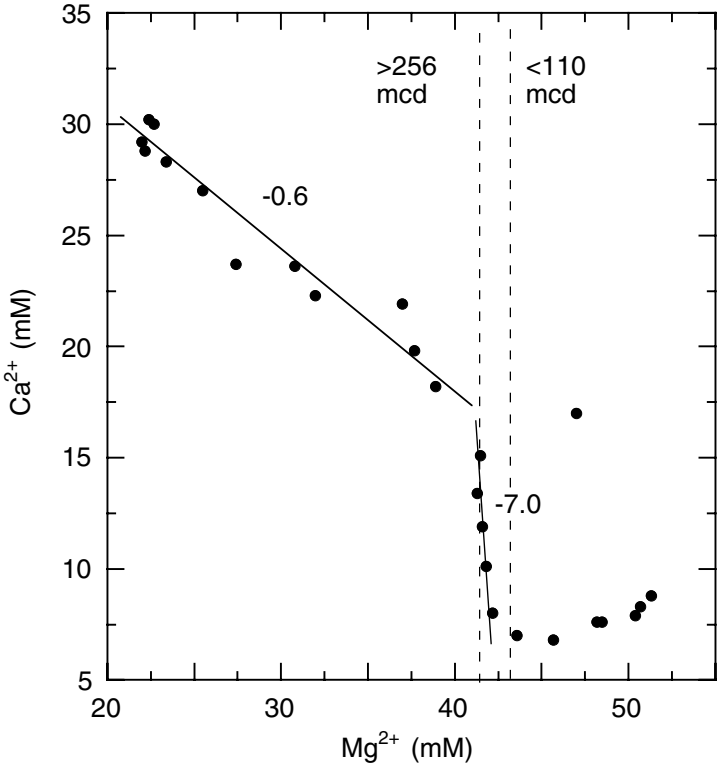

Figure F24. Magnetic susceptibility measurements at Site 1148 plotted for each hole. APC = advanced hydraulic piston corer, XCB = extended core barrel.

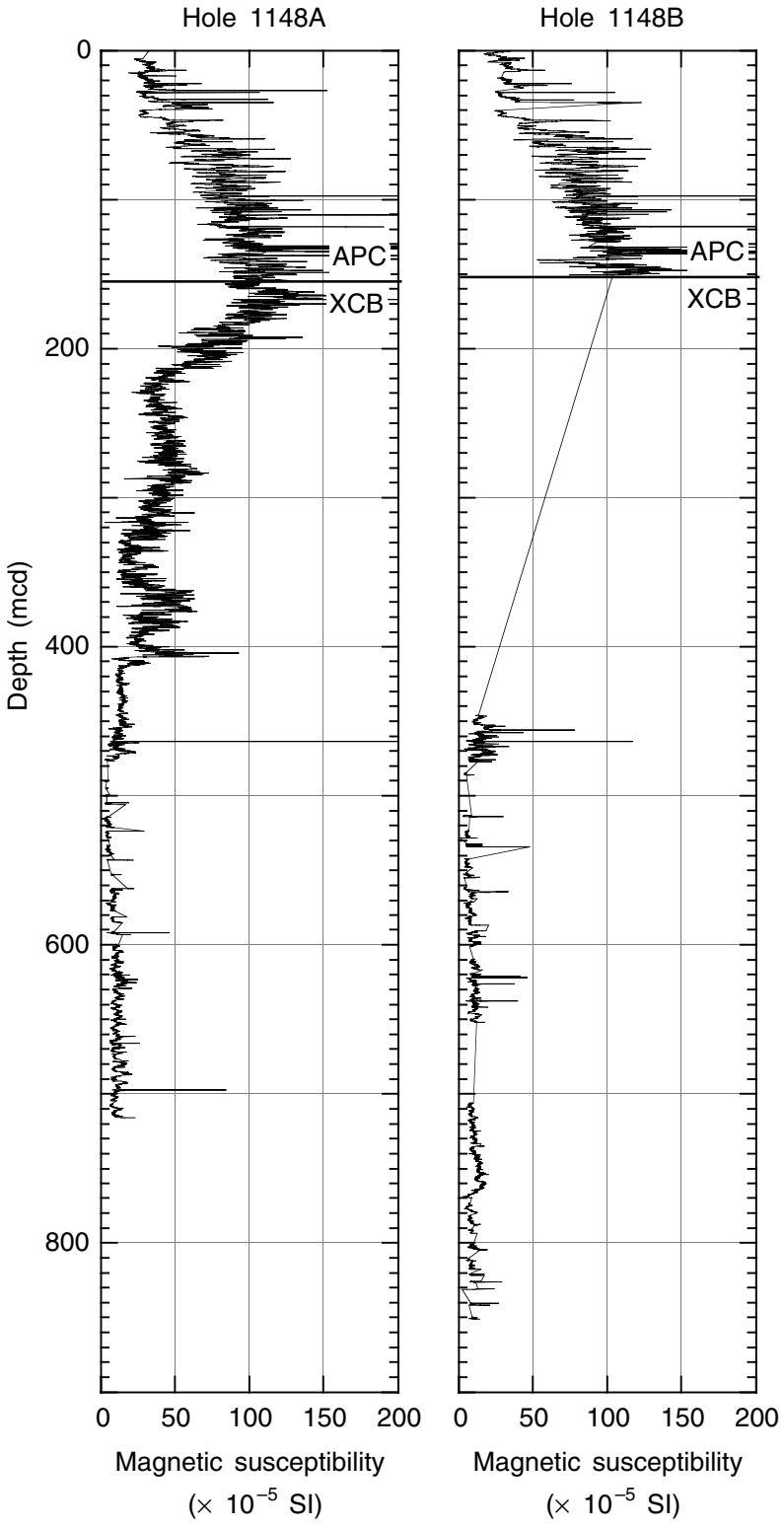

Figure F25. Natural gamma radiation measurements at Site 1148 smoothed with a 20-point moving average, plotted for each hole. APC = advanced hydraulic piston corer, XCB = extended core barrel.

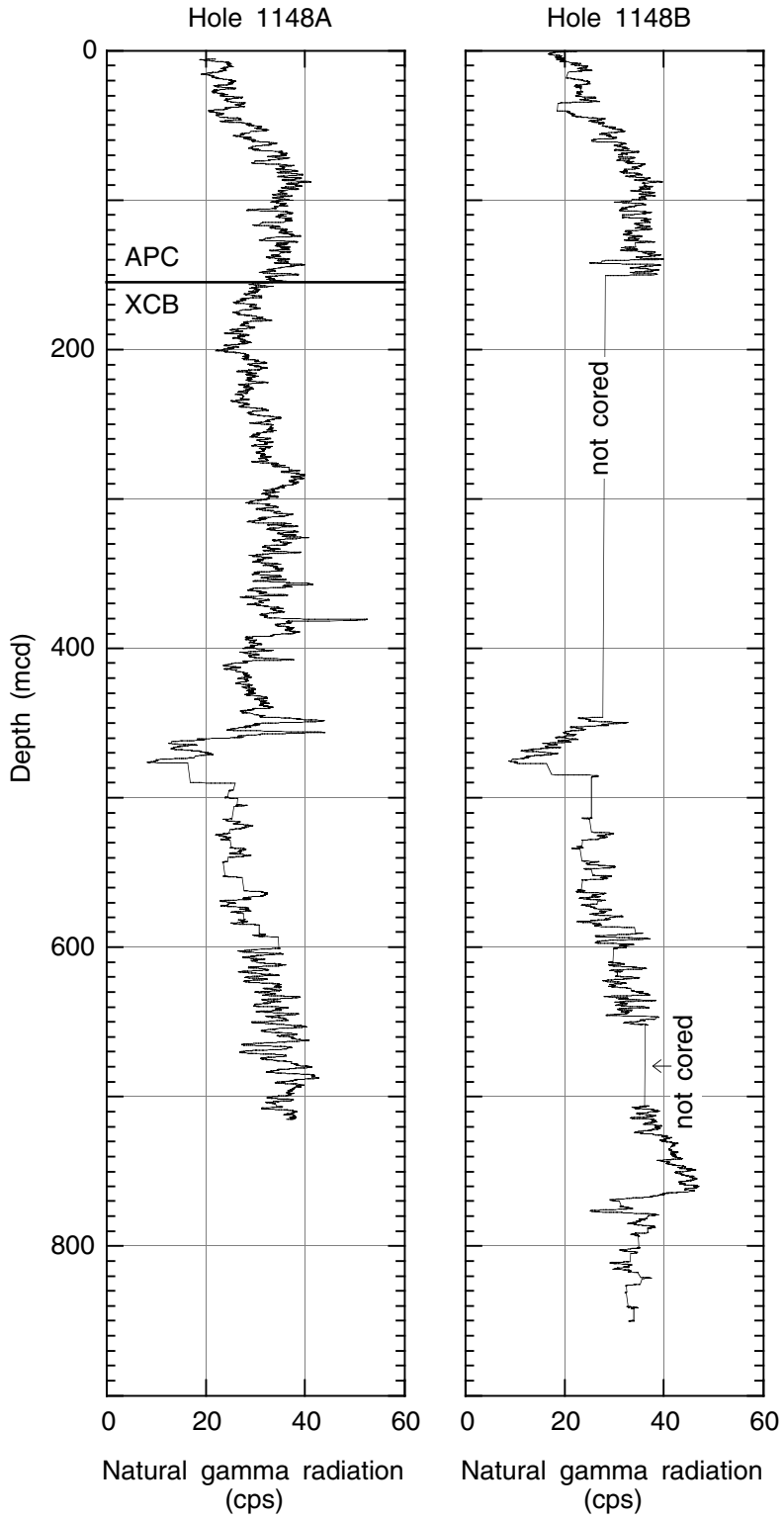

Figure F26. Bulk density measurements from GRA (line) and MAD methods (open circles) at Site 1148 plotted for each hole. APC = advanced hydraulic piston corer, XCB = extended core barrel.

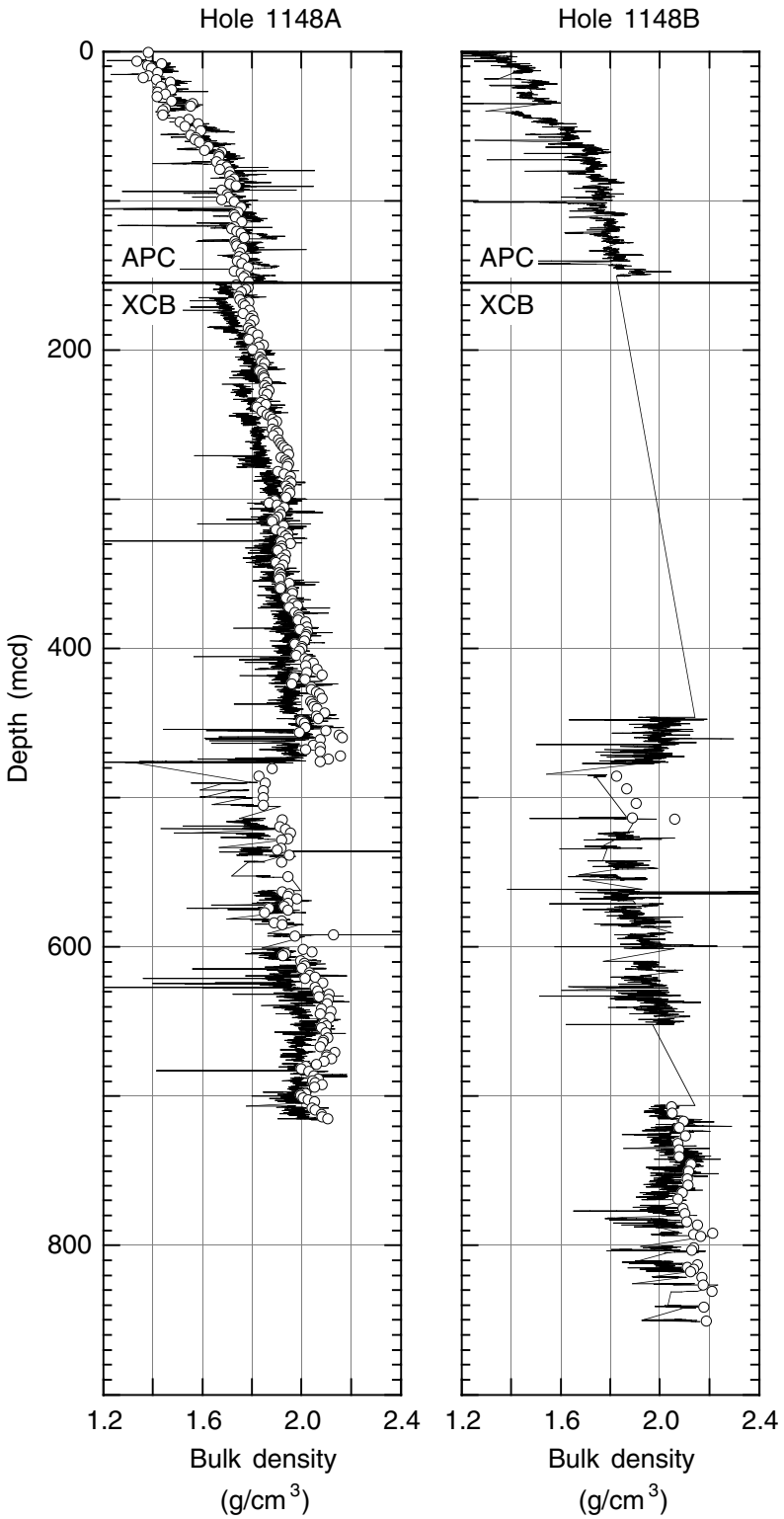

Figure F27. Porosity, grain density, and dry density values obtained from the MAD method. APC = advanced hydraulic piston corer, XCB = extended core barrel.

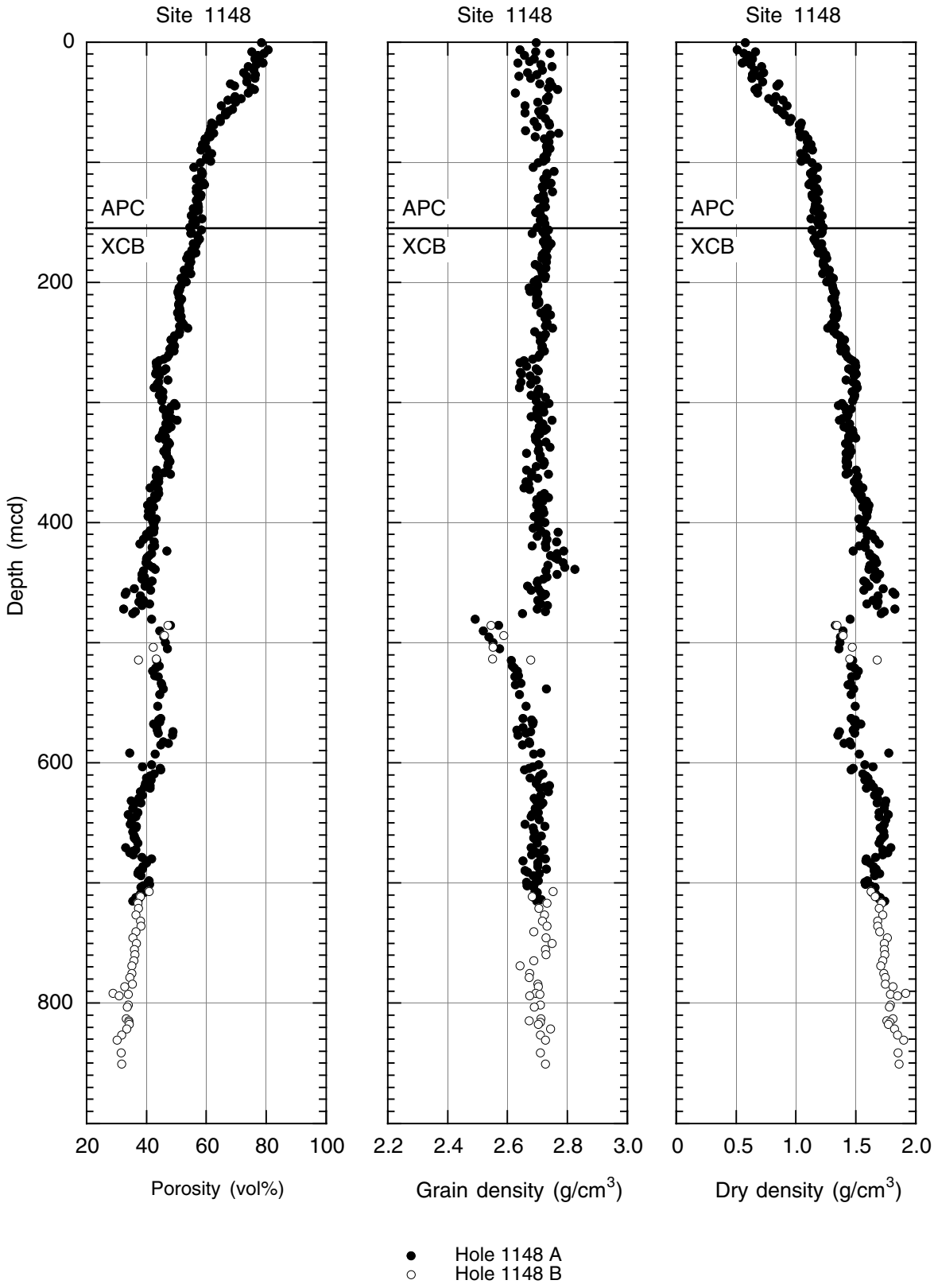

Figure F28. Color spectral reflectance measurements from split-core surfaces at Site 1148 smoothed with a 20-point moving average, plotted for each hole. L*, a*, and b* are standard parameters calculated by the Minolta CM-2002 photo spectrometer from the spectral data. L* = black line, a*/ b* = gray line, APC = advanced hydraulic piston corer, XCB = extended core barrel.

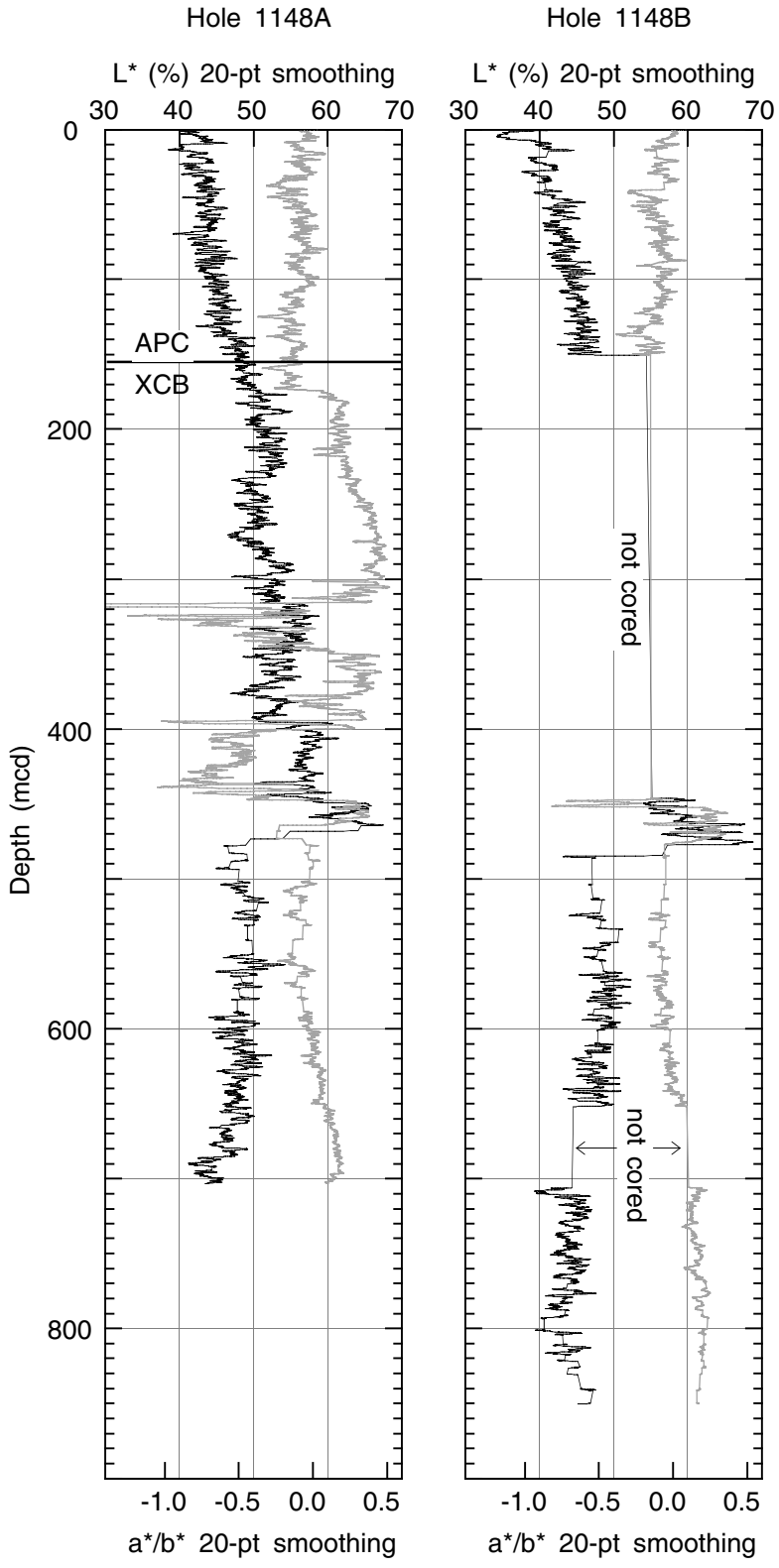

Figure F29. *P*-wave velocity measurements for Hole 1148A. *P*-wave velocity sensors (PWS) 1–3 are different sensors for x, y, and z directions. APC = advanced hydraulic piston corer, XCB = extended core barrel.

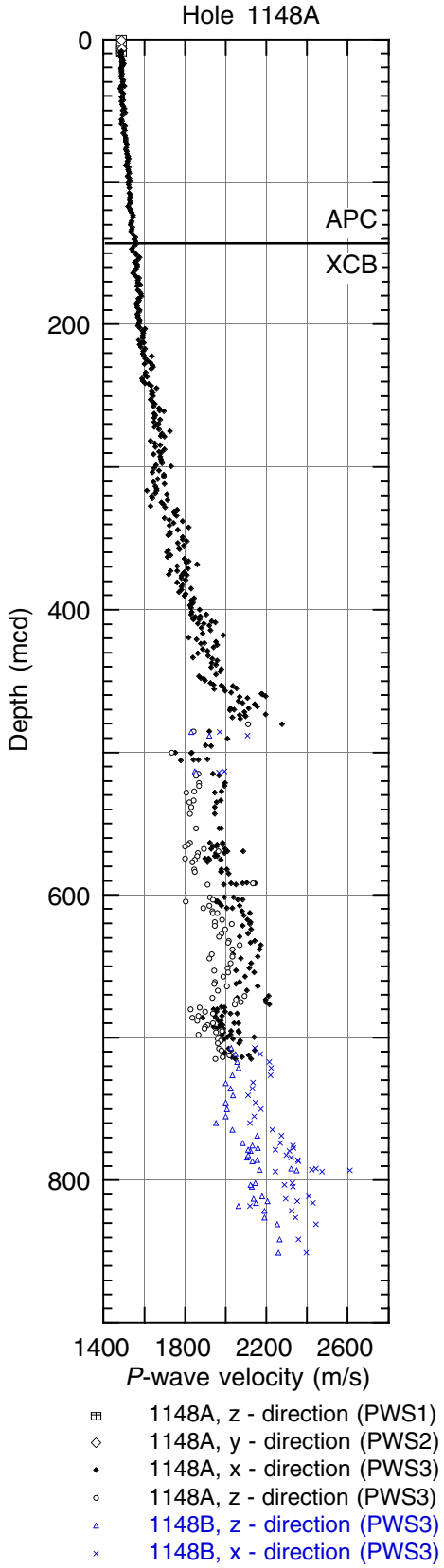

Figure F30. Thermal conductivity measurements at Site 1148. APC = advanced hydraulic piston corer, XCB = extended core barrel.

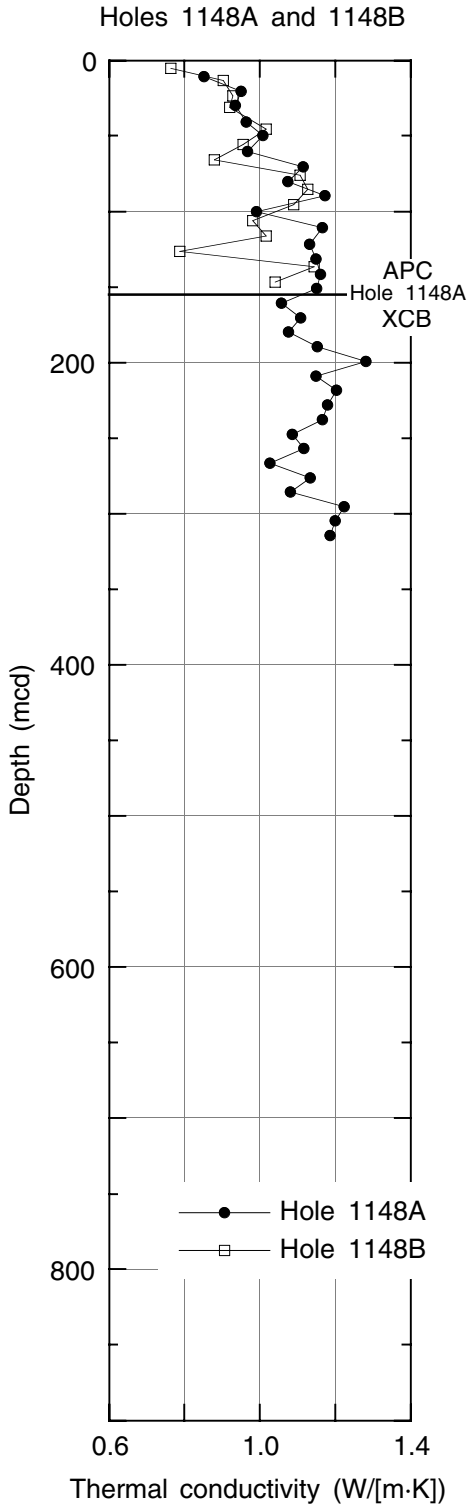

Figure F31. Downhole temperature measurements at Site 1148. **A.** Bottom-water temperature at Hole 1148B taken before Core 184-1148B-1H was shot. This value is taken as approximate bottom-water temperature at Site 1148. **B–D.** Downhole sediment temperature records and calculated equilibrium temperatures at Hole 1148A. Open circles = original temperature measurements, solid circles = selected section of data used in calculating the equilibrium temperature.

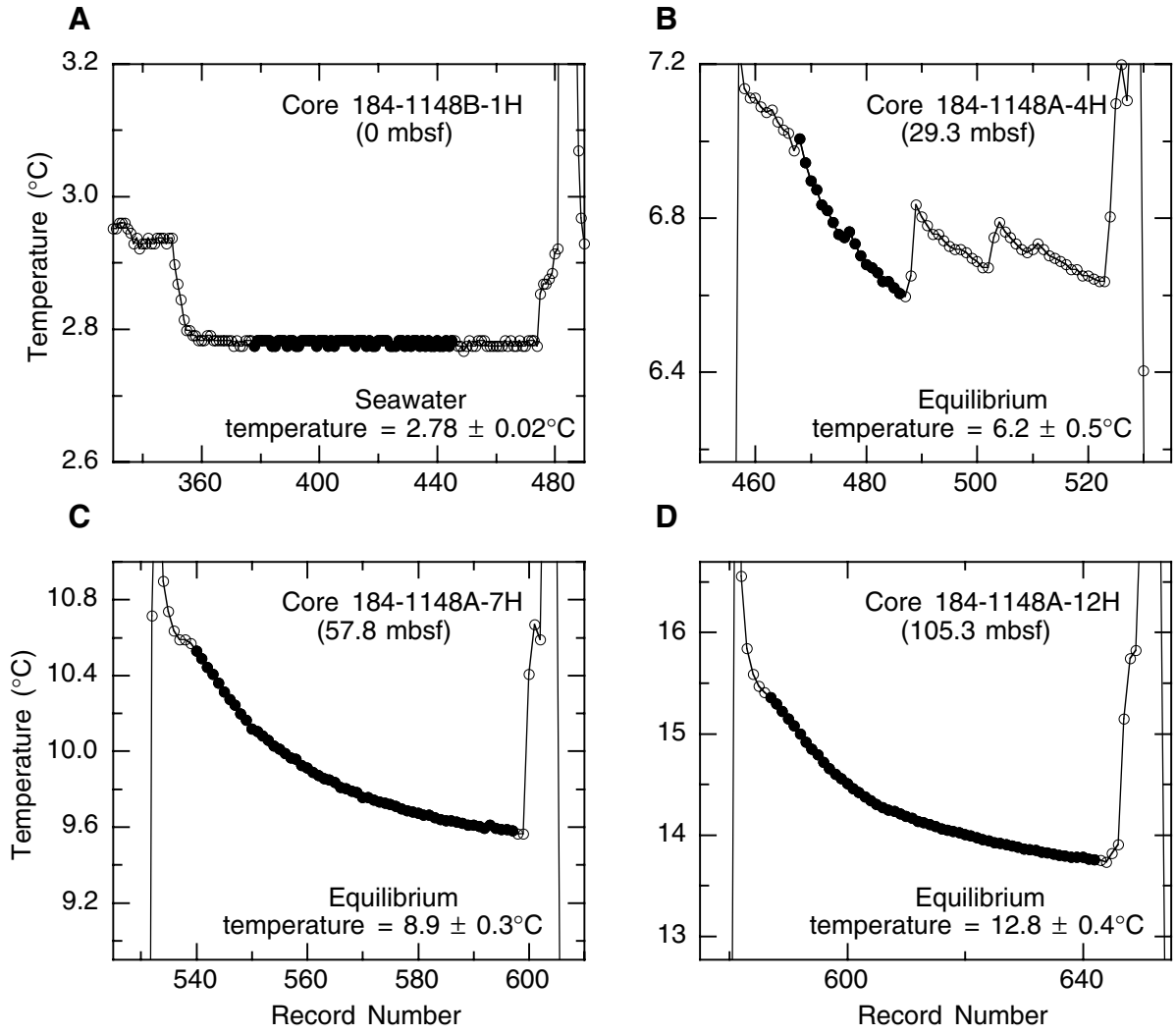

Figure F32. Downhole temperature gradient at Site 1148. T = temperature (°C) at depth (mbsf), R = correlation coefficient.

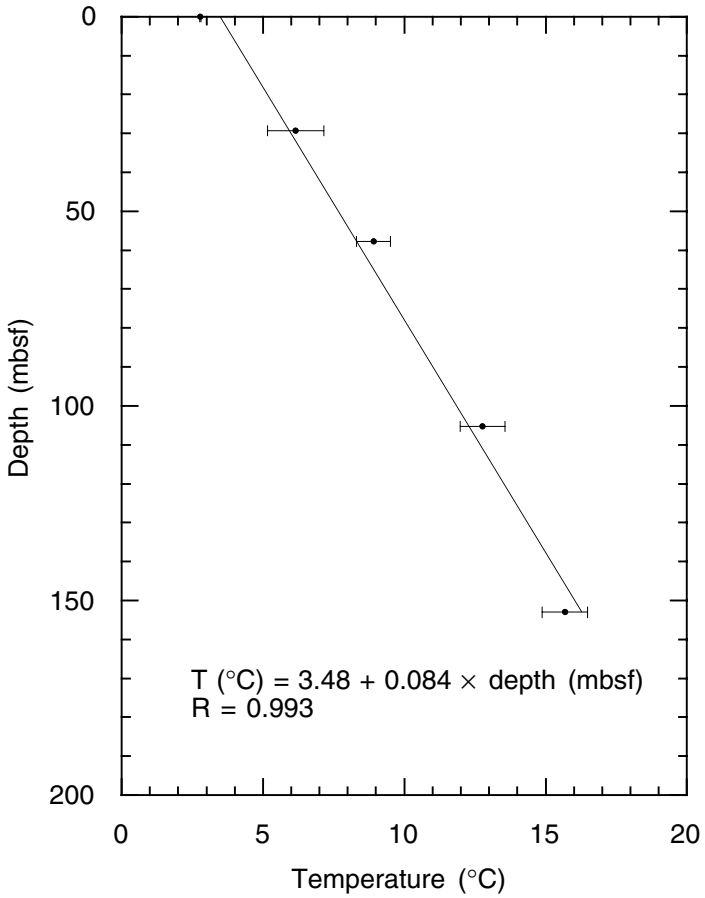

Figure F33. Graphic summary of downhole logging operations for Hole 1148A. The seafloor was identified based on a step in natural gamma activity at the sediment/water boundary. FMS = Formation MicroScanner, LSS = long-spaced sonic, GHMT = geological high-resolution magnetic tool.

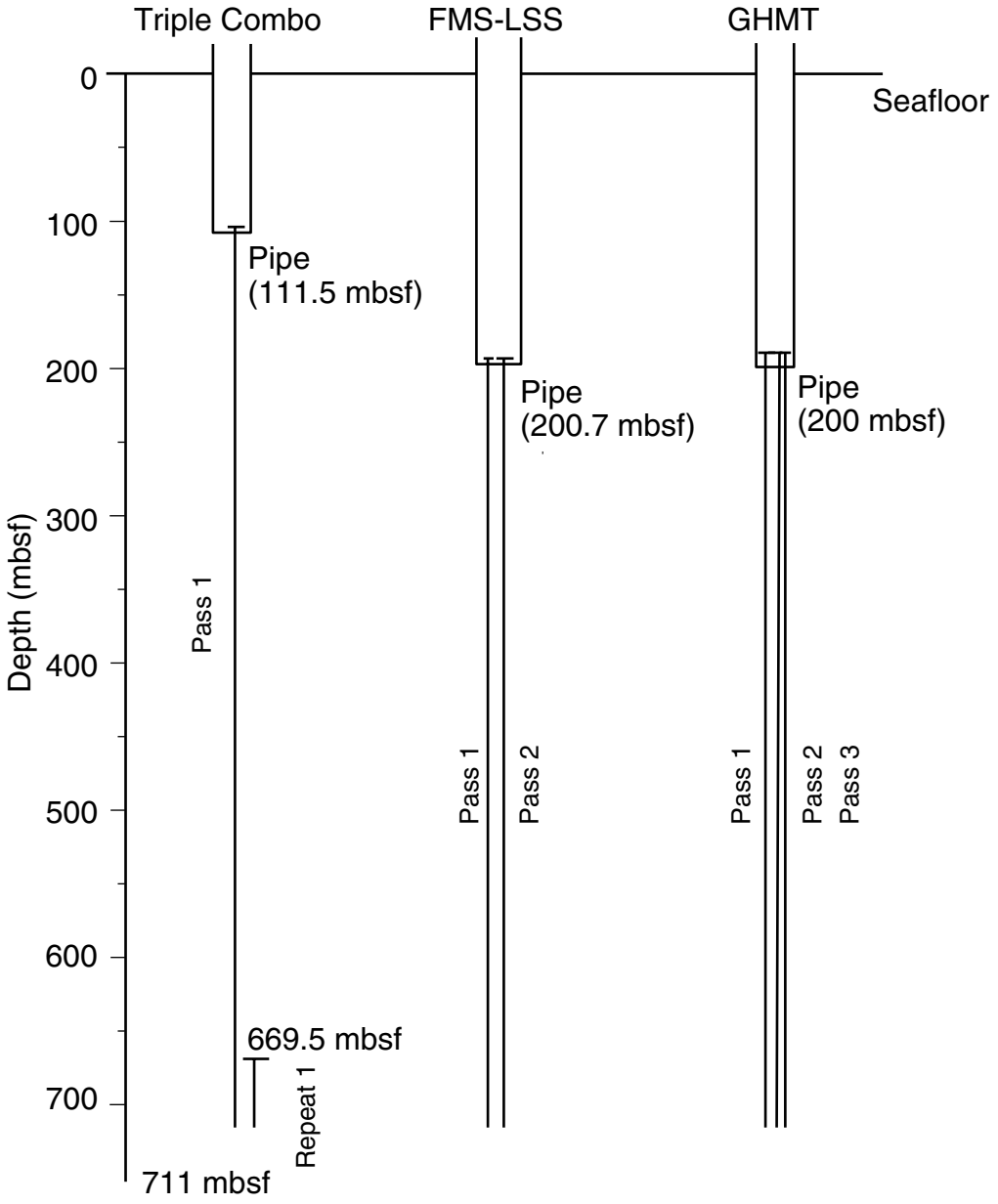

Figure F34. Downhole logs of hole diameter (as measured by caliper opening), neutron porosity (neut.), bulk density, electrical resistivity (SFL = spherically focused log, IMPH = medium induction phasor-processed resistivity, IDPH = deep induction phasor-processed resistivity), magnetic susceptibility (pass 1 and pass 2 of the GHMT tool string), and *P*-wave velocity from Hole 1148A. IU = instrument units.

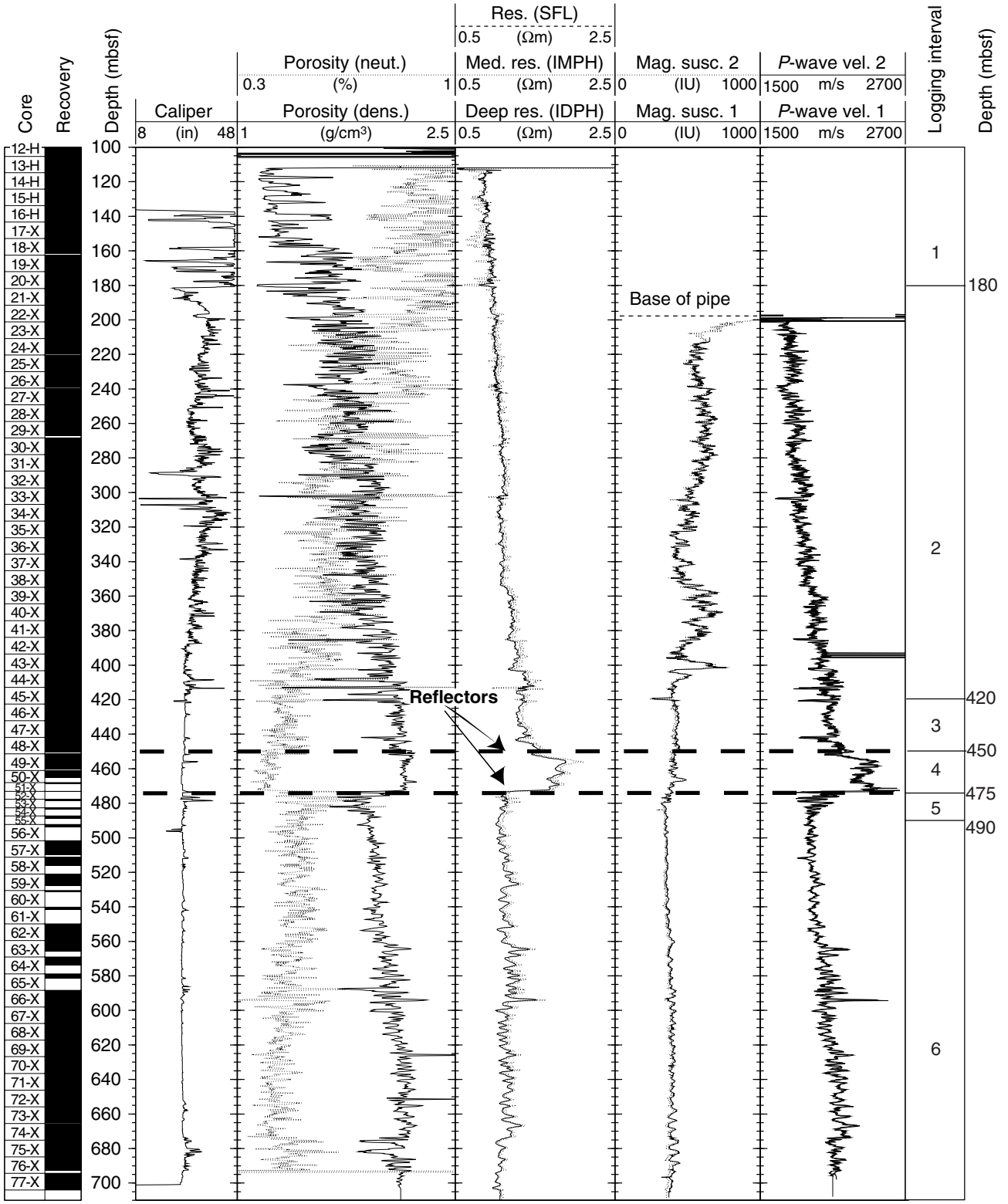

Figure F35. Downhole logs of gamma ray (HSGR = standard gamma ray), computed gamma ray (HCGR = HSGR minus uranium contribution), and potassium, thorium, and uranium from the natural gamma-ray tool (NGT) and hostile environment natural gamma-ray sonde (HNGS). The gamma ray and computed gamma ray values are from the HNGS tool.

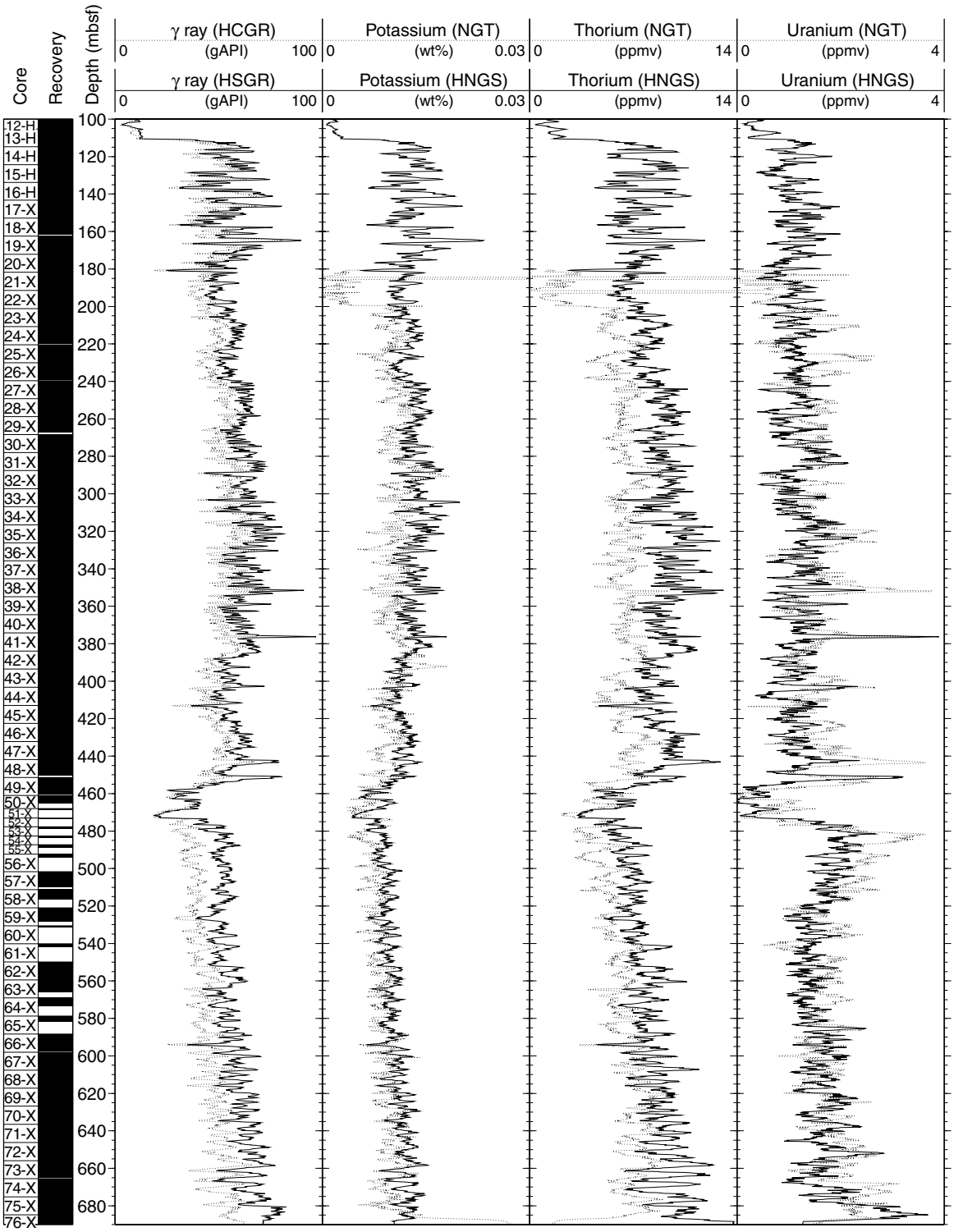

Figure F36. Comparison of core moisture and density (MAD) porosity and downhole log bulk density porosity, gamma radiation, and *P*-wave velocity from downhole logging and discrete *P*-wave velocity measurements (PWS3). Also shown is total magnetic field from downhole logging. Large-amplitude spikes in the magnetic field were edited out. PWS3 = *P*-wave sensor 3, HSGR = standard gamma ray, MST = multisensor track, NGR = natural gamma ray, HLDS = hostile environment lithodensity sonde. (**Figure shown on next page.**)

Figure F36. (Caption on previous page.)

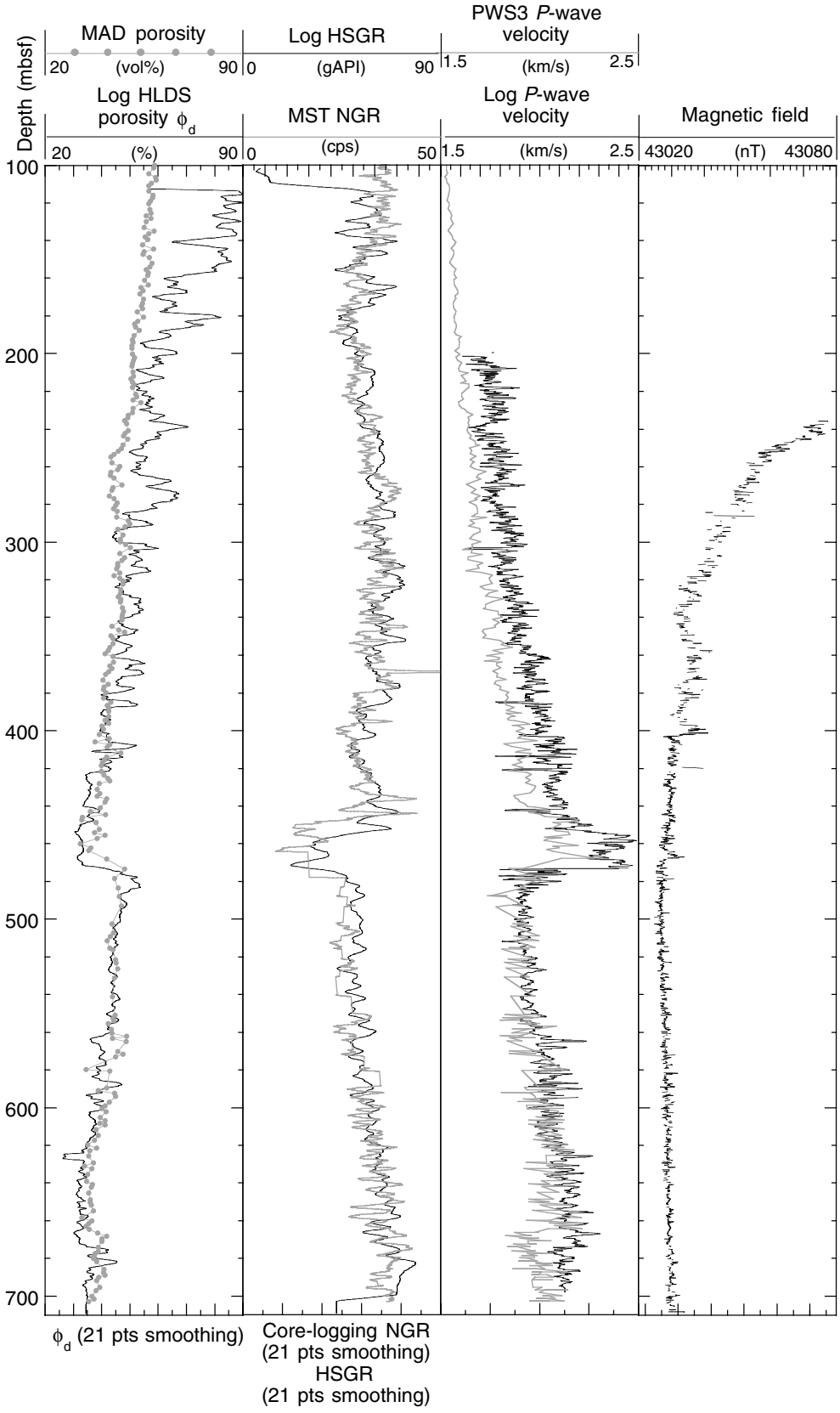

Figure F37. Comparison of magnetic susceptibility from core logging with the multisensor track (MST) and downhole measurements (pass 1 of the GHMT tool string), of thorium measured by the NGT tool string and photoelectric effect (PEF) from the HLDS, of $CaCO_3$ from core samples and PEF, and of bulk density from downhole and core logging. GRA = gamma-ray attenuation, MAD = moisture and density, IU = instrument units. (**Figure shown on next page.**)

Figure F37. (Caption on previous page.)

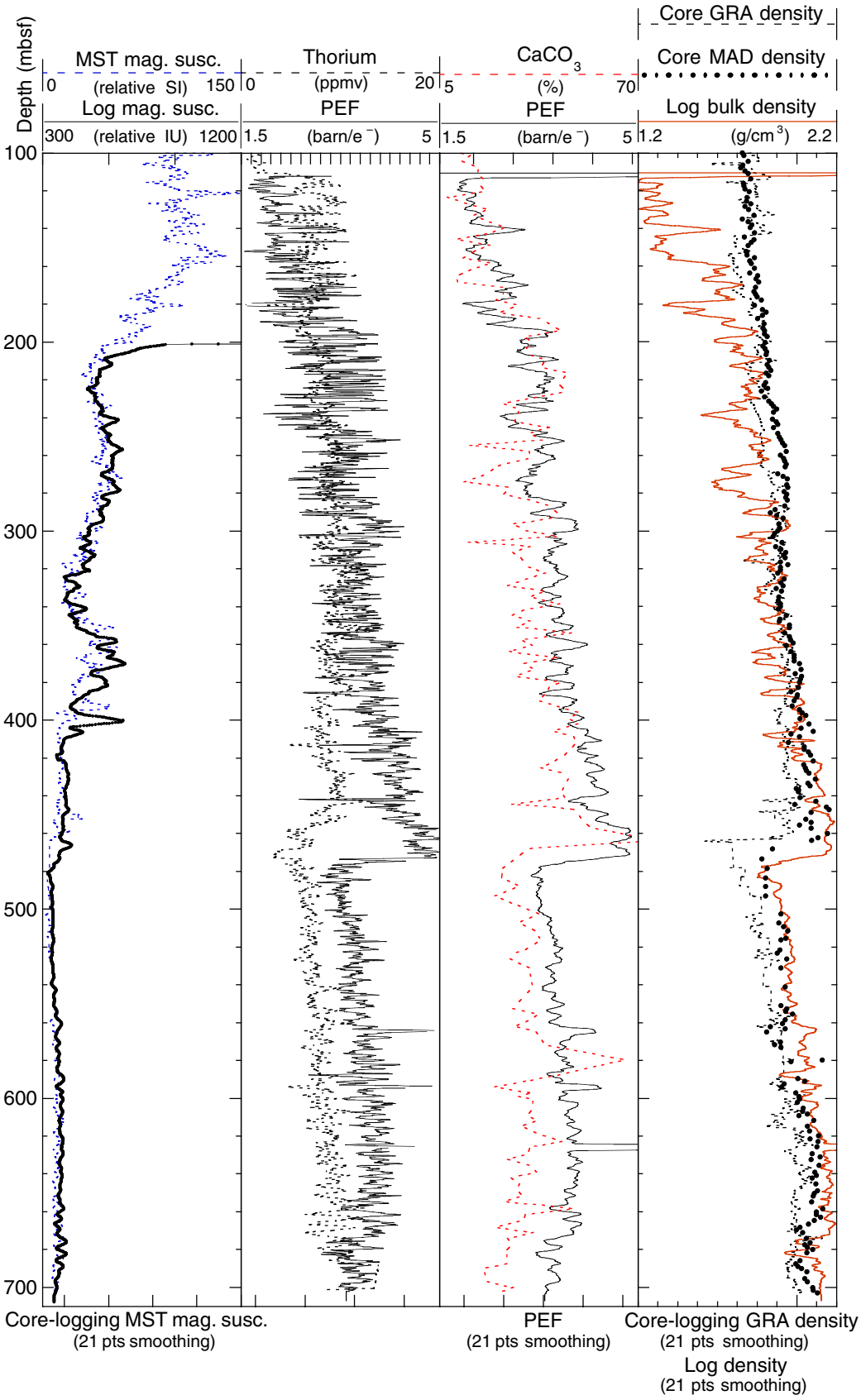

Figure F38. Formation MicroScanner (FMS) image from downhole logging data displaying alternation of relatively conductive (darker) and resistive (lighter) intervals.

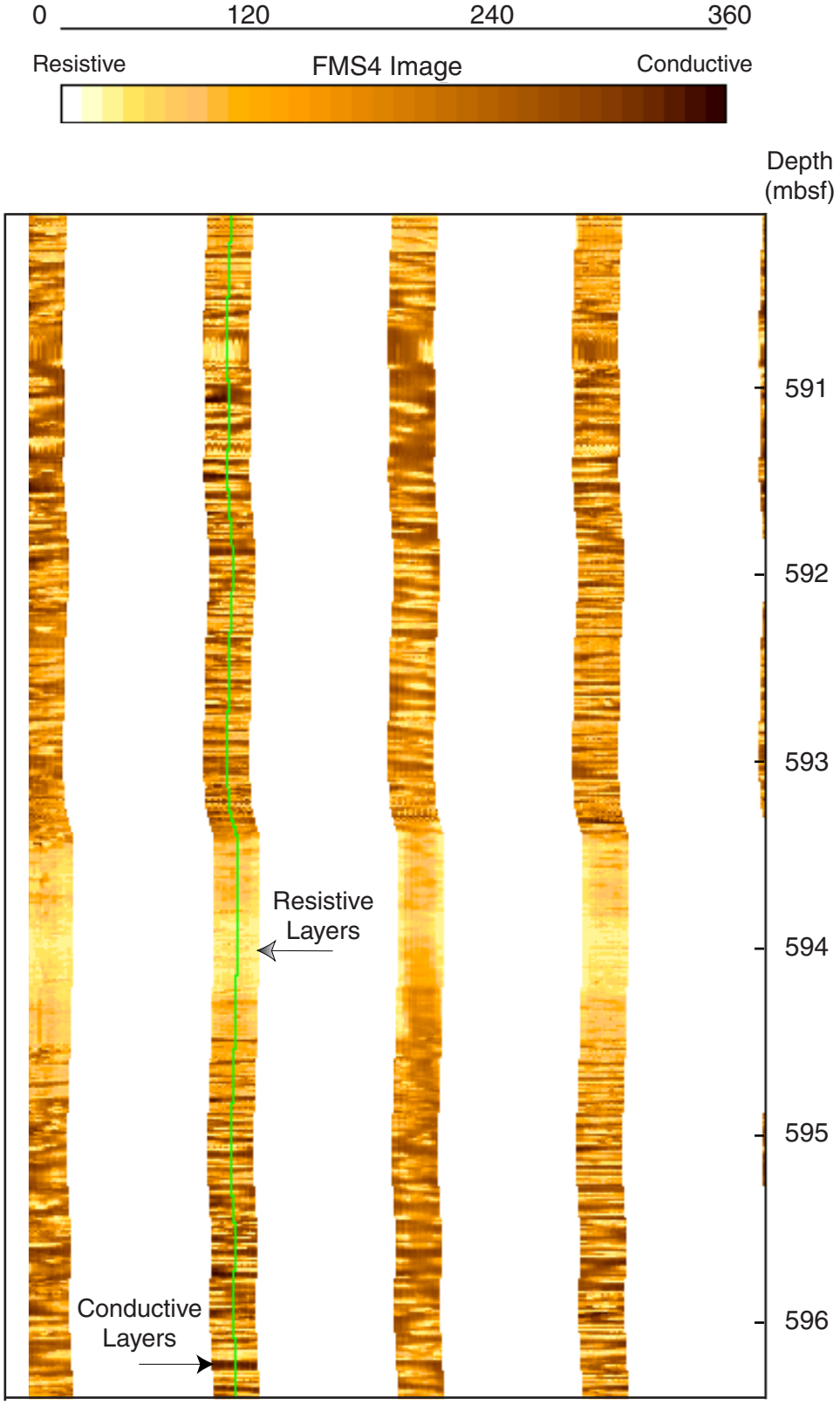

Table T1. Site 1148 coring summary. (See table notes. Continued on next two pages.)

Core	Date (1999)	Time (UTC + 8 hr)	Depth Top (mbsf)	Depth Bottom (mbsf)	Depth Top (mcd)	Length (m) Cored	Length (m) Recovered	Recovery (%)
184-1148A-								
1H	30 March	2240	0.0	0.8	0.00	0.8	0.73	91.3
2H	30 March	2325	0.8	10.3	5.65	9.5	9.64	101.5
3H	31 March	0015	10.3	19.8	15.15	9.5	9.62	101.3
4H	31 March	0125	19.8	29.3	24.65	9.5	9.73	102.4
5H	31 March	0210	29.3	38.8	34.15	9.5	9.54	100.4
6H	31 March	0300	38.8	48.3	44.60	9.5	9.93	104.5
7H	31 March	0405	48.3	57.8	55.20	9.5	9.42	99.2
8H	31 March	0450	57.8	67.3	65.17	9.5	9.71	102.2
9H	31 March	0535	67.3	76.8	74.97	9.5	9.64	101.5
10H	31 March	0620	76.8	86.3	84.47	9.5	9.91	104.3
11H	31 March	0720	86.3	95.8	95.02	9.5	9.70	102.1
12H	31 March	0830	95.8	105.3	105.47	9.5	9.90	104.2
13H	31 March	0915	105.3	114.8	116.40	9.5	9.39	98.8
14H	31 March	1005	114.8	124.3	126.35	9.5	9.17	96.5
15H	31 March	1050	124.3	133.8	136.30	9.5	9.32	98.1
16H	31 March	1140	133.8	143.3	146.02	9.5	9.45	99.5
17X	31 March	1255	143.3	152.9	155.52	9.6	9.83	102.4
18X	31 March	1510	152.9	162.5	165.12	9.6	8.67	90.3
19X	31 March	1555	162.5	172.1	174.72	9.6	9.83	102.4
20X	31 March	1640	172.1	181.8	184.32	9.7	9.53	98.2
21X	31 March	1735	181.8	191.5	194.02	9.7	9.84	101.4
22X	31 March	1830	191.5	201.1	203.72	9.6	9.79	102.0
23X	31 March	1920	201.1	210.8	213.32	9.7	9.65	99.5
24X	31 March	2010	210.8	220.4	223.02	9.6	8.85	92.2
25X	31 March	2110	220.4	230.0	232.62	9.6	9.82	102.3
26X	31 March	2200	230.0	239.6	242.22	9.6	8.92	92.9
27X	31 March	2245	239.6	249.2	251.82	9.6	9.87	102.8
28X	31 March	2345	249.2	258.8	261.42	9.6	9.87	102.8
29X	1 April	0045	258.8	268.4	271.02	9.6	8.47	88.2
30X	1 April	0140	268.4	278.0	280.62	9.6	9.84	102.5
31X	1 April	0235	278.0	287.6	290.22	9.6	9.85	102.6
32X	1 April	0345	287.6	297.3	299.82	9.7	9.71	100.1
33X	1 April	0500	297.3	306.9	309.52	9.6	9.75	101.6
34X	1 April	0615	306.9	316.6	319.12	9.7	9.87	101.8
35X	1 April	0725	316.6	326.2	328.82	9.6	9.68	100.8
36X	1 April	0845	326.2	335.8	338.42	9.6	9.89	103.0
37X	1 April	1000	335.8	345.3	348.02	9.5	9.75	102.6
38X	1 April	1110	345.3	354.9	357.52	9.6	9.86	102.7
39X	1 April	1225	354.9	364.5	367.12	9.6	9.81	102.2
40X	1 April	1345	364.5	374.2	376.72	9.7	9.78	100.8
41X	1 April	1510	374.2	383.9	386.42	9.7	9.99	103.0
42X	1 April	1630	383.9	393.5	396.12	9.6	9.62	100.2
43X	1 April	1800	393.5	403.2	405.72	9.7	9.68	99.8
44X	1 April	1925	403.2	412.9	415.42	9.7	9.90	102.1
45X	1 April	2050	412.9	422.5	425.12	9.6	9.94	103.5
46X	1 April	2215	422.5	432.2	434.72	9.7	9.41	97.0
47X	1 April	2345	432.2	441.8	444.42	9.6	9.96	103.8
48X	2 April	0115	441.8	451.4	454.02	9.6	8.61	89.7
49X	2 April	0255	451.4	461.0	463.62	9.6	9.15	95.3
50X	2 April	0455	461.0	468.0	473.22	7.0	4.15	59.3
51X	2 April	0640	468.0	473.1	480.22	5.1	0.53	10.4
52X	2 April	0820	473.1	477.7	485.32	4.6	0.37	8.0
53X	2 April	1000	477.7	482.7	489.92	5.0	1.05	21.0
54X	2 April	1140	482.7	487.3	494.92	4.6	1.15	25.0
55X	2 April	1310	487.3	492.3	499.52	5.0	1.42	28.4
56X	2 April	1455	492.3	501.7	504.52	9.4	1.84	19.6
57X	2 April	1615	501.7	511.3	513.92	9.6	8.19	85.3
58X	2 April	1755	511.3	521.0	523.52	9.7	5.21	53.7
59X	2 April	1925	521.0	530.6	533.22	9.6	7.16	74.6
60X	2 April	2110	530.6	540.2	542.82	9.6	0.88	9.2
61X	2 April	2305	540.2	549.9	552.42	9.7	1.40	14.4
62X	3 April	0050	549.9	559.5	562.12	9.6	9.54	99.4
63X	3 April	0225	559.5	569.1	571.72	9.6	6.37	66.4
64X	3 April	0405	569.1	578.8	581.32	9.7	4.54	46.8
65X	3 April	0555	578.8	588.4	591.02	9.6	2.64	27.5
66X	3 April	0745	588.4	598.0	600.62	9.6	9.09	94.7

Table T1 (continued).

Core	Date (1999)	Time (UTC + 8 hr)	Depth Top (mbsf)	Depth Bottom (mbsf)	Depth Top (mcd)	Length (m) Cored	Length (m) Recovered	Recovery (%)
67X	3 April	0920	598.0	607.6	610.22	9.6	9.81	102.2
68X	3 April	1100	607.6	617.2	619.82	9.6	9.86	102.7
69X	3 April	1235	617.2	626.8	629.42	9.6	9.88	102.9
70X	3 April	1410	626.8	636.5	639.02	9.7	9.36	96.5
71X	3 April	1555	636.5	646.2	648.72	9.7	9.85	101.5
72X	3 April	1750	646.2	655.9	658.42	9.7	9.70	100.0
73X	3 April	1945	655.9	665.5	668.12	9.6	8.96	93.3
74X	3 April	2130	665.5	675.2	677.72	9.7	9.89	102.0
75X	3 April	2255	675.2	684.8	687.42	9.6	9.55	99.5
76X	4 April	0040	684.8	694.4	697.02	9.6	8.09	84.3
77X	4 April	0225	694.4	704.0	706.62	9.6	9.80	102.1
					Totals:	704.0	632.07	89.8
184-1148B-								
1H	5 April	2105	0.0	8.1	0.00	8.1	8.04	99.3
2H	5 April	2210	8.1	17.6	8.10	9.5	6.61	69.6
3H	5 April	2305	17.6	27.1	18.45	9.5	7.10	74.7
4H	6 April	0005	27.1	36.6	26.07	9.5	9.62	101.3
Drilled			36.6	40.6				
5H	6 April	0045	40.6	50.1	40.25	9.5	9.33	98.2
6H	6 April	0130	50.1	59.6	50.45	9.5	9.61	101.2
7H	5 April	0215	59.6	69.1	60.90	9.5	9.36	98.5
8H	5 April	0300	69.1	78.6	70.82	9.5	9.18	96.6
9H	5 April	0350	78.6	88.1	80.17	9.5	9.30	97.9
10H	5 April	0435	88.1	97.6	90.42	9.5	9.77	102.8
11H	5 April	0525	97.6	107.1	100.92	9.5	9.66	101.7
12H	5 April	0720	107.1	116.6	111.18	9.5	9.81	103.3
13H	6 April	0800	116.6	126.1	121.30	9.5	8.97	94.4
14H	6 April	0855	126.1	135.6	131.30	9.5	9.70	102.1
15H	6 April	0945	135.6	145.1	141.85	9.5	9.41	99.1
Drilled			145.1	439.9				
16X	6 April	2200	439.9	449.5	446.15	9.6	9.83	102.4
17X	7 April	0000	449.5	459.1	455.75	9.6	9.82	102.3
18X	7 April	0145	459.1	468.7	465.35	9.6	9.57	99.7
19X	7 April	0335	468.7	478.3	474.95	9.6	2.98	31.0
20X	7 April	0545	478.3	483.1	484.55	4.8	2.31	48.1
21X	7 April	0800	483.1	487.9	489.35	4.8	0.22	4.6
22X	7 April	1015	487.9	497.5	494.15	9.6	0.29	3.0
23X	7 April	1205	497.5	506.9	503.75	9.4	0.26	2.8
24X	7 April	1405	506.9	516.6	513.15	9.7	1.20	12.4
25X	7 April	1545	516.6	526.2	522.85	9.6	5.64	58.8
26X	7 April	1730	526.2	535.9	532.45	9.7	2.01	20.7
27X	7 April	1915	535.9	545.5	542.15	9.6	6.13	63.9
28X	7 April	2105	545.5	555.2	551.75	9.7	3.53	36.4
29X	7 April	2300	555.2	564.8	561.45	9.6	8.14	84.8
30X	8 April	0115	564.8	574.5	571.05	9.7	9.89	102.0
31X	8 April	0325	574.5	584.2	580.75	9.7	6.52	67.2
32X	8 April	0515	584.2	593.8	590.45	9.6	9.80	102.1
33X	8 April	0710	593.8	603.4	600.05	9.6	1.61	16.8
34X	8 April	0900	603.4	613.0	609.65	9.6	7.58	79.0
35X	8 April	1110	613.0	622.6	619.25	9.6	8.83	92.0
36X	8 April	1325	622.6	632.2	628.85	9.6	9.12	95.0
37X	8 April	1545	632.2	641.9	638.45	9.7	8.90	91.8
38X	8 April	1715	641.9	646.0	648.15	4.1	4.18	102.0
Drilled			646.0	699.8				
39X	9 April	0020	699.8	709.5	706.05	9.7	9.80	101.0
40X	9 April	0155	709.5	719.1	715.75	9.6	9.77	101.8
41X	9 April	0335	719.1	728.7	725.35	9.6	8.73	90.9
42X	9 April	0505	728.7	738.3	734.95	9.6	9.77	101.8
43X	9 April	0645	738.3	748.0	744.55	9.7	9.76	100.6
44X	9 April	0825	748.0	757.3	754.25	9.3	9.66	103.9
45X	9 April	0955	757.3	766.9	763.55	9.6	7.02	73.1
46X	9 April	1120	766.9	775.2	773.15	8.3	7.23	87.1
47X	9 April	1445	775.2	784.8	781.45	9.6	7.19	74.9
48X	9 April	1645	784.8	794.5	791.05	9.7	2.81	29.0
49X	9 April	1925	794.5	804.1	800.75	9.6	4.23	44.1

Table T1 (continued).

Core	Date (1999)	Time (UTC + 8 hr)	Depth Top (mbsf)	Depth Bottom (mbsf)	Depth Top (mcd)	Length (m) Cored	Length (m) Recovered	Recovery (%)
50X	9 April	2150	804.1	808.7	810.35	4.6	4.92	107.0
51X	10 April	0035	808.7	814.7	814.95	6.0	3.24	54.0
52X	10 April	0240	814.7	819.3	820.95	4.6	1.32	28.7
53X	10 April	0425	819.3	824.4	825.55	5.1	1.32	25.9
54X	10 April	0655	824.4	834.0	830.65	9.6	0.52	5.4
55X	10 April	0940	834.0	843.6	840.25	9.6	1.78	18.5
56X	10 April	1300	843.6	853.2	849.85	9.6	1.53	15.9
					Cored:	500.6	364.43	72.8
					Drilled:	352.6		
					Total:	853.2		

Notes: UTC = Universal Time Coordinated. This table is also available in **ASCII format.**

Table T2. Site 1148 coring summary by section.

Core	Date (1999)	Time (UTC + 8 hr)	Core depth (mbsf) Top	Core depth (mbsf) Bottom	Length (m) Cored	Length (m) Recovered	Recovery (%)	Section	Length (m) Liner	Length (m) Curated	Section depth (mbsf) Top	Section depth (mbsf) Bottom	Top depth (mcd)	Catwalk samples	Comments
184-1148A-															
1H	30 March	2240	0.0	0.8	0.8	0.73	91.3								
								1	0.60	0.60	0.00	0.60	0.00		
								CC(w/1)	0.13	0.13	0.60	0.73	0.60	PAL	
								Totals:	0.73	0.73					
2H	30 March	2325	0.8	10.3	9.5	9.64	101.5								
								1	1.50	1.50	0.80	2.30	5.65		
								2	1.50	1.50	2.30	3.80	7.15		
								3	1.50	1.50	3.80	5.30	8.65	IW	
								4	1.50	1.50	5.30	6.80	10.15	HS	
								5	1.50	1.50	6.80	8.30	11.65		
								6	1.50	1.50	8.30	9.80	13.15		
								7	0.42	0.42	9.80	10.22	14.65		
								CC(w/7)	0.22	0.22	10.22	10.44	15.07	PAL	
								Totals:	9.64	9.64					
3H	31 March	0015	10.3	19.8	9.5	9.62	101.3								
								1	1.43	1.43	10.30	11.73	15.15		
								2	1.50	1.50	11.73	13.23	16.58		
								3	1.50	1.50	13.23	14.73	18.08	IW	
								4	1.50	1.50	14.73	16.23	19.58	HS	
								5	1.50	1.50	16.23	17.73	21.08		
								6	1.50	1.50	17.73	19.23	22.58		
								7	0.56	0.56	19.23	19.79	24.08		
								CC(w/7)	0.13	0.13	19.79	19.92	24.64	PAL	
								Totals:	9.62	9.62					
4H	31 March	0125	19.8	29.3	9.5	9.73	102.4								Adara; oriented
								1	1.50	1.50	19.80	21.30	24.65		
								2	1.50	1.50	21.30	22.80	26.15		
								3	1.50	1.50	22.80	24.30	27.65	IW	
								4	1.50	1.50	24.30	25.80	29.15	HS	
								5	1.50	1.50	25.80	27.30	30.65		
								6	1.50	1.50	27.30	28.80	32.15		
								7	0.36	0.36	28.80	29.16	33.65		
								CC(w/7)	0.37	0.37	29.16	29.53	34.01	PAL	
								Totals:	9.73	9.73					
5H	31 March	0210	29.3	38.8	9.5	9.54	100.4								Oriented
								1	1.50	1.50	29.30	30.80	34.15		
								2	1.50	1.50	30.80	32.30	35.65		
								3	1.50	1.50	32.30	33.80	37.15	IW	
								4	1.50	1.50	33.80	35.30	38.65	HS	
								5	1.50	1.50	35.30	36.80	40.15		
								6	1.50	1.50	36.80	38.30	41.65		
								7	0.48	0.48	38.30	38.78	43.15		
								CC(w/7)	0.06	0.06	38.78	38.84	43.63	PAL	All to PAL
								Totals:	9.54	9.54					

Notes: UTC = Universal Time Coordinated. The notation "CC(w/x)" refers to the D-tube in which the core catcher is stored, where x is the section number (1–8 or CC). NS = no section, IW = interstitial waters, HS = headspace, PAL = paleontology, DVTP = Davis-Villinger temperature probe. Only a portion of this table appears here. The complete table is available in **ASCII format.**

Table T3. Site 1148 composite depths.

Core	Depth (mbsf)	Cumulative offset (m)	Depth (mcd)
184-1148A-			
1H	0.0	0.00	0.00
2H	0.8	4.85	5.65
3H	10.3	4.85	15.15
4H	19.8	4.85	24.65
5H	29.3	4.85	34.15
6H	38.8	5.80	44.60
7H	48.3	6.90	55.20
8H	57.8	7.37	65.17
9H	67.3	7.67	74.97
10H	76.8	7.67	84.47
11H	86.3	8.72	95.02
12H	95.8	9.67	105.47
13H	105.3	11.10	116.40
14H	114.8	11.55	126.35
15H	124.3	12.00	136.30
16H	133.8	12.22	146.02
17X	143.3	12.22	155.52
18X	152.9	12.22	165.12
19X	162.5	12.22	174.72
20X	172.1	12.22	184.32
21X	181.8	12.22	194.02
22X	191.5	12.22	203.72
23X	201.1	12.22	213.32
24X	210.8	12.22	223.02
25X	220.4	12.22	232.62
26X	230.0	12.22	242.22
27X	239.6	12.22	251.82
28X	249.2	12.22	261.42
29X	258.8	12.22	271.02
30X	268.4	12.22	280.62
31X	278.0	12.22	290.22
32X	287.6	12.22	299.82
33X	297.3	12.22	309.52
34X	306.9	12.22	319.12
35X	316.6	12.22	328.82
36X	326.2	12.22	338.42
37X	335.8	12.22	348.02
38X	345.3	12.22	357.52
39X	354.9	12.22	367.12
40X	364.5	12.22	376.72
41X	374.2	12.22	386.42
42X	383.9	12.22	396.12
43X	393.5	12.22	405.72
44X	403.0	12.22	415.42
45X	412.9	12.22	425.12
46X	422.5	12.22	434.72
47X	432.2	12.22	444.42
48X	441.8	12.22	454.02
49X	451.4	12.22	463.62
50X	461.0	12.22	473.22
51X	468.0	12.22	480.22
52X	473.1	12.22	485.32
53X	477.7	12.22	489.92
54X	482.7	12.22	494.92
55X	487.3	12.22	499.52
56X	492.3	12.22	504.52
57X	501.7	12.22	513.92
58X	511.3	12.22	523.52
59X	521.0	12.22	533.22
60X	530.6	12.22	542.82
61X	540.2	12.22	552.42
62X	549.9	12.22	562.12
63X	559.5	12.22	571.72
64X	569.1	12.22	581.32
65X	578.8	12.22	591.02
66X	588.4	12.22	600.62
67X	598.0	12.22	610.22
68X	607.6	12.22	619.82
69X	617.2	12.22	629.42
70X	626.8	12.22	639.02
71X	636.5	12.22	648.72
72X	646.2	12.22	658.42
73X	655.9	12.22	668.12
74X	665.5	12.22	677.72
75X	675.2	12.22	687.42
76X	684.8	12.22	697.02
77X	694.4	12.22	706.62
184-1148B-			
1H	0.0	0.00	0.00
2H	8.1	0.00	8.10
3H	17.6	0.85	18.45
4H	27.1	–1.03	26.07
5H	40.6	–0.35	40.25
6H	50.1	0.35	50.45
7H	59.6	1.30	60.90
8H	69.1	1.72	70.82
9H	78.6	1.57	80.17
10H	88.1	2.32	90.42
11H	97.6	3.32	100.92
12H	107.1	4.08	111.18
13H	116.6	4.70	121.30
14H	126.1	5.20	131.30
15H	135.6	6.25	141.85
16X	439.9	6.25	446.15
17X	449.5	6.25	455.75
18X	459.1	6.25	465.35
19X	468.7	6.25	474.95
20X	478.3	6.25	484.55
21X	483.1	6.25	489.35
22X	487.9	6.25	494.15
23X	497.5	6.25	503.75
24X	506.9	6.25	513.15
25X	516.6	6.25	522.85
26X	526.2	6.25	532.45
27X	535.9	6.25	542.15
28X	545.5	6.25	551.75
29X	555.2	6.25	561.45
30X	564.8	6.25	571.05
31X	574.5	6.25	580.75
32X	584.2	6.25	590.45
33X	593.8	6.25	600.05
34X	603.4	6.25	609.65
35X	613.0	6.25	619.25
36X	622.6	6.25	628.85
37X	632.2	6.25	638.45
38X	641.9	6.25	648.15
39X	699.8	6.25	706.05
40X	709.5	6.25	715.75
41X	719.1	6.25	725.35
42X	728.7	6.25	734.95
43X	738.3	6.25	744.55
44X	748.0	6.25	754.25
45X	757.3	6.25	763.55
46X	766.9	6.25	773.15
47X	775.2	6.25	781.45
48X	784.8	6.25	791.05
49X	794.5	6.25	800.75
50X	804.1	6.25	810.35
51X	808.7	6.25	814.95
52X	814.7	6.25	820.95
53X	819.3	6.25	825.55
54X	824.4	6.25	830.65
55X	834.0	6.25	840.25
56X	843.6	6.25	849.85

Note: This table is also available in **ASCII format.**

Table T4. Site 1148 splice tie points.

Hole, core, section, interval (cm)	Depth (mbsf)	Depth (mcd)		Hole, core, section, interval (cm)	Depth (mbsf)	Depth (mcd)
184-				184-		
1148B-5H-5, 32	46.92	46.57				
1148B-5H-6, 47	48.57	48.22	Tie to	1148A-6H-3, 62	42.42	48.22
1148A-6H-6, 102	47.32	53.12	Tie to	1148B-6H-2, 117	52.77	53.12
1148B-6H-6, 122	58.82	59.17	Tie to	1148A-7H-3, 97	52.27	59.17
1148A-7H-5, 22	54.52	61.42	Tie to	1148B-7H-1, 52	60.12	61.42
1148B-7H-5, 117	66.74	68.04	Tie to	1148A-8H-2, 137	60.67	68.04
1148A-8H-6, 127	66.57	73.94	Tie to	1148B-8H-3, 12	72.22	73.94
1148B-8H-6, 102	77.62	79.34	Tie to	1148A-9H-3, 137	71.67	79.34
1148A-9H-7, 48	76.58	84.25	Tie to	1148B-9H-3, 108	82.68	84.25
1148B-9H-6, 117	87.27	88.84	Tie to	1148A-10H-3, 137	81.17	88.84
1148A-10H-7, 42	86.22	93.89	Tie to	1148B-10H-3, 47	91.57	93.89
1148B-10H-6, 22	95.82	98.14	Tie to	1148A-11H-3, 12	89.42	98.14
1148A-11H-7, 32	94.89	103.61	Tie to	1148B-11H-2, 117.5	100.29	103.61
1148B-11H-7, 27	106.37	109.69	Tie to	1148A-12H-3, 122	100.02	109.69
1148A-12H-6, 27	103.60	113.27	Tie to	1148B-12H-2, 57.5	109.19	113.27
1148B-12H-6, 122	115.82	119.90	Tie to	1148A-13H-3, 49	108.80	119.90
1148A-13H-7, 32	114.37	125.47	Tie to	1148B-13H-3, 117	120.77	125.47
1148B-13H-5, 17	122.77	127.47	Tie to	1148A-14H-1, 112	115.92	127.47
1148A-14H-6, 42	122.72	134.27	Tie to	1148B-14H-2, 147	129.07	134.27
1148B-14H-5, 57	132.67	137.87	Tie to	1148A-15H-2, 7	125.87	137.87
1148A-15H-6, 42	132.22	144.22	Tie to	1148B-15H-2, 87	137.97	144.22
1148B-15H-7, 67	144.17	150.42	Tie to	1148A-16H-3, 139	138.20	150.42
1148A-16H-7, 40	143.12	155.34				

Note: This table is also available in **ASCII format.**

Table T5. Light-colored, carbonate-rich layers observed in cores recovered at Site 1148. (Continued on next three pages.)

Core, section, interval (cm)	Top		Bottom		Thickness (cm)
	Depth (mbsf)	Depth (mcd)	Depth (mbsf)	Depth (mcd)	
182-1148A-					
10H-2, 20-120	78.50	86.17	79.50	87.17	100
10H-3, 105, to 10H-4, 56	80.85	88.52	81.86	89.53	101
11H-2. 0-32	87.80	96.52	88.12	96.84	32
11H-3, 12-62	89.42	98.14	89.92	98.64	50
12H-2, 0-60	97.30	106.97	97.90	107.57	60
13H-1, 25-65	105.55	116.65	105.95	117.05	40
13H-5, 30-65	111.35	122.45	111.70	122.80	35
14H-1, 20-85	115.00	126.55	115.65	127.20	65
15H-2, 30-130	126.10	138.10	127.10	139.10	100
15H-3, 92, to 15H-5, 53	128.22	140.22	130.83	142.83	261
16H-1, 1-110	133.80	146.02	134.90	147.12	110
16H-2, 24-120	135.54	147.76	136.50	148.72	96
16H-3, 18-43	136.98	149.20	137.23	149.45	25
16H-4, 38-143	138.68	150.90	139.73	151.95	105
17X-2, 13-43	144.93	157.15	145.14	157.36	21
17X-3, 94-114	147.24	159.46	147.44	159.66	20
17X-5, 10-20	149.40	161.62	149.50	161.72	10
17X-5, 80, to 17X-6, 15	150.10	162.32	150.95	163.17	85
18X-1, 0-135	152.90	165.12	154.25	166.47	135
18X-2, 11-34	154.51	166.73	154.74	166.96	23
18X-2, 78-107	155.18	167.40	155.47	167.69	29
18X-3, 6-23	155.96	168.18	156.13	168.35	17
18X-3, 127-138	157.17	169.39	157.28	169.50	11
18X-4, 113-132	158.53	170.75	158.72	170.94	19
18X-5, 14-30	159.04	171.26	159.20	171.42	16
18X-5, 74, to 18X-7, 36	159.64	171.86	161.42	173.64	178
19X-1, 40-60	162.90	175.12	163.10	175.32	20
19X-1, 92-112	163.42	175.64	163.62	175.84	20
19X-2, 40-92	164.40	176.62	164.92	177.14	52
19X-2, 117-150	165.17	177.39	165.50	177.72	33
19X-3, 16-43	165.66	177.88	165.93	178.15	27
19X-3, 121-138	166.71	178.93	166.88	179.10	17
19X-4, 26-65	167.26	179.48	167.65	179.87	39
19X-4, 112-136	168.12	180.34	168.36	180.58	24
19X-5, 32-98	168.82	181.04	169.48	181.70	66
19X-5, 139, to 19X-6, 63	169.89	182.11	170.63	182.85	74
19X-6, 111-142	171.11	183.33	171.42	183.64	31
20X-2, 62-98	174.22	186.44	174.58	186.80	36
20X-2, 113-131	174.73	186.95	174.91	187.13	18
20X-4, 16-86	176.76	188.98	177.46	189.68	70
20X-4, 113-126	177.73	189.95	177.86	190.08	13
20X-5, 42-63	178.52	190.74	178.73	190.95	21
20X-5, 90-97	179.00	191.22	179.07	191.29	7
20X-5, 125-139	179.35	191.57	179.49	191.71	14
20X-6, 44-64	180.04	192.26	180.24	192.46	20
20X-6, 90-96	180.50	192.72	180.56	192.78	6
20X-6, 125-134	180.85	193.07	180.94	193.16	9
20X-7, 14, to 21X-1, 29	181.24	193.46	182.09	194.31	85
21X-1, 57-83	182.37	194.59	182.63	194.85	26
21X-1, 140, to 21X-2, 7	183.20	195.42	183.37	195.59	17
21X-2, 28-90	183.58	195.80	184.20	196.42	62
21X-2, 128, to 21X-3, 14	184.58	196.80	184.94	197.16	36
21X-3, 32-60	185.12	197.34	185.40	197.62	28
21X-3, 78-102	185.58	197.80	185.82	198.04	24
21X-3, 141, to 21X-4, 35	186.21	198.43	186.65	198.87	44
21X-4, 60-102	186.90	199.12	187.32	199.54	42
21X-4, 130, to 21X-5, 65	187.60	199.82	188.45	200.67	85
21X-5, 92-139	188.72	200.94	189.19	201.41	47
21X-6, 17-58	189.47	201.69	189.88	202.10	41
21X-6, 86-131	190.16	202.38	190.61	202.83	45
21X-7, 10, to 22X-1, 20	190.90	203.12	191.70	203.92	80
22X-1, 97-118	192.47	204.69	192.68	204.90	21
22X-1, 137, to 22X-2, 12	192.87	205.09	193.12	205.34	25
22X-2, 94-130	193.94	206.16	194.30	206.52	36

Table T5 (continued).

Core, section, interval (cm)	Top		Bottom		Thickness (cm)
	Depth (mbsf)	Depth (mcd)	Depth (mbsf)	Depth (mcd)	
22X-3, 29-59	194.79	207.01	195.09	207.31	30
22X-3, 75-113	195.25	207.47	195.83	208.05	58
22X-4, 24-45	196.24	208.46	196.45	208.67	21
22X-4, 78-93	196.78	209.00	196.93	209.15	15
22X-5, 26-69	197.76	209.98	198.19	210.41	43
22X-5, 97-135	198.47	210.69	198.85	211.07	38
22X-6, 33-70	199.33	211.55	199.70	211.92	37
22X-6, 142, to 22X-7, 28	200.42	212.64	200.78	213.00	36
23X-1, 0-32	201.10	213.32	201.42	213.64	32
23X-1, 82-99	201.92	214.14	202.09	214.31	17
23X-1, 129, to 23X-2, 60	202.39	214.61	203.20	215.42	81
23X-2, 102-139	203.62	215.84	203.99	216.21	37
23X-3, 26-83	204.36	216.58	204.93	217.15	57
23X-4, 49-73	206.09	218.31	206.33	218.55	24
23X-4, 123-150	206.83	219.05	207.10	219.32	27
23X-5, 11-38	207.21	219.43	207.48	219.70	27
23X-5, 61-80	207.71	219.93	207.90	220.12	19
23X-5, 122, to 23X-6, 16	208.32	220.54	208.76	220.98	44
23X-6, 46-59	209.06	221.28	209.19	221.41	13
23X-6, 133-150	209.93	222.15	210.10	222.32	17
23X-7, 28-45	210.38	222.60	210.55	222.77	17
24X-1, 6-65	210.86	223.08	211.45	223.67	59
24X-1, 105-119	211.85	224.07	211.99	224.21	14
24X-2, 48-76	212.78	225.00	213.06	225.28	28
24X-2, 91-131	213.21	225.43	213.61	225.83	40
24X-3, 87-109	214.67	226.89	214.89	227.11	22
24X-4, 71-113	216.01	228.23	216.43	228.65	42
24X-4, 142-150	216.72	228.94	216.80	229.02	8
24X-5, 14-38	216.94	229.16	217.18	229.40	24
24X-5, 52-65	217.32	229.54	217.45	229.67	13
24X-5, 90-106	217.70	229.92	217.86	230.08	16
24X-5, 136, to 24X-6, 14	218.16	230.38	218.44	230.66	28
24X-6, 52-68	218.82	231.04	218.98	231.20	16
24X-CC, 11-31	219.28	231.50	219.48	231.70	20
25X-1, 39-142	220.79	233.01	221.82	234.04	103
25X-2, 21-123	222.11	234.33	223.13	235.35	102
25X-3, 22-71	223.62	235.84	224.11	236.33	49
25X-3, 93, to 25X-4, 80	224.33	236.55	225.70	237.92	137
25X-4, 100-129	225.90	238.12	226.19	238.41	29
25X-5, 17-97	226.57	238.79	227.37	239.59	80
25X-6, 31-75	228.21	240.43	228.65	240.87	44
25X-6, 118-132	229.08	241.30	229.22	241.44	14
25X-7, 22-43	229.62	241.84	229.83	242.05	21
25X-CC, 18-32	230.01	242.23	230.15	242.37	14
26X-1, 30-42	230.30	242.52	230.42	242.64	12
26X-1, 131-149	231.31	243.53	231.49	243.71	18
26X-2, 31-52	231.81	244.03	232.02	244.24	21
26X-2, 116-123	232.66	244.88	232.73	244.95	7
26X-3, 53-60	233.53	245.75	233.60	245.82	7
26X-4, 18-33	234.68	246.90	234.83	247.05	15
26X-4, 87-116	235.37	247.59	235.66	247.88	29
26X-5, 62-122	236.62	248.84	237.22	249.44	60
26X-6, 16-22	237.66	249.88	237.72	249.94	6
26X-6, 90, to 26X-CC, 40	238.40	250.62	238.85	251.07	45
27X-1, 37-54	239.97	252.19	240.14	252.36	17
27X-1, 88-98	240.48	252.70	240.58	252.80	10
27X-2, 20-46	241.30	253.52	241.56	253.78	26
27X-2, 103-112	242.13	254.35	242.22	254.44	9
27X-3, 25-57	242.85	255.07	243.17	255.39	32
27X-3, 84-102	243.44	255.66	243.62	255.84	18
27X-4, 4-44	244.14	256.36	244.54	256.76	40
27X-4, 90-113	245.00	257.22	245.23	257.45	23
27X-5, 45-62	246.05	258.27	246.22	258.44	17
27X-6, 31-46	247.41	259.63	247.56	259.78	15
27X-6, 130-150	248.40	260.62	248.60	260.82	20

Table T5 (continued).

Core, section, interval (cm)	Top		Bottom		Thickness (cm)
	Depth (mbsf)	Depth (mcd)	Depth (mbsf)	Depth (mcd)	
28X-2, 80, to 28X-3, 4	251.50	263.72	252.24	264.46	74
28X-3, 48-57	252.68	264.90	252.77	264.99	9
28X-3, 123-131	253.43	265.65	253.51	265.73	8
28X-4, 36-96	254.06	266.28	254.66	266.88	60
28X-4, 140-150	255.10	267.32	255.20	267.42	10
28X-5, 113-145	256.33	268.55	256.65	268.87	32
28X-6, 48-57	257.18	269.40	257.27	269.49	9
28X-6, 134-147	258.04	270.26	258.17	270.39	13
28X-7, 12-33	258.32	270.54	258.53	270.75	21
29X-1, 0-56	258.80	271.02	259.36	271.58	56
29X-1, 83-95	259.63	271.85	259.75	271.97	12
29X-2, 43-54	260.73	272.95	260.84	273.06	11
29X-3, 65-74	262.45	274.67	262.54	274.76	9
29X-3, 99-110	262.79	275.01	262.9	275.12	11
29X-3, 142, to 29X-4, 10	263.22	275.44	263.40	275.62	18
29X-4, 35-40	263.65	275.87	263.70	275.92	5
29X-4, 61-69	263.91	276.13	263.99	276.21	8
29X-4, 125-146	264.55	276.77	264.76	276.98	21
29X-5, 45-59	265.25	277.47	265.39	277.61	14
29X-5, 118-150	265.98	278.2	266.30	278.52	32
29X-6, 54-63	266.84	279.06	266.93	279.15	9
30X-1, 96-103	269.36	281.58	269.43	281.65	7
30X-3, 25-36	271.65	283.87	271.76	283.98	11
30X-3, 88-92	272.28	284.50	272.32	284.54	4
30X-3, 116-125	272.56	284.78	272.65	284.87	9
30X-4, 32-43	273.22	285.44	273.33	285.55	11
30X-5, 40-72	274.80	287.02	275.12	287.34	32
30X-5, 100-108	275.40	287.62	275.48	287.70	8
30X-6, 33-49	276.23	288.45	276.39	288.61	16
30X-6, 94-106	276.84	289.06	276.96	289.18	12
30X-6, 130-136	277.20	289.42	277.26	289.48	6
31X-1, 118-134	279.18	291.40	279.34	291.56	16
31X-1, 143, to 31X-2, 10	279.43	291.65	279.60	291.82	17
31X-2, 23-31	279.73	291.95	279.81	292.03	8
31X-2, 130-144	280.80	293.02	280.94	293.16	14
31X-3, 76-94	281.76	293.98	281.94	294.16	18
31X-4, 0-12	282.50	294.72	282.62	294.84	12
31X-4, 65-80	283.15	295.37	283.30	295.52	15
31X-4, 102-122	283.52	295.74	283.72	295.94	20
31X-5, 37-50	284.37	296.59	284.50	296.72	13
31X-5, 75-81	284.75	296.97	284.81	297.03	6
31X-6, 41-56	285.91	298.13	286.06	298.28	15
31X-6, 79-88	286.29	298.51	286.38	298.60	9
31X-6, 103-120	286.53	298.75	286.70	298.92	17
31X-CC, 17-30	287.55	299.77	287.68	299.90	13
32X-1, 0-68	287.60	299.82	288.28	300.50	68
32X-1, 105, to 32X-2, 8	288.65	300.87	289.18	301.40	53
32X-2, 29-42	289.39	301.61	289.52	301.74	13
32X-2, 70-83	289.80	302.02	289.93	302.15	13
32X-2, 112, to 32X-3, 39	290.22	302.44	290.99	303.21	77
32X-3, 101, to 32X-4, 3	291.61	303.83	292.13	304.35	52
32X-4, 23-37	292.33	304.55	292.47	304.69	14
32X-4, 51-63	292.61	304.83	292.73	304.95	12
32X-4, 98-143	293.08	305.30	293.53	305.75	45
32X-5, 34-51	293.94	306.16	294.11	306.33	17
32X-5, 73-120	294.33	306.55	294.80	307.02	47
32X-5, 137-150	294.97	307.19	295.10	307.32	13
32X-6, 46-60	295.56	307.78	295.70	307.92	14
33X-1, 0-37	297.30	309.52	297.67	309.89	37
33X-2, 19-33	298.99	311.21	299.13	311.35	14
33X-2, 93-107	299.73	311.95	299.87	312.09	14
33X-3, 7-39	300.37	312.59	300.69	312.91	32
33X-3, 94-120	301.24	313.46	301.50	313.72	26
33X-4, 21-48	302.01	314.23	302.28	314.50	27
33X-4, 107-128	302.87	315.09	303.08	315.30	21

Table T5 (continued).

Core, section, interval (cm)	Top Depth (mbsf)	Top Depth (mcd)	Bottom Depth (mbsf)	Bottom Depth (mcd)	Thickness (cm)
33X-5, 40-103	303.70	315.92	304.33	316.55	63
33X-6, 14-35	304.94	317.16	305.15	317.37	21
33X-6, 54-68	305.34	317.56	305.48	317.70	14
33X-7, 38-44	306.68	318.90	306.74	318.96	6
34X-1, 0, to 34X-2, 56	306.90	319.12	307.65	319.87	75
34X-2, 93-107	308.02	320.24	308.16	320.38	14
34X-3, 23-56	308.82	321.04	309.15	321.37	33
34X-3, 83-104	309.42	321.64	309.63	321.85	21
34X-3, 132, to 34X-4, 9	309.91	322.13	310.18	322.40	27
34X-4, 26-43	310.35	322.57	310.52	322.74	17
34X-4, 74-109	310.83	323.05	311.18	323.40	35
34X-5, 23-45	311.82	324.04	312.04	324.26	22
34X-5, 61-80	312.20	324.42	312.39	324.61	19
34X-5, 96, to 34X-6, 23	312.55	324.77	313.32	325.54	77
34X-6, 46-61	313.55	325.77	313.70	325.92	15
34X-6, 79-90	313.88	326.10	313.99	326.21	11
34X-6, 105-119	314.14	326.36	314.28	326.50	14
34X-6, 134, to 34X-7, 23	314.43	326.65	314.82	327.04	39
34X-8, 24, to 34X-CC, 26	316.33	328.55	316.66	328.88	33
184-1148B-					
10H-2, 145, to 10H-3, 102	91.05	93.37	92.12	94.44	107
10H-6, 20-103	95.80	98.12	96.63	98.95	83
11H-1, 22-105	97.82	101.14	98.65	101.97	83
11H-2, 62-120	99.72	103.04	100.30	103.62	58
11H-3, 5, to 11H-5, 55	100.65	103.97	104.15	107.47	350
12H-1, 0-92	107.10	111.18	108.02	112.10	92
12H-2, 14-140	108.74	112.82	110.00	114.08	126
12H-3, 37-109	110.47	114.55	111.19	115.27	72
12H-4, 19-139	111.79	115.87	112.99	117.07	120
13H-1, 95, to 13H-2, 123	117.55	122.25	119.33	124.03	178
13H-3, 26-101	119.86	124.56	120.61	125.31	75
13H-3, 113, to 13H-4, 133	120.73	125.43	122.43	127.13	170
14H-1, 29-112	126.39	131.59	127.22	132.42	83
14H-2, 27-127	127.87	133.07	128.87	134.07	100
14H-3, 25-33	129.35	134.55	129.43	134.63	8
14H-4, 9-38	130.69	135.89	130.98	136.18	29
14H-5, 98-144	133.08	138.28	133.54	138.74	46
14H-6, 15-58	133.75	138.95	134.18	139.38	43
15H-1, 10-85	135.70	141.95	136.45	142.70	75
15H-3, 2, to 15H-4, 3	138.62	144.87	139.85	146.10	151
15H-4, 30-112	140.12	146.37	140.94	147.19	82
15H-5, 30-91	141.62	147.87	142.23	148.48	61

Table T6. Volcanic ash layers recovered at Site 1148.

Core, section, interval (cm)	Top Depth (mbsf)	Top Depth (mcd)	Bottom Depth (mbsf)	Bottom Depth (mcd)	Thickness (cm)	Remarks/comments
184-1148A-						
2H-6, 41	8.71	13.56			<1	Light gray volcanic ash as burrow fill
3H-4, 78-81	15.51	20.36	15.54	20.39	3	Black pumice lump, 4 cm long
4H-2, 86-89	22.16	27.01	22.19	27.04	3	Light gray ash layer, mottles and burrows with ash between 79 and 92 cm
4H-3, 71	23.51	28.36			<1	Small burrow filled with beige ash
4H-6, 86-90	28.16	33.01	28.20	33.05	4	Black volcanic ash, overlain by a turbidite
6H-2, 86-91	41.16	46.96	41.21	47.01	5	Beige ash in burrows
6H-2, 129-133	41.59	47.39	41.63	47.43	4	Beige ash in burrows
11H-2, 133-136	89.13	97.85	89.16	97.88	3	Medium gray volcanic ash layer with green clay at the bottom
12H-4, 39-44	100.69	110.36	100.74	110.41	5	Bioturbated dark gray ash layer and ash in burrows
18X-2, 46-48	154.86	167.08	154.88	167.10	2	Medium gray ash with green clay mottles above and below
33X-3, 115-120	301.45	313.67	301.50	313.72	5	Dispersed ash in greenish gray reduction zone (low magnetic susceptibility)
33X-5, 95-101	304.25	316.47	304.31	316.53	6	Black ash layer in greenish gray reduction zone (low magnetic susceptibility)
184-1148B-						
3H-1, 77-81	18.37	19.22	18.41	19.26	4	Light gray ash layer with small ash-filled burrows below
5H-3, 137-138	44.97	44.62	44.98	44.63	1	Pumice clast
5H-5, 76-77	47.36	47.01	47.37	47.02	1	Light gray ash layer
5H-5, 89-89	47.49	47.14			<1	Burrow filled with light gray ash
6H-5, 94-100	57.04	57.39	57.10	57.45	6	Dispersed volcanic ash
10H-5, 135-138	95.45	97.77	95.48	97.80	3	Medium gray volcanic ash layer with sharp base and gradational upper contact

Table T7. Summary of biohorizons at Site 1148. (**See table notes.** Continued on next page.)

Code	Events	Depth range of stratigraphic datums: Top — Core, section, interval (cm)	Top — Depth (mbsf)	Top — Depth (mcd)	Bottom — Core, section, interval (cm)	Bottom — Depth (mbsf)	Bottom — Depth (mcd)	Age (Ma)	Average depth (mcd)	Average sedimentation rate (m/m.y.)
		184-1148A-			184-1148A-					
CN	FO *E. huxleyi* acme	1H-CC, 7-13	0.70	**0.70**	2H-CC, 15-22	10.41	15.26	0.09	7.98	
PF	LO pink *G. ruber*	1H-CC, 7-13	0.70	0.70	2H-CC, 15-22	10.41	**15.26**	0.12	7.98	
CN	FO *E. huxleyi*	3H-CC, 6-13	19.89	**24.73**	4H-CC, 30-37	29.50	34.35	0.26	29.54	
PF	FO pink *G. ruber*	3H-CC, 6-13	19.89	**24.73**	4H-CC, 30-37	29.50	34.35	0.40	29.54	
CN	LO *P. lacunosa*	3H-CC, 6-13	19.89	24.73	4H-CC, 30-37	29.50	**34.35**	0.46	29.54	
BF	LO *Stilostomella*	5H-CC, 0-6	38.81	43.66	6H-CC, 22-29	48.70	54.50	0.75	49.08	75
CN	*LO R.asanoi*	6H-CC, 22-29	48.70	54.50	7H-CC, 0-10	57.67	**64.59**	0.83	59.55	
CN	LO small *Gephyrocapsa* acme	7H-CC, 0-10	57.69	64.59	8H-CC, 13-18	67.49	**74.85**	1.01	69.72	
CN	FO *R. asanoi*	8H-CC, 13-18	67.48	**74.85**	9H-CC, 19-26	76.91	84.61	1.16	79.73	
CN	FO small *Gephyrocapsa* acme	10H-CC, 18-25	86.68	**94.35**	11H-CC, 4-11	95.97	104.69	1.22	99.52	
CN	LO *C. macintyrei*	12H-CC, 0-7	105.67	115.34	13H-CC, 9-16	114.66	**125.76**	1.59	120.55	
PF	LO *G. fistulosus*	12H-CC, 0-7	105.67	115.34	13H-CC, 9-16	114.66	**125.76**	1.77	120.55	
CN	FO medium *Gephyrocapsa* spp.*	12H-CC, 0-7	105.67	**115.34**	13H-CC, 9-16	114.66	125.76	1.69	120.55	
CN	LO *D. brouweri*	13H-CC, 9-16	114.66	125.76	14H-CC, 0-8	123.93	**135.49**	1.95	130.63	
PF	FO *G. truncatulinoides*	13H-CC, 9-16	114.66	**125.76**	14H-CC, 0-8	123.93	135.49	2.00	130.63	
CN	LO *D. pentaradiatus*	14H-CC, 0-8	123.94	135.49	15H-CC, 0-8	133.58	**145.59**	2.52	140.54	
CN	LO *D. surculus*	15H-CC, 0-8	133.54	133.59	16H-CC, 0-8	143.21	**155.44**	2.53	144.52	
CN	LO *D. tamalis*	16H-CC, 0-8	143.22	155.44	17X-CC, 31-38	153.10	**165.32**	2.83	160.38	
PF	LO *G. altispira*	16H-CC, 0-8	143.22	155.44	17X-CC, 31-38	153.10	**165.32**	3.09	160.38	
PF	LO *S. seminulina*	16H-CC, 0-8	143.22	155.44	17X-CC, 31-38	153.10	**165.32**	3.12	160.38	
PF	FO *G. tosaensis*	16H-CC, 0-8	143.22	**155.44**	17X-CC, 31-38	153.10	165.32	3.35	160.38	
CN	LO *Sphenolithus abies/neoabies*	17X-CC, 31-38	153.10	165.32	18X-CC, 44-51	161.54	**173.76**	3.66	169.54	
CN	LO *R. pseudoumbilicus*	17X-CC, 31-38	153.10	165.32	18X-CC, 44-51	161.54	**173.76**	3.82	169.54	
PF	*Pulleniatina* (sin. to dex. coiling change)	17X-CC, 31-38	153.10	165.32	18X-CC, 44-51	161.54	173.76	3.95	169.54	
PF	LO *G. nepenthes*	18X-CC, 44-51	161.54	173.76	19X-CC, 21-27	172.30	**184.52**	4.2	179.14	
CN	LO *A. tricorniculatus*	18X-CC, 44-51	161.54	173.76	19X-CC, 21-27	172.30	**184.52**	4.56	179.14	
CN	LO *C. acutus*	17X-CC, 31-38	153.10	165.32	18X-CC, 44-51	161.54	**173.76**	4.99	169.54	
CN	LO *T. rugosus*	19X-CC, 21-27	172.30	184.52	20X-CC, 0-7	181.60	**193.82**	5.23	189.17	
CN	FO *C. acutus*	18X-CC, 44-51	161.54	**173.76**	19X-CC, 21-27	172.30	184.52	5.37	179.14	
CN	LO *D. quinqueramus*	19X-CC, 21-27	172.30	184.52	20X-CC, 0-7	181.60	**193.82**	5.54	189.17	
PF	FO *S. dehiscens* s.l.	19X-CC, 21-27	172.30	**184.52**	20X-CC, 0-7	181.60	193.82	5.54	189.17	
PF	FO *G. tumida*	20X-CC, 0-7	181.60	**193.82**	21X-CC, 30-37	191.61	203.83	5.82	198.83	
CN	LO *A. amplificus*	20X-CC, 0-7	181.60	193.82	21X-CC, 30-37	191.61	**203.83**	5.99	198.83	
PF	FO *G. conglobatus*	21X-CC, 30-37	191.61	**203.83**	22X-CC, 26-33	201.26	213.48	6.2	208.66	16
CN	FO *A. amplificus*	21X-CC, 30-37	191.61	**203.83**	22X-CC, 26-33	201.26	213.48	6.76	208.66	
CN	FO *A. primus*	22X-CC, 26-33	201.26	**213.48**	23X-CC, 13-20	210.72	222.94	7.39	218.21	
CN	FO *D. quinqueramus*	24X-CC, 41-48	219.62	**231.84**	25X-CC, 32-39	230.19	242.41	8.2	237.13	
CN	FO *D. pentaradiatus*	27X-CC, 45-52	249.44	**261.66**	28X-CC, 23-30	259.04	271.26	8.55	266.46	
PF	FO *G. plesiotumida*	27X-CC, 45-52	249.44	**261.66**	28X-CC, 23-30	259.04	271.26	8.58	266.46	
PF	FO *G. extremus*	27X-CC, 45-52	249.44	**261.66**	28X-CC, 23-30	259.04	271.26	8.58	266.46	
CN	LO *D. hamatus*	26X-CC, 40-47	238.89	251.11	27X-CC, 45-52	249.44	**261.66**	9.4	256.39	
CN	FO *D. hamatus*	27X-CC, 45-52	249.44	**261.66**	28X-CC, 23-30	259.04	271.26	10.38	266.46	
PF	LO *G. mayeri*	28X-CC, 23-30	259.04	271.26	29X-CC, 26-33	267.24	**279.46**	10.49	275.36	
CN	FO *C. coalithus*	29X-CC, 26-33	267.24	**279.46**	30X-CC, 29-36	278.21	290.43	10.79	284.95	
PF	FO *G. nepenthes*	29X-CC, 26-33	267.24	**279.46**	30X-CC, 29-36	278.21	290.43	11.19	284.95	
CN	FO *D. kugleri*	30X-CC, 29-36	278.21	**290.43**	31X-CC, 40-47	287.82	300.04	11.8	295.24	
CN	FO *T. rugosus*	31X-CC, 40-47	287.82	**300.04**	32X-CC, 16-26	297.26	309.50	12.62	304.77	
CN	LO *Cy. floridanus*	31X-CC, 40-47	287.82	300.04	32X-CC, 16-26	297.26	**309.50**	13.19	304.77	
CN	LO *S. heteromorphus*	31X-CC, 40-47	287.82	300.04	32X-CC, 16-26	297.26	**309.50**	13.57	304.77	
PF	FO *Orbulina* spp.	32X-CC, 16-26	297.28	**309.50**	33X-CC, 21-31	307.00	319.24	15.1	314.37	
CN	LO *H. ampliaperta*	33X-CC, 21-31	307.02	319.24	34X-CC, 30-37	316.74	**328.96**	15.6	324.10	
PF	FO *P. sicana*	36X-CC, 35-42	336.06	**348.28**	37X-CC, 19-26	345.52	357.74	16.4	353.01	
PF	LO *C. dissimilis**	38X-CC, 32-39	355.13	367.35	39X-CC, 26-33	364.68	**376.90**	17.3	372.13	
CN	FO *S. heteromorphus*	38X-CC, 32-39	355.13	**367.35**	39X-CC, 26-33	364.68	376.90	18.2	372.13	
CN	LO *S. belemnos*	38X-CC, 32-39	355.13	367.35	39X-CC, 26-33	364.68	**376.90**	18.3	372.13	
PF	FO *G. praescitula*	39X-CC, 26-33	364.68	**376.90**	40X-CC, 26-33	374.25	386.47	18.5	381.69	
CN	FO *S. belemnos*	40X-CC, 26-33	374.25	**386.47**	41X-CC, 40-47	384.16	396.38	19.2	391.43	14
PF	LO *P. kugleri*	42X-CC, 24-31	393.49	405.71	43X-CC, 36-43	403.15	**415.37**	21.5	410.54	
CN	FO *D. druggii*	49X-CC, 48-55	460.52	**472.74**	50X-CC, 34-41	465.12	477.34	23.2	475.04	
PF	FO *G. dehiscens*	47X-CC, 41-48	442.13	**454.35**	48X-CC, 20-27	450.38	472.74	23.2	463.55	
PF	FO *P. kugleri**	47X-CC, 41-48	442.13	**454.35**	48X-CC, 20-27	450.38	472.74	23.8	463.55	
PF	FO *P. pseudokugleri*	49X-CC, 48-55	460.52	**472.74**	50X-CC, 34-41	465.12	477.34	25.9	475.04	
PF	LO *P. opima opima*	49X-CC, 48-55	460.52	472.74	50X-CC, 34-41	465.12	**477.34**	27.1	475.04	
CN	LO *S. distentus**	49X-CC, 48-55	460.52	472.74	50X-CC, 34-41	465.12	**477.34**	27.5	475.04	61
PF	LO *C. cubensis* (common)	52X-CC, 30-37	473.44	485.66	53X-CC, 30-37	478.72	**490.94**	28.5	488.30	
PF	FO *G. angulosuturalis*	65X-CC, 27-34	581.41	**593.63**	66X-CC, 33-40	597.46	609.68	29.4	601.66	

Table T7 (continued).

Code	Events	Depth range of stratigraphic datums: Top: Core, section, interval (cm)	Top: Depth (mbsf)	Top: Depth (mcd)	Bottom: Core, section, interval (cm)	Bottom: Depth (mbsf)	Bottom: Depth (mcd)	Age (Ma)	Average depth (mcd)	Average sedimentation rate (m/m.y.)
CN	FO *S. ciperoensis*	66X-CC, 33-40	597.46	**609.68**	67X-CC, 30-37	607.78	620.00	29.9	614.84	
PF	LO *T. ampliapertura*	68X-CC, 24-31	617.43	629.65	69X-CC, 36-43	627.05	**639.27**	30.3	634.46	
PF	FO *P. opima opima**	71X-CC, 37-43	646.32	**658.54**	72X-CC, 34-40	655.87	668.09	30.6	663.32	

Notes: Sources of reference age for all biostratigraphic events are listed in Tables **T2,** p. 42, and **T3,** p. 43, in the "Explanatory Notes" chapter. CN = calcareous nannofossils, PF = planktonic foraminifers, BF = benthic foraminifers, FO = first occurrence, LO = last occurrence. * = events used in calculating average sedimentation rate. Depth for the top and bottom of biostratigraphic events = the mean of the sample interval. Depth in bold indicates where biohorizon is recorded in the studied samples; depth range between the top and bottom is the interval where the real bioevent may occur. Bars in average sedimentation rate column indicate the range of samples to which the average sedimentation rate applies.

Table T8. Calcareous nannofossil checklist for Site 1148. (**See table notes.** Continued on next four pages.)

Age	Zone		Core, section, interval (cm)	Depth (mcd)	Abundance	Preservation	*Amaurolithus amplificus*	*Amaurolithus delicatus*	*Amaurolithus primus*	*Amaurolithus tricorniculatus*	*Caicidiscus leptoporus*	*Caicidiscus macintyrei*	*Caicidiscus premacintyrei*	*Catinaster calyculus*	*Catinaster coalitus*	*Ceratolithus acutus*	*Ceratolithus armatus*	*Ceratolithus cristatus*	*Ceratolithus rugosus*	*Chiasmolithus altus*	*Coccolithus miopelagicus*	*Coccolithus pelagicus*	*Coronocyclus nitescens*	*Cyclicargolithus floridanus*	*Dictyococcites bisectus*	*Discoaster aaamanteus*	*Discoaster berggrenii*	*Discoaster bollii*	*Discoaster brouweri*	*Discoaster calcaris*	*Discoaster deflandrei*	*Discoaster druggii*	*Discoaster exilis*	*Discoaster hamatus*	*Discoaster kugleri*	*Discoaster moorei*	*Discoaster pentaradialus*	*Discoaster petaliformis*	*Discoaster prepentaradiatus*	*Discoaster quinqueramus*	*Discoaster surculus*	*Discoaster tamalis*	*Discoaster tanii*	*Discoaster variabilis*	*Emiliania huxleyi*	*Florisphaera profunda*	*Gephyrocapsa caribbeanica*	*Gephyrocapsa margerelii*
			184-1148A-																																											
			1H-CC, 7-13	0.70	A	VG					C							R																										A	D		R
Pleistocene	NN21b	CN15	2H-CC, 15-22	15.26	A	M					C							R																	R								C	C		R
	NN21a		3H-CC, 6-13	24.74	A	G					F							R																	R								F	A		C
			4H-CC, 30-37	34.35	A	M					C																																	A	F	C
	NN19b	CN14a	5H-CC, 0-6	43.66	A	M					C																																	A		
			6H-CC, 22-29	54.50	A	M					F																																	A		
			7H-CC, 0-10	64.57	A	M					C							R																											A	F	F
			8H-CC, 13-18	74.86	A	M					C							R				R																							D		R
		CN13	9H-CC, 19-26	84.58	A	G					C							R																											A	F	
			10H-CC, 18-25	94.35	A	G					C							R																											A	C	
			11H-CC, 4-11	104.69	A	G					F							R																											A		R
			12H-CC, 0-7	115.34	A	P					C							R				F																							D		
	NN19a		13H-CC, 9-16	125.76	A	M					C							R				R																							D		
			14H-CC, 0-8	135.48	A	M					C	F						R				R							C							R									A		
	NN18	CN12d	15H-CC, 0-8	145.58	A	M					C	C						R											C							C			R					A		
late Pliocene	NN17	CN12c	16H-CC, 0-8	155.43	C	P					F	C						R											C							A			R					A		
	NN16	CN12b	17X-CC, 31-38	165.32	A	M					F	C						R											C							A			F					A		
		CN12a	18X-CC, 44-51	173.76	A	M					R	C						R											C							A			F	R				A		
early Pliocene	NN15-12	CN11-10	19X-CC, 21-27	184.52	A	M		R			C	C				R												C							A			F	F				A		
			20X-CC, 0-7	193.82	A	M		R	R	R	R	C				F			R			C							C							A			F		F			A		
			21X-CC, 30-37	203.83	A	M			R	R	C	C										C					C		C							A		C	F		F			A		
	NN11	CN9	22X-CC, 26-33	213.48	A	G	R	R	R	R	C	C										C					A		C							A		C	F					A		
			23X-CC, 13-20	222.94	A	G		R	R		C	C										C					A		C							C		C	F			F		C		
			24X-CC, 41-48	231.84	A	G					C	C										C					A		C							C		F	F			F		A		
			25X-CC, 32-39	242.41	A	G					F	C										C					A		C							C		F	F			F		A		
late Miocene	NN10	CN8	26X-CC, 40-47	251.11	A	G					F	C										F							C							F			F					C		
			27X-CC, 45-52	261.66	A	G					F	C										F							F							R			F					C		
	NN9	CN7	28X-CC, 23-30	271.26	A	M					F	C			R							F							F			R						R					C		
			29X-CC, 26-33	279.46	A	M					F	C		F	C							A									F		F						R					C		
	NN8	CN6	30X-CC, 29-36	290.43	A	M						C			C							C		F						R	F	F			R	R			R					C		
	NN7	CN5b	31X-CC, 40-47	300.04	A	M					F	C										C	R				F			C				F	R									A		
	NN6	CN5a	32X-CC, 16-26	309.48	A	M					F	R									R	C		C					C	R	R				R									C		
	NN5	CN 4	33X-CC, 21-31	319.22	A	M						F	F								R	C	F	A					F	F		R				F								C		
middle Miocene			34X-CC, 30-37	328.96	A	P					F		F								R	C	R	C						C	F				F									C		
			35X-CC, 14-21	338.47	A	P					F		F								R	C	R	C						R	C				F	R								C		
			36X-CC, 35-42	348.28	A	M					R		F								R	F	F	A						C						R									C		
	NN4	CN 3	37X-CC, 19-26	357.74	C	P					R		R								F	F		A			F		F	C	R	F			R	C								C		
early-middle Miocene			38X-CC, 32-39	367.35	A	M					F		R								R	C	F	A						C	F				R									R		
			39X-CC, 26-33	376.90	A	M					F		R								F	C	F	F						C	F				F									F		
early Miocene	NN3	CN2	40X-CC, 26-33	386.47	A	M							R									C		A		R				C	F				F									R		
			41X-CC, 40-47	396.38	A	M							R									C		A			F			C	F													C		

Table T8 (continued).

Age	Zone		Core, section, interval (cm)	Depth (mcd)	Abundance	Preservation	*Amaurolithus amplificus*	*Amaurolithus delicatus*	*Amaurolithus primus*	*Amaurolithus tricorniculatus*	*Calcidiscus leptoporus*	*Calcidiscus macintyrei*	*Calcidiscus premacintyrei*	*Catinaster calyculus*	*Catinaster coalitus*	*Ceratolithus acutus*	*Ceratolithus armatus*	*Ceratolithus cristatus*	*Ceratolithus rugosus*	*Chiasmolithus altus*	*Coccolithus miopelagicus*	*Coccolithus pelagicus*	*Coronocyclus nitescens*	*Cyclicargolithus floridanus*	*Dictyococcites bisectus*	*Discoaster adamanteus*	*Discoaster berggrenii*	*Discoaster bollii*	*Discoaster brouweri*	*Discoaster calcaris*	*Discoaster deflandrei*	*Discoaster druggii*	*Discoaster exilis*	*Discoaster hamatus*	*Discoaster kugleri*	*Discoaster moorei*	*Discoaster pentaradiatus*	*Discoaster petaliformis*	*Discoaster prepentaradiatus*	*Discoaster quinqueramus*	*Discoaster surculus*	*Discoaster tamalis*	*Discoaster tanii*	*Discoaster variabilis*	*Emiliania huxleyi*	*Florisphaera profunda*	*Gephyrocapsa caribbeanica*	*Gephyrocapsa margarelii*
early Miocene	NN2	CN1c	42X-CC, 24-31	405.71	A	M							R									C		A					C	F												C	R		
			43X-CC, 36-43	415.37	A	M							R									C		A					C	F												C	F		
			44X-CC, 38-45	425.29	A	M							F									C		A					C	F												C			
			45X-CC, 41-48	435.03	A	M							F									C		A					C	R												C	R		
			46X-CC, 42-49	444.10	A	M																C		A					C	R												C	F		
			47X-CC, 41-48	454.35	A	M																C		A					C	R												C			
			48X-CC, 20-27	462.60	A	M																C		A	R				C	R												C			
			49X-CC, 48-55	472.74	A	M															F	C		A	R	R			C	R															
			50X-CC, 34-41	477.34	A	M															F	F	R	A		F				R															
late Oligocene	NP24	CN19a	51X-CC, 30-37	480.72	A	M														R	F	C	R	A	F					F															
			52X-CC, 30-37	485.66	A	M															F	C	R	A	F					F															
			53X-CC, 30-37	490.94	A	M															R	C	R	A	C					F															
			54X-CC, 28-35	496.04	A	M															F	F		A	F					R															
			55X-CC, 15-22	500.91	A	M															F	C		A	C					C															
			56X-CC, 30-37	506.33	A	M																C		A	C					C															
			57X-CC, 34-41	522.08	A	M																C		A	R					C															
			58X-CC, 35-42	528.70	A	M																C		A	C					C															
			59X-CC, 29-37	540.34	A	M																C		A	C					C															
			60X-CC, 30-37	543.67	A	M																C		A	C					C															
			61X-CC, 29-36	553.79	A	M																C		A	C					C															
			62X-CC, 18-25	571.63	A	M																C	R	A	F					F															
			63X-CC, 29-36	578.06	A	M															F	C	R	A	F					R												R				
			64X-CC, 29-36	585.83	A	M															F	C	R	A	R					F												R				
			65X-CC, 27-34	593.63	A	M															F	C	R	A	C					F												F				
			66X-CC, 33-40	609.68	A	M																C		A	C					R												R				
			67X-CC, 30-37	620.00	A	M																C		A	C					R												R				
early Oligocene	NP23		68X-CC, 24-31	629.65	A	M																C		A	C					R															
			69X-CC, 36-43	639.27	A	M																C		A	C					R															
			70X-CC, 35-42	648.35	A	M																C		A	C					R															
		CP18	71X-CC, 37-43	658.54	A	M																C		A	C					R															
			72X-CC, 34-40	668.09	A	M																C		A	C					R															
			73X-CC, 28-38	677.03	A	M																C		A	C					R															
			74X-CC, 39-48	687.57	A	M																C		A	C					R															
		CP17	75X-CC, 33-40	696.94	A	M																C		A	C					R															
			76X-CC, 33-40	705.08	A	M																C		A	R					R															
			77X-CC, 32-39	716.39	A	M															R	C		C	R					F												R				
			184-1148B-																		F																									
			56X-CC, 31-37	851.35	C	M																C		A	C					R												R				

Table T8 (continued).

Age	Zone		Core, section, interval(cm)	Depth (mcd)	Abundance	Preservation	*Gephyrocapsa oceanica*	small *Gephyrocapsa* spp.	*Helicosphaera ampliaperta*	*Helicosphaera carteri*	*Helicosphaera euphratis*	*Helicosphaera granulata*	*Helicosphaera hyalina*	*Helicosphaera recta*	*Helicosphaera sellii*	*Oolithotus antillarum*	*Pontosphaera* spp.	*Pseudoemiliania lacunosa*	*Reticulofenestra asanoi*	*Reticulofenestra pseudoumbilicus*	*Reticulofenestra* spp. (small-medium)	*Rhabdosphaera clavigera*	*Scapholithus fossilis*	*Sphenolithus abies/neoabies*	*Sphenolithus belemnos*	*Sphenolithus ciperoensis*	*Sphenolithus compactus*	*Sphenolithus conicus*	*Sphenolithus delphix*	*Sphenolithus dissimilis*	*Sphenolithus distentus*	*Sphenolithus heteromorphus*	*Sphenolithus moriformis*	*Sphenolithus predistentus*	*Sphenolithus pseudoradians*	*Syracosphaera pulchra*	*Syracosphaera* spp.	*Thorosphaera flabellata*	*Triquetrorhabdulus carinatus*	*Triquetrorhabdulus rugosus*	*Umbellosphaera irregularis*	*Umbellosphaera tenuis*	*Umbilicosphaera sibogae*	*Zygrhablithus bijugatus*
			184-1148A-																																						
			1H-CC, 7-13	0.70	A	VG	C	C		C			R				R					R	R												F	R	R					C
Pleistocene	NN21b	CN15	2H-CC, 15-22	15.26	A	M	C	D		F							R					R												R		R					C
	NN21a		3H-CC, 6-13	24.74	A	G	A	A		F						F					C													C				R	R	C
	NN19b	CN14a	4H-CC, 30-37	34.35	A	M	A	A		C						R		C			F	R												C						C
			5H-CC, 0-6	43.66	A	M	A	A		F						F		C			F	R												F						F
			6H-CC, 22-29	54.50	A	M	A	C		F						R		C			R													F						F
			7H-CC, 0-10	64.57	A	M	C	A		F			R			F	R	C	R		F													F						F
			8H-CC, 13-18	74.86	A	M		C		F							R	C	F		F													F						
		CN13	9H-CC, 19-26	84.58	A	G	C	D		C			R			F	R	C			C	R												C				R		C
			10H-CC, 18-25	94.35	A	G	C	A		C						R	F	C			C	R												C						C
			11H-CC, 4-11	104.69	A	G	F	F		R						R		C			C	R												C						C
			12H-CC, 0-7	115.34	A	P	R	C		C								C			C	R												F						C
	NN19a		13H-CC, 9-16	125.76	A	M				C					R			C		C	C												F						F
			14H-CC, 0-8	135.48	A	M		C		F							R	C		A	F	R	R											F	R					F
late Pliocene	NN18	CN12d	15H-CC, 0-8	145.58	A	M				F							R	C		A	R												R		R				F
	NN17	CN12c	16H-CC, 0-8	155.43	C	P				F							R	C		A																			F
	NN16	CN12b	17X-CC, 31-38	165.32	A	M				F							R	F		A																				
		CN12a	18X-CC, 44-51	173.76	A	M				R							R	F	C	A	R		C													R					
early Pliocene	NN15	CN11	19X-CC, 21-27	184.52	A	M				R								R	C	A			A																	
	NN14-12	CN10	20X-CC, 0-7	193.82	A	M													C	A			A																	
late Miocene	NN11	CN9	21X-CC, 30-37	203.83	A	M													C	A			A															R		
			22X-CC, 26-33	213.48	A	G													C	A			A															R		
			23X-CC, 13-20	222.94	A	G													C	A			A															F		
			24X-CC, 41-48	231.84	A	G				C									C	A			A															F		
			25X-CC, 32-39	242.41	A	G				C									C	A			A															F		
	NN10	CN8	26X-CC, 40-47	251.11	A	G				F									C	A			A															F		
			27X-CC, 45-52	261.66	A	G													A	A			A															R		
	NN 9	CN7	28X-CC, 23-30	271.26	A	M				F									A	A			A															R		
			29X-CC, 26-33	279.46	A	M				F									A	C			C									F						F		
	NN 8	CN6	30X-CC, 29-36	290.43	A	M						R							C	A			C															F		F
	NN 7	CN5b	31X-CC, 40-47	300.04	A	M				F									C	A			C									R						F		C
middle Miocene	NN 6	CN5a	32X-CC, 16-26	309.48	A	M				C										A											A									C
	NN 5	CN 4	33X-CC, 21-31	319.22	A	M				C		R								A											A									C
			34X-CC, 30-37	328.96	A	P			R	F		F					R			A											A	C								C
			35X-CC, 14-21	338.47	A	P			R	C		F								A						F					A	F								C
			36X-CC, 35-42	348.28	A	M			R	F		F							F	A						C					A									C
	NN 4	CN 3	37X-CC, 19-26	357.74	C	P			R										C	C						C					C									C

Table T8 (continued).

Age	Zone		Core, section, interval(cm)	Depth (mcd)	Abundance	Preservation	*Gephyrocapsa oceanica*	small *Gephyrocapsa* spp.	*Helicosphaera ampliaperta*	*Helicosphaera carteri*	*Helicosphaera euphratis*	*Helicosphaera granulata*	*Helicosphaera hyalina*	*Helicosphaera recta*	*Helicosphaera sellii*	*Oolithotus antillarum*	*Pontosphaera* spp.	*Pseudoemiliania lacunosa*	*Reticulofenestra asanoi*	*Reticulofenestra pseudoumbilicus*	*Reticulofenestra* spp. (small-medium)	*Rhabdosphaera clavigera*	*Scapholithus fossilis*	*Sphenolithus abies/neoabies*	*Sphenolithus belemnos*	*Sphenolithus ciperoensis*	*Sphenolithus compactus*	*Sphenolithus conicus*	*Sphenolithus delphix*	*Sphenolithus dissimilis*	*Sphenolithus distentus*	*Sphenolithus heteromorphus*	*Sphenolithus moriformis*	*Sphenolithus predistentus*	*Sphenolithus pseudoradians*	*Syracosphaera pulchra*	*Syracosphaera* spp.	*Thorosphaera flabellata*	*Triquetrorhabdulus carinatus*	*Triquetrorhabdulus rugosus*	*Umbellosphaera irregularis*	*Umbellosphaera tenuis*	*Umbilicosphaera sibogae*	*Zygrhablithus bijugatus*
early-middle Miocene	NN 3	CN2	38X-CC, 32-39	367.35	A	M			R											A					F					A										C	
			39X-CC, 26-33	376.90	A	M			R										C	F				C	C															F	
early Miocene			40X-CC, 26-33	386.47	A	M			F	F									R	A				C	F																
			41X-CC, 40-47	396.38	A	M													R	A					C	C		C													
	NN2	CN1c	42X-CC, 24-31	405.71	A	M													R	A					C	C		C											F		
			43X-CC, 36-43	415.37	A	M				F									R	A						C		C											R		
			44X-CC, 38-45	425.29	A	M			R	F										A					C	C		C											R		
			45X-CC, 41-48	435.03	A	M				F										A						C		C											R		
early Miocene	NN2	CN1c	46X-CC, 42-49	444.10	A	M													R	A						C		C											R		
			47X-CC, 41-48	454.35	A	M														A						C		C											R		
			48X-CC, 20-27	462.60	A	M																		R		C						C							F		R
			49X-CC, 48-55	472.74	A	M																		R		C		R											F		R
			50X-CC, 34-41	477.34	A	M														F										F											F
late Oligocene	NP24	CN19a	51X-CC, 30-37	480.72	A	M														C					C					F		C								C
			52X-CC, 30-37	485.66	A	M								R						C					C					F		C									F
			53X-CC, 30-37	490.94	A	M					F			R						C					C					C		C									F
			54X-CC, 28-35	496.04	A	M					F									C					F					F		F									F
			55X-CC, 15-22	500.91	A	M					R									A					F					F		C	F								
			56X-CC, 30-37	506.33	A	M					R									A					R					F		C	F					F			R
			57X-CC, 34-41	522.08	A	M					F									A					R					F		C	F								R
			58X-CC, 35-42	528.70	A	M					F									A					R					F		C	F					F			R
			59X-CC, 29-37	540.34	A	M					F									A					R					F		C	F					F			R
			60X-CC, 30-37	543.67	A	M					F									A					R					F		C	F								R
			61X-CC, 29-36	553.79	A	M					F									A					R					F		C	F								
			62X-CC, 18-25	571.63	A	M					F			F						C					R					F		C	C	C							R
			63X-CC, 29-36	578.06	A	M					R			R						C					R					C		C	C	C							F
			64X-CC, 29-36	585.83	A	M					R			R						C					R					R		C	C	C							F
			65X-CC, 27-34	593.63	A	M				R	R			R						A					R					R		C	C	C							F
			66X-CC, 33-40	609.68	A	M					F			R						A					R					R		C	C	C		R					F
			67X-CC, 30-37	620.00	A	M				R	F			R						A										C		C	C	C							F
early Oligocene	NP23	CP18	68X-CC, 24-31	629.65	A	M				R	R			R						A										C		C	C	F							F
			69X-CC, 36-43	639.27	A	M														A										C		C	C	F		R					F
			70X-CC, 35-42	648.35	A	M				R				R						A										F		C	C	F							F
			71X-CC, 37-43	658.54	A	M				R	R									A										F		C	C	F							R
			72X-CC, 34-40	668.09	A	M				R										A										R		C	C	R							F
			73X-CC, 28-38	677.03	A	M				R	R			R						A												C	C	R							R
		CP17	74X-CC, 39-48	687.57	A	M				F	F			R						A												C	A	R							R
			75X-CC, 33-40	696.94	A	M				R	R			R						A												C	A	R							R
			76X-CC, 33-40	705.08	A	M				R	R			F						C												F	F								F
			77X-CC, 32-39	716.39	A	M				R	R			R						A												C	C								C

Table T8 (continued).

Age	Zone		Core, section, interval(cm)	Depth (mcd)	Abundance	Preservation	*Gephyrocapsa oceanica*	small *Gephyrocapsa* spp.	*Helicosphaera ampliaperta*	*Helicosphaera carteri*	*Helicosphaera euphratis*	*Helicosphaera granulata*	*Helicosphaera hyalina*	*Helicosphaera recta*	*Helicosphaera sellii*	*Oolithotus antillarum*	*Pontosphaera* spp.	*Pseudoemiliania lacunosa*	*Reticulofenestra asanoi*	*Reticulofenestra pseudoumbilicus*	*Reticulofenestra* spp. (small-medium)	*Rhabdosphaera clavigera*	*Scapholithus fossilis*	*Sphenolithus abies/neoabies*	*Sphenolithus belemnos*	*Sphenolithus ciperoensis*	*Sphenolithus compactus*	*Sphenolithus conicus*	*Sphenolithus delphix*	*Sphenolithus dissimilis*	*Sphenolithus distentus*	*Sphenolithus heteromorphus*	*Sphenolithus moriformis*	*Sphenolithus predistentus*	*Sphenolithus pseudoradians*	*Syracosphaera pulchra*	*Syracosphaera* spp.	*Thorosphaera flabellata*	*Triquetrorhabdulus carinatus*	*Triquetrorhabdulus rugosus*	*Umbellosphaera irregularis*	*Umbellosphaera tenuis*	*Umbilicosphaera sibogae*	*Zygrhablithus bijugatus*
			184-1148B- 56X-CC, 31-37	851.35	C	M					F C		F								C										C	C								

Notes: D = dominant, A = abundant, C = common, F = few/frequent, R = rare, VG = very good, G = good, M = moderate, P = poor. See **"Biostratigraphy,"** p. 9, in the "Explanatory Notes" chapter.

Table T9. Planktonic foraminifer checklist for Site 1148. (**See table notes.** Continued on next two pages.)

Age	Zone	Core, section, interval (cm)	Depth (mcd)	Abundance	Preservation	*Cassigerinella chipolensis*	*Catapsydrax dissimilis*	*Catapsydrax unicavus*	*Chiloguembelina cubensis*	*Dentoglobigerina altispira*	*Globigerina angulisuturalis*	*Globigerina ciperoensis*	*Globigerinatella insueta*	*Globigerinoides altiapertura*	*Globigerinoides conglobatus*	*Globigerinoides extremus*	*Globigerinoides fistulosus*	*Globigerinoides obliquus*	*Globigerinoides ruber*	*Globigerinoides ruber* (pink)	*Globigerinoides sacculifer*	*Globigerinoides trilobus*	*Globoquadrina binaiensis*	*Globoquadrina dehiscens*	*Globoquadrina tripartita*	*Globorotalia crassaformis*	*Globorotalia inflata*	*Globorotalia margaritae*	*Globorotalia menardii*	*Globorotalia multicamerata*	*Globorotalia peripheroacuta*	*Globorotalia peripheroronda*	*Globorotalia plesiotumida*	*Globorotalia praescitula*	*Globorotalia tosaensis*	*Globorotalia truncatulinoides*	*Globorotalia tumida*	*Jenkinsella siakensis*	*Neogloboquadrina acostaensis*	*Neogloboquadrina dutertrei*	*Orbulina suturalis*	*Orbulina universa*	*Paragloborotalia kugleri*	*Paragloborotalia mayeri*	*Paragloborotalia opima nana*	*Paragloborotalia opima opima*	*Paragloborotalia pseudokugleri*	*Praeorbulina glomerosa*	*Praeorbulina sicana*	*Pulleniatina* (sinistral)	*Pulleniatina obliquiloculata*	*Pulleniatina primalis*	*Sphaeroidinella dehiscens*	*Sphaeroidinellopsis kochi*	*Sphaeroidinellopsis seminulina*	*Subbotina gortanii*	*Turborotalia ampliapertura*	*Globoturborotalita*
Pleistocene	N22	184-1148A-																																																								
		1H-CC, 7-13	0.70	A	M														A								F		F							P				A											F							
		2H-CC, 15-22	15.26	A	M														A	F							F		F							R				A											F							
		3H-CC, 6-13	24.74	A	M														A	P							F		F							R				A											F							
		4H-CC, 30-37	34.35	A	M														A								F		R											A											F							
		5H-CC, 0-6	43.66	A	M														A								F		P											A											F							
		6H-CC, 22-29	54.50	A	M														A							R	F									P				A											F							
		7H-CC, 0-10	64.57	A	M														A								A		R							R				A																		
		8H-CC, 13-18	74.85	A	M														A								P		R							R				A											F							
		9H-CC, 19-26	84.58	A	M														A								F									P				A											F		R					
		10H-CC, 18-25	94.35	A	M														A								F									R	R			F											P		R					
		11H-CC, 4-11	104.69	A	M																								F							P															A		F					
		12H-CC, 0-7	115.34	A	M														F										R							P				A											A		F					
late Pliocene		13H-CC, 9-16	125.76	A	M												P										R		R							P															F		A					
	N21	14H-CC, 0-8	135.48	A	M																						R			P							F														P		A					
		15H-CC, 0-8	145.58	A	M												P		A											R							F																A					
		16H-CC, 0-8	155.43	A	M																									P					P		F																A					
early Pliocene	N20	17X-CC, 31-38	165.32	A	M					P																				P							R																F		R			
	N19	18X-CC, 44-51	173.76	A	P					R					P	R														P							F													P			R		F			
		19X-CC, 21-27	184.52	A	G																																R																P	P	F			P
late Miocene	N18	20X-CC, 0-7	193.82	A	G																																P																P	P	A			R
	N17b	21X-CC, 30-37	203.83	A	M										P																								P															P	A			R
		22X-CC, 26-33	213.48	A	G										P	P																							R																A			R
	N17a	23X-CC, 13-20	222.94	A	M																																		R																A			
		24X-CC, 41-48	231.84	A	M											P																							R																			R
		25X-CC, 32-39	242.41	A	M													R																					P																A			A
		26X-CC, 40-47	251.11	A	M											P		A															P						P																			P
		27X-CC, 45-52	261.66	A	M													R															P																						A			F
	N16-15	28X-CC, 23-30	271.26	A	M													R			A																					F																R
	N14	29X-CC, 26-33	279.46	A	G																																	R				R		F														P
middle Miocene	N13	30X-CC, 29-36	290.43	A	G																																	R						R														
		31X-CC, 40-47	300.04	A	M																																	F				R		R														
	N10	32X-CC, 16-26	309.48	A	M																										R	P									P	R																
	N8	33X-CC, 21-31	319.22	A	M					A																						R						F						R														
		34X-CC, 30-37	328.96	A	G																											R												F				P	P									
		35X-CC, 14-21	338.47	A	G								P						A													P		P															P									
		36X-CC, 35-42	348.28	A	G								P																			P		R														P	P									
early Miocene	N7	37X-CC, 19-26	357.74	A	M								P																			P												R														
		38X-CC, 32-39	367.35	A	M																											P		P				R																				
	N6	39X-CC, 26-33	376.90	A	G		P																P									P		P				R						R														
	N5	40X-CC, 26-33	386.47	A	G		P	R																R																				R														

Table T9 (continued).

Age	Zone	Core, section, interval (cm)	Depth (mcd)	Abundance	Preservation	*Cassigerinella chipolensis*	*Catapsydrax dissimilis*	*Catapsydrax unicavus*	*Chiloguembelina cubensis*	*Dentoglobigerina altispira*	*Globigerina angulisuturalis*	*Globigerina ciperoensis*	*Globigerinatella insueta*	*Globigerinoides altiapertura*	*Globigerinoides conglobatus*	*Globigerinoides extremus*	*Globigerinoides fistulosus*	*Globigerinoides obliquus*	*Globigerinoides ruber*	*Globigerinoides ruber* (pink)	*Globigerinoides sacculifer*	*Globigerinoides trilobus*	*Globoquadrina binaiensis*	*Globoquadrina dehiscens*	*Globoquadrina tripartita*	*Globorotalia crassaformis*	*Globorotalia inflata*	*Globorotalia margaritae*	*Globorotalia menardii*	*Globorotalia multicamerata*	*Globorotalia peripheroacuta*	*Globorotalia peripheroronda*	*Globorotalia plesiotumida*	*Globorotalia praescitula*	*Globorotalia tosaensis*	*Globorotalia truncatulinoides*	*Globorotalia tumida*	*Jenkinsella siakensis*	*Neogloboquadrina acostaensis*	*Neogloboquadrina dutertrei*	*Orbulina suturalis*	*Orbulina universa*	*Paragloborotalia kugleri*	*Paragloborotalia mayeri*	*Paragloborotalia opima nana*	*Paragloborotalia opima opima*	*Paragloborotalia pseudokugleri*	*Praeorbulina glomerosa*	*Praeorbulina sicana*	*Pulleniatina* (sinistral)	*Pulleniatina obliquiloculata*	*Pulleniatina primalis*	*Sphaeroidinella dehiscens*	*Sphaeroidinellopsis kochi*	*Sphaeroidinellopsis seminulina*	*Subbotina gortanii*	*Turborotalia ampliapertura*	*Globoturborotalita*
		41X-CC, 40-47	396.38	A	M		F	P																																				R														
		42X-CC, 24-31	405.71	A	G		F	P						P									P															P						R														
early Miocene	N4	43X-CC, 36-43	415.37	A	M		R																															P					R				P											
		44X-CC, 38-45	425.29	A	M		R	P																P																			R				P											
		45X-CC, 41-48	435.03	A	M		R																															P					R				P											
		46X-CC, 42-49	444.10	A	M		R	P																P																			R				P											
		47X-CC, 41-48	454.35	A	M					R													P	P																			F				R											
late Oligocene		48X-CC, 20-27	462.60	A	G		P			P														P																							R											
		49X-CC, 48-55	472.74	A	M																	P		R																							F											
	P21b	50X-CC, 34-41	477.34	A	P		P					R																																	P		R											
		51X-CC, 30-37	480.72	A	P		P				P												P																						R		R											
early Oligocene		52X-CC, 30-37	485.66	A	P																																									A												
	P21a	53X-CC, 30-37	490.94	A	P																																									A												
		54X-CC, 28-35	496.04	A	P																																									A												
		55X-CC, 15-22	500.91	A	M				F			P																																		A										A		
		56X-CC, 30-37	506.33	A	P				F			R																																		A										R		
		57X-CC, 34-41	522.08	A	P				R			P																																		A												
		58X-CC, 35-42	528.70	A	M				A		P	P																																		R										R		
		59X-CC, 29-37	540.34	A	G																																									R										R		
		60X-CC, 30-37	543.67	A	G						P																																			R										R		
		61X-CC, 29-36	553.79	A	P																																									A												
		62X-CC, 18-25	571.63	A	M				F		R																																			F										R		
		63X-CC, 29-36	578.06	A	P				F		R																																													P		
		64X-CC, 29-36	585.83	A	P				R		A																																			P										R		
		65X-CC, 27-34	593.63	A	M				R		P	P																																		A												
	P20	66X-CC, 33-40	609.68	A	P						R	P																																		P										P		
		67X-CC, 30-37	620.00	A	M				F		P	P																																		P												
		68X-CC, 24-31	629.65	A	P	P			F			R																																		R												
		69X-CC, 36-43	639.27	A	P							R																																		R												
	P19	70X-CC, 35-42	648.35	A	M				R			P																																		P												
		71X-CC, 37-43	658.54	A	M				R			P																																		F											P	
		72X-CC, 34-40	668.09	A	M							P																																		P												
		73X-CC, 28-38	677.03	A	G				F																																					P												
		74X-CC, 39-48	687.57	A	G				R			P																																	F												P	
		75X-CC, 33-40	696.94	A	G							R																																	P												P	
		76X-CC, 33-40	705.08	A	G							P																																	P												P	
		77X-CC, 32-39	716.39	A	M	R			F																R																				P											R	P	

Table T9 (continued).

Age	Zone	Core, section, interval (cm)	Depth (mcd)	Abundance	Preservation	*Cassigerinella chipolensis*	*Catapsydrax dissimilis*	*Catapsydrax unicavus*	*Chiloguembelina cubensis*	*Dentoglobigerina altispira*	*Globigerina angulisuturalis*	*Globigerina ciperoensis*	*Globigerinatella insueta*	*Globigerinoides altiapertura*	*Globigerinoides conglobatus*	*Globigerinoides extremus*	*Globigerinoides fistulosus*	*Globigerinoides obliquus*	*Globigerinoides ruber*	*Globigerinoides ruber* (pink)	*Globigerinoides sacculifer*	*Globigerinoides trilobus*	*Globoquadrina binaiensis*	*Globoquadrina dehiscens*	*Globoquadrina tripartita*	*Globorotalia crassaformis*	*Globorotalia inflata*	*Globorotalia margaritae*	*Globorotalia menardii*	*Globorotalia multicamerata*	*Globorotalia peripheroacuta*	*Globorotalia peripheroronda*	*Globorotalia plesiotumida*	*Globorotalia praescitula*	*Globorotalia tosaensis*	*Globorotalia truncatulinoides*	*Globorotalia tumida*	*Jenkinsella siakensis*	*Neogloboquadrina acostaensis*	*Neogloboquadrina dutertrei*	*Orbulina suturalis*	*Orbulina universa*	*Paragloborotalia kugleri*	*Paragloborotalia mayeri*	*Paragloborotalia opima nana*	*Paragloborotalia opima opima*	*Paragloborotalia pseudokugleri*	*Praeorbulina glomerosa*	*Praeorbulina sicana*	*Pulleniatina* (sinistral)	*Pulleniatina obliquiloculata*	*Pulleniatina primalis*	*Sphaeroidinella dehiscens*	*Sphaeroidinellopsis kochi*	*Sphaeroidinellopsis seminulina*	*Subbotina gortanii*	*Turborotalia ampliapertura*	*Globoturborotalita*
		184-1148B- 56X-CC, 31-37	851.35 609.68	A	G	R			R																																				P												P	

Notes: A = abundant, F = few/frequent, R = rare, G = good, M = moderate, P = poor. See **"Biostratigraphy,"** p. 9, in the "Explanatory Notes" chapter.

Table T10. Age-depth relationship derived from the magnetic polarity time scale, Site 1148.

Polarity event	Age (Ma)	Depth (mcd)	
		Hole 1148A	Hole 1148B
Brunhes/Matuyama	0.78	55.2	55.1
upper Jaramillo	0.99	69.1	
lower Jaramillo	1.07	73.0	
upper Olduvai	1.77	111.4	
lower Olduvai	1.95	118.5	

Table T11. Sedimentation and accumulation rates for selected intervals, based on age-depth model and rates presented in Figure F18, p. 64.

	Bottom of interval					
	Age (Ma)	Depth (mcd)	LSR total (m/m.y.)	LSR carbonate (m/m.y.)	MAR total ($g/cm^2/k.y.$)	MAR carbonate ($g/cm^2/k.y.$)
Brunhes/Matuyama	0.78	55.20				
Pleistocene/Pliocene	1.77	110.28	63	6.0	5.4	0.52
Pliocene/Miocene	5.32	190.32	27	4.5	3.2	0.54
upper/middle Miocene	11.2	284.11	16	5.3	2.2	0.72
middle/lower Miocene	16.4	339.73	11	3.6	1.6	0.52
Hiatus top	24.5	472.82	17	6.9	2.6	1.09
Hiatus bottom	27.5	480.29	3	1.7	0.5	0.28
upper/lower Oligocene	28.5	529.44	55	17.0	7.8	2.40
Bottom of hole	33.2	851.40	68	22.4	18.8	3.60

Note: LSR = linear sedimentation rate for total sediment and inorganic carbonate, MAR = mass accumulation rate for total sediment and inorganic carbonate.

Table T12. Methane, ethane, ethene, propane, butane, and pentane concentrations obtained by headspace analysis, Hole 1148A. (**See table note.** Continued on next page.) **[N1]**

Core, section, interval (cm)	Depth (mbsf)	Depth (mcd)	C_1/C_2	C_1 (ppmv)	C_2 (ppmv)	C_2= (ppmv)	C_3 (ppmv)	I-C_4 (ppmv)	N-C_4 (ppmv)	I-C_5 (ppmv)	N-C_5 (ppmv)
184-1148A-											
2H-4, 0-5	5.30	10.15	—	3.4							
3H-4, 0-5	14.73	19.58	—	4.7							
4H-4, 0-5	24.30	29.15	—	4.0							
5H-4, 0-5	33.80	38.65	—	3.8							
6H-4, 0-5	43.30	49.10	—	3.7							
7H-4, 0-5	52.80	59.70	—	4.4							
8H-4, 0-5	62.30	69.67	—	3.8							
9H-4, 0-5	71.80	79.47	—	3.3							
10H-4, 0-5	81.30	88.97	—	3.3							
11H-4, 0-5	90.80	99.52	—	3.2							
12H-4, 0-5	100.30	109.97	—	3.8							
13H-4, 0-5	109.80	120.90	—	4.5							
14H-4, 0-5	119.30	130.85	—	4.8							
15H-4, 0-5	128.80	140.80	—	5.4							
16H-4, 0-5	138.30	150.52	—	7.7							
17X-4, 0-5	147.80	160.02	—	7.0							
18X-4, 0-5	157.40	169.62	—	11.0							
19X-4, 0-5	167.00	179.22	—	6.7							
20X-4, 0-5	176.60	188.82	—	7.8							
21X-4, 0-5	186.30	198.52	—	8.2							
22X-4, 0-5	196.00	208.22	—	9.4							
23X-4, 0-5	205.60	217.82	—	7.1							
24X-4, 0-5	215.30	227.52	—	6.6							
25X-4, 0-5	224.90	237.12	—	7.0							
26X-4, 0-5	234.50	246.72	—	7.5							
27X-4, 0-5	244.10	256.32	—	7.5							
28X-4, 0-5	253.70	265.92	—	8.3							
29X-4, 0-5	263.30	275.52	—	8.6							
30X-4, 0-5	272.90	285.12	—	8.5							
31X-4, 0-5	282.50	294.72	—	7.0							
32X-4, 0-5	292.10	304.32	—	9.1							
33X-4, 0-5	301.80	314.02	—	11.6							
34X-4, 0-5	310.09	322.31	—	10.3							
35X-4, 0-5	321.10	333.32	—	9.0							
36X-4, 0-5	330.70	342.92	—	9.4							
37X-4, 0-5	340.30	352.52	—	12.9							
38X-4, 0-5	349.80	362.02	—	8.4							
39X-4, 0-5	359.40	371.62	—	6.4							
40X-2, 0-5	366.00	378.22	—	7.5							
40X-4, 0-5	369.00	381.22	—	6.3							
41X-4, 0-5	378.70	390.92	—	5.5							
42X-4, 0-5	388.40	400.62	—	4.0							
43X-4, 0-5	398.00	410.22	—	4.9							
44X-4, 0-5	407.70	419.92	—	5.4							
45X-4, 0-5	417.40	429.62	—	8.0							
46X-4, 0-5	427.00	439.22	—	8.8							
47X-4, 0-5	436.70	448.92	—	14.1							
48X-4, 0-5	446.30	458.52	—	16.2							
49X-4, 0-5	455.90	468.12	—	25.7							
50X-2, 0-5	462.50	474.72	—	53.3							
51X-1, 11-16	468.11	480.33	99.0	47.5	0.5	0.2					
52X-CC, 0-5	473.10	485.32	30.9	24.7	0.8	0.5					
53X-CC, 0-5	478.38	490.60	32.3	25.8	0.8	0.2					
54X-1, 0-5	482.70	494.92	20.8	31.2	1.5	0.7	0.5				
55X-1, 0-5	487.30	499.52	14.9	25.3	1.7	0.4					
56X-1, 0-5	492.30	504.52	14.5	29.0	2.0	0.3	0.2				
57X-4, 0-5	506.20	518.42	16.4	101.8	6.2	0.4	2.1				
58X-3, 0-5	513.90	526.12	18.0	102.8	5.7	0.3	2.0				
58X-3, 5-6	513.95	526.12	19.9	139.1	7.0	0.2	2.0				
59X-4, 0-5	525.50	537.72	22.9	213.0	9.3	0.3	3.5				
60X-CC, 25-30	531.36	543.58	21.9	262.9	12.0	0.5	5.7				
61X-CC, 24-49	541.48	553.70	23.9	339.2	14.2	0.5	6.8				
62X-4, 0-5	554.40	566.62	26.4	200.7	7.6	0.2	3.2				
63X-3, 0-5	562.20	574.42	23.6	63.7	2.7		1.4				
64X-2, 0-5	570.60	582.82	23.6	520.9	22.1		10.2				
65X-2, 0-5	580.30	592.52	22.9	568.6	24.8	0.2	9.6				

Table T12 (continued).

Core, section, interval (cm)	Depth (mbsf)	Depth (mcd)	C_1/C_2	C_1 (ppmv)	C_2 (ppmv)	C_2= (ppmv)	C_3 (ppmv)	I-C_4 (ppmv)	N-C_4 (ppmv)	I-C_5 (ppmv)	N-C_5 (ppmv)
66X-4, 0-5	592.90	605.12	22.1	471.4	21.3		8.6				
67X-4, 0-5	602.50	614.72	22.4	290.6	13.0		5.7				
68X-8, 66-71	617.10	629.32	18.5	420.2	22.7	0.2	9.5				
69X-4, 0-5	621.70	633.92	20.9	288.4	13.8		5.5				
70X-4, 0-5	631.30	643.52	18.8	274.6	14.6		6.3				
71X-4, 0-5	641.00	653.22	18.0	269.4	15.0	0.2	7.2				
72X-4, 0-5	650.70	662.92	17.1	331.5	19.4		8.8				
73X-4, 0-5	660.40	672.62	17.0	303.7	17.9	0.2	8.1				
74X-4, 0-5	670.00	682.22	16.8	300.6	17.9		8.6				
75X-4, 0-5	679.01	691.23	16.4	213.0	13.0		6.3	11.2		19.6	7.5
76X-4, 0-5	689.09	701.31	16.3	221.6	13.6		7.0			18.3	7.5
77X-4, 0-5	698.90	711.12	15.7	327.0	20.9	0.2	10.6	16.8	11.6	25.2	6.7

Note: — = no C_2.

Table T13. Methane, ethane, ethene, propane, butane, and pentane concentrations obtained by headspace analysis, Hole 1148B.

Core, section, interval (cm)	Depth (mbsf)	Depth (mcd)	C_1/C_2	C_1 (ppmv)	C_2 (ppmv)	$C_{2=}$ (ppmv)	C_3 (ppmv)	I-C_4 (ppmv)	N-C_4 (ppmv)	I-C_5 (ppmv)	N-C_5 (ppmv)	I-C_6 (ppmv)	N-C_6 (ppmv)
184-1148B-													
34X-4, 0-5	607.90	614.15	21.4	307.4	14.4		6.3						
35X-4, 0-5	617.50	623.75	21.6	170.6	7.9		3.2						
36X-4, 0-5	627.10	633.35	19.4	102.1	5.3		2.1				7.7		
36X-CC, 38-43	631.60	637.85	20.1	198.8	9.9	0.2	4.1						
37X-4, 0-5	636.70	642.95	20.1	282.8	14.1		0.4						
37X-CC, 26-31	640.97	647.22	7.5	145.5	19.4		3.6				7.3		
38X-CC, 25-30	645.94	652.19	18.2	272.5	15.0		7.0						
39X-CC, 27-29	709.49	715.74	16.3	125.9	7.7	0.1	4.0			5.8	11.5		
40X-CC, 29-31	719.17	725.42	17.3	53.6	3.1		1.5				6.8		
41X-CC, 37-39	727.74	733.99	15.6	101.9	6.6	0.1	3.7	6.7	9.4	6.5	16.5	5.4	6.4
42X-CC, 33-35	738.38	744.63	6.1	190.3	31.1	0.2	9.8	19.1	16.8	16.7	42.8		11.0
43X-CC, 0-5	747.72	753.97	5.0	166.5	33.1	0.1	8.3	26.0	18.6	22.5	49.5	8.0	11.3
44X-CC, 0-5	757.28	763.53	4.0	94.3	23.5	0.2	3.7	16.6	13.2	9.5	25.5		
45X-CC, 0-5	763.92	770.17	4.3	70.4	16.5		2.7	10.6	7.1	7.4	17.5		4.9
46X-CC, 0-5	773.72	779.97	4.3	105.2	24.3		5.0	14.3	13.7	11.7	27.4	3.2	5.0
47X-CC, 33-34	782.30	788.55	11.7	88.7	7.6		5.1	10.4	9.3	7.7	19.7	10.4	7.7
48X-CC, 24-25	787.53	793.78	4.9	82.7	17.0		5.3	10.5	13.9	8.2	26.7		
49X-CC, 34-35	798.65	804.90	10.5	87.3	8.3	0.1	9.4	11.2	11.3	12.0	33.0	13.7	10.6
50X-CC, 23-24	808.81	815.06	17.8	65.9	3.7		3.2	6.0		5.4	12.3		
51X-CC, 25-27	811.85	818.10	13.8	76.6	5.6		3.3	7.2			13.2		
52X-CC, 31-32	815.94	822.19	14.1	76.4	5.4		4.5			6.9	14.5		
53X-CC, 22-23	820.54	826.79	12.5	108.5	8.7		5.9	6.6	4.8	5.1	11.8		
54X-CC, 0-5	824.62	830.87	12.7	91.7	7.2	0.1	5.8	7.6	8.5	9.7	22.5		12.7
55X-CC, 0-5	835.39	841.64	11.4	77.9	6.8	0.1	5.7	8.7	5.3	7.5	18.0	9.4	8.6
56X-CC, 30-31	845.06	851.31	18.1	38.1	2.1	0.1	4.0			7.9	13.4		11.2

Table T14. Inorganic carbon, carbonate, total carbon, total organic carbon, total nitrogen, and total sulfur contents at Site 1148. (See table note. Continued on next two pages.)

Core, section, interval (cm)	Depth (mbsf)	Depth (mcd)	IC (wt%)	$CaCO_3$ (wt%)	TC (wt%)	TOC (wt%)	TN (wt%)	TS (wt%)	C/N	S/C
184-1148A-										
2H-2, 107-108	3.37	8.22	0.45	3.78						
2H-4, 107-108	6.37	11.22	0.64	5.36	1.22	0.58	0.14	0.21	4.1	0.4
2H-6, 107-108	9.37	14.22	1.15	9.62						
3H-2, 107-108	12.80	17.65	0.92	7.64						
3H-4, 107-108	15.80	20.65	1.17	9.75	1.74	0.57	0.10	0.39	5.7	0.7
3H-6, 107-108	18.80	23.65	1.19	9.88						
4H-2, 107-108	22.37	27.22	2.02	16.80						
4H-4, 107-108	25.37	30.22	2.10	17.46	2.89	0.79	0.18	0.34	4.4	0.4
4H-6, 107-108	28.37	33.22	1.70	14.12						
5H-2, 107-108	31.87	36.72	2.00	16.63						
5H-4, 107-108	34.87	39.72	1.94	16.15	2.37	0.43	0.14	0.25	3.1	0.6
5H-6, 107-108	37.87	42.72	1.59	13.26						
6H-2, 107-108	41.37	47.17	0.15	1.23						
6H-4, 107-108	44.37	50.17	0.95	7.92	1.39	0.44	0.09	0.13	4.9	0.3
6H-6, 107-108	47.37	53.17	0.80	6.70						
7H-2, 107-108	50.87	57.77	1.27	10.59						
7H-4, 107-108	53.87	60.77	1.22	10.20	1.65	0.43	0.13	0.41	3.3	1.0
7H-6, 107-108	56.87	63.77	1.91	15.92						
8H-2, 107-108	60.37	67.74	0.22	1.80						
8H-4, 107-108	63.37	70.74	1.17	9.72	1.57	0.40	0.11	0.12	3.7	0.3
8H-6, 107-108	66.37	73.74	1.66	13.86						
9H-2, 107-108	69.87	77.54	0.34	2.84						
9H-4, 107-108	72.87	80.54	0.98	8.19	1.29	0.31	0.07	0.00	4.4	
9H-6, 107-108	75.67	83.34	0.71	5.94						
10H-2, 107-108	79.37	87.04	2.14	17.83						
10H-4, 107-108	82.37	90.04	1.05	8.74	1.49	0.44	0.13	0.23	3.4	0.5
10H-6, 107-108	85.37	93.04	0.54	4.51						
11H-2, 107-108	88.87	97.59	1.32	11.02						
11H-4, 107-108	91.87	100.59	0.60	4.98	0.87	0.27	0.10	0.15	2.7	0.6
11H-7, 107-108	95.64	104.36	0.25	2.07						
12H-2, 107-108	98.37	108.04	0.83	6.92						
12H-4, 107-108	101.37	111.04	1.80	14.98	2.00	0.20	0.11	0.00	1.8	
12H-6, 107-108	104.40	114.07	1.48	12.30						
13H-2, 107-108	107.87	118.97	2.15	17.90						
13H-4, 107-108	110.87	121.97	2.07	17.21	2.27	0.20	0.11	0.03	1.9	0.1
13H-6, 107-108	113.62	124.72	2.31	19.23						
14H-2, 107-108	117.37	128.92	2.22	18.52						
14H-4, 107-108	120.37	131.92	2.38	19.86	2.53	0.15	0.12	0.03	1.2	0.2
14H-6, 107-108	123.37	134.92	0.88	7.33						
15H-2, 107-108	126.87	138.87	1.67	13.87						
15H-4, 107-108	129.87	141.87	2.50	20.80	2.62	0.12	0.07	0.00	1.8	
15H-6, 107-108	132.87	144.87	1.95	16.28						
16H-2, 107-108	136.37	148.59	2.47	20.58						
16H-4, 107-108	139.37	151.59	3.21	26.72	3.29	0.08	0.07	0.12	1.2	1.5
16H-6, 107-108	142.37	154.59	2.60	21.67						
17X-2, 107-108	145.87	158.09	1.24	10.33						
17X-4, 107-108	148.87	161.09	2.57	21.41	2.67	0.10	0.07	0.08	1.4	0.8
17X-6, 107-108	151.87	164.09	1.97	16.42						
18X-2, 107-108	155.47	167.69	1.51	12.56						
18X-4, 107-108	158.47	170.69	2.64	21.96	2.74	0.10	0.10	0.02	1.0	0.2
18X-6, 57-58	160.97	173.19	1.98	16.52						
19X-2, 107-108	165.07	177.29	1.24	10.32						
19X-4, 107-108	168.07	180.29	1.29	10.77	1.43	0.14	0.06	0.08	2.3	0.6
19X-6, 107-108	171.07	183.29	3.08	25.67						
20X-2, 107-108	174.67	186.89	3.10	25.83						
20X-4, 107-108	177.67	189.89	2.82	23.47	2.97	0.15	0.10	0.00	1.5	
20X-6, 107-108	180.67	192.89	3.67	30.61						
21X-2, 107-108	184.37	196.59	2.93	24.37						
21X-4, 107-108	187.37	199.59	4.53	37.75	4.48	0.00	0.05	0.00	0.0	
21X-6, 107-108	190.37	202.59	4.91	40.88						
22X-2, 107-108	194.07	206.29	5.36	44.68						
22X-4, 107-108	197.07	209.29	3.93	32.76	3.90	0.00	0.09	0.00	0.0	
22X-6, 107-108	200.07	212.29	4.21	35.03						
23X-2, 107-108	203.67	215.89	4.01	33.42						
23X-4, 107-108	206.67	218.89	4.12	34.34	4.16	0.04	0.11	0.04	0.3	1.1
23X-6, 107-108	209.67	221.89	4.76	39.63						

Table T14 (continued).

Core, section, interval (cm)	Depth (mbsf)	Depth (mcd)	IC (wt%)	$CaCO_3$ (wt%)	TC (wt%)	TOC (wt%)	TN (wt%)	TS (wt%)	C/N	S/C
24X-2, 107-108	213.37	225.59	4.58	38.13						
24X-4, 107-108	216.37	228.59	5.62	46.84	5.73	0.11	0.04	0.01	2.8	0.1
25X-2, 107-108	222.97	235.19	5.33	44.37						
25X-4, 107-108	225.97	238.19	5.56	46.29	5.63	0.08	0.04	0.01	1.9	0.1
25X-6, 107-108	228.97	241.19	4.45	37.05						
26X-2, 107-108	232.57	244.79	3.04	25.36						
26X-4, 107-108	235.57	247.79	3.75	31.21	3.90	0.16	0.04	0.00	3.5	
27X-2, 107-108	242.17	254.39	3.55	29.57						
27X-4, 107-108	245.17	257.39	4.91	40.93	5.01	0.10	0.04	0.00	2.4	
27X-6, 107-108	248.17	260.39	4.12	34.32						
28X-2, 107-108	251.77	263.99	4.63	38.59						
28X-4, 107-108	254.77	266.99	1.79	14.95	1.91	0.12	0.09	0.00	1.2	
28X-6, 107-108	257.77	269.99	4.12	34.34						
29X-2, 107-108	261.37	273.59	4.15	34.56						
29X-4, 107-108	264.37	276.59	3.07	25.61	3.21	0.14	0.11	0.00	1.3	
30X-2, 107-108	270.97	283.19	2.24	18.69						
30X-4, 107-108	273.97	286.19	1.56	13.02	1.63	0.06	0.11	0.00	0.6	
30X-6, 107-108	276.97	289.19	3.37	28.11						
31X-2, 107-108	280.57	292.79	3.11	25.94						
31X-4, 107-108	283.57	295.79	4.14	34.48	4.17	0.03	0.09	0.00	0.3	
31X-6, 107-108	286.57	298.79	4.94	41.13						
32X-2, 120-121	290.30	302.52	5.22	43.48						
32X-4, 107-108	293.17	305.39	5.00	41.64	5.07	0.07	0.10	0.00	0.7	
32X-6, 107-108	296.17	308.39	3.43	28.54						
33X-2, 107-108	299.87	312.09	3.99	33.28						
33X-4, 107-108	302.87	315.09	5.26	43.81	5.33	0.07	0.03	0.01	1.9	0.1
33X-6, 107-108	305.87	318.09	1.72	14.30						
34X-2, 107-108	308.16	320.38	4.16	34.63						
34X-4, 107-108	311.16	323.38	3.47	28.94	3.49	0.02	0.07	0.00	0.3	
34X-6, 107-108	314.16	326.38	3.78	31.46						
35X-2, 107-108	319.17	331.39	4.11	34.23						
35X-4, 107-108	322.17	334.39	4.75	39.58	4.78	0.03	0.04	0.00	0.7	
35X-6, 107-108	325.17	337.39	4.06	33.81						
36X-2, 107-108	328.77	340.99	3.27	27.24						
36X-4, 107-108	331.77	343.99	4.78	39.83	4.84	0.06	0.03	0.00	1.7	
36X-6, 107-108	334.77	346.99	4.14	34.45						
37X-2, 107-108	338.37	350.59	5.33	44.37						
37X-4, 93-94	341.23	353.45	3.98	33.17	4.00	0.02	0.09	0.00	0.2	
37X-6, 115-116	344.46	356.68	3.44	28.67						
38X-2, 91-92	347.71	359.93	4.15	34.59						
38X-4, 111-112	350.91	363.13	3.62	30.17	3.63	0.01	0.04	0.00	0.3	
38X-6, 107-108	353.87	366.09	5.78	48.18						
39X-2, 109-110	357.49	369.71	3.78	31.46						
39X-4, 109-110	360.49	372.71	4.26	35.45	4.26	0.01	0.09	0.00	0.1	
39X-6, 110-111	363.50	375.72	3.32	27.69						
40X-2, 106-107	367.06	379.28	5.25	43.76						
40X-4, 104-105	370.04	382.26	3.90	32.51	4.00	0.10	0.03	0.00	2.8	
40X-6, 117-118	373.17	385.39	4.32	35.98						
41X-2, 107-108	376.77	388.99	3.60	29.98						
41X-4, 107-108	379.77	391.99	5.35	44.58	5.37	0.02	0.03	0.00	0.7	
41X-6, 105-106	382.75	394.97	4.90	40.78						
42X-2, 106-107	386.46	398.68	4.72	39.33						
42X-4, 118-119	389.58	401.80	4.44	36.97	4.56	0.12	0.03	0.00	3.8	
42X-6, 119-120	392.59	404.81	5.14	42.81						
43X-2, 107-108	396.07	408.29	6.11	50.93						
43X-4, 107-108	399.07	411.29	5.67	47.21	5.78	0.11	0.03	0.00	4.1	
43X-6, 107-108	402.07	414.29	6.03	50.23						
44X-2, 107-108	405.77	417.99	5.05	42.03						
44X-4, 107-108	408.77	420.99	5.86	48.82	5.98	0.12	0.03	0.00	3.9	
44X-6, 107-108	411.77	423.99	5.98	49.83						
45X-2, 107-108	415.47	427.69	5.72	47.66						
45X-4, 107-108	418.47	430.69	5.50	45.85	3.62	0.00	0.04	0.00	0.0	
45X-6, 107-108	421.47	433.69	5.14	42.78						
46X-2, 107-108	425.07	437.29	4.58	38.12						
46X-4, 107-108	428.07	440.29	5.45	45.44	5.53	0.08	0.03	0.00	2.7	
46X-6, 107-108	431.07	443.29	5.67	47.25						

Table T14 (continued).

Core, section, interval (cm)	Depth (mbsf)	Depth (mcd)	IC (wt%)	$CaCO_3$ (wt%)	TC (wt%)	TOC (wt%)	TN (wt%)	TS (wt%)	C/N	S/C
47X-2, 107-108	434.77	446.99	5.52	46.02						
47X-4, 107-108	437.77	449.99	5.39	44.91	5.43	0.04	0.03	0.00	1.3	
47X-6, 107-108	440.77	452.99	5.51	45.94						
48X-2, 107-108	444.37	456.59	3.43	28.60						
48X-4, 107-108	447.37	459.59	5.90	49.14	5.91	0.01	0.02	0.00	0.4	
49X-2, 107-108	453.97	466.19	6.27	52.23						
49X-4, 107-108	456.97	469.19	6.57	54.73	6.74	0.17	0.03	0.00	7.0	
49X-6, 107-108	459.97	472.19	7.72	64.29						
50X-2, 107-108	463.57	475.79	9.14	76.14	9.17	0.03	0.02	0.00	1.8	
51X-1, 6-7	468.06	480.28	4.08	33.96	4.19	0.12	0.02	0.00	4.9	
52X- CC, 16-17	473.26	485.48	3.58	29.82	4.05	0.47	0.05	0.60	10.3	1.3
53X-1, 61-62	478.31	490.53	3.08	25.69	3.52	0.44	0.05	0.89	9.0	2.0
54X-1, 67-69	483.37	495.59	3.03	25.27	3.48	0.44	0.05	0.52	9.3	1.2
55X-1, 63-64	487.93	500.15	3.74	31.12	4.15	0.42	0.10	0.59	4.3	1.4
56X-1, 56-57	492.86	505.08	2.77	23.05	3.24	0.47	0.09	0.64	5.1	1.3
57X-1, 91-92	502.61	514.83	4.49	37.43						
57X-4, 94-95	507.14	519.36	3.70	30.83	4.00	0.30	0.06	0.77	5.4	2.6
57X-5, 147-148	509.17	521.39	4.06	33.79						
58X-1, 26-27	511.56	523.78	4.35	36.20						
58X-3, 142-143	515.32	527.54	4.54	37.80	4.80	0.26	0.09	0.49	3.0	1.9
58X-4, 67-68	516.07	528.29	4.60	38.32						
59X-1, 40-42	521.40	533.62	3.98	33.14						
59X-2, 52-54	523.02	535.24	3.53	29.40	3.82	0.29	0.12	1.03	2.4	3.6
59X-4, 65-67	526.15	538.37	3.38	28.14						
60X-1, 39-41	530.99	543.21	4.11	34.27	4.32	0.20	0.05	0.31	4.0	1.5
61X-1, 77-79	540.97	553.19	4.26	35.47	4.53	0.27	0.06	0.37	4.6	1.3
62X-2, 107-108	552.47	564.69	3.47	28.93						
62X-4, 107-108	555.47	567.69	4.49	37.39	4.70	0.22	0.06	0.27	3.6	1.3
62X-6, 107-108	558.47	570.69	4.15	34.56						
63X-2, 107-108	562.07	574.29	3.56	29.64						
63X-4, 107-108	564.77	576.99	4.39	36.59	4.69	0.30	0.09	1.16	3.3	3.9
64X-2, 107-108	571.67	583.89	4.72	39.28	5.37	0.66	0.05	0.38	13.1	0.6
65X-1, 103-105	579.83	592.05	7.89	65.69	7.98	0.09	0.03	0.46	3.0	5.1
66X-2, 107-108	590.97	603.19	4.00	33.29						
66X-4, 107-108	593.97	606.19	2.78	23.13	3.21	0.44	0.08	0.34	5.5	0.8
66X-6, 107-108	596.97	609.19	4.22	35.19						
67X-1, 104-105	599.04	611.26	3.70	30.80						
67X-2, 105-106	600.55	612.77	4.23	35.27	4.61	0.37	0.06	0.10	6.2	0.3
67X-5, 105-106	605.05	617.27	4.28	35.62						
68X-2, 83-84	609.11	621.33	4.02	33.46						
68X-4, 105-106	611.73	623.95	4.43	36.93	4.65	0.22	0.05	0.29	4.4	1.3
68X-6, 118-119	614.82	627.04	3.80	31.65						
69X-2, 106-107	619.76	631.98	4.65	38.76						
69X-4, 108-109	622.78	635.00	5.41	45.11	5.70	0.29	0.05	0.59	5.8	2.0
69X-6, 104-105	625.74	637.96	4.15	34.59						
70X-2, 110-111	629.40	641.62	4.07	33.88						
70X-4, 112-113	632.42	644.64	3.25	27.08	3.45	0.20	0.05	0.47	3.9	2.4
70X-6, 105-106	635.36	647.58	4.12	34.28						
71X-2, 104-105	639.04	651.26	4.41	36.74						
71X-4, 115-116	642.15	654.37	3.40	28.36	3.74	0.33	0.11	0.43	3.0	1.3
71X-6, 116-117	645.16	657.38	3.75	31.20						
72X-2, 103-104	648.73	660.95	3.64	30.35						
72X-4, 107-108	651.77	663.99	3.88	32.34	4.26	0.38	0.05	0.74	7.6	1.9
72X-6, 106-107	654.76	666.98	3.14	26.17						
73X-2, 105-106	658.45	670.67	5.86	48.80						
73X-4, 104-105	661.44	673.66	3.97	33.07	4.31	0.34	0.06	0.45	5.7	1.3
73X-6, 103-104	664.43	676.65	3.88	32.35						
74X-2, 107-108	668.07	680.29	2.79	23.28						
74X-4, 107-108	671.07	683.29	4.27	35.57	4.76	0.49	0.06	0.56	8.1	1.2
74X-6, 102-103	674.02	686.24	3.26	27.16						
75X-2, 107-108	677.58	689.80	3.47	28.89						
75X-4, 107-108	680.08	692.30	3.24	26.98	3.63	0.39	0.06	0.37	6.5	0.9
76X-2, 107-108	687.37	699.59	3.24	26.96						
76X-4, 107-108	690.16	702.38	2.33	19.37	2.77	0.45	0.07	0.55	6.4	1.2
77X-2, 107-108	696.97	709.19	2.47	20.54						
77X-4, 107-108	699.97	712.19	3.50	29.14	3.93	0.44	0.06	0.38	7.3	0.9
77X-6, 107-108	702.97	715.19	2.91	24.21						

Note: IC = inorganic carbon, $CaCO_3$ = carbonate, TC = total carbon, TOC = total organic carbon, TN = total nitrogen, TS = total sulfur, C/N = carbon/nitrogen ratio, S/C = sulfur/carbon ratio.

Table T15. Rock-Eval pyrolysis results for selected samples, Hole 1148A.

Sample	Depth (mbsf)	Depth (mcd)	T_{max}	S_1	S_2	S_3	PI	HI	OI	TOC (R-E)	TOC (TC – IC)
184-1148A-											
Interval 1:											
2H-4, 107-108	6.37	11.22	384	0.07	0.32	2.33	0.18	80	582	0.40	0.58
3H-4, 107-108	15.80	20.65	372	0.06	0.18	2.12	0.25	50	588	0.36	0.57
4H-4, 107-108	25.37	30.22	393	0.13	0.50	2.75	0.21	84	466	0.59	0.79
5H-4, 107-108	34.87	39.72	375	0.06	0.17	2.46	0.27	80	1171	0.21	0.43
6H-4, 107-108	44.37	50.17	374	0.04	0.12	1.41	0.25	40	470	0.30	0.44
10H-4, 107-108	82.37	90.04	374	0.03	0.09	1.24	0.25	45	620	0.20	0.44
51X-1, 6-7	468.06	480.28	371	0.02	0.03	0.68	0.50	150	3400	0.02	0.12
Interval 2:											
52X-CC, 16-17	473.26	485.48	417	0.06	0.76	2.03	0.07	146	390	0.52	0.47
53X-1, 61-62	478.31	490.53	408	0.04	0.54	1.24	0.07	131	302	0.41	0.44
54X-1, 67-69	483.37	495.59	409	0.04	0.55	0.97	0.05	141	248	0.39	0.44
55X-1, 63-64	487.93	500.15	412	0.03	0.54	1.21	0.05	131	295	0.41	0.42
56X-1, 56-57	492.86	505.08	408	0.03	0.64	1.31	0.06	145	297	0.44	0.47
Interval 3:											
64X-2, 107-108	571.67	583.89	414	0.01	0.29	0.53	0.03	103	189	0.28	0.66
67X-2, 105-106	600.55	612.77	415	0.01	0.35	0.53	0.03	120	179	0.29	0.37
70X-4, 112-113	632.42	644.64	415	0.01	0.32	0.53	0.03	114	189	0.28	0.20
74X-4, 107-108	671.07	683.29	424	0.01	0.73	0.53	0.01	169	120	0.43	0.49
75X-4, 107-108	680.08	692.30	424	0.02	0.45	0.51	0.04	132	150	0.34	0.39
76X-4, 107-108	690.16	702.38	415	0.02	0.51	0.89	0.04	115	202	0.44	0.45
77X-4, 107-108	699.97	712.19	419	0.01	0.43	0.63	0.02	122	180	0.35	0.44

Notes: T_{max} = temperature (°C) of maximum release of pyrolysis HC, S_1 = mg/g volatile HC, S_2 = pyrolysis HC mg/g, S_3 = pyrolysis CO_2 mg/g, PI = production index, HI = hydrogen index, OI = oxygen index, TOC = total organic carbon, R-E = Rock-Eval, TC = total carbon, IC = inorganic carbon. For methods, see **"Organic Geochemistry,"** p. 14, in the "Explanatory Notes" chapter.

Table T16. Composition of interstitial waters in Holes 1148A and 1148B.

Core, section, interval (cm)	Depth (mbsf)	Depth (mcd)	pH	Alkalinity (mM)	Salinity	Cl^- (mM)	Na^+ (mM)	K^+ (mM)	Mg^{2+} (mM)	Ca^{2+} (mM)	SO_4^{2-} (mM)	HPO_4^{2-} (µM)	NH_4^+ (mM)	H_4SiO_4 (µM)	Li^+ (µM)	Sr^{2+} (µM)
184-1148A-																
2H-3, 145-150	5.28	10.13	7.50	10.25	35.0	548.0	469	11.7	51.3	8.8	21.6	47.7	0.87	631	22	87
3H-3, 145-150	14.71	19.56	7.35	11.64	34.5	557.0	477	11.2	50.7	8.3	19.1	46.1	0.89	702	23	90
4H-3, 145-150	24.28	29.13	7.31	11.32	34.5	557.5	475	10.9	50.4	7.9	17.6	31.3	1.00	735	27	92
5H-3, 145-150	33.78	38.63	7.29	11.21	34.0	559.5	479	10.7	48.5	7.6	16.4	20.2	0.97	670	30	98
6H-3, 145-150	43.28	49.08	7.16	10.76	34.0	560.0	481	10.1	48.2	7.6	16.5	13.8	1.03	605	33	106
9H-3, 145-150	71.78	79.45	7.34	8.79	34.0	559.0	480	8.5	45.7	6.8	13.7	1.0	1.10	227	26	136
12H-3, 145-150	100.28	109.95	7.32	7.21	34.0	560.0	482	7.3	43.6	7.0	12.6	0.3	1.19	214	27	191
15H-3, 145-150	128.78	140.78	7.28	4.94	33.0	557.0	482	6.3	42.2	8.0	13.1	0.2	0.96	223	30	277
18X-3, 145-150	157.38	169.60	7.30	3.43	33.5	558.0	477	5.9	41.8	10.1	14.0	0.2	0.98	195	35	368
21X-3, 145-150	186.28	198.50	7.31	3.05	34.0	559.0	477	5.5	41.6	11.9	15.1	0.2	0.75	175	52	463
24X-3, 145-150	215.28	227.50	7.30	3.02	34.0	559.5	477	6.0	41.3	13.4	16.0	0.2	0.66	167	97	625
27X-3, 145-150	244.08	256.30	7.19	2.93	34.0	553.0	473	5.4	41.5	15.1	15.8	0.2	0.61	218	172	697
30X-3, 140-150	272.85	285.07	7.12	3.89	34.0	555.0	453	5.0	47.0	17.0	16.2	0.5	0.70	274	630	819
33X-3, 140-150	301.75	313.97	7.13	3.44	34.0	559.5	465	5.0	38.9	18.2	14.9	0.3	0.76	267	930	878
36X-3, 140-150	330.65	342.87	7.05	3.89	33.5	556.0	463	4.3	37.7	19.8	15.1	0.2	0.64	349	1210	926
39X-3, 140-150	359.35	371.57	7.33	4.66	33.0	547.5	453	4.0	37.0	21.9	13.4	0.3	0.70	400	1460	1008
42X-3, 140-150	388.35	400.57	7.50	3.41	33.0	555.0	465	4.4	32.0	22.3	11.9	0.2	0.85	406	1480	989
45X-3, 135-150	417.33	429.55	7.06	3.46	33.0	551.5	459	4.1	30.8	23.6	10.7	0.2	0.90	316	1700	996
48X-3, 135-150	446.23	458.45			33.0	558.5		4.4	27.4	23.7	9.1	0.2	1.07	271	1910	1009
57X-3, 140-150	506.15	518.37	6.75	6.13	31.0	538.5	441	3.6	25.5	27.0	4.9	0.3	0.93	658	2020	1028
62X-3, 135-150	554.33	566.55	6.96	3.76	33.0	562.0	462	3.8	23.4	28.3	4.4	0.5	1.10	511	1990	1070
65X-1, 135-150	580.23	592.45			32.0	559.0		3.3	22.2	28.8	4.0	0.5	1.39	495	1920	994
68X-7, 115-130	616.37	628.59			33.0	568.0		3.4	22.0	29.2	3.7	0.3	1.20	104	1770	1045
71X-3, 135-150	640.93	653.15	7.52	1.85	36.0	569.0	465	3.1	22.7	30.0	3.7	0.2	1.18	127	1720	1100
74X-3, 135-150	669.93	682.15	7.66	2.00	33.0	568.0	466	3.0	22.4	30.2	4.7	0.2	1.22	97	1710	1151
184-1148B-																
18X-3, 135-150	463.53	469.78	6.96	3.42	33.5	566.0										
20X-1, 132-150	479.71	485.96	6.87	5.17	33.0	565.0										
25X-3, 135-150	521.03	527.28	6.91	4.56	32.5	547.0										
39X-3, 135-150	704.23	710.48			32.5	559.0										
42X-3, 135-152	733.14	739.39			33.0	577.0										
45X-3, 135-150	761.73	767.98	7.61	1.58	33.5	565.0										
49X-1, 135-150	795.93	802.18	7.76	1.40	33.5	573.0										

Table T17. Thermal conductivity measurements at Site 1148. (See table note. Continued on next two pages.)

Leg	Site	Hole	Core	Type	Section	Top interval (cm)	Depth (mbsf)	Depth (mcd)	Thermal conductivity (W/[m·K])	Thermal conductivity (3-pt mean)
184	1148	A	2	H	4	75	6.05	10.90	0.857	
184	1148	A	2	H	4	75	6.05	10.90	0.843	
184	1148	A	2	H	4	75	6.05	10.90	0.854	0.85
184	1148	A	3	H	4	75	15.48	20.33	0.949	
184	1148	A	3	H	4	75	15.48	20.33	0.943	
184	1148	A	3	H	4	75	15.48	20.33	0.961	0.95
184	1148	A	4	H	4	75	25.05	29.90	0.962	
184	1148	A	4	H	4	75	25.05	29.90	0.906	
184	1148	A	4	H	4	75	25.05	29.90	0.937	0.94
184	1148	A	5	H	5	75	36.05	40.90	0.949	
184	1148	A	5	H	5	75	36.05	40.90	0.995	
184	1148	A	5	H	5	75	36.05	40.90	0.948	0.96
184	1148	A	6	H	4	75	44.05	49.85	1.012	
184	1148	A	6	H	4	75	44.05	49.85	1.015	
184	1148	A	6	H	4	75	44.05	49.85	0.999	1.01
184	1148	A	7	H	4	75	53.55	60.45	0.984	
184	1148	A	7	H	4	75	53.55	60.45	0.953	
184	1148	A	7	H	4	75	53.55	60.45	0.966	0.97
184	1148	A	8	H	4	75	63.05	70.42	1.145	
184	1148	A	8	H	4	75	63.05	70.42	1.096	
184	1148	A	8	H	4	75	63.05	70.42	1.102	1.11
184	1148	A	9	H	4	75	72.55	80.22	1.089	
184	1148	A	9	H	4	75	72.55	80.22	1.065	
184	1148	A	9	H	4	75	72.55	80.22	1.068	1.07
184	1148	A	10	H	4	75	82.05	89.72	1.171	
184	1148	A	10	H	4	75	82.05	89.72	1.159	
184	1148	A	10	H	4	75	82.05	89.72	1.190	1.17
184	1148	A	11	H	4	75	91.55	100.27	1.009	
184	1148	A	11	H	4	75	91.55	100.27	0.979	
184	1148	A	11	H	4	75	91.55	100.27	0.988	0.99
184	1148	A	12	H	4	75	101.05	110.72	1.159	
184	1148	A	12	H	4	75	101.05	110.72	1.174	
184	1148	A	12	H	4	75	101.05	110.72	1.165	1.17
184	1148	A	13	H	4	75	110.55	121.65	1.118	
184	1148	A	13	H	4	75	110.55	121.65	1.146	
184	1148	A	13	H	4	75	110.55	121.65	1.136	1.13
184	1148	A	14	H	4	75	120.05	131.60	1.126	
184	1148	A	14	H	4	75	120.05	131.60	1.167	
184	1148	A	14	H	4	75	120.05	131.60	1.155	1.15
184	1148	A	15	H	4	75	129.55	141.55	1.162	
184	1148	A	15	H	4	75	129.55	141.55	1.163	
184	1148	A	15	H	4	75	129.55	141.55	1.158	1.16
184	1148	A	16	H	4	75	139.05	151.27	1.154	
184	1148	A	16	H	4	75	139.05	151.27	1.150	
184	1148	A	16	H	4	75	139.05	151.27	1.150	1.15
184	1148	A	17	X	4	75	148.55	160.77	1.052	
184	1148	A	17	X	4	75	148.55	160.77	1.086	
184	1148	A	17	X	4	75	148.55	160.77	1.036	1.06
184	1148	A	18	X	4	75	158.15	170.37	1.121	
184	1148	A	18	X	4	75	158.15	170.37	1.055	
184	1148	A	18	X	4	75	158.15	170.37	1.148	1.11
184	1148	A	19	X	4	75	167.75	179.97	1.084	
184	1148	A	19	X	4	75	167.75	179.97	1.057	
184	1148	A	19	X	4	75	167.75	179.97	1.087	1.08
184	1148	A	20	X	4	75	177.35	189.57	1.122	
184	1148	A	20	X	4	75	177.35	189.57	1.190	
184	1148	A	20	X	4	75	177.35	189.57	1.146	1.15
184	1148	A	21	X	4	75	187.05	199.27	1.271	
184	1148	A	21	X	4	75	187.05	199.27	1.289	
184	1148	A	21	X	4	75	187.05	199.27	1.285	1.28
184	1148	A	22	X	4	75	196.75	208.97	1.140	
184	1148	A	22	X	4	75	196.75	208.97	1.188	
184	1148	A	22	X	4	75	196.75	208.97	1.120	1.15
184	1148	A	23	X	4	75	206.35	218.57	1.263	
184	1148	A	23	X	4	75	206.35	218.57	1.182	
184	1148	A	23	X	4	75	206.35	218.57	1.167	1.20
184	1148	A	24	X	4	75	216.05	228.27	1.220	

Table T17 (continued).

Leg	Site	Hole	Core	Type	Section	Top interval (cm)	Depth (mbsf)	Depth (mcd)	Thermal conductivity (W/[m·K])	Thermal conductivity (3-pt mean)
184	1148	A	24	X	4	75	216.05	228.27	1.170	
184	1148	A	24	X	4	75	216.05	228.27	1.147	1.18
184	1148	A	25	X	4	75	225.65	237.87	1.170	
184	1148	A	25	X	4	75	225.65	237.87	1.173	
184	1148	A	25	X	4	75	225.65	237.87	1.158	1.17
184	1148	A	26	X	4	75	235.25	247.47	1.106	
184	1148	A	26	X	4	75	235.25	247.47	1.076	
184	1148	A	26	X	4	75	235.25	247.47	1.077	1.09
184	1148	A	27	X	4	75	244.85	257.07	1.119	
184	1148	A	27	X	4	75	244.85	257.07	1.118	
184	1148	A	27	X	4	75	244.85	257.07	1.115	1.12
184	1148	A	28	X	4	75	254.45	266.67	1.034	
184	1148	A	28	X	4	75	254.45	266.67	1.029	
184	1148	A	28	X	4	75	254.45	266.67	1.017	1.03
184	1148	A	29	X	4	75	264.05	276.27	1.141	
184	1148	A	29	X	4	75	264.05	276.27	1.135	
184	1148	A	29	X	4	75	264.05	276.27	1.125	1.13
184	1148	A	30	X	4	75	273.65	285.87	1.075	
184	1148	A	30	X	4	75	273.65	285.87	1.074	
184	1148	A	30	X	4	75	273.65	285.87	1.095	1.08
184	1148	A	31	X	4	75	283.25	295.47	1.232	
184	1148	A	31	X	4	75	283.25	295.47	1.214	
184	1148	A	31	X	4	75	283.25	295.47	1.225	1.22
184	1148	A	32	X	4	75	292.85	305.07	1.228	
184	1148	A	32	X	4	75	292.85	305.07	1.188	
184	1148	A	32	X	4	75	292.85	305.07	1.186	1.20
184	1148	A	33	X	4	75	302.55	314.77	1.250	
184	1148	A	33	X	4	75	302.55	314.77	1.153	
184	1148	A	33	X	4	75	302.55	314.77	1.158	1.19
184	1148	B	1	H	4	75	5.25	5.25	0.750	
184	1148	B	1	H	4	75	5.25	5.25	0.767	
184	1148	B	1	H	4	75	5.25	5.25	0.773	0.76
184	1148	B	2	H	4	75	13.35	13.35	0.909	
184	1148	B	2	H	4	75	13.35	13.35	0.900	
184	1148	B	2	H	4	75	13.35	13.35	0.897	0.90
184	1148	B	3	H	4	75	22.68	23.53	0.917	
184	1148	B	3	H	4	75	22.68	23.53	0.933	
184	1148	B	3	H	4	75	22.68	23.53	0.933	0.93
184	1148	B	4	H	4	75	32.18	31.15	0.933	
184	1148	B	4	H	4	75	32.18	31.15	0.907	
184	1148	B	4	H	4	75	32.18	31.15	0.920	0.92
184	1148	B	5	H	4	75	45.85	45.50	1.026	
184	1148	B	5	H	4	75	45.85	45.50	1.021	
184	1148	B	5	H	4	75	45.85	45.50	1.002	1.02
184	1148	B	6	H	4	75	55.35	55.70	0.956	
184	1148	B	6	H	4	75	55.35	55.70	0.952	
184	1148	B	6	H	4	75	55.35	55.70	0.960	0.96
184	1148	B	7	H	4	75	64.82	66.12	0.853	
184	1148	B	7	H	4	75	64.82	66.12	0.880	
184	1148	B	7	H	4	75	64.82	66.12	0.905	0.88
184	1148	B	8	H	4	75	74.35	76.07	1.086	
184	1148	B	8	H	4	75	74.35	76.07	1.112	
184	1148	B	8	H	4	75	74.35	76.07	1.123	1.11
184	1148	B	9	H	4	75	83.85	85.42	1.091	
184	1148	B	9	H	4	75	83.85	85.42	1.127	
184	1148	B	9	H	4	75	83.85	85.42	1.163	1.13
184	1148	B	10	H	4	75	93.35	95.67	1.094	
184	1148	B	10	H	4	75	93.35	95.67	1.064	
184	1148	B	10	H	4	75	93.35	95.67	1.115	1.09
184	1148	B	11	H	4	75	102.85	106.17	0.993	
184	1148	B	11	H	4	75	102.85	106.17	0.978	
184	1148	B	11	H	4	75	102.85	106.17	0.975	0.98
184	1148	B	12	H	4	75	112.35	116.43	1.019	
184	1148	B	12	H	4	75	112.35	116.43	1.010	
184	1148	B	12	H	4	75	112.35	116.43	1.024	1.02
184	1148	B	13	H	4	75	121.85	126.55	0.788	

Table T17 (continued).

Leg	Site	Hole	Core	Type	Section	Top interval (cm)	Depth (mbsf)	Depth (mcd)	Thermal conductivity (W/[m·K])	Thermal conductivity (3-pt mean)
184	1148	B	13	H	4	75	121.85	126.55	0.789	
184	1148	B	13	H	4	75	121.85	126.55	0.784	0.79
184	1148	B	14	H	4	75	131.35	136.55	1.146	
184	1148	B	14	H	4	75	131.35	136.55	1.127	
184	1148	B	14	H	4	75	131.35	136.55	1.162	1.15
184	1148	B	15	H	4	75	140.57	146.82	1.038	
184	1148	B	15	H	4	75	140.57	146.82	1.041	
184	1148	B	15	H	4	75	140.57	146.82	1.045	1.04

Note: This table is also available in **ASCII format.**

Table T18. Summary of logging operations at Site 1148.

Date (April 1999)	Time (UTC)	
4	0950	Hole preparation complete, rig up wireline.
4	1036	Rig into hole with HNGS-APS-HLDS-DIT.
4	1323	Uplog at 275 m/hr from 711 to 669.5 mbsf. Rig into hole to total depth.
4	1342	Uplog at 275 m/hr from 711 mbsf to EOP. Pull out of hole.
4		Pipe trip to new EOP at 200.7 mbsf.
4	2030	Rig into hole with NGT-FMS-LSS.
4	2251	Uplog at 275 m/hr from 711 mbsf to EOP. Rig into hole to total depth.
5	0105	Uplog at 275 m/hr from 711 mbsf to EOP. Pull out of hole.
		Wiper trip to new EOP at 200 mbsf.
5	0635	Rig into hole with NGT-GHMT-GPIT.
5	0921	Uplog at 550 m/hr from 711 mbsf to EOP. Rig into hole to total depth.
5	1035	Uplog at 550 m/hr from 711 mbsf to EOP. Rig into hole to total depth.
5	1205	Uplog at 550 m/hr from 711 mbsf to EOP. Pull out of hole.
5	1500	End of logging operations.

Note: UTC = Universal Time Coordinated, HNGS = hostile environment natural gamma-ray sonde, APS = accelerator porosity sonde, HLDS = hostile environment lithodensity sonde, DIT = dual-induction tool, EOP = end of pipe, NGT = natural gamma-ray tool, FMS = Formation MicroScanner, LSS = long-spaced sonic logging tool, GHMT = geological high-resolution magnetic tool, GPIT = general-purpose inclinometer tool.

CHAPTER NOTES*

N1. 13 March 2001—Errata: After this chapter was published, it was found that the "Core, section, interval (cm)" column of Table T12 was incorrect. The corrected column appears in this version.

*Dates reflect file corrections or revisions.